UNIVERSITY OF CALIFORNIA

Los Angeles

Analytical Modeling of Cyclic Shear - Flexure Interaction in Reinforced Concrete Structural Walls

A dissertation in partial satisfaction of the

requirements for the degree Doctor of Philosophy

in Civil Engineering

by

Kristijan Imre Kolozvari

2013

ABSTRACT OF THE DISSERTATION

Analytical Modeling of Cyclic Shear - Flexure Interaction in Reinforced Concrete Structural Walls

by

Kristijan Imre Kolozvari

Doctor of Philosophy in Civil Engineering

University of California, Los Angeles, 2013

Professor John W. Wallace, Chair

A study was conducted to develop a modeling approach that integrates flexure and shear interaction under cyclic loading conditions to obtain reliable predictions of inelastic responses of reinforced concrete (RC) structural walls. The proposed modeling approach incorporates cyclic RC panel constitutive behavior based on an interpretation of the fixed-strut-angle approach into a two-dimensional fiber-based macroscopic model. Coupling of axial and shear responses under cyclic loading is achieved at the fiber (panel) level, which further allows coupling of flexural and shear responses at the element level.

The sensitivity of model results to various modeling parameters (e.g., material constitutive parameters and modeling parameters), wall configuration parameters (e.g., aspect ratio, boundary and web reinforcement ratios), and response parameters (levels of wall axial load and shear) was

investigated to demonstrate the ability of the model to predict the behavior or RC walls for a broad range of conditions. The proposed analytical model was validated and calibrated against experimental results obtained from six large-scale, heavily instrumented, cantilever structural wall specimens characterized with different aspect ratios (1.5, 2.0 and 3.0), axial load levels (0.0025 $A_g f'_c$, 0.07 $A_g f'_c$ and 0.10 $A_g f'_c$) and wall shear stress levels (between approximately 4 and 8 $\sqrt{f'_c}$ psi) tested under combined constant axial load and reversed cyclic lateral loading applied at the top of the wall.

Comparisons of experimental and analytical model results for moderately slender RC walls (aspect ratio 1.5 and 2.0) revealed that the model successfully captures experimentally observed interaction between nonlinear shear and flexural deformations under cyclic loading and predicts lateral strength and stiffness that is within 10% of experimentally measured values. In addition, the magnitudes and relative contributions of shear and flexural deformations along the wall height were predicted closely at low and moderate drift levels, whereas at drift levels larger than 2.0%, model results were within 25% of experimentally measured deformation components. As well, localized nonlinear responses such as vertical tensile and compressive strains and wall rotations at the wall base were well predicted by the model. The model results were less accurate for the slender (aspect ratio 3.0) RC wall specimen in terms of relative contributions of shear and flexural deformations and magnitudes of compressive strains.

Demonstrated model sensitivity to parameters of the implemented RC panel behavior suggested the need for calibration of these parameters for reliable predictions of nonlinear wall behavior. Given the limited model calibration performed in this study, additional work is needed,

particularly for slender RC walls where preliminary results were less accurate. Finally, the implementation of the model into a publicly available computational platform is required to enable more detailed system level studies and future model development.

The dissertation of Kristijan Imre Kolozvari is approved.

Kutay Orakcal

Ajit Mal

Jiun-Shyan Chen

Jian Zhang

John W. Wallace, Committee Chair

University of California, Los Angeles

2013

TABLE OF CONTENT

LIST OF FIGURES

LIST OF TABLES

ACKGNOWLEDGEMENTS

I would like to express my deepest gratitude to my research advisor, Professor John W. Wallace, for his invaluable guidance and support throughout my PhD studies at the University of California, Los Angeles. Special appreciation is extended to the members of the Doctoral Committee, Professors Jiun-Shyan Chen, Jian Zhang and Ajit Mal for their insightful comments. Particularly, I would like to express my gratitude to Professor Kutay Orakcal whose continuous involvement in research was greatly helpful. I would also like to thank Dr. Thien A. Tran for sharing the experimental data used in this research and collaboration.

My great appreciation is further extended to my aunt, Judit Cakanj, for her financial support throughout my PhD studies. Finally, I would like to thank to my parents Ljiljana Kolozvari and Imre Kolozvari for their love, support and guidance throughout my life. This Dissertation is dedicated to them.

VITA

2006	B.S., Structural Engineering Faculty of Civil Engineering, University of Belgrade, Serbia
2009	M.S., Structural Engineering Department of Civil and Environmental Engineering University of California, Los Angeles, USA
2003-2006	Teaching Assistant Faculty of Civil Engineering, University of Belgrade, Serbia
2007-2009	Structural Engineer Del-Ing. Ltd., Belgrade, Serbia
2009-2013	Graduate Student Researcher Department of Civil and Environmental Engineering University of California, Los Angeles, USA
2011-2013	Teaching Assistant Department of Civil and Environmental Engineering University of California, Los Angeles, USA

PUBLICATIONS AND PRESENTATIONS

Kolozvari, K., Tran, T., Orakcal, K., Wallace, J. "Modeling of Cyclic Shear-Flexure Interaction in Reinforced Concrete Structural Walls," *Proceedings of the 15th World Conference in Earthquake Engineering*, Lisbon, Portugal, September 2012, (Accepted for publication and presentation).

Kolozvari, K., Orakcal, K., Wallace, J. "Modeling of Cyclic Shear-Flexure Interaction in Reinforced Concrete Structural Walls - Model Description," *ASCE Journal of Structural Engineering*, (Under review).

Kolozvari, K., Tran, T., Orakcal, K., Wallace, J. "Modeling of Cyclic Shear-Flexure Interaction in Reinforced Concrete Structural Walls – Experimental Validation," *ASCE Journal of Structural Engineering*, (Under review).

Kolozvari, K., Orakcal, K., Wallace, J. "Modeling of Cyclic Shear-Flexure Interaction in Reinforced Concrete Structural Walls," *15th World Conference in Earthquake Engineering*, Lisbon, Portugal, September 2012, e.poster presentation.

Kolozvari, K., Orakcal, K., Wallace, J. "Cyclic Shear-Flexure Interaction in Reinforced Concrete Structural Walls - Modeling and Validation," *EERI Annual Meeting*, Seattle, WA, February 2013, poster presentation.

Kolozvari, K., Orakcal, K., Wallace, J. "Modeling of Shear-Flexure Interaction in Reinforced Concrete Structural Walls," *NEES Quake Summit*, July 2012, Boston, MA, poster presentation.

CHAPTER 1

INTRODUCTION

1.1 General

Reinforced concrete (RC) structural walls are very effective in resisting lateral loads imposed by wind and earthquake ground motions due to their high strength and stiffness. Their role is to provide sufficient lateral strength and stiffness to limit nonlinear behavior and lateral deformations during service level earthquakes, as well as to limit lateral deformations and provide nonlinear deformation capacity (ductility) during design and maximum considered earthquake level shaking.

Wall behavior is generally classified according to wall aspect ratio (h_w / l_w), or shear-span-to-depth ratio (M / Vl_w), as either shear-controlled (walls with aspect ratio less than approximately 1.0 to 1.5) or flexure-controlled (aspect ratios greater than 2.5 to 3.0). For walls between these aspect ratios, herein referred to as moderate aspect ratio walls, although flexural yielding is expected, nonlinear shear deformations may be significant and lead to reduced lateral stiffness, strength and ductility. Experimental results have shown that flexural and shear yielding occur near-simultaneously even when the wall nominal shear strength is as much as twice the shear developed at flexural yielding (Massone and Wallace, 2004) suggesting that there is an interaction between nonlinear flexural and shear modes of behavior, commonly referred to as shear-flexure interaction (SFI). This interaction has been observed experimentally even in

relatively slender RC walls with aspect ratios of 3.0 (Thomsen and Wallace, 1995) and 4.0 (Sayre, 2003), with shear deformations contributing approximately by 30% and 10% to lateral displacement at the first story and roof-level, respectively (Massone and Wallace, 2004). Recent test results reported by Tran and Wallace (2012) show that the degree of interaction increases for walls with aspect ratios of 1.5 and 2.0, with nonlinear shear deformations constituting as much as 35% and 30% of the wall top displacement, respectively.

Given the crucial role of RC walls in building seismic performance, it is essential that analytical models capably of capturing observed nonlinear hysteretic behavior are available. The use of element models based on uniaxial material stress-strain or force-deformation relations (so-called multiple-spring models), such as displacement-based or force-based fiber models and the Multiple-Vertical-Line-Element-Model (MVLEM, Vulcano et al., 1988; Fischinger et al., 1990; Orakcal et al., 2004), have become very common in both research (OpenSees, McKenna et al., 2000) and engineering practice (Perform-3D, Computers and Structures Inc., 2006). Although multiple-spring approaches have been shown to reasonably represent axial-bending behavior of reinforced concrete walls (Orakcal and Wallace, 2006; Wallace, 2007), these models generally do not incorporate experimentally-observed SFI, instead describing the shear behavior of a RC wall using ad-hoc force deformation rules defined independently from the axial/bending modeling parameters (Vulcano and Bertero 1987; Orakcal et al. 2004). Hence, most multiple-spring models have been calibrated using test results from relatively slender walls only, and even in those cases, the shear response tends to underestimate the non-linear shear deformations (Massone and Wallace, 2004). Previous research has shown that analytical predictions obtained using models that consider uncoupled axial/flexural and shear behavior may underestimate axial

compressive strains even in relatively slender RC walls controlled by flexure (Orakcal and Wallace, 2006), and overestimate the lateral load capacity of moderate-aspect-ratio walls (Tran, 2012) and low-aspect-ratio walls (Massone et al, 2006).

Various approaches have been proposed to capture the observed coupling between nonlinear flexural and shear behavior in RC walls (Colotti, 1993; Elwood, 2002; Massone et al., 2006 and 2009; Mullapudi and Ayoub, 2009; Jiang and Kurama, 2010; Zhang and Xu, 2010; Beyer et al., 2011; Panagiotou et al., 2011; Fischinger et al. 2012). Most of these approaches are based on use of fiber-type models (e.g. MVLEM) with interaction incorporated through biaxial representation of concrete behavior (e.g. modified compression field theory; Vecchio and Collins, 1986) within each macro-fiber, such as models proposed by Colotti (1993), Massone et al. (2006, 2009), Jiang and Kurama (2010), and Fischinger et al. (2012); this approach has been shown to be capable of capturing SFI in RC walls. Massone et al. (2006, 2009) provided comparisons of model predictions against experimental results for walls with aspect ratio (shear-span-to-depth ratio) of 3.0 (Thomsen and Wallace, 1995) as well as for walls with the shear-span-to-depth ratio of 0.5 (Massone, 2006; Massone et al, 2009). Although these studies indicate that the modeling approach captured nonlinear shear deformations and the coupling between shear and flexural responses, the model was limited to monotonic loading conditions. Jiang and Kurama (2010) provided comparisons between analytical and experimental results for a wall specimen with aspect ratio of 2.4 (Oesterle et al., 1979); however, the comparisons were presented only for lateral-load-versus-top displacement relations and for boundary longitudinal reinforcement (axial) strain, both of which are not overly sensitive to SFI (Orakcal and Wallace, 2006); the same holds for analytical model proposed by Mullapudi and Ayoub (2009) by Mullapudi et al.

(2009). A methodology based on a strut-and-tie (truss) modeling approach proposed by Panagiotou et al. (2011) has been shown to be a viable method to capture SFI; however, due to overlapping areas of vertical, horizontal, and diagonal concrete struts in the model, achieving accurate displacement responses over a broad range of response amplitudes is a challenge. As well, strut angles are pre-defined and do not change during the analysis, which may allow for reasonably comparisons with tests on isolated cantilever walls, but does not address variation in strut angles due to changes in axial load for walls with some degree of coupling. The approach proposed by Beyer et al. (2011) determines the degree of interaction from empirical relations derived from test results. Although this approach has been shown to produce reasonable estimation of the ratio between shear and flexural deformations for walls controlled by flexure, albeit with significant dispersion, the approach is limited due to its reliance on test data. The model by Elwood (2002) and Zhang and Xu (2010) are derived from column experimental results and have not been validated for structural walls. Overall, relatively little work has been completed to validate SFI models, primarily due to the lack of high-quality data to accomplish the validation work.

In summary, modeling approaches available in the literature for representing experimentally-observed SFI behavior are characterized with four significant shortcomings: (1) models are empirical or have cumbersome formulations, (2) models are capable of simulating monotonic responses only, (3) sensitivity of model results to material and modeling parameters have not been studied in detail, and (4) models have not been sufficiently validated against global (load-displacement) behavior and local responses (rotations, curvatures, strains) due to lack of detailed experimental data for walls characterized with modest to significant SFI. Therefore, there is a

need for a relatively simple analytical modeling approach that is able to predict important response characteristics of RC walls by incorporating coupling between axial/flexural and shear responses under reversed-cyclic loading conditions. In addition, the model needs to be validated at both global and local response levels for a range of response amplitudes against detailed data from heavily-instrumented tests of moderate-aspect ratio wall specimens.

1.2 Scope

Given the aforementioned shortcomings, a research project was initiated at the University of California Los Angeles (UCLA) to develop an analytical modeling approach that incorporates the interaction between axial/flexure and shear behavior as well as to calibrate and validate the model using detailed experimental data. The extensive experimental response information used for development and validation of the analytical model presented here were provided by a companion experimental study by Tran and Wallace (2012), also conducted at UCLA, which investigated cyclic response of five moderate aspect ratio RC wall specimens characterized with significant SFI and nonlinear shear deformations. In addition, analytical model results were calibrated against experimental data obtained for a RC wall specimen with aspect ratio of 3.0 (Thomsen and Wallace, 1995) in order to investigate the model capability to describe response of RC walls with flexure-dominated behavior.

The proposed modeling approach involves incorporating a cyclic constitutive RC panel model based on a fixed-crack-angle approach into the fiber-based (multi-spring) model formulation to simulate the observed coupling between nonlinear axial/flexural and shear responses in RC walls. The coupling of axial and shear responses is accounted for at the RC panel (macro-fiber)

level, which further allows coupling of flexural and shear responses at the model element level. Conceptually, the approach is similar to the one proposed by Massone et al. (2006), except that proposed approach includes reverse-cyclic material models, whereas the approach by Massone (2006) considered only monotonic responses due to limitations imposed by the implemented rotating-crack angle RC panel model.

In summary, the primary objectives of the presented study are to:

1) develop macroscopic modeling approach to simulate the coupling between axial/flexural and shear behavior of RC structural walls under reversed-cyclic loading by identifying and implementing a cyclic RC panel behavior into a fiber-based model formulation;

2) assess characteristics of model predictions at various response levels and locations;

3) investigate the sensitivity of model results to variations in model parameters and the capability of the model to capture important response features for walls with various modes of behavior and failure mechanisms;

4) calibrate the parameters of constitutive relationships for materials, RC panel model, and wall geometry against experimental results;

5) conduct comprehensive studies to compare analytical model results and experimental results at various response levels and locations to assess the robustness and accuracy of the analytical model and to recommend appropriate relations and values for material and model parameters as well as to identify potential model improvements;

6) implement the new cyclic SFI model along with the RC panel model and constitutive material models used in its formulation into the open-source computational platform developed by the Pacific Earthquake Engineering Research (PEER) Center, OpenSees (McKenna et al., 2000) so that it is available for public use and future development.

1.3 Organization

This dissertation is divided into eight chapters. Chapter 2 provides a summary of experimental evidence of SFI and an overview of previous research conducted on modeling of SFI in RC structural walls. A description of the proposed analytical model, including model formulation, implemented RC panel behavior, the cyclic material constitutive relationships, and numerical solution strategies adopted to conduct nonlinear analyses using the analytical model are given in Chapter 3. Chapter 4 provides a description of model attributes and summarizes results of model predictions to assess model capabilities and sensitivities to various model parameters and wall configurations. Chapter 5 provides a description of the experimental program used to validate the analytical model for moderately slender RC walls with aspect ratios of 1.5 and 2.0, as well as detailed information on model calibration for these wall specimens. Chapter 6 provides comparisons of model results with experimental results for walls with aspect ratios of 1.5 and 2.0 at various response levels and locations, whereas Chapter 7 provides similar information for a RC wall with aspect ratio of 3.0. A summary and conclusions, along with recommendations for model improvements, are presented in Chapter 8.

CHAPTER 2

LITERATURE REVIEW

An overview of experimental studies on reinforced concrete (RC) structural walls that provide evidence of interaction between shear and axial/bending (flexural) responses is presented at the beginning of this chapter, followed by an overview of prior research on modeling of nonlinear behavior of RC walls including models with uncoupled and coupled shear and flexural responses.

2.1 Experimental Evidence of Shear-Flexure Interaction

Interaction between nonlinear shear and flexural behavior in RC walls was first observed from experimental results by Oesterle et al. (1976 and 1979) obtained for moderately-slender RC wall specimens of aspect ratio 2.4. These experimental data indicated that inelastic shear deformations occur even for walls that yield in flexure, and that the nonlinear deformations in shear and flexure occured nearly simultaneously, which demonstrated coupling between nonlinear shear and flexural behavior, commonly referred to as shear-flexure interaction (SFI). To better understand these observations, Massone and Wallace (2004) conducted detailed assessments of experimental results for two, well instrumented slender RC wall specimens with rectangular cross sections (specimens RW2 tested by Thomsen and Wallace (1995), and specimen SRCW1 tested by Sayre (2003)) by determining the deformations associated with flexure and shear to assess their relative contributions to displacement responses. In addition, recent experimental

study by Tran and Wallace (2012), conducted on five heavily instrumented moderately-slender RC wall specimens, provided detailed experimental data for RC walls that experienced significant nonlinear shear deformations and SFI. An overview of studies by Massone and Wallace (2004) and Tran and Wallace (2012) is presented in the following sections.

2.1.1 Massone and Wallace (2004)

2.1.1.1 Overview of Experimental Program

Two, approximately quarter-scale, slender cantilever RC wall specimens were used to assess the relative deformations associated with shear and flexure: (1) RW2 tested by Thomsen and Wallace (2004), and (2) SRCW1 tested by Sayre (2003). Wall specimens were proportioned and detailed using a capacity design approach for shear and a displacement-based design approach for wall boundary element detailing. Specimen RW2 was 3.66 m (12 ft) tall and 102 mm (4 in.) thick, with a web length of 1.22 m (4 ft), while specimen SRCW1 was 4.88 m (16 ft) tall, 152 mm (6 in.) thick, and 1.22 m (4 ft) long. Specimens were tested in the upright position under reversed cyclic loading conditions and a constant axial load of approximately $0.10A_g f'_c$. Cyclic lateral displacements were applied to the walls by a hydraulic actuator at 3.81 m (12.5 ft) above the base of specimen RW2, and at 4.88 m (16 ft) above the base of specimen SRCW1; therefore, shear-span-to-depth ratio (M/Vl_w), or aspect ratio (h_w/l_w), of wall specimens RW2 and SRCW1 were 3.0 and 4.0, respectively.

Longitudinal boundary reinforcement of specimen RW2 consisted of 8 - #3 (A_b = 71 mm^2 = 0.11 in^2) bars, whereas web reinforcement consisted of two curtains of deformed #2 (A_b = 32 mm^2 = 0.049 in^2) bars placed horizontally and vertically with a spacing of 189 mm (7.5 in.) on center.

Specimen SRCW1 was characterized with vertical reinforcement at wall boundaries that consisted of a W6x9 section (A_{b1} = 1729 mm^2 = 2.68 in^2) surrounded by 8 - #4 (A_{b2} = 1032 mm^2 = 1.60 in^2) bars, and web reinforcement that consisted of two curtains of horizontal and vertical #3 bars at a spacing of 152 mm (6 in.) on center. Grade 60 (414 MPa) bars were used for longitudinal and web reinforcement of both wall specimens, whereas A572 Grade 50 (345 MPa) W6x9 sections were used for SRCW1. Design concrete compressive strengths were 27.6 MPa (4,000 psi) for specimen RW2 and 345 MPa (5000 psi) for specimen SRCW1.

Both wall specimens were heavily instrumented to measure displacements, loads, and strains at critical locations. Wire potentiometers (WPs) were mounted to a rigid steel reference frame to measure lateral displacements over the wall height as shown on Figure 2-1. Displacements measured with the WPs were corrected using the measurements from linear potentiometers (LPs) mounted horizontally and vertically on the wall foundation, which measured any horizontal slip of the foundation block (pedestal) along the strong floor as well as rotations caused by uplift of the pedestal from the strong floor. In addition, two WPs mounted directly to the wall ends measured axial (vertical) displacements at the wall boundaries used to calculate wall base rotations by dividing the difference in relative axial displacements by the distance between the potentiometers. Shear deformations within the first two levels of specimen RW2 and first three levels of specimen SRCW1 were determined using measurements from WPs placed on the walls diagonally in an “X” configuration as shown on Figure 2-1.

Vertically oriented linear variable differential transducers (LVDTs) over the wall length just above the wall-pedestal interface were used to obtain average axial strains and to enable calculation of section curvatures. Strains in the reinforcing steel were measured using strain

gauges mounted near the wall base and at other locations. Further details of experimental programs are provided in papers by Thomsen and Wallace (2004) and Sayre (2003).

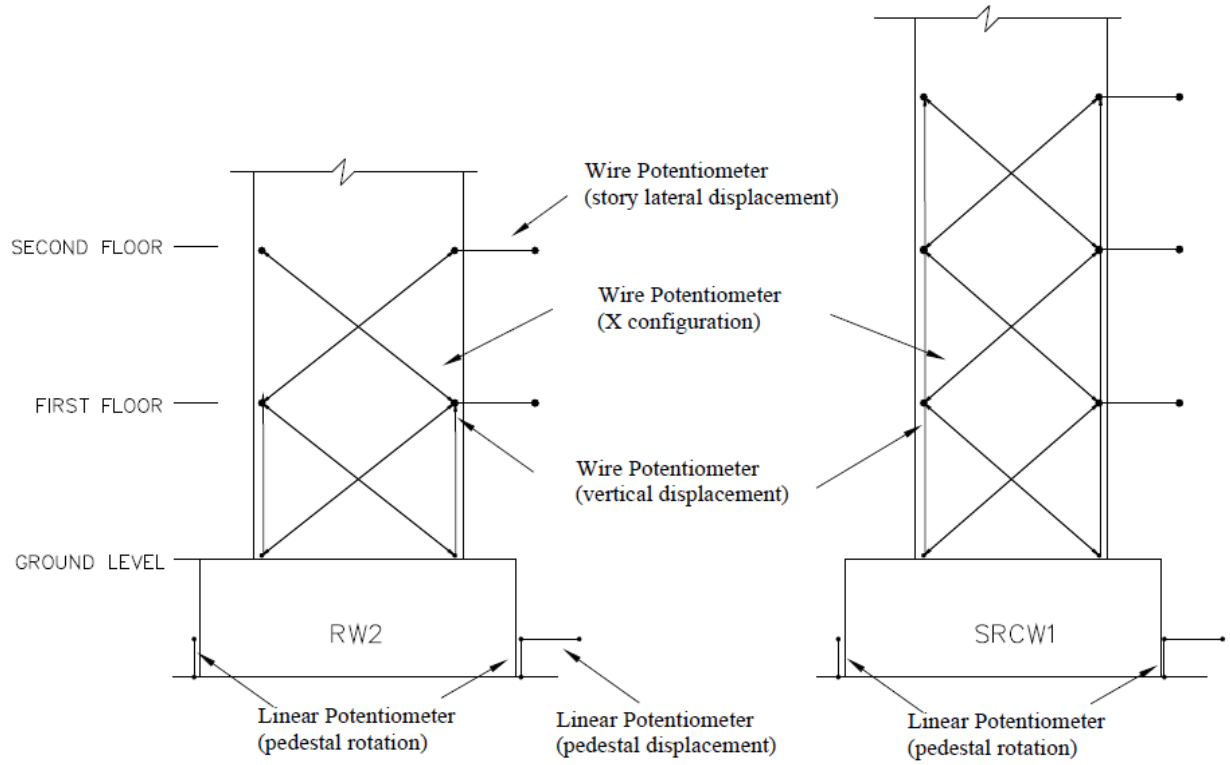

Figure 2-1 Instrumentation Provided (Massone and Wallace, 2004)

2.1.1.2 Determination of Flexural and Shear Deformations

The flexural displacement of the top of a wall section (story height in this case) is calculated according to following expression:

$$U_f = \alpha \cdot \theta \cdot h \tag{2-1}$$

where θ is the rotation over the story level, h is the story height, and α is the relative distance from the top of the story level to the centroid of estimated curvature distribution (center of

rotation). Massone and Wallace (2004) used a value of $\alpha = 0.67$, which is consistent with the value determined by other researchers (e.g., Thomsen and Wallace, 2004).

A common approach used to determine average (story) shear deformations for shear wall tests is to use measurements from displacement gauges placed diagonally in an "X" configuration as shown on Figure 2-1 and Figure 2-2. Massone and Wallace (2004) suggested that the average shear deformations calculated using this methodology may be overestimated due to the influence of flexural deformations when the center of rotation of the story does not coincide with the geometric center of the story height, and proposed a correction of average shear deformations obtained from the "X" configuration using the story flexural displacements derived from vertical WPs at the wall boundaries by adding a second order terms:

$$U_{s,X,corrected} = U_{s,X,original} + \left(\frac{1}{2} - \alpha\right) \cdot \theta \cdot h \tag{2-2}$$

where $U_{s,X,original}$ is obtained using only the "X" configuration of sensors as:

$$U_{s,X,original} = \frac{\sqrt{D_1^2 - h^2} - \sqrt{D_2^2 - h^2}}{2} \tag{2-3}$$

In the expression above D_1 and D_2 are measurements obtained from "X" configuration and h is the height of the wall story as shown on Figure 2-2.

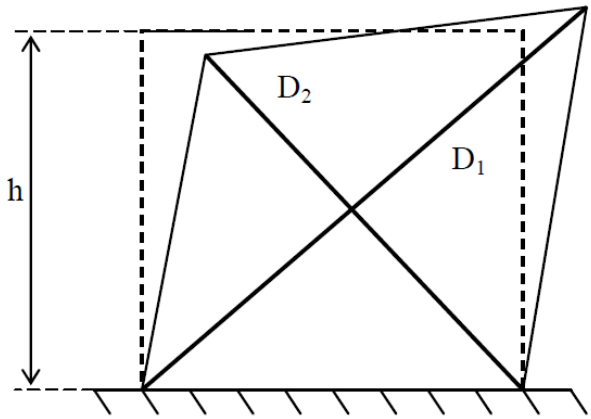

Figure 2-2 Measurements Obtained from "X" Configuration

2.1.1.3 Force versus Flexural and Shear Displacement Relations

Using the methodology described in the previous section, Massone and Wallace (2004) separated contributions of shear and flexural deformations to wall lateral displacements for each story with diagonal LVDTs and at the top of the wall. The applied shear force versus flexural and shear displacements within the first and second stories of specimen RW2 are presented in Figure 2-3, whereas Figure 2-4 plots the same relationships for the first through third stories of specimen SRCW1. Figure 2-3 and Figure 2-4 also include the analytical results obtained from linear-elastic analysis that uses flexural stiffness of a "fully-cracked" section calculated from a sectional analysis as secant stiffness to the point of first yield of reinforcement, and an elastic shear stiffness.

Since vertical potentiometers were not provided during testing along the second story height of specimen RW2 (Figure 2-1), shear displacement at the second story level of this specimen were evaluated using only measurements from potentiometers in "X" configuration using the Eq. 2-3 without the correction given by Eq. 2-2. It can be observed from Figure 2-3 that yielding of the

flexural reinforcement occurs primarily in the first two story levels at a lateral load close to that associated with the lateral load to reach the wall nominal moment (131 kN = 29.4 kips), while nonlinear shear deformations occurred at the first story despite a nominal shear capacity (V_n = 276 kN = 62 kips) of approximately twice the applied story shear (133 kN = 30 kips). As well, the observed results clearly demonstrate coupling of wall inelastic shear and flexural responses; i.e., inelastic flexural deformations appear to have led simultaneously to inelastic shear deformations.

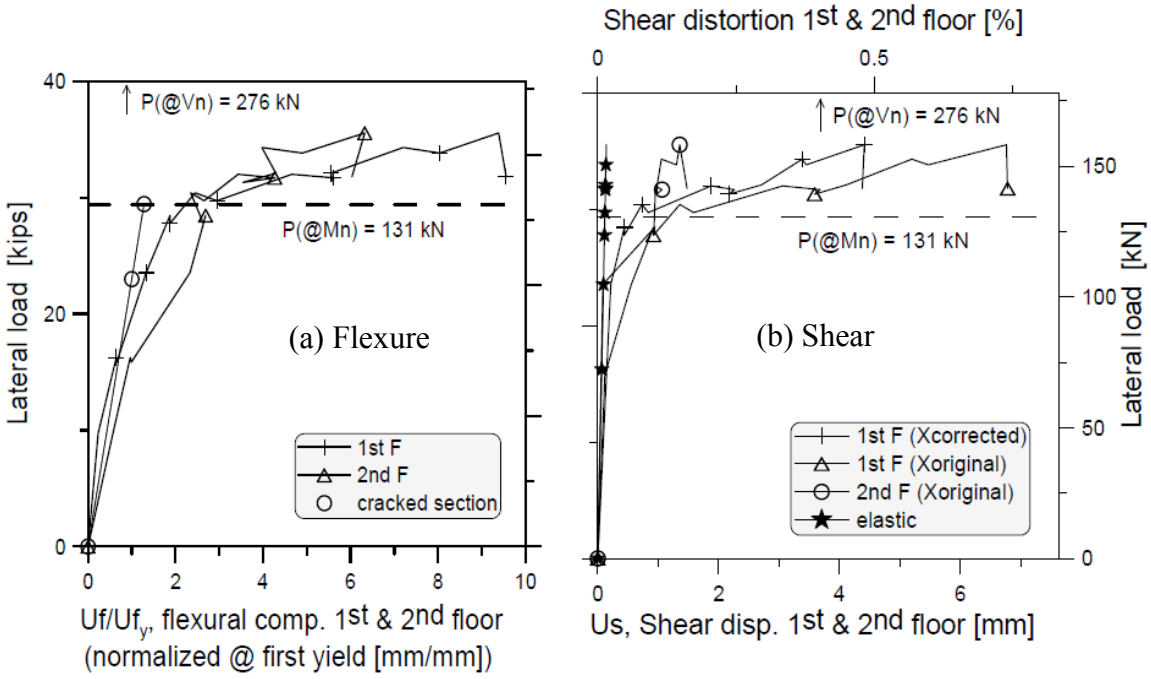

Figure 2-3 First and Second Story Deformations: RW2 (Massone and Wallace, 2004)

Similar relationships for specimen SRCW1 are presented in Figure 2-4. For this wall specimen, vertical and diagonal WPs were provided along the bottom three stories of specimen SRCW1 (Figure 2-1) and the shear displacement measurements at the first, second, and third story levels were corrected based on Eq. 2-2. The story shear force versus flexural displacement relationships

shown in Figure 2-4(a) reveal findings similar to those for specimen RW2, except that slip between the structural steel section and concrete appears to have contributed significantly to a loss of stiffness within the first story of specimen SRCW1. The story shear force versus shear displacement relationships shown on Figure 2-4(b) reveal that inelastic shear behavior was experienced within the first and second stories of the wall, despite a nominal shear capacity (V_n = 651 kN = 146.3 kips) of approximately twice the applied story shear (70 kips = 310 kN). The observed inelastic shear deformations in the first story level, and also to a lesser degree in the second story level, clearly demonstrate the coupling of inelastic flexural and shear deformations. In addition, the flexural and shear force-deformation relationships reach yielding at approximately the same level of lateral load.

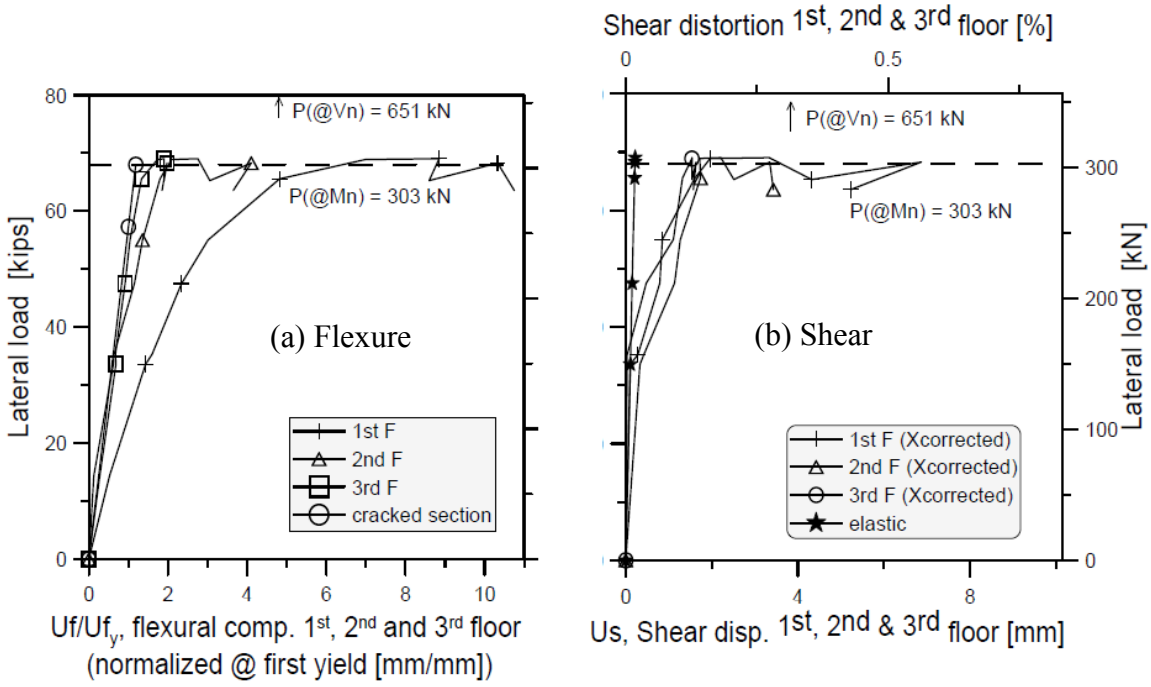

Figure 2-4 Story Deformations: SRCW1 (Massone and Wallace, 2004)

Experimental results presented in this section show that nonlinear shear deformations contributed approximately 30% and 10% to lateral displacement at the first story and roof-level, respectively, even in relatively slender RC walls with aspect ratios of 3.0 and 4.0 (Massone and Wallace, 2004). In addition, results indicated that flexural and shear yielding occur roughly simultaneously even when the wall nominal shear strength was as much as twice the shear developed at flexural yielding, suggesting the interaction between nonlinear flexural and shear behavior.

2.1.2 Tran and Wallace (2012)

Experimental studies conducted by Tran and Wallace (2012) included five one-third scale cantilever RC wall specimens subjected to combination of constant axial load and reversed-cyclic lateral loading applied at the top of the walls. Specimens were heavily instrumented to obtain detailed response information. The primary objectives of the test program were to investigate the impact of level of axial stress and average shear stress on the wall failure modes and lateral deformation capacity, as well as to assess the distribution and magnitude of lateral deformations associated with shear and flexure. The primary test variables included wall aspect ratio (1.5 and 2.0), axial load level ($0.025\,A_g f'_c$ and $0.10\,A_g f'_c$), and wall shear stress level (between approximately 0.33 and $0.66\sqrt{f'_c}$ MPa or 4 and $8\sqrt{f'_c}$ psi). The five RC wall specimens were 15 cm (6 in.) thick and 122 cm (48 in.) long, with lateral load applied at either 183 cm (72 in.) or 244 cm (96 in.) above the wall-foundation block interface, i.e. aspect ratio of walls was 1.5 and 2.0, respectively. The ratios of horizontal and vertical web reinforcement are the same and higher than the minimum requirement of 0.0025 from Chapter 21 of ACI 318-11.

The minimum and maximum ratios of vertical boundary reinforcement ρ_b for the five specimens were 3.23% and 7.11%. Specimens were designed to yield in flexure before reaching the ACI 318-11 nominal shear strength.

Test results indicated that substantial loss of lateral load capacity was observed at approximately 3.0% drift for all test specimens, with significant strength loss was impacted by wall aspect ratio, axial load level, and shear stress level. Various mechanisms led to strength loss, i.e., diagonal tension failure, web crushing, sliding shear, and buckling of vertical reinforcement. The deformations associated with flexure and shear for all five wall specimens were separated by the use of methodology presented by Massone and Wallace (2004) described in Section 2.1.1.2. Experimental results revealed interaction between flexural and shear behavior for all five RC wall specimens, i.e., the results indicated that nonlinear flexural and shear deformations occurred near-simultaneously (at approximately same level of lateral load). In addition, the average contributions of nonlinear shear deformations to wall top lateral displacement ranged from 20% to 30% for 2.0 aspect ratio walls, and from 30% to 50% for 1.5 aspect ratio walls. Therefore, experimental data obtained from the heavily instrumented wall specimens provided detailed response information for walls that experienced significant nonlinear shear deformations and demonstrated SFI. Results from these tests are used in this study to validate the proposed modeling approach for cyclic SFI. Additional information regarding this experimental program is provided in Chapter 5, whereas more detailed information can be found in the dissertation by Tran (2012).

2.2 Analytical Modeling of RC Structural Walls

Analytical modeling of the inelastic response of RC walls can be accomplished either by using microscopic models based on a detailed interpretation of local behavior, or by using macroscopic (phenomenological) models based on capturing overall wall behavior with reasonable accuracy. Micro-models, such as detailed nonlinear, three-dimensional, finite element models, can provide a refined definition of local responses. However, the efficiency, practicality and reliability of these models are questionable due to complexities involved in their development and in the interpretation of the results. In contrast, macro-models are more practical and effective in analyzing reinforced concrete structural walls and buildings where walls are used as lateral-force-resisting system because the models are relatively simple to implement and computationally efficient. This is particularly true for tall buildings. However, their application may be restricted based on the simplifying assumptions upon which the models are based. An effective analytical model should be relatively simple to implement and reasonably accurate in predicting the nonlinear hysteretic response of RC walls and wall systems.

2.2.1 Models with Uncoupled Shear and Flexural Responses

Various analytical approaches have been developed to predict nonlinear response of RC walls. Hysteretic behavior of structural walls is commonly modeled by using the idealized beam-column element along the centroidal axis of the wall with rigid links at locations of beam girders. This model consists of linear-elastic flexural element along the length of the wall, and inelastic rotational and axial springs at each end of the element to account for nonlinear behavior of

critical regions (Figure 2-5). Nonlinear behavior of flexural and axial springs is described by implemented moment-rotation and force-deformation relationships, respectively.

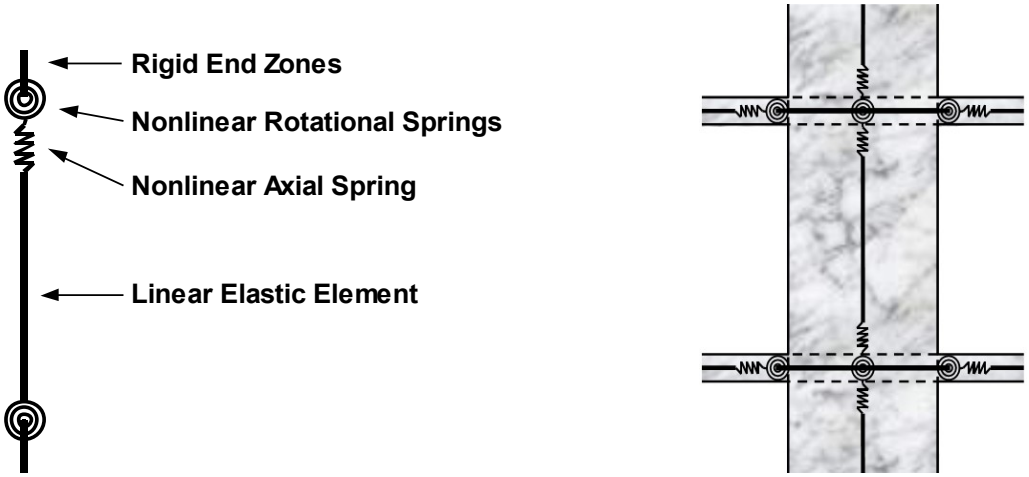

(a) Beam-column element (b) Model configuration

Figure 2-5 Beam-column element model (Orakcal et al., 2004)

Although this model is simple and computationally efficient, it does not capture the variation of the neutral axis along the depth of the wall cross section, rocking of the wall, or properly account for interaction with frame members connected to the wall (both in-plane and out-of-plane), which are very important for inelastic response of the walls (Orakcal et al., 2004).

The use of element models based on uniaxial material force-deformation or stress-strain relations, such as displacement/force-based fiber models or the Multiple-Vertical-Line-Element-Model (Vulcano et al., 1988; Fischinger et al., 1990; Orakcal et al., 2004), have become very common in both research (OpenSees, McKenna and Fenves, 2007) and engineering practice (Perform-3D, CSI, 2006). The Multiple-Vertical-Line-Element-Model (MVLEM), with its relatively simple model formulation, numerical stability, efficiency, and reasonably accurate

predictions of flexural responses (Orakcal and Wallace, 2006) successfully balances the simplicity of a macroscopic model and the refinements of a microscopic model. A structural wall is modeled as a stack of *n* MVLEM elements, which are placed upon one another as shown on Figure 2-6(a). The flexural response is simulated by a multi-uniaxial-element-in-parallel model with infinitely rigid beams at the top and bottom of floor levels. Two external elements represented the axial stiffness of the boundary columns (k_1 and k_m), while two or more interior elements (k_2,…,k_{m-1}) represent the axial and flexural stiffness of the central wall panel (Figure 2-6(b)). The shear response of the wall is modeled by using a horizontal spring placed at the height *ch* (Figure 2-6(b)) whose behavior is typically described with nonlinear ad-hoc force-deformation rules such as an origin-oriented hysteresis model (Kabeyasawa et al., 1983, Figure 2-7).

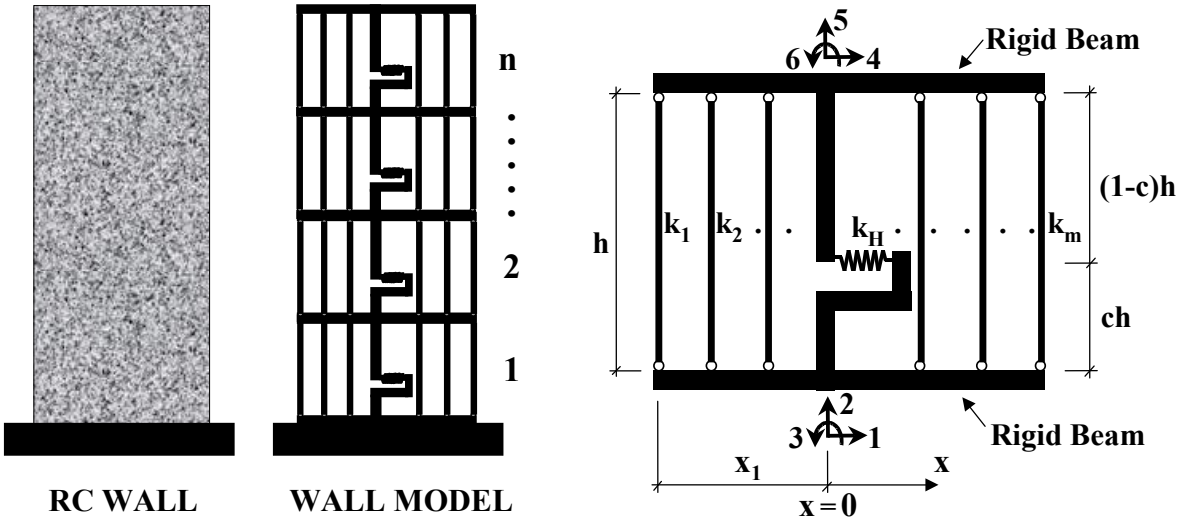

(a) MVLE Wall Model (b) Model Element

Figure 2-6 Multiple-Vertical-Line-Element-Model (MVLEM, Vulcano et al., 1988)

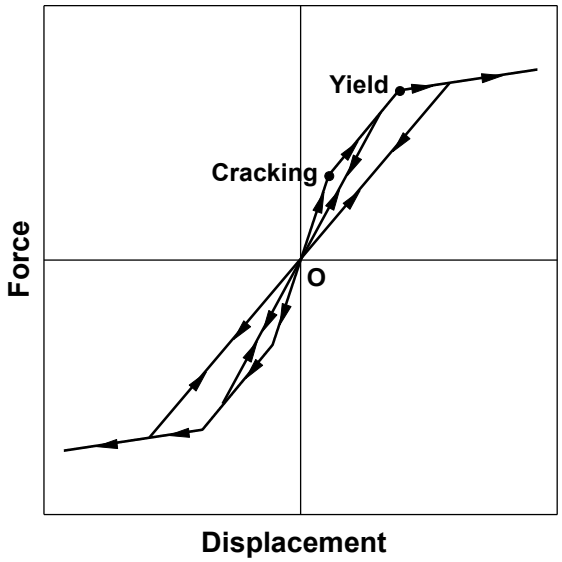

Figure 2-7 Origin-oriented hysteresis model (Kabeyasawa et al., 1983)

In the MVLEM, the relative rotation between top and bottom faces of the wall element (curvatures) are concentrated at the center of rotation defined for each element at the height *ch* assuming a constant value (uniform distribution) of wall curvature over the height of each wall element, as oppose to the displacement-based fiber model in which linear variation of curvature is used between the element nodes (Figure 2-8). Rotations and resulting transverse displacements are calculated based on the wall curvature, derived from section and material properties, corresponding to the bending moment at height *ch* of each model element. A value of $c = 0.4$ was recommended by Vulcano et al. (1988) and verified by Orakcal and Wallace (2006) based on comparison of the model response with experimental results.

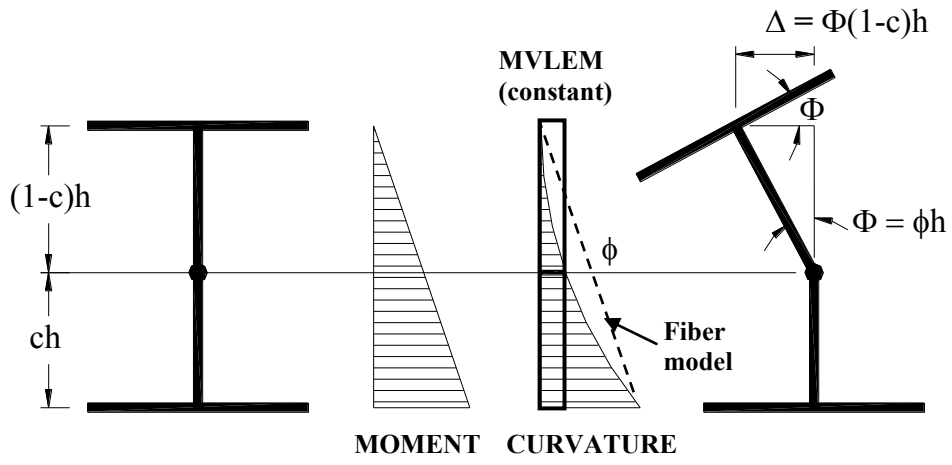

Figure 2-8 Flexural Deformations of the MVLEM Element (Orakcal et al., 2004)

The MVLEM was improved by implementing refined hysteretic uniaxial stress-strain material models instead of simplified force-deformation rules (Fischinger et al., 1990) to predict the inelastic response of slender RC walls (Orakcal, 2004; Orakcal et al., 2004; Orakcal and Wallace, 2006). The stress-strain model for reinforcing steel was the hysteretic model of Menegotto and Pinto (1973), as extended by Filippou et al. (1983) to include isotropic strain hardening effects (Figure 2-9). Uniaxial behavior of concrete was described by the constitutive model proposed by Chang and Mander (1994), which has the capabilities of addressing important features of concrete hysteretic behavior such as the progressive degradation of stiffness of the unloading and reloading curves for increasing values of strain, the effects of confinement, tension stiffening and gradual crack closure (Figure 2-10).

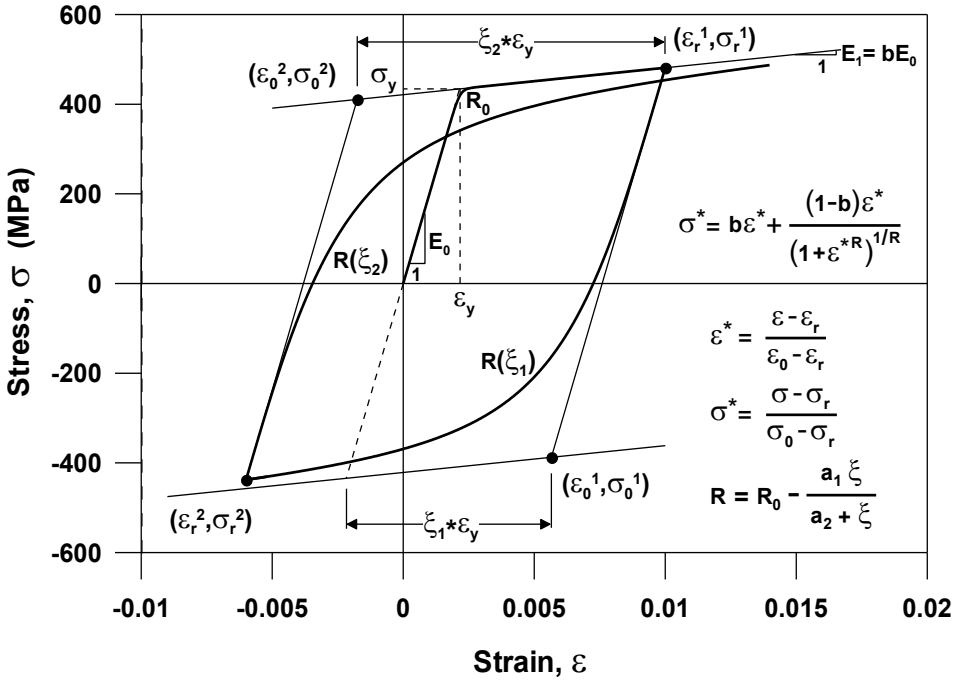

Figure 2-9 Uniaxial Constitutive Model for Steel (Orakcal et a., 2004)

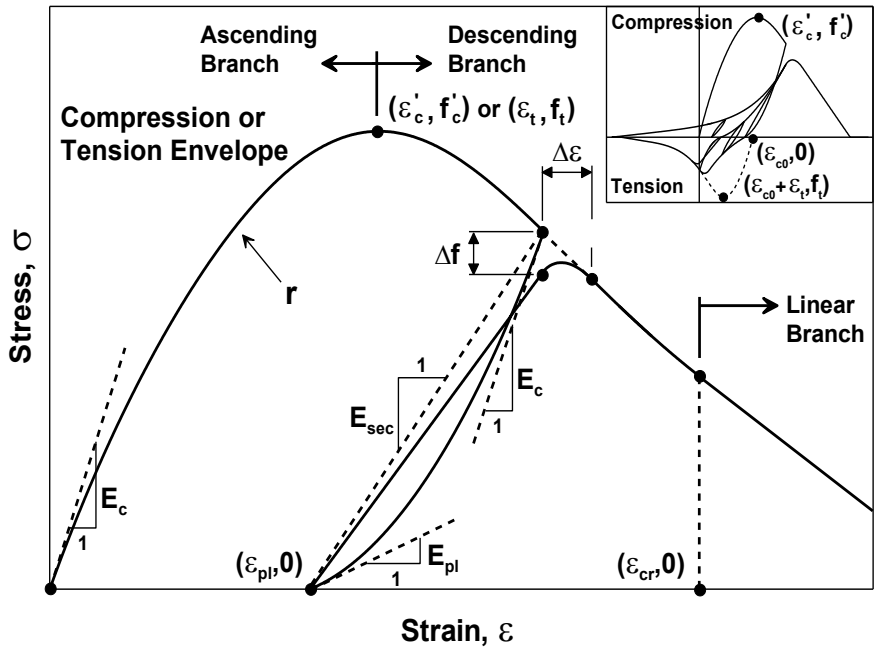

Figure 2-10 Uniaxial Constitutive Model for Concrete (Orakcal et al., 2004)

The comparison of experimentally measured and analytically predicted lateral load versus wall top flexural response of a RC wall specimen RW2 of Thomsen and Wallace (2004) is shown on Figure 2-11. It can be observed from the figure that cyclic properties of flexural load-deformation response, including stiffness degradation, hysteretic shape, plastic (residual) displacements, and pinching behavior are accurately predicted by the MVLEM. Figure 2-12 compares measured average concrete strains at the base of the wall and predicted strain responses at applied peak positive top displacement. The results illustrate that the analytical model predicts reasonably well the tensile strain profile, but significantly underestimates the compressive strains. Orakcal and Wallace (2006) associated the underestimation of compressive strains with the inability of the MVLEM to capture nonlinear shear behavior and shear-flexure interaction, which were observed in the wall specimen within the first story height (Massone and Wallace, 2004).

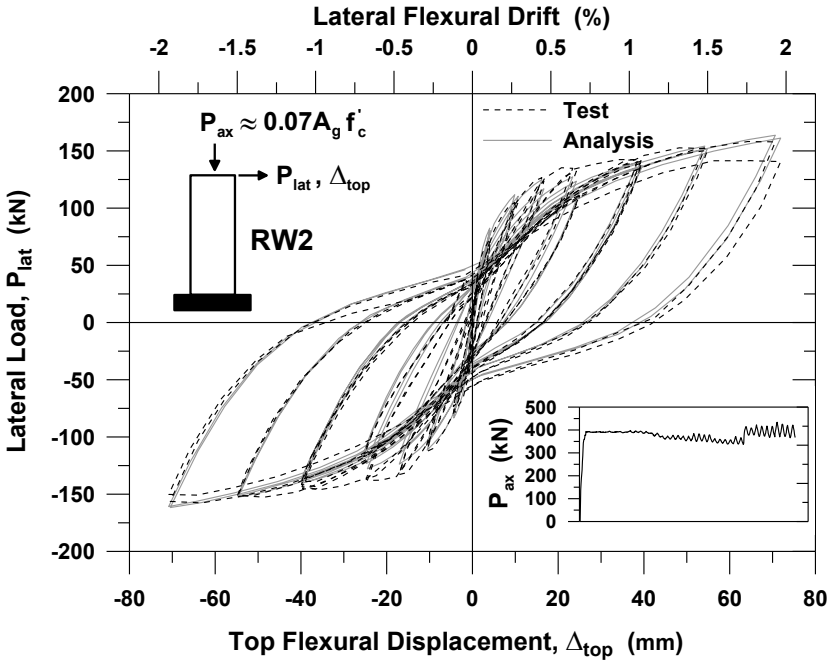

Figure 2-11 Measured vs. Predicted Load-Deformation Responses (Orakcal and Wallace, 2006)

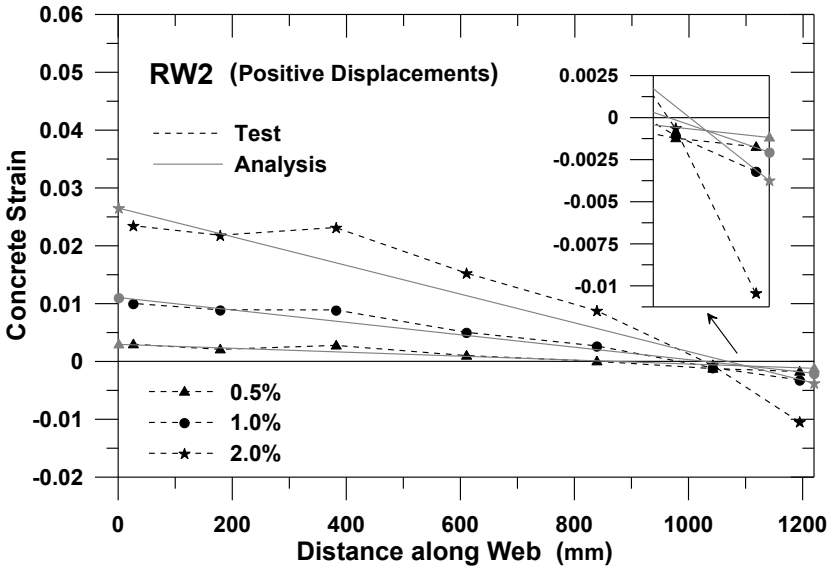

Figure 2-12 Measured vs. Predicted Concrete Strains (Orakcal and Wallace, 2006)

Although the majority of available modeling approaches, including fiber-based analytical models, have been shown to represent axial-bending behavior of RC walls reasonably well (Orakcal and Wallace, 2006; Wallace, 2007), they typically describe the shear behavior of a RC wall independently from the axial/bending modeling parameters by using ad-hoc force deformation rules (Vulcano and Bertero 1987; Orakcal et al. 2004). Therefore, these models usually do not incorporate experimentally-observed shear-flexure interaction.

2.2.2 Models with coupled axial, shear and flexural responses

Various approaches have been proposed to capture the observed coupling between nonlinear flexural and shear behavior in RC walls. Beyer et al. (2011) accounted for shear-flexure interaction by studying the ratio of shear-to-flexural deformations in RC wall tests. In the proposed empirical (or semi-empirical) approach, the ratio between flexural and shear deformations is derived from wall geometry, axial strains, and cracking angle. Based on

assessing experimental results from quasi-static reversed cyclic tests on 34 slender reinforced concrete structural walls, the following empirical relation between shear and flexural deformations was derived.

$$\frac{\Delta_s}{\Delta_f} = C_1 \frac{\varepsilon_m}{\phi \tan\beta} \frac{1}{H_n} \tag{2-4}$$

where ε_m and ϕ are respectively the mean axial strain and curvature of the wall over the height of the plastic hinge length, assumed to be constant; β is the cracking angle outside the fanned crack pattern, as observed within the plastic zone, where cracks are approximately parallel; H_n is the distance from the top of the wall to the centroid of the plastic hinge; C_1 is the correction factor accounting for the reduction of the ratio $\frac{1}{\tan\beta}$ compared to $\frac{1}{\tan\overline{\beta}}$, where $\overline{\beta}$ is the cracking angle representative of the fanned crack pattern within the plastic zone, and estimated to be 1.5 from the database considered in the study.

The comparison of the shear-to-flexural deformations predicted by the use of Eq. 2-4 and measured experimentally is presented in Figure 2-13. As can be seen from the figure, although the empirical relation between shear and flexural deformations is capable of capturing the general trend of the Δ_s/Δ_f ratio for walls controlled by flexure (i.e., walls that yield in flexure prior to reaching the nominal shear strength calculated according to ACI 318-11), a significant variation between the model and test results still exists. Therefore, the approach is limited due to its reliance on test data, i.e. interpolation and extrapolation without an underlying behavior-based model.

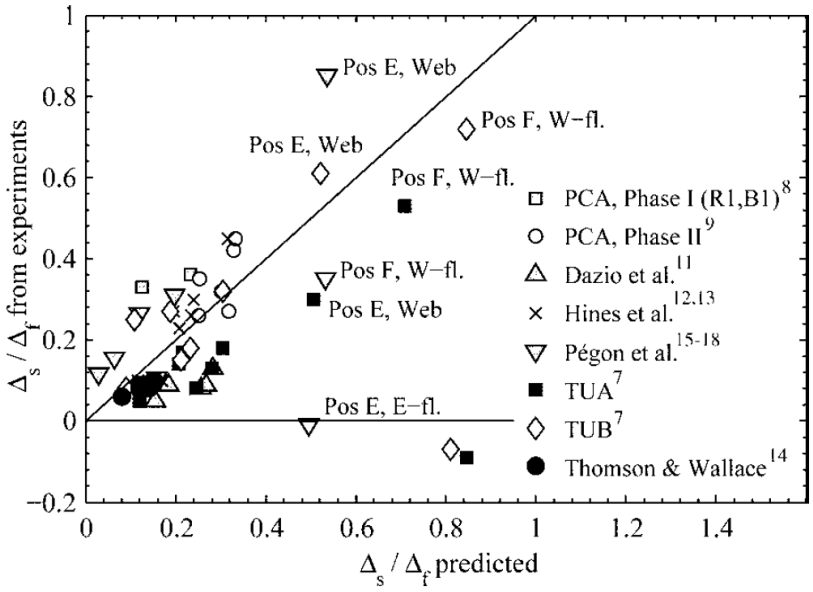

Figure 2-13 Comparison of predicted Δ_s/Δ_f ratios to ones determined from experimental measurements (Beyer et al. 2011)

Zhang and Xu (2010, 2012) developed a modeling methodology based on the concentrated plastic hinge approach that captures the interaction between axial, flexural and shear responses in RC columns. Inelastic response is modeled by the use of flexural and shear springs located in the column plastic hinge regions, whose behavior is governed by the flexural and shear backbone curves and a set of leading/unloading rules to describe the hysteretic characteristics of the response (e.g., pinching behavior, loading/re-loading stiffness, softening and strength degradation); hysteretic model for shear by Ozcebe and Saatcioglu (1989) and hysteretic model for flexure by Takeda et al. (1970) were used as a basis to develop two improved hysteretic models for flexure and shear responses, respectively. Flexural and shear backbone curves are obtained by separating flexural and shear deformations from the total monotonic force-displacement relationship (backbone curve) of a column that accounts for shear-flexure

interaction, which can be obtained either experimentally or analytically. In the modeling approach proposed by Zhang and Xu, the moment curvature ($M-\varphi$) and the shear force-shear strain ($V-\gamma$) relationships are obtained for each section of a RC column by the use of Modified Compression Field Theory (MCFT, Vecchio and Collins 1986) based on the column geometry, reinforcement configuration, material properties, and applied external loads (Figure 2-14). Subsequently, the flexural deformation (Δ_f) and shear deformation (Δ_s) are obtained by integrating the curvature and shear strain in each section along the column length, which yield the bending moment-to-rotation angle ($M-\theta$) and shear force-to-shear displacement ($V-\Delta_s$) relationships used to define the envelopes of force-deformation behaviors of flexural and shear springs. Thus, the analytical model captures shear-flexure interaction at both section level, when theoretically generating the backbone curves, and at element level, through global and local equilibrium.

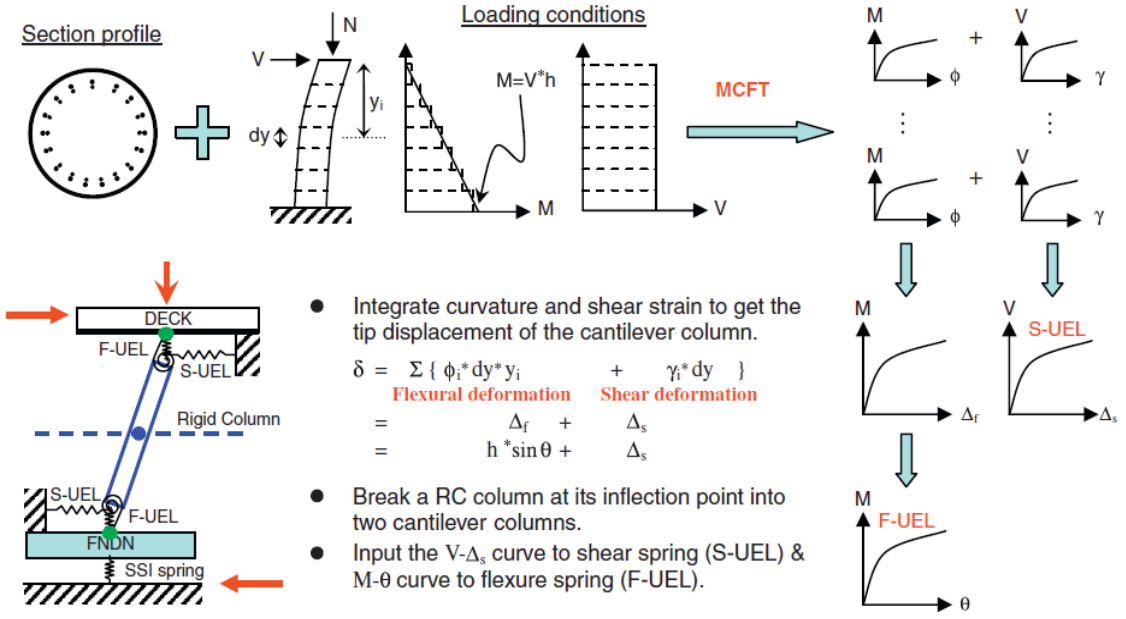

Figure 2-14 Implementation of Shear-Flexure Interaction Scheme (Zhang and Xu, 2010)

The model is characterized by relatively simple formulation and computational efficiency when comparing to the spread plasticity models or fiber models. Model calibration is performed using a large number of column specimens from static cyclic tests to dynamic shake table tests. It was shown that the model was able to capture realistically the pinching behavior, stiffness softening, and strength deterioration of columns subjected to cyclic load reversals when the improved hysteretic rules were implemented. The good agreement between numerical prediction and experimental data were observed for columns with significant shear-flexure interaction, different aspect ratios, levels of axial load, modes of failure (flexure- and shear-dominant columns) and loading (quasi-static and dynamic); for example, Figure 2-15 compares measured and predicted responses of RC columns with significant shear-flexure interaction. The limitations of the model come from the MCFT theory including the ability to capture the response only up to its peak strength (force-based approach), the limitations in model applications for extremely short columns (aspect ratio lower then 2.5), and the inability of the model to account for the bond slip.

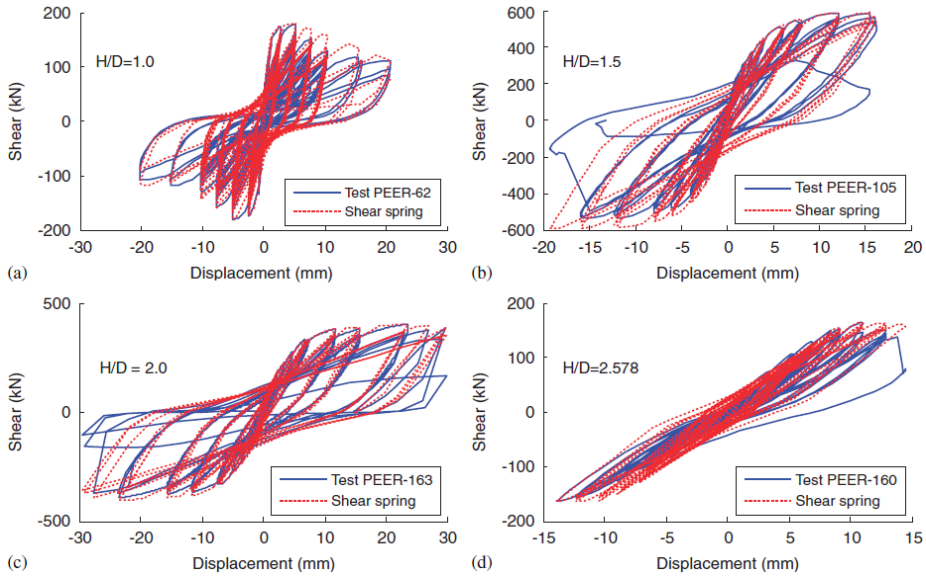

Figure 2-15 Measured and Predicted Response of RC Columns (Zhang and Xu, 2010)

A strut-and-tie (truss) approach proposed by Panagiotou et al. (2012) provides an alternative methodology to capture interaction between shear and flexural responses in RC walls. A structural wall is modeled using nonlinear vertical, horizontal and diagonal truss elements connected at nodes along which cyclic uniaxial material laws for concrete and steel are applied (Figure 2-16); the vertical and horizontal truss elements represent reinforcing bars and their surrounding concrete, whereas diagonal truss elements represent the concrete only. The layout of diagonal truss elements resembles, but does not need to match, the principal compressive stress trajectories when approaching the ultimate load. Shear-flexure interaction in a structural element is modeled by reducing the capacity of a diagonal concrete truss element as a function of transverse tensile strain by the use of concrete uniaxial material law that couples the element's compressive stress-strain behavior with the tensile strain normal to the element axis (Figure 2-17).

The nonlinear cyclic truss model is validated against RC wall specimens with significant flexure-shear interaction (shear span-to-depth ratios between 0.45 and 2.9) subjected to reversed-cyclic loading conditions. The analytical model predicts reasonably well the post-cracking cyclic force displacement response of RC walls in terms of strength and stiffness with moderate computational effort. Due to the overlapping areas of vertical, horizontal and diagonal concrete elements, pre-cracking stiffness and strength of walls are overestimated by the model, which is a common shortcoming of strut-and-tie models (Ramirez and Breen, 1991). In addition, the predicted overall force-deformation response, especially the local element response involving softening, is sensitive to the element size. Therefore, the consideration of the effects of element length is required not only in the determination of the uniaxial stress-strain behavior of concrete

but also to determine the relation between the concrete compressive stress-strain behavior and normal tensile strain. Although the model represents a viable way to capture SFI in RC walls, achieving accurate displacement predictions over a broad range of response amplitudes can be a challenge due aforementioned shortcomings. In addition, studies reported in the literature are limited to isolated, cantilever wall tests, i.e., they do not address the impact of coupling and significant variation of wall axial load during the load history.

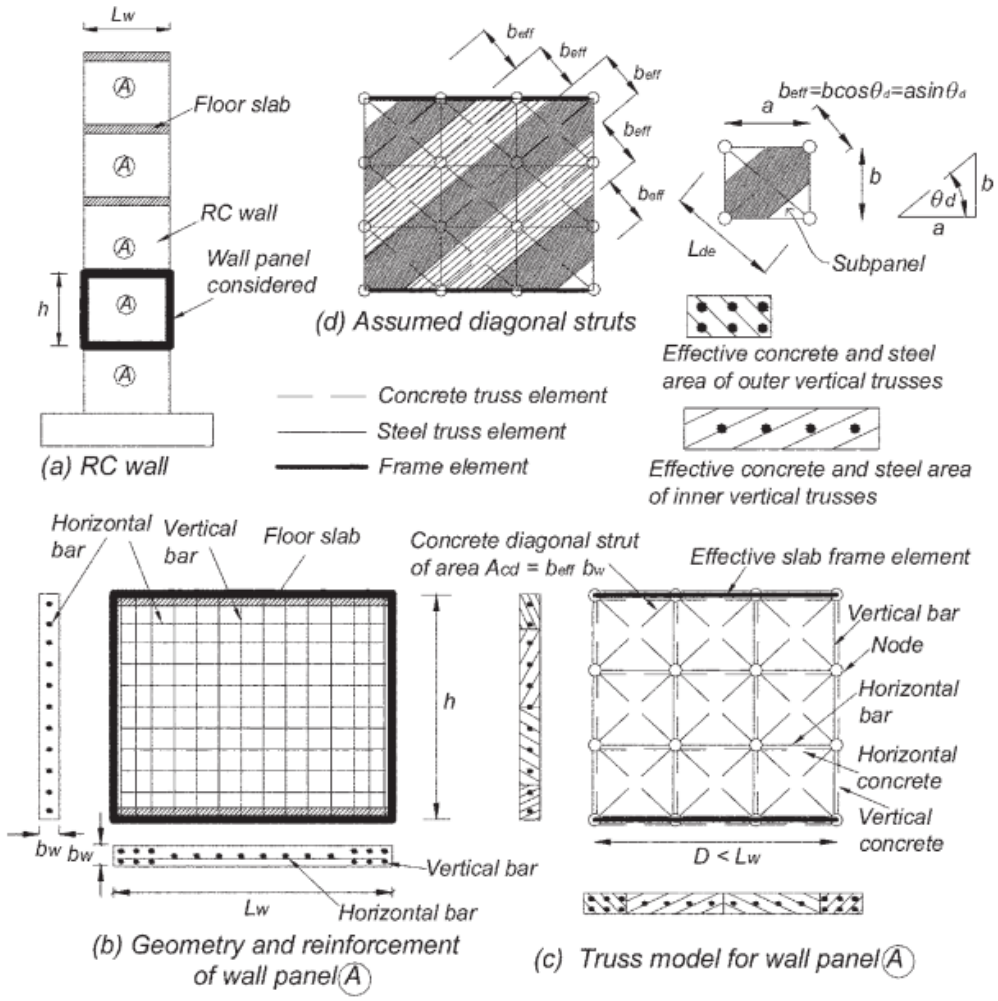

Figure 2-16 RC Wall and Wall Panel Truss Model (Panagiotou et al., 2012)

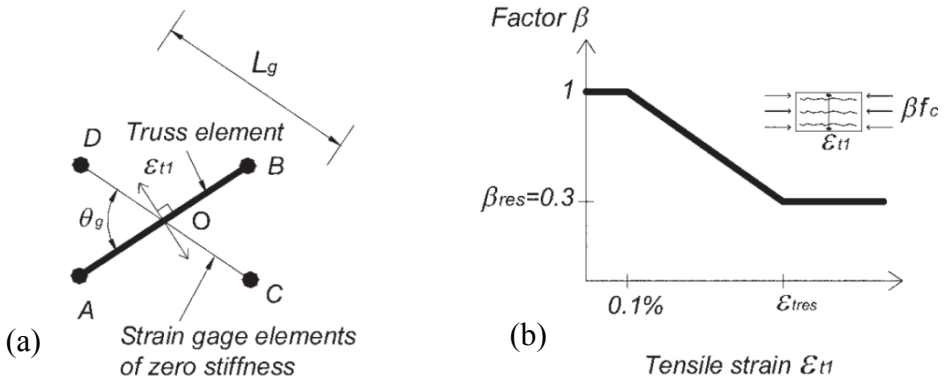

Figure 2-17 Coupled Compression-Tension Model for Diagonal Truss Elements: (a) Coupled Compression-Tension Truss elements, (b) Concrete Compressive Stress Reduction due to Normal Tensile Strain (Panagiotou et al., 2012)

A methodology developed by Petrangeli (1999), which involved incorporating RC panel behavior into a fiber-based (multi-spring) model formulation, provides a means to capture interaction between axial, flexural and shear responses in the nonlinear range for RC walls. Several analytical models can be found in the literature that followed this approach. The analytical model proposed by Massone et al. (2006, 2009) involved modifying the MVLEM by assigning a shear spring to each uniaxial element, which is then treated as a RC panel element subjected to in-plane uniform normal and shear stresses, as shown on Figure 2-18. Therefore, the coupling between flexural and shear responses is incorporated directly at the model element level through coupling of axial and shear responses at the panel (macro-fiber) level. A rotating-angle modeling approach, such as the Modified Compression-Field Theory (MCFT; Vecchio and Collins, 1986) or the Rotating-Angle Softened-Truss-Model (RA-STM; Hsu, 1993; Belarbi and Hsu, 1994 and 1995; Pang and Hsu, 1995), was used to model the constitutive panel behavior. The model formulation involved the following assumptions: plane section remains plane, strain

fields acting on concrete and reinforcing steel are identical (perfect bond between reinforcement and concrete), shear strains are uniformly distributed along the wall length, principle stress and strain directions coincide, and dowel action of reinforcement is equal to zero.

Material constitutive model used in this study to represent the monotonic behavior of reinforcing steel (Figure 2-19) was the well-known model by Menegotto and Pinto (1973). A softened constitutive relationship for concrete in compression (Figure 2-20(a)), calibrated against a large set of experimental results, was implemented in this model to consider the reduction in principal compressive stress in compression due to cracking under tensile strains in the orthogonal direction. Concrete in tension is described with the stress-strain relationship proposed by Belarbi and Hsu (1994) to take into account the effect of tension stiffening (Figure 2-20(b)). Stress-strain relationships for concrete and steel were applied in the directions of principal strains which were assumed to coincide with the directions of principal stresses.

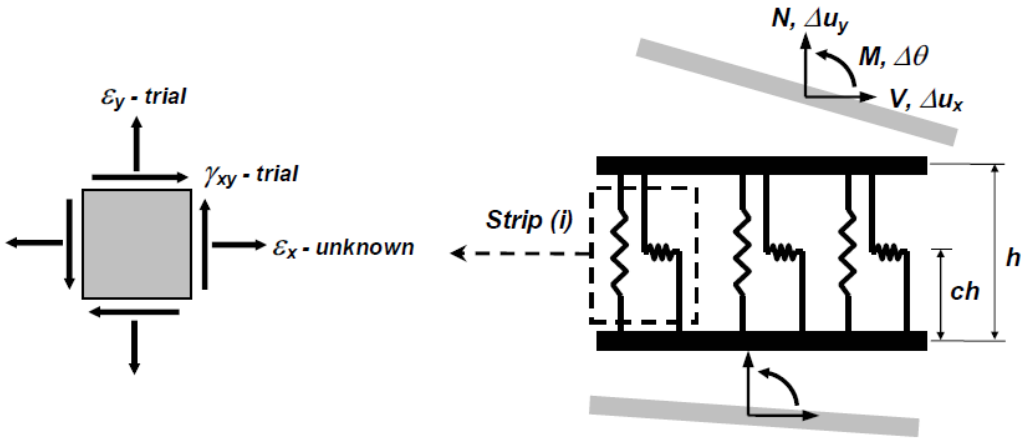

Figure 2-18 Coupled Model Element (Massone et al., 2006, 2009)

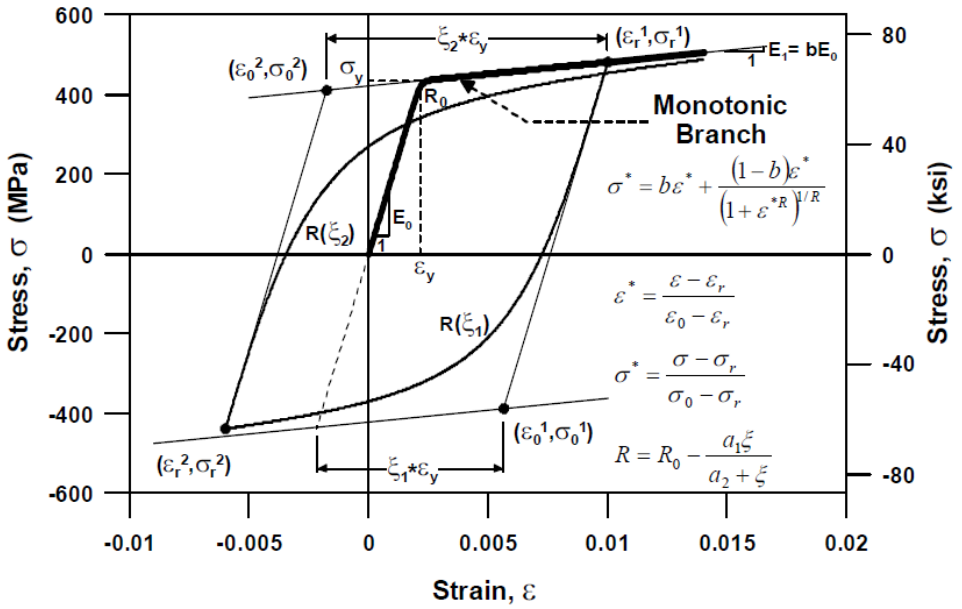

Figure 2-19 Constitutive Model for Reinforcing Steel (Massone et al, 2006)

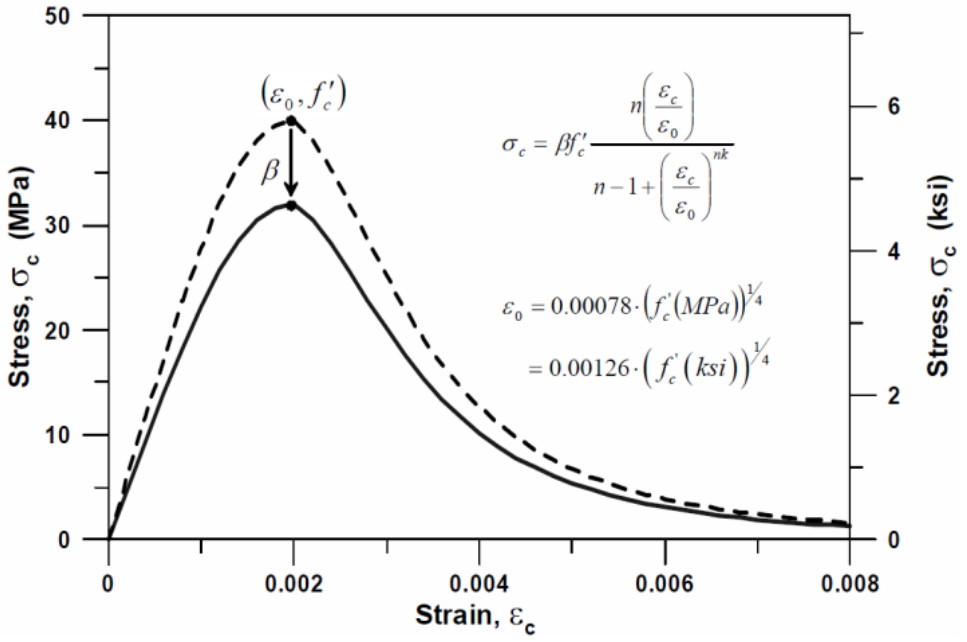

(a) Compression

Figure 2-20 Constitutive models for concrete (Massone et al., 2006)

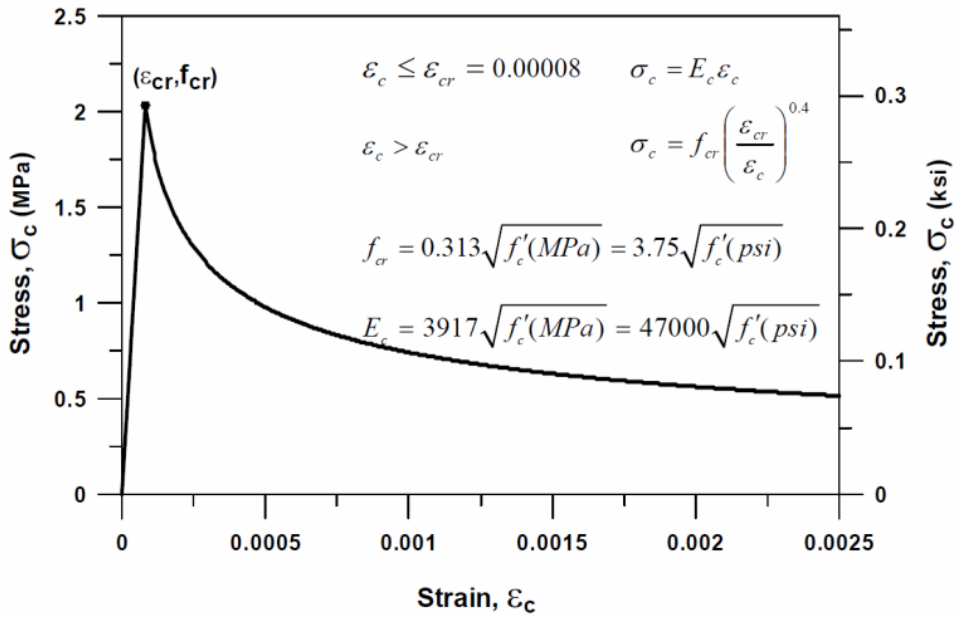

(b) Tension

Figure 2-20 (cont.) Constitutive models for concrete (Massone et al., 2006)

The model successfully captured shear-flexure interaction with generally good correlation between analytical and experimental results, particularly for moderately-slender wall (Figure 2-21). The results shown in Figure 2-22 illustrate that model was able to account for shear-flexure interaction by capturing simultaneous nonlinear flexural and shear deformations. Since the model uses monotonic material models and a RC panel model based on the rotating-angle approach, the prediction of the cyclic responses was not possible using the model proposed by Massone (2006, 2009), which is considered a major shortcoming. Therefore, the model was not able to account for cyclic degradation, which resulted in the overestimation of flexural deformations and the underestimation of shear deformations as shown on Figure 2-22. In the case of short walls, discrepancies between experimental and analytical results were more significant because the assumption that shear strains are uniformly distributed across the wall cross section was not

reasonable in this case; the validity of modeling approach and the model assumptions were shown to be violated with the decrease of the wall shear span ratios (aspect ratios).

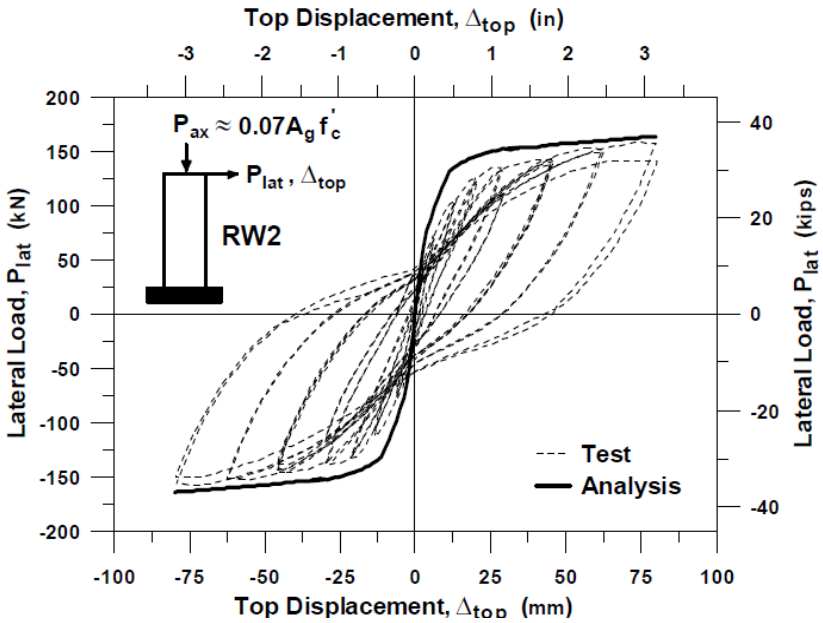

Figure 2-21 Lateral load – top displacement response of specimen RW2 (Massone, 2006)

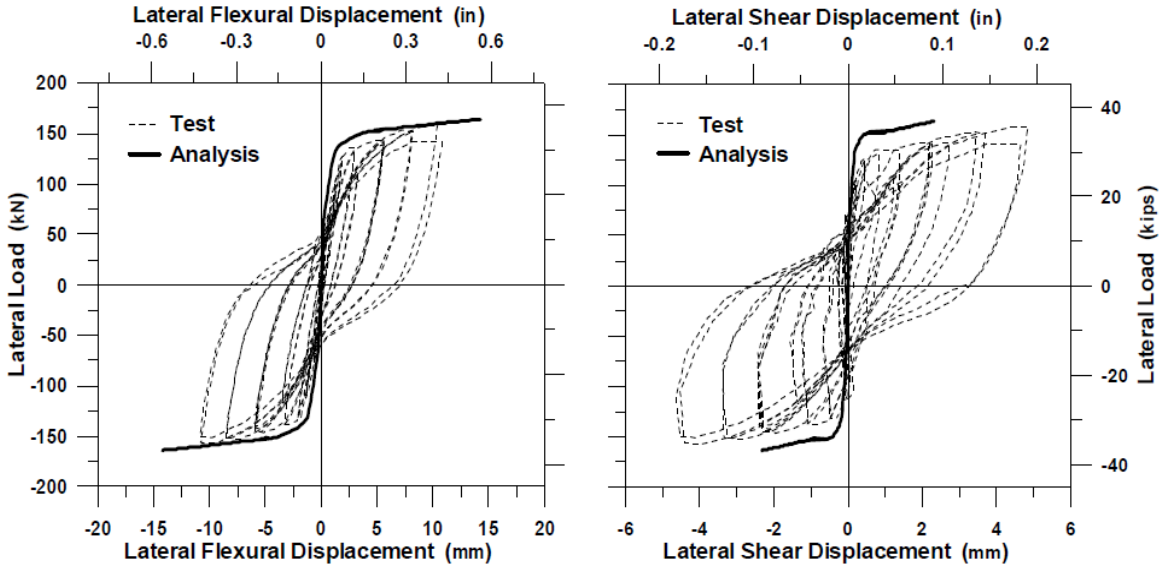

Figure 2-22 Lateral load – displacement responses at first story level (RW2) (Massone, 2006)

Another analytical model that follows this approach is proposed by Mullapudi and Ayoub (2009) and evaluated for RC walls by Mullapudi et al. (2009). This model incorporates a RC panel behavior described by a softened membrane model (SMM, Zhu and Hsu, 2002), derived from fixed-angle softened-truss-model (FA-STM, Pang and Hsu 1996), into a Timoshenko fiber beam-column element formulation, i.e., one-dimensional Timoshenko beam theory was adopted in the formulation to account for shear deformation effects. The SMM used to evaluate the concrete constitutive law under biaxial loading within each fiber incorporates the so-called Hsu/Zhu ratios (Poisson ratios of cracked RC), which enables the descending branch of the shear stress-strain curves of membrane elements to be predicted; in contrast, the FA-STM can predict the pre-peak behavior of RC members only. The model uses the cyclic constitutive relationships proposed by Yassin (1994), and accounts for the biaxial softening effect of concrete, the tension stiffening effect on concrete and steel, and the impact of concrete confinement, although with reduced accuracy relative to other models (Orakcal, 2004). The longitudinal steel fibers are assumed to follow a stress-strain relation based Menegotto-Pinto steel model (1973). Element forces are obtained by performing an equilibrium-based numerical integration on the section axial, flexural, and shear behaviors along the element length. Transverse strains are internal variables determined by imposing equilibrium at each fiber between concrete and transverse steel reinforcement. The limitations of the present model come from the simplified assumptions of SMM, such as the directions of the average principal strains remain coincident with the directions of the average principal stresses in the RC fiber, as well as the fiber beam formulation, such as plane sections remaining plane assumption and uniform shear strain distribution across the cross section. In addition, bond slip and bar buckling effects are ignored.

The proposed analytical model was used to simulate the behavior of two aspect ratio 2.0 RC walls tested by Lefas and Kotsovos (1990), specimen SW 31 tested under monotonic loading and specimen SW 33 tested under cyclic loading, as well as the behavior of RC columns that experienced shear-dominated behavior. The comparisons between the experimental and analytical results revealed that the model captures reasonably well the overall load-deformation response of considered wall specimens under monotonic and cyclic loading, as well as the vertical strains at the wall boundary. In addition, Mullapudi et al. (2009) investigated the sensitivity of analytical model results under monotonic loading to changes in wall slenderness ratio, transverse reinforcement ratio, and axial force using specimen SW 31 as the baseline model. Analytical results showed that the model captured systematic changes in local wall responses (e.g., normalized shear stress, distribution of normalized principal strains, and longitudinal boundary strains) with changes in mentioned wall parameters, whereas the sensitivity of global responses (e.g., lateral-load-versus-total-displacement) were not provided. Although the analytical model provided reasonably accurate predictions of behavior of moderate aspect ratio RC walls, the model validation studies were presented for a limited number of RC walls specimens (one monotonic and one cyclic test) as well as limited range of wall responses, i.e., lateral-load-versus-top-wall-displacement response and vertical boundary strain only, which are not overly sensitive to SFI (Orakcal and Wallace, 2006)

Jiang and Kurama (2010) also introduced analytical model derived from the microplane fiber formulation proposed by Petrangeli (1999). The interaction between shear, flexural and axial behavior was captured by monitoring the shear strain field and the lateral strain in addition to the axial strain field at a cross sectional level. The axial strain field was obtained based on the plane

section assumption, while the shear strain field was assigned over the cross section using different shape functions (e.g., constant, parabolic). The lateral strain field, as the only unknown, was then determined from the equilibrium between the concrete and the transverse steel reinforcement in the transverse direction at a fiber level or at a cross section level. Assumed fiber strain field and concrete fiber strains are presented on Figure 2-23(a) and (b), respectively.

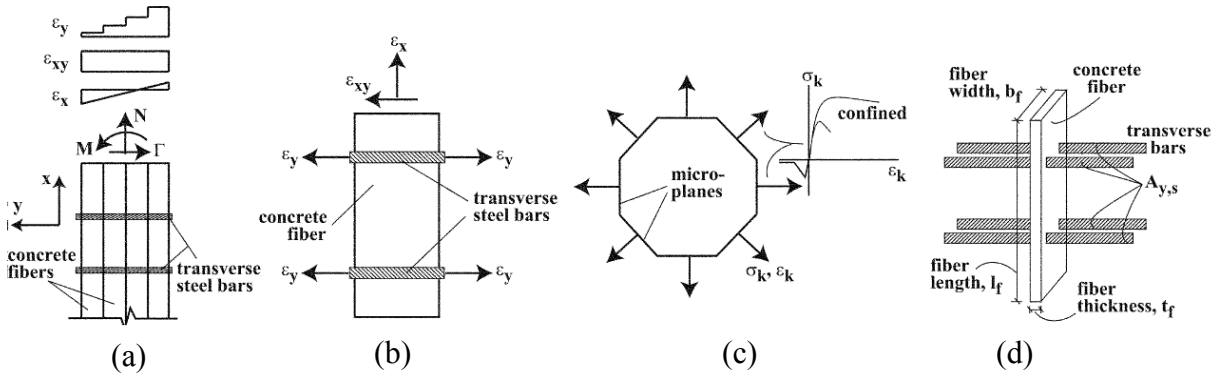

Figure 2-23 Fiber element with nonlinear shear deformations (Jiang and Kurama, 2010): (a) fiber strain field, (b) concrete fiber strains, (c) microplanes, and (d) tributary transverse steel reinforcement

The nonlinear shear-resisting mechanism for RC members was governed by the concrete behavior and its interactions with the reinforcing steel. The material behavior of concrete was described by the implementation of the "microplane" approach developed by Bazant et al. (1996), which accounts for the interaction between axial, transverse, and shear strain fields at the concrete and steel material levels based on basic uniaxial stress-strain relationships for steel and concrete. The structural response was then determined by monitoring uniaxial stress-strain relationships on the microplanes. A typical discretization with eight microplanes was assumed

(Figure 2-23(c)), in which all microplanes in a concrete fiber have the same uniaxial stress-strain relationships (assuming isotropy).

Longitudinal reinforcing bars were modeled using steel fibers in the directions of the reinforcement, while transverse reinforcement at each cross-section was represented as a tributary reinforcement within the concrete fiber formulation (Figure 2-23(d)). The stress-strain relationship for steel was idealized as a multilinear curve with a "gradual-softening" to take into account for the Bauschinger effect. In modeling of reinforcing steel, only the axial stresses and strains were considered (i.e., dowel action on the reinforcement was neglected).

The analytical model proposed by Jiang and Kurama (2010) was able to successfully capture hysteretic behavior of the longitudinal, transversal reinforcement and concrete as well as nonlinear axial-transverse-shear interaction for walls with aspect ratio 2.4 (Oesterle et al., 1979). The model was capable of predicting the lateral response characteristics reasonably well including stiffness, strength, ultimate displacement, and general shape of the hysteresis loops, as well as the concrete crushing and strength degradation under reversed-cyclic loading; comparison between predicted and measured load versus deformation response for specimen R2 of Oesterle et al. 1979 is shown on Figure 2-24. Although this modeling approach presents reasonably accurate and relatively simple tool to capture the fundamental response characteristics of medium-rise RC shear walls, problems related to fiber formulation associated to numerical stability and sensitivity of results to the choice of Gauss integration points were not resolved. In addition, the ability of the model to capture responses that are more sensitive to shear-flexure interaction were not studied (just lateral load versus top displacement and boundary vertical reinforcement strain).

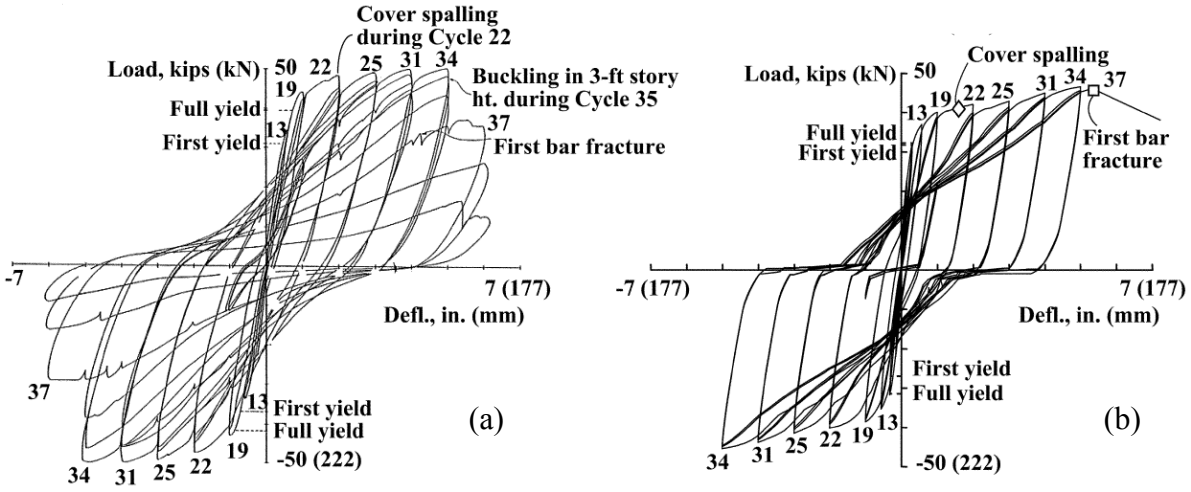

Figure 2-24 Measured (a) and Estimated (b) lateral load versus deformation response (Jiang and Kurama, 2010) of Specimen R2 (Oesterle et al., 1979)

Based on the same methodology (Petrangeli, 1999), Fischinger et al. (2012) presented a multiple spring model to capture interaction between shear and flexural behavior by assigning a shear spring to each macro-fiber of MVLEM (Fischinger et al., 1990), as shown on Figure 2-25(a). Each of these horizontal springs was composed of three components (i.e., three springs working in parallel, Figure 2-25(b)) accounting for three shear resisting mechanisms in each model macro-fiber as illustrated on Figure 2-25(c): (1) interlock of aggregate particles in the crack (HSA), (2) dowel effect of vertical bars (HSD) and (3) axial resistance of horizontal/shear bars (HSS). The current characteristics of each component depend on the deformations at the crack within the individual strip (i.e., crack width) and the constitutive relations for the individual springs, which are based on the semi-empirical relations found in the literature (Rejec, 2011).

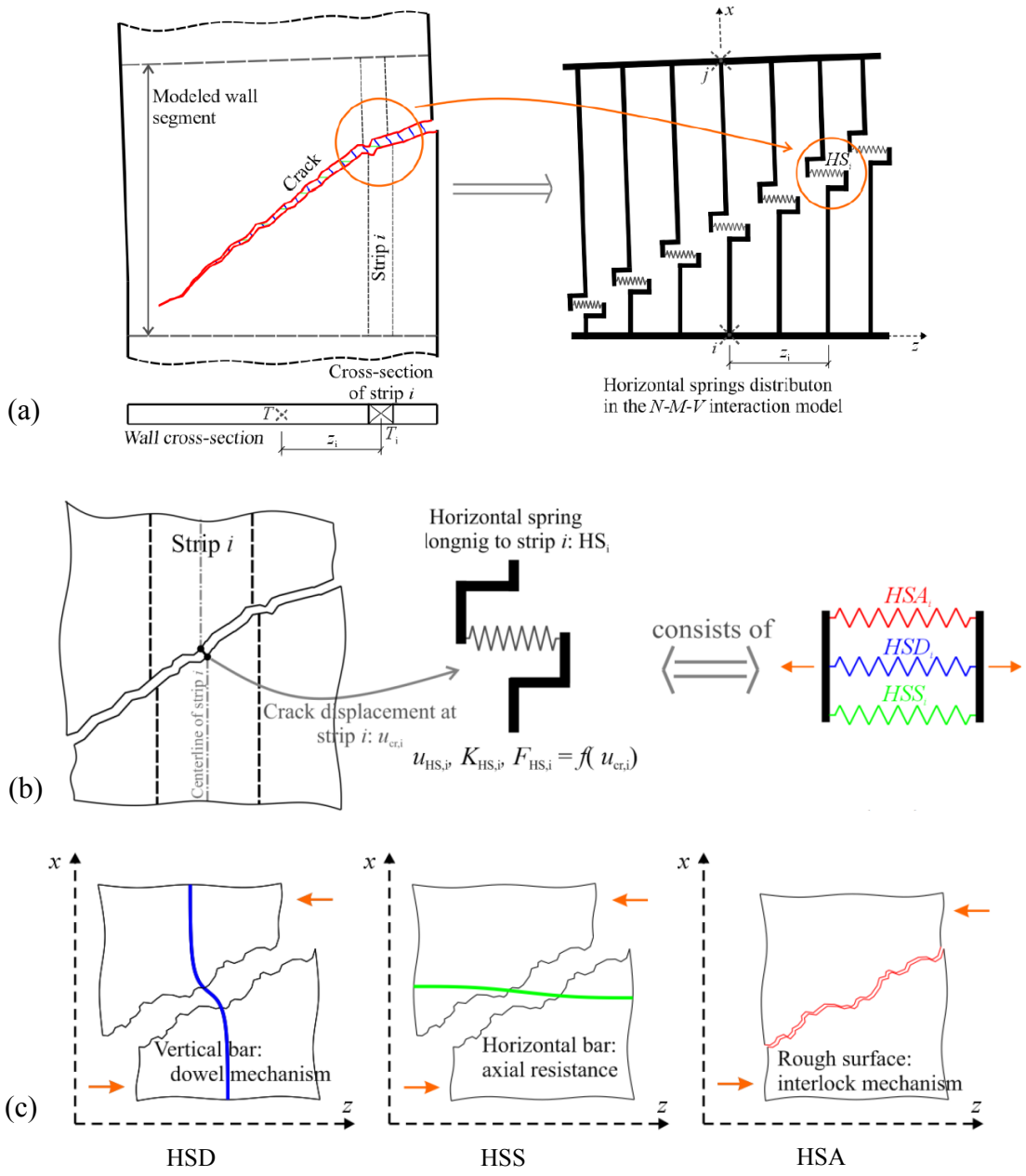

Figure 2-25 Upgraded MVLEM (Fischinger et al., 2012): (a) Multiple Horizontal Springs in Upgraded MVLEM, (b) Horizontal Shear Spring at Each MVLEM Macro-Fiber, (c) Mechanisms of Shear Force Transfers over the Cracks

(a) Shear Failure in the First Story

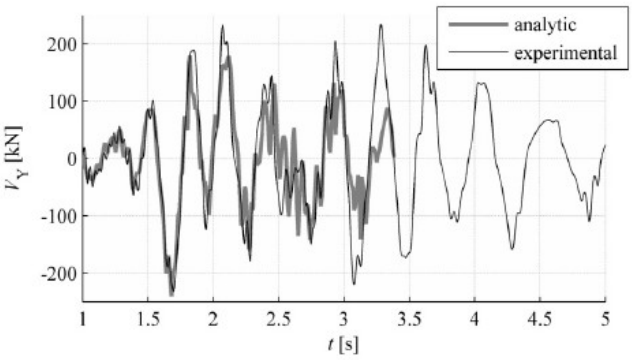

(b) Measure and Predicted Base Shear Response

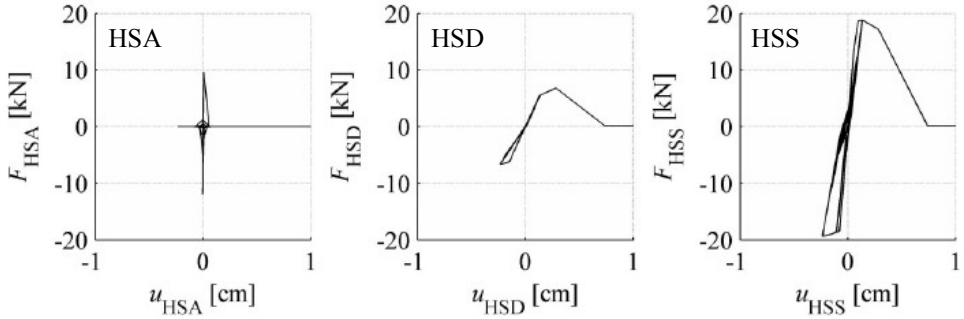

(c) Response of Shear Springs Accounting for Different Mechanisms

Figure 2-26 Experimental and Analytical Wall Responses

The analytical model was validated against test results for a 5-story coupled wall tested on the shaking table under biaxial excitation. It has been observed that the model successfully predicts the activation, strength degradation and/or failure of all components of shear resisting mechanism in model macro-fibers (i.e., HSA, HSS and HSD springs shown in Figure 2-26(c)), and therefore, predicts the shear failure pattern of the webs in wall piers due to biaxial loading similar to one observed during the test (Figure 2-26(a)). As well, it has been shown that the model captures global responses (e.g., base shear, Figure 2-26(b)) reasonably well. Although the model presents a promising way of capturing SFI in RC walls, it has not been validated in detail against extensive experimental data.

In summary, available models that capture interaction between shear and flexural responses in RC walls are characterized with the following shortcomings: the models are empirical or have cumbersome formulations, models are capable of simulating monotonic responses only, sensitivity of model results to material and modeling parameters have not been studied in detail, and models have not been sufficiently validated against global (load-displacement) behavior and local responses (rotations, curvatures, strains) due to lack of detailed experimental data for walls characterized with modest to significant SFI. Therefore, there is a need for a relatively simple analytical modeling approach that is able to predict important response characteristics of RC walls by incorporating coupling between axial/flexural and shear responses under reversed-cyclic loading conditions. In addition, the model needs to be validated at both global and local response levels for a range of response amplitudes against detailed data from heavily-instrumented tests of moderate-aspect ratio wall specimens.

Given the aforementioned shortcomings, the objective of this study is to develop a novel modeling approach that captures interaction between axial/flexural and shear behavior in RC walls under cyclic loading, as well as to calibrate the model using experimental results that include very detailed instrumentation. The adopted approach to incorporate SFI involves the implementation of a RC panel behavior into the fiber-based wall model, the MVLEM (Orakcal et al., 2004). The behavior of RC panel elements under reversed cyclic loading conditions is described with a two-dimensional constitutive RC panel model based on a fixed-crack-angle approach. Therefore, the coupling of axial and shear responses is enabled at the panel (macro-fiber) level, which further allows coupling of flexural and shear responses at the model element level. In addition, recently obtained detailed response information from heavily instrumented

wall specimens tested by Tran and Wallace (2012) is used for validation and calibration of the proposed analytical models at various response levels and locations.

CHAPTER 3

CYCLIC SHEAR-FLEXURE INTERACTION MODEL

The proposed analytical model incorporates reinforced concrete (RC) panel behavior into a two-dimensional macroscopic fiber model to capture experimentally observed shear-flexure interaction (SFI) in RC structural walls. In this study, the Multiple-Vertical-Line-Element-Model (MVLEM) implemented by Orakcal et al. (2004) is chosen as the baseline model for the implementation of a new cyclic SFI model because of its relatively simple formulation, numerical stability, efficiency, and reasonably accurate predictions of flexural responses (Orakcal and Wallace, 2006). The behavior of RC panel elements under reversed cyclic loading conditions is described with a two-dimensional constitutive RC panel model based on the Fixed-Strut-Angle-Model (FSAM; Ulugtekin, 2010; Orakcal et al., 2012), which is developed from the fixed-crack angle approach (Pang and Hsu, 1996; Hsu and Zhang, 1996; Mansour and Hsu, 2005). The coupling of axial and shear responses is achieved at the panel (macro-fiber) level, which further allows coupling of flexural and shear responses at the model element level. Conceptually, the approach is similar to the one proposed by Massone et al. (2006) who captured only monotonic responses by implementing a constitutive RC panel behavior described by a rotating-crack angle model (Pang and Hsu, 1995) into MVLEM; however, extensions to capture cyclic responses for this modeling approach proved cumbersome due to the formulation of the rotating-crack angle panel model.

This chapter provides a brief description of the baseline MVLEM, detailed descriptions of the proposed SFI analytical model and FSAM panel model, and an overview of implemented material constitutive models and nonlinear solution strategy.

3.1. Baseline Model: Multiple-Vertical-Line-Element-Model

The baseline Multiple-Vertical-Line-Element-Model (MVLEM) proposed by Vulcano et al. (1988) is a two-dimensional fiber-based analytical model for simulation of nonlinear responses of RC walls. A structural wall is modeled as a stack of *n* model elements shown on Figure 3-1(a) placed upon one another. The flexural response is simulated by a series of uniaxial elements (macro-fibers), which represent wall boundary elements and a central wall panel, connected to rigid beams at the top and bottom levels. The stiffness properties and force-displacement relationships of the uniaxial elements are derived according to cyclic constitutive models for concrete and reinforcing steel and the tributary areas assigned to each uniaxial element. The relative rotations between top and bottom faces of the wall element (curvatures) are concentrated at the center of rotation defined for each element at height *ch*. The distribution of wall curvature over the height of each wall element is assumed to be uniform, as oppose to a displacement-based fiber model, in which linear distribution of curvature is assumed between element nodes (Figure 3-1 (b)). Rotations and resulting transverse displacements are calculated based on wall curvature, derived from section and material properties, corresponding to the bending moment at height *ch* of each element. A value of $c = 0.4$ was recommended by Vulcano et al. (1988) and verified Orakcal and Wallace (2006) based on comparison of model responses with experimental results. Shear response of the wall is modeled by a horizontal spring placed at the height *ch*, with

behavior typically described by nonlinear ad-hoc force-deformation rules (e.g., an origin-oriented hysteresis model as first proposed by Kabeyasawa et al., 1983). Since shear and axial-flexural behaviors are described independently, there is no coupling between these responses in the original MVLEM (Figure 3-2).

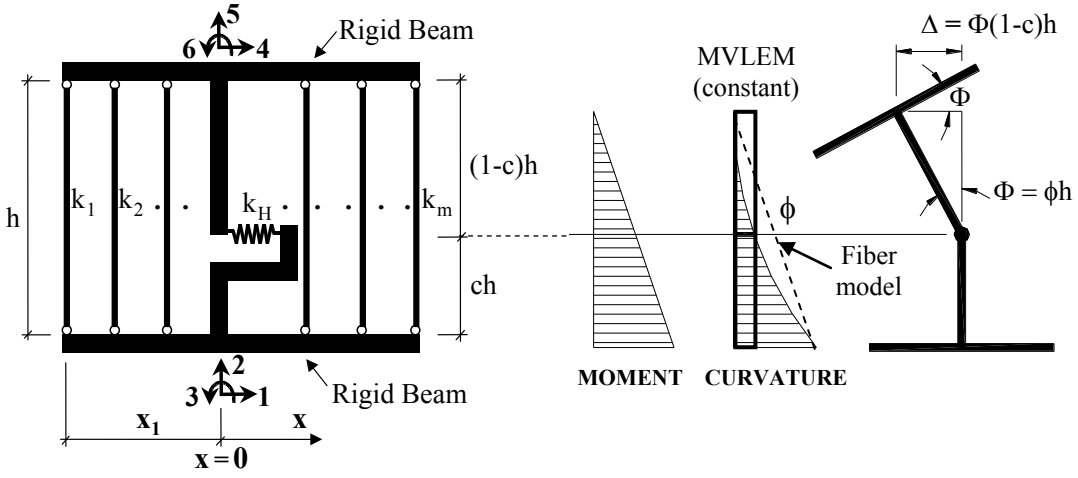

(a) Model Element Formulation (b) Rotations and Displacements

Figure 3-1 MVLEM element

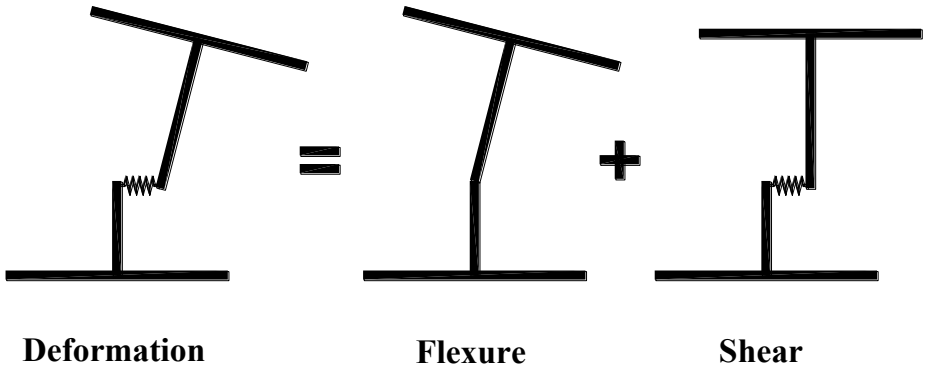

Figure 3-2 Uncoupled Shear and Flexural Deformations (Orakcal et al., 2004)

3.2. Proposed Model: Shear-Flexure Interaction MVLEM

3.2.1. General Model Description

The formulation of the proposed MVLEM with shear-flexure interaction (so-called SFI-MVLEM, Figure 3-3(c)) involves modifying the original formulation of the MVLEM (Figure 3-3(a), Vulcano et al., 1988; Orakcal et al., 2004), with uncoupled shear and flexural responses, by replacing each uniaxial element (macro-fiber) with a RC panel element subjected to membrane actions as shown on Figure 3-3(b). The behavior of RC panel elements under reversed cyclic loading conditions is described with constitutive RC panel model based on a Fixed-Strut-Angle-Model (FSAM) developed by Ulugtekin et al. (2010). In this study, the original formulation of FSAM is modified by implementing shear aggregate interlock (Orakcal et al., 2012) and dowel action associated with reinforcement (as described in Section 3.3) along inclined cracks of a RC panel to obtain improved model predictions. A RC panel model represents a two-dimensional constitutive behavior that relates the strain field imposed on a RC panel (ε_x, ε_y and γ_{xy}) to the resulting stress field (σ_x, σ_y and τ_{xy}), as shown in Figure 3-3(b). Therefore, the coupling of axial and shear responses is achieved at the macro-fiber level, which further incorporates interaction between shear and flexural/axial forces and deformations at the model element level.

The proposed model formulation involves three main assumptions: (a) plane sections remain plane, (b) shear strains are uniformly distributed across the wall cross-section, and (c) the sum of horizontal stresses associated with steel and concrete (i.e., resultant stress σ_x) along the length of the wall are equal to zero. Assumptions (a) and (b) are characteristics of the original MVLEM

formulation, while assumption (c) is required in the formulation of the SFI-MVLEM to satisfy equilibrium of RC panel elements in the horizontal (x) direction. Similar to the original MVLEM, flexural response of the wall element is captured through axial deformations of RC panel elements (macro-fibers) in the vertical (y) direction (Figure 3-3(c)), which corresponds to deformations of uniaxial fiber elements in the original model formulation (Figure 3-3(a)), and the relative rotation between the top and bottom faces of the wall element occurs on the central axis of the element at height *ch* (Figure 3-3(c)). The shear deformation of a SFI-MVLEM element occurs also at the element height of *ch* imposing shear strain (assumed to be uniformly distribution along the wall length) on each RC panel within a SFI-MVLEM element. Since the shear deformation of a SFI-MVLEM element is captured through shear deformations of its individual panels, the shear spring from the original MVLEM formulation (Figure 3-3(a)) is removed in the SFI-MVLEM formulation as shown on Figure 3-3(c). Rotations and resulting lateral displacements are calculated based on the wall curvature and shear deformations coupled at the model element level, derived from section and material properties of RC panel elements, respectively, corresponding to the bending moment and shear force at height *ch* of each element.

The assumption of a uniform distribution of shear strains does not significantly influence the predicted wall behavior in the case of slender RC walls because lateral displacement is primarily due to flexural deformations. However, using the same assumption for short walls may not be reasonable due to the possible presence of different deformation modes (e.g., warping) or load transfer mechanisms (e.g., strut action, or contribution of shear deformations). Also, the relatively small height of the wall may not be adequate to allow redistribution of stresses concentrated within the proximity of the points of load application or supports (so-called Saint-

Venant's effect). Such effects in the case of short RC walls can introduce non-uniformity in stresses and strains that may change the observed wall responses considerably. In addition, the assumption of zero resultant horizontal stress (σ_x) along the length of the wall implies that the resultant stresses from reinforcing steel and concrete within each RC panel element are equal to zero, which is consistent with the boundary conditions at the sides of a wall if no transverse loads are applied over its height. Massone et al. (2006) showed that assumptions of zero resultant horizontal stress, uniform shear strain distribution, and the plane-sections-remain-plane are reasonable for RC walls with aspect ratio greater than 1.0. Therefore, it is expected that application of the proposed modeling approach is limited to medium-rise and high-rise RC walls with aspect ratio or moment-to-shear span ratio greater than 1.0.

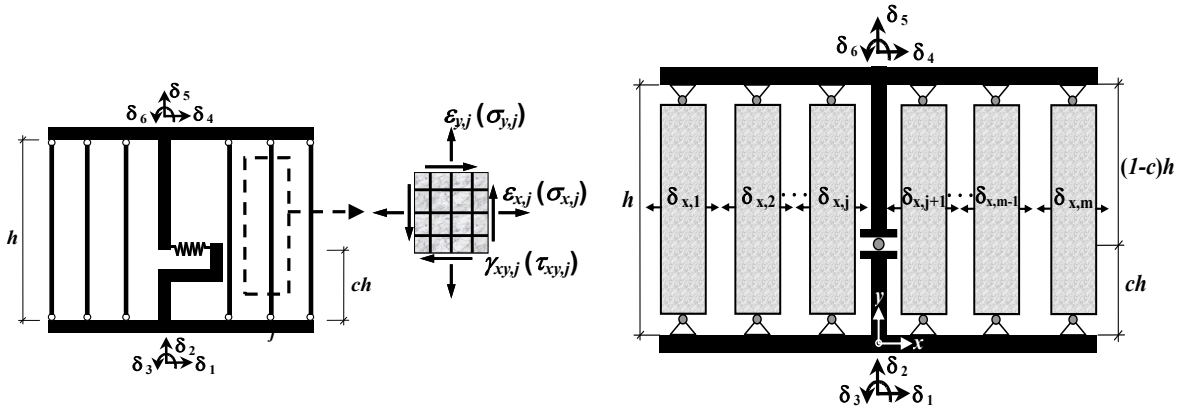

(a) Original MVLEM (b) RC panel element (c) SFI-MVLEM

Figure 3-3: Implementation of RC Panel Behavior into MVLEM

3.2.2. Model Element Degrees of Freedom

Each SFI-MVLEM element is characterized with six external degrees of freedom located at the center of the top and bottom rigid beams of a model element $\{\delta_N\} = \{\delta_1 \quad \delta_2 \quad . \quad . \quad . \quad \delta_6\}^T$ (Figure 3-4) that represent horizontal and vertical displacements and rotations at the top and bottom element nodes. Deformation components at these degrees of freedom are used for calculation of normal strain in the vertical direction $\varepsilon_{y,j}$ and shear strain $\gamma_{xy,j}$ for each RC panel element (macro-fiber) based on the plane section kinematic assumption and the assumption of uniform distribution of shear stresses along the wall cross-section. Normal strain in horizontal direction on each RC panel element $\varepsilon_{x,j}$, necessary to complete the strain field in each panel, is defined by the use of additional (internal) deformational degrees of freedom defined in the horizontal direction $\{\delta_x\} = \{\delta_{x,1} \quad \delta_{x,2} \quad . \quad . \quad . \quad \delta_{x,m}\}^T$, where *m* is the number of panel macro-fibers in one model element, as shown on Figure 3-4. The displacement at each degree of freedom $\delta_{x,j}$ is equal to deformation (extension) in the horizontal direction $u_{x,j}$ of each RC panel element ($u_{x,j} = \delta_{x,j}$). These internal deformational degrees of freedom in the horizontal direction on the panel macro-fibers $\{\delta_x\}$ are assumed to be kinematically independent from the six external nodal displacement degrees of freedom at the top and bottom of the element $\{\delta_N\}$. Therefore, the total number of degrees of freedom necessary to describe the deformation of one SFI-MVLEM element is increased from 6, in the original formulation of the MVLEM, to 6+*m*.

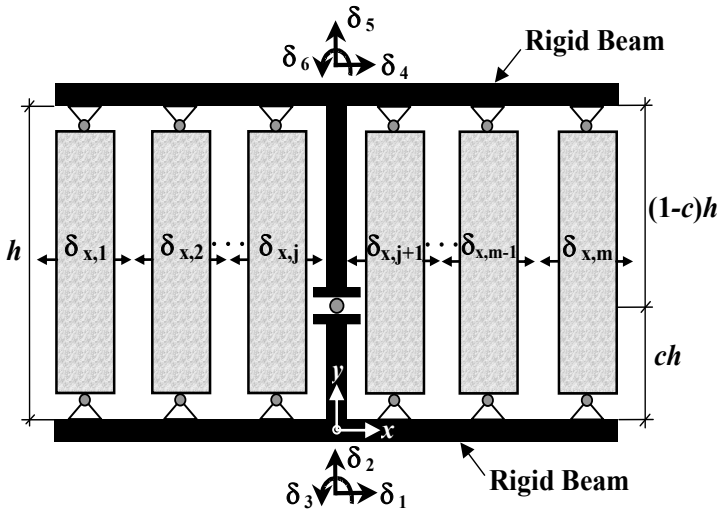

Figure 3-4 SFI-MVLEM Element - Degrees of Freedom

Let $\{\delta\}$ be the vector that represents the displacement components at all 6+*m* degrees of freedom of a MVLEM element shown on Figure 3-4. The components of vector $\{\delta\}$ can be separated into two sub-vectors: (1) $\{\delta_N\}$ which represents the six nodal degrees of freedom, and (2) $\{\delta_x\}$ which represents the internal degrees of freedom in the horizontal direction at each RC panel element. Hence, displacement vector $\{\delta\}$ can be written as:

$$\{\delta\} = \{\delta_N \quad \delta_x\}^T \tag{3-1}$$

where: $\{\delta_N\} = \{\delta_1 \quad \delta_2 \quad \delta_3 \quad \delta_4 \quad \delta_5 \quad \delta_6\}^T$, and $\{\delta_x\} = \{\delta_{x,1} \quad \delta_{x,2} \quad . \quad . \quad . \quad \delta_{x,m}\}^T$.

3.2.3. Calculation of Strain Fields on RC Panel Elements

Let the deformations in *y*-direction (vertical direction) of *m* RC panel elements in a SFI-MVLEM are represented by vector $\{u_y\}$.

$$\{u_y\} = \{u_{y,1} \quad u_{y,2} \quad . \quad . \quad . \quad u_{y,m}\}^T \tag{3-2}$$

The relationship between elements of this vector and the displacements at six nodal degrees of freedom $\{\delta_N\}$ is given by:

$$\{u_y\} = [a] \cdot \{\delta_N\} \tag{3-3}$$

where $[a]$ is the geometric transformation matrix that converts the displacement components at the nodal degrees of freedom $\{\delta_N\}$ to panel element deformations in the *y*-direction $\{u_y\}$ based on the plane-sections-remain-plane assumption.

$$[a] = \begin{bmatrix} 0 & -1 & -x_1 & 0 & 1 & x_1 \\ 0 & -1 & -x_2 & 0 & 1 & x_2 \\ . & . & . & . & . & . \\ . & . & . & . & . & . \\ 0 & -1 & -x_j & 0 & 1 & x_j \\ . & . & . & . & . & . \\ . & . & . & . & . & . \\ 0 & -1 & -x_m & 0 & 1 & x_m \end{bmatrix} \tag{3-4}$$

The average normal strain in the *y*-direction for *j*-th RC panel element ($\varepsilon_{y,j}$) is then calculated by dividing the deformation in the *y*-direction ($u_{y,j}$) by the model element height *h*:

$$\varepsilon_{y,j} = \frac{u_{y,j}}{h} \tag{3-5}$$

Similarly, shear deformation of a SFI-MVLEM element (u_{Sh}) is calculated at the element height of *ch* based on the deformation components at the six nodal degrees of freedom $\{\delta_N\}$ as:

$$u_{Sh} = \{b\}^T \{\delta_N\} \tag{3-6}$$

where the geometric transformation vector $\{b\}$ is defined as:

$$\{b\}^T = \begin{Bmatrix} 1 & 0 & -c \cdot h & -1 & 0 & -(1-c) \cdot h \end{Bmatrix} \tag{3-7}$$

Assuming that the distribution of shear strains along the length of the wall is constant and that the shear deformation of model element occurs in the horizontal plane of the wall, the shear strain for each RC panel element $\gamma_{xy,j}$ is calculated by dividing the shear deformation of a SFI-MVLEM element (u_{Sh}) by the element height *h*:

$$\gamma_{xy,j} = -\frac{u_{Sh}}{h} \tag{3-8}$$

Normal strain in horizontal direction (*x*-direction) for *j*-th RC panel element ($\varepsilon_{x,j}$) is obtained by dividing its deformation in the horizontal *x*-direction, defined by the extensional degree of freedom ($\delta_{x,j} = u_{x,j}$), by the width of that RC panel element in horizontal *x*-direction as:

$$\varepsilon_{x,j} = \frac{u_{x,j}}{b_j} \tag{3-9}$$

Therefore, strain field used to define deformation of each RC panel element is described by three strain degrees of freedom $\varepsilon_{x,j}$, $\varepsilon_{y,j}$ and $\gamma_{xy,j}$.

3.2.4. Element Stiffness Matrix

For any level of deformation imposed on the degrees of freedom of a model element $\{\delta\}$, the strain field acting on each of its RC panels is obtained as described in the previous section. The stiffness properties and force-deformation relationships of the panel macro-fibers are then defined according to one of three behavioral stages of the implemented constitutive panel model (as described in Section 3.3) and the tributary areas of concrete and reinforcing steel assigned to each panel macro-fiber. Since the deformation of each RC panel element is described by three strain degrees of freedom ($\varepsilon_{x,j}$, $\varepsilon_{y,j}$ and $\gamma_{xy,j}$), the tangent stiffness properties of a single RC panel element are given by the following 3x3 partial stiffness matrix:

$$\left[K_p\right]_j = \begin{bmatrix} \frac{\partial \sigma_x}{\partial \varepsilon_x} & \frac{\partial \sigma_x}{\partial \varepsilon_y} & \frac{\partial \sigma_x}{\partial \gamma_{xy}} \\ \frac{\partial \sigma_y}{\partial \varepsilon_x} & \frac{\partial \sigma_y}{\partial \varepsilon_y} & \frac{\partial \sigma_y}{\partial \gamma_{xy}} \\ \frac{\partial \tau_{xy}}{\partial \varepsilon_x} & \frac{\partial \tau_{xy}}{\partial \varepsilon_y} & \frac{\partial \tau_{xy}}{\partial \gamma_{xy}} \end{bmatrix}_j \tag{3-10}$$

For any prescribed strain level ($\varepsilon_{x,j}$, $\varepsilon_{y,j}$ and $\gamma_{xy,j}$), the axial stiffness in *x* and *y* directions ($k_{x,j}$ and $k_{y,j}$) and the shear stiffness ($k_{H,j}$) of the *j*-th RC panel element are derived as:

$$k_{x,j} = \left(\frac{\partial F_x}{\partial u_x}\right)_j = \left(\frac{\partial F_x}{\partial \sigma_x}\right)_j \cdot \left(\frac{\partial \sigma_x}{\partial \varepsilon_x}\right)_j \cdot \left(\frac{\partial \varepsilon_x}{\partial u_x}\right)_j = \left(\frac{\partial \sigma_x}{\partial \varepsilon_x}\right)_j \cdot \frac{A_{x,j}}{b_j} \tag{3-11}$$

$$k_{y,j} = \left(\frac{\partial F_y}{\partial u_y}\right)_j = \left(\frac{\partial F_y}{\partial \sigma_y}\right)_j \cdot \left(\frac{\partial \sigma_y}{\partial \varepsilon_y}\right)_j \cdot \left(\frac{\partial \varepsilon_y}{\partial u_y}\right)_j = \left(\frac{\partial \sigma_y}{\partial \varepsilon_y}\right)_j \cdot \frac{A_{y,j}}{h} \tag{3-12}$$

$$k_{Sh,j} = \left(\frac{\partial F_H}{\partial u_H}\right)_j = \left(\frac{\partial F_H}{\partial \tau_{xy}}\right)_j \cdot \left(\frac{\partial \tau_{xy}}{\partial \gamma_{xy}}\right)_j \cdot \left(\frac{\partial \gamma_{xy}}{\partial u_H}\right)_j = \left(\frac{\partial \tau_{xy}}{\partial \gamma_{xy}}\right)_j \cdot \frac{A_{y,j}}{h} \tag{3-13}$$

where $(\partial\sigma_x/\partial\varepsilon_x)_j$, $(\partial\sigma_y/\partial\varepsilon_y)_j$ and $(\partial\tau_{xy}/\partial\gamma_{xy})_j$ are the diagonal elements of the panel partial stiffness matrix $[K_p]_j$, b_j is the panel width in horizontal *x*-direction, h is the model element height in vertical *y*-direction, t is the wall thickness, and $A_{x,j}$ and $A_{y,j}$ are tributary areas of vertical and horizontal faces of *j*-th RC panel element (Figure 3-5) calculated as:

$$A_{x,j} = h \cdot t \tag{3-14}$$

$$A_{y,j} = b_j \cdot t \tag{3-15}$$

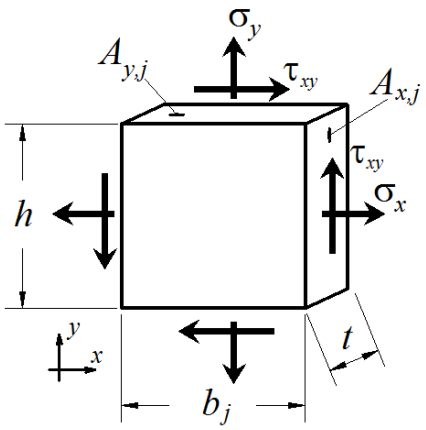

Figure 3-5 Panel Stresses and Tributary Areas

As mentioned earlier, shear behavior is considered in the horizontal plane of the RC wall; therefore, the panel shear stiffness given by Eq. 3-13 is calculated using the tributary area of horizontal face of the panel macro-fiber. The shear stiffness of a SFI-MVLEM element (k_{Sh}) for

a prescribed shear deformation (u_{Sh}) is calculated as a sum of shear stiffness of all RC panel elements in one model element as:

$$k_{Sh} = \sum_{j=1}^{m} k_{Sh,j} \tag{3-16}$$

For a specified set of displacement components at the six nodal degrees of freedom of a SFI-MVLEM wall element $\{\delta_N\}$ (Figure 3-4), the element stiffness matrix relative to these degrees of freedom $[K_e]_N$ is:

$$[K_e]_N = [\beta]^T \cdot [K]_N \cdot [\beta] \tag{3-17}$$

where $[\beta]$ denotes the geometric transformation matrix converting the element degrees of freedom to the element deformations of extension, relative rotation at the bottom, and relative rotation at the top of each wall element (Figure 3-6).

$$[\beta] = \begin{bmatrix} 0 & -1 & 0 & 0 & 1 & 0 \\ -1/h & 0 & 1 & 1/h & 0 & 0 \\ -1/h & 0 & 0 & 1/h & 0 & 1 \end{bmatrix} \tag{3-18}$$

The element stiffness matrix relative to the three pure deformation degrees of freedom shown in Figure 3-6 is given by:

$$[K]_N = \begin{bmatrix} \sum_{j=1}^{m} k_{y,j} & -\sum_{j=1}^{m} k_{y,j} x_j & \sum_{j=1}^{m} k_{y,j} x_j \\ & k_{Sh} c^2 h^2 + \sum_{j=1}^{m} k_{y,j} x_j{}^2 & k_{Sh} c(1-c) h^2 - \sum_{j=1}^{m} k_{y,j} x_j{}^2 \\ symm. & & k_{Sh} (1-c)^2 h^2 + \sum_{j=1}^{m} k_{y,j} x_j{}^2 \end{bmatrix} \quad (3\text{-}19)$$

where k_{Sh} is the stiffness of the horizontal spring of the MVLEM element (Eq. 3-16), $k_{y,j}$ is the stiffness of the *j*-th RC panel element in the *y*-direction (Eq. 3-12), and x_j is the distance of the *j*-th RC panel element to the central axis of the element (Figure 3-4).

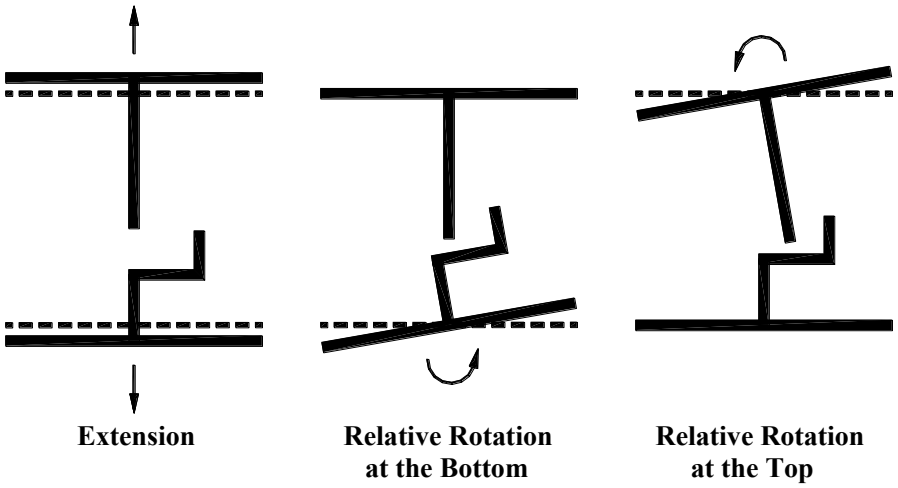

Figure 3-6 Element Deformations of the MVLEM Element (Vulcano et al, 1988)

Given that the horizontal degrees of freedom at each macro-fiber $\{\delta_x\}$ are independent from each other, the element stiffness matrix relative to these degrees of freedom is a diagonal matrix consisting of stiffness in the horizontal direction of each RC panel macro-fiber $k_{x,j}$ (Eq. 3-11) as:

$$[K_e]_x = diag[k_{x,1} \quad k_{x,2} \quad . \quad . \quad k_{x,m}]_{m,m} \tag{3-20}$$

The element stiffness matrix is now assembled from element stiffness sub-matrices $[K_e]_N$ and $[K_e]_x$. Since the deformations at six degrees of freedom $\{\delta_N\}$ and deformations at *m* extensional degrees of freedom $\{\delta_x\}$ are kinematically independent, the element stiffness matrix is a block matrix consisted two sub-matrices $[K_e]_N$ and $[K_e]_x$ given by:

$$[K_e] = \left[\begin{array}{c:c} [K_e]_N & [0] \\ \hdashline [0] & [K_e]_x \end{array}\right] \tag{3-21}$$

3.2.5. Element Force Vector

The force vector of a SFI-MVLEM element is assembled from the axial forces in the horizontal and vertical directions ($F_{x,j}$ and $F_{y,j}$) and shear forces in a horizontal plane ($F_{Sh,j}$) of all RC panel elements within the model element, calculated based on resulting panel axial and shear stresses and corresponding tributary areas (Figure 3-5). Resulting forces for *j*-th RC panel element are given as:

$$F_{x,j} = \sigma_{x,j} \cdot A_{x,j} \tag{3-22}$$

$$F_{y,j} = \sigma_{y,j} \cdot A_{y,j} \tag{3-23}$$

$$F_{Sh,j} = \tau_{xy,j} \cdot A_{y,j} \tag{3-24}$$

where $\sigma_{x,j}$, $\sigma_{y,j}$ and $\tau_{xy,j}$ are the axial and shear stresses obtained from the constitutive RC panel behavior for the prescribed strain field ($\varepsilon_{x,j}$, $\varepsilon_{y,j}$ and $\gamma_{xy,j}$), and $A_{x,j}$ and $A_{y,j}$ are panel tributary areas calculated according to Eq. 3-14 and 3-15, respectively (Figure 3-5).

Total shear force in one model element (F_{Sh}) is obtained as the sum of resultant shear forces on each RC panel element ($F_{Sh,j}$, Eq. 3-24) along the length of the wall as:

$$F_{Sh} = \sum_{j=1}^{m} F_{Sh,j} \tag{3-25}$$

Similar to the element stiffness matrix, the resisting (internal) force vector can be written as a combination of two sub-vectors, the force vector relative to the six degrees of freedom $\left[F_{\text{int},e}\right]_N$ and the force vector relative to *m* extensional degrees of freedom $\left[F_{\text{int},e}\right]_x$ as:

$$\left\{F_{\text{int},e}\right\} = \begin{Bmatrix} \left\{F_{\text{int},e}\right\}_N \\ \text{-------} \\ \left\{F_{\text{int},e}\right\}_x \end{Bmatrix} \tag{3-26}$$

where:

$$\left\{F_{\text{int},e}\right\}_N = \tag{3-27}$$
$$= \left\{ F_{Sh};\quad -\sum_{j=1}^{m} F_{y,j};\quad -F_{Sh}ch - \sum_{j=1}^{m} F_{y,j}x_j;\quad -F_{Sh};\quad \sum_{j=1}^{m} F_{y,j};\quad -F_{Sh}(1-c)h + \sum_{j=1}^{m} F_{y,j}x_j; \right\}^T$$

and:

$$\{F_{\text{int},e}\}_x = \{F_{x,6+1};\quad F_{x,6+2};\quad .\quad .\quad F_{x,6+m};\}^T \tag{3-28}$$

In Eq. 3-27 and 3-28, $F_{x,j}$ (Eq. 3-22) and $F_{y,j}$ (Eq. 3-23) are the forces in *x* and *y* directions in the *j*-th RC panel element, respectively, and F_{Sh} (given by Eq. 3-24 and 3-25) is the total shear force in one model element.

3.2.6. Global System Matrices

A complete wall model is assembled by stacking SFI-MVLEM elements on top of each other as shown on Figure 3-7(a). The total number of degrees of freedom s in the complete wall model is:

$$N = (3 \cdot n + 3) + m \cdot n \tag{3-29}$$

where *n* is the number of SFI-MVLEM elements in a wall model and *m* is the number of RC panel elements per model element. Figure 3-7 illustrates the assembly of stiffness matrix and force vector for the complete wall model from the element stiffness matrices and force vectors for the case when *n* = 3 and *m* = 4. The total number of degrees of freedom for this wall model according to Eq. 3-29 is *N* = 24. On Figure 3-7 only, brackets representing matrices and vectors as well as the subscript "*int*" in the global and element force vectors (Eq. 3-26 to 3-28) are dropped for the sake of simplicity (e.g., $K_{e,x}$ and $F_{e,x}$ are used instead of $[K_e]_x$ and $\{F_{\text{int},e}\}_x$, respectively), and subscript *e* corresponds to the model element number (e.g., *e* = 1, 2, 3 for *n*=3).

The global stiffness matrix $[K]$ (Figure 3-7(c)) is a square matrix of dimension *N*×*N*, assembled from the element stiffness matrices $[K_e]$ (Figure 3-7(b)). As given by Eq. 3-17, the element

stiffness matrix $[K_e]$ is a block matrix consisting of two sub-matrixes $[K_e]_N$ and $[K_e]_x$ corresponding to the element degrees of freedom $\{\delta_e\}_N$ and $\{\delta_e\}_x$, respectively. The components of global stiffness matrix $[K]$ that correspond to the nodal degrees of freedom $\{\delta_N\} = \{\delta_1 \quad ... \quad \delta_{12}\}$ (Figure 3-7(a)) are grouped in global sub-matrix $[K]_N$, which is assembled from for model element sub-matrices $[K_e]_N$ (Eq. 3-18, Figure 3-7(b)), and located in the upper left corner of global stiffness matrix $[K]$ (Figure 3-7(c)). The components of global stiffness matrix $[K]_x$ corresponding to the $n \times m$ extensional degrees of freedom $\{\delta_x\} = \{\delta_{13} \quad ... \quad \delta_{24}\}$ (Figure 3-7(a)) are assembled from diagonal model element sub-matrices $[K_e]_x$ (Eq. 3-21, Figure 3-7(b)), and located in the lower right corner of global stiffness matrix $[K]$ (Figure 3-7(c)).

Global force vector $\{F_{\text{int}}\}$ (Figure 3-7(d)) has dimension of $N \times 1$ and is assembled from element force vectors $\{F_{\text{int},e}\}$ (Eq., 3-26, Figure 3-7(b)). Each element force vector $\{F_{\text{int},e}\}$ consists of two sub-vectors $\{F_{\text{int}}\}_N$ and $\{F_{\text{int}}\}_x$ that correspond to degrees of freedom $\{\delta_e\}_N$ and $\{\delta_e\}_x$, respectively. The elements of the force vectors of each model element $\{F_{\text{int},e}\}_N$ are grouped in global force sub-vector $\{F_{\text{int}}\}_N$ and located at upper part of global force vector $\{F_{\text{int}}\}$ (elements 1 to 12, Figure 3-7(d)), while the elements of force vectors of each element $\{F_{\text{int},e}\}_x$ (Figure 3-

7(b)) are grouped in global force sub-vector $\{F_{\text{int}}\}_x$ and located at lower part of global force vector $\{F_{\text{int}}\}$ (elements 12 to 24, Figure 3-7(d)).

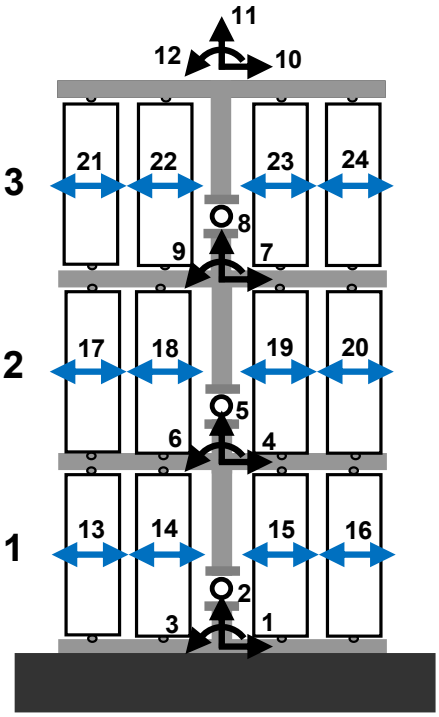

(a) Complete Wall Model with DOFs

n = 3: # of MVLEM-SFI elements

m = 4: # of RC panel elements

N = 24: Total # of DOFs

e = 1, 2, 3

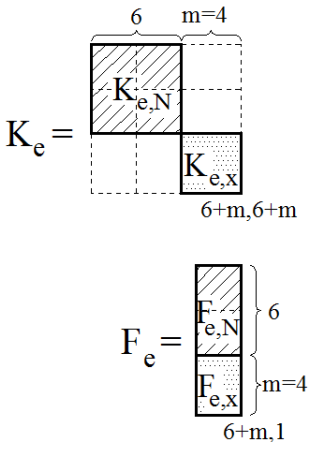

(b) Element Stiffness Matrix and Force Vector

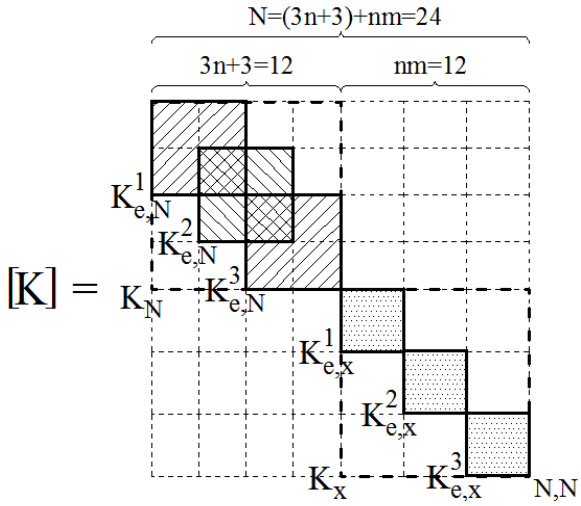

(c) Global Stiffness Matrix

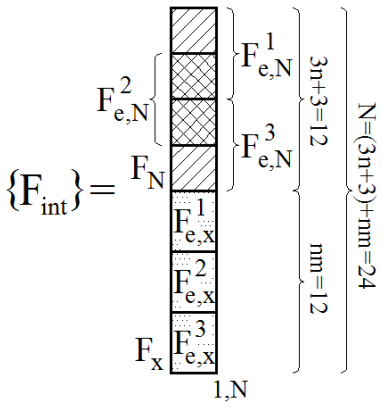

(d) Global Force Vector

Figure 3-7 Sample Model Assembly

Global stiffness matrix $[K]$ and force vector $\{F_{\text{int}}\}$ are used in solving the nonlinear quasi-static problem by performing nonlinear solution strategy as explained in Section 3.5.

3.3. Constitutive Reinforced Concrete Panel Behavior

The constitutive RC panel behavior under generalized reversed-cyclic in-plane membrane actions is described by the Fixed-Strut-Angle-Model (FSAM) proposed by Ulugtekin (2010), which was shown to replicate the results of cyclic panel tests available in the literature with reasonable accuracy. The FSAM is developed from the fixed-angle-softened-truss approach introduced by Pang and Hsu (1996) and Hsu and Zhang (1997) for monotonic loading, and extended by Mansour and Hsu (2005) for reversed-cyclic loading conditions. Shear aggregate interlock (Orakcal et al., 2012) and dowel action of web reinforcement are incorporated into the original formulation of the original FSAM to improve the predictions of SFI-MVLEM. A description of the implemented RC panel model formulation is provided in this section. Additional details can be found in thesis by Ulugtekin (2010).

3.3.1. Modified Fixed-Strut-Angle-Model

Strains calculated at each load-step/iteration (as described in the previous section) are applied to each of the RC panel element (macro-fiber) in the SFI-MVLEM wall model. The components of the strain field acting on concrete and reinforcing steel of a RC panel element are assumed to be equal to each other, implying the assumption of a perfect bond between concrete and reinforcing steel bars. The inherent assumptions in the formulation of the original FSAM (Ulugtekin, 2010) are that the directions of principal stress in concrete coincide with the directions of cracks,

implying zero shear stress action along cracks, and therefore, zero shear aggregate interlock and that dowel action on the reinforcement is equal to zero. Therefore, in the original FSAM, the reinforcing bars develop uniaxial stresses under uniaxial strains in their longitudinal directions and concrete behavior is based on uniaxial stress–strain relationships applied in biaxial directions with orientations determined by the state of concrete cracking. A modified formulation of FSAM, with implemented shear aggregate interlock model (Orakcal et al., 2012) and a simple model to account for dowel action of reinforcement, is incorporated into SFI-MVLEM to obtain improved predictions of cyclic response of RC structural walls; the influence of shear aggregate interlock and dowel actions on model predictions, as well as sensitivity of predicted wall responses to model parameters that represent these behaviors are discussed in Chapter 4. Behavior of the RC constitutive panel model is characterized with three stages of RC concrete panel behavior: (a) uncracked concrete, (b) formation of the first crack, and (c) formation of the second crack; each of these stages is described in the following sub-sections.

3.3.1.1. Uncracked Panel Behavior

Initially, the state of concrete is uncracked. In this state, the constitutive behavior of the RC panel element is represented with a rotating strut approach similar to the Modified Compression Field Theory (Vecchio and Collins, 1986) that uses monotonic stress–strain envelopes for concrete and steel, which is reasonable assumption for the uncracked stage of concrete behavior. The strain field imposed on concrete is transformed into principal strain directions (Figure 3-8(a)), which are assumed to coincide with principal stress directions, according to following expressions:

$$\theta = \frac{1}{2} \cdot \tan^{-1} \cdot \left(\frac{\gamma_{xy}}{\varepsilon_x - \varepsilon_y} \right) \tag{3-30}$$

$$\varepsilon_1 = \frac{\varepsilon_x + \varepsilon_y}{2} + \frac{\gamma_{xy}}{2 \cdot \sin 2\theta} \tag{3-31}$$

$$\varepsilon_2 = \frac{\varepsilon_x + \varepsilon_y}{2} - \frac{\gamma_{xy}}{2 \cdot \sin 2\theta} \tag{3-32}$$

where θ is a principal strain direction, and ε_1 and ε_2 are principal strains based on applied strain field (ε_x, ε_y and γ_{xy}).

Monotonic uniaxial stress-strain relationships for concrete are applied along the principal strain directions to obtain concrete principal stresses σ_{c1} and σ_{c2} (Figure 3-8(b)). Although stress–strain relationships for concrete applied in principal directions are fundamentally uniaxial in nature, they incorporate biaxial softening effects including compression softening and biaxial damage (as described in Sections 3.4.3 and 3.4.5). Therefore, the principal stresses in concrete (σ_{c1} and σ_{c2}) are softened by the use of softening coefficient β as:

$$\sigma_{c1soft} = \beta \cdot \sigma_{c1} \tag{3-33}$$

$$\sigma_{c2soft} = \beta \cdot \sigma_{c2} \tag{3-34}$$

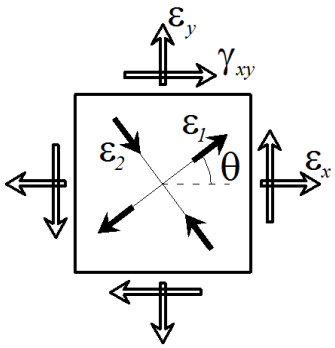

(a) Applied Strain Field and Corresponding Principal Strains of Unckracked Panel

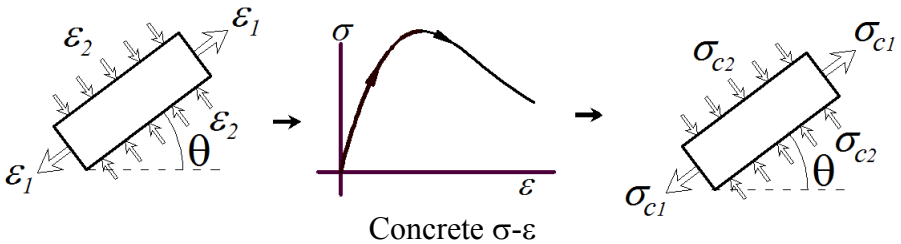

(b) Calculation of Stresses in Concrete using the Monotonic Constitutive Model

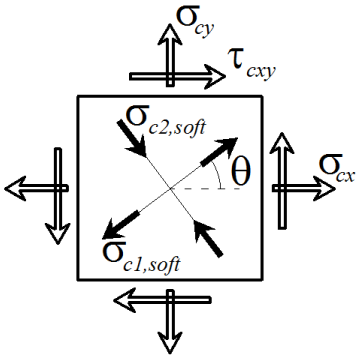

(c) Back-Transformation of Softened Concrete Stresses

Figure 3-8 Uncracked Panel Behavior

The final (softened) concrete stress values are then back transformed into the *x*-*y* coordinate system (Figure 3-8(c)) to obtain the concrete stress state (σ_{cx}, σ_{cy} and τ_{cxy}) as:

$$\sigma_{cx} = \frac{\sigma_{c1soft} + \sigma_{c2soft}}{2} + \frac{\sigma_{c1soft} - \sigma_{c2soft}}{2} \cdot \cos 2\theta \tag{3-35}$$

$$\sigma_{cy} = \frac{\sigma_{c1soft} + \sigma_{c2soft}}{2} - \frac{\sigma_{c1soft} - \sigma_{c2soft}}{2} \cdot \cos 2\theta \tag{3-36}$$

$$\tau_{cxy} = \frac{\sigma_{c1soft} - \sigma_{c2soft}}{2} \cdot \sin 2\theta \tag{3-37}$$

A monotonic uniaxial stress-strain relationship for reinforcing steel is applied along x and y directions to obtain stresses in horizontal and vertical reinforcement (σ_{sx} and σ_{sy}) as shown on Figure 3-9.

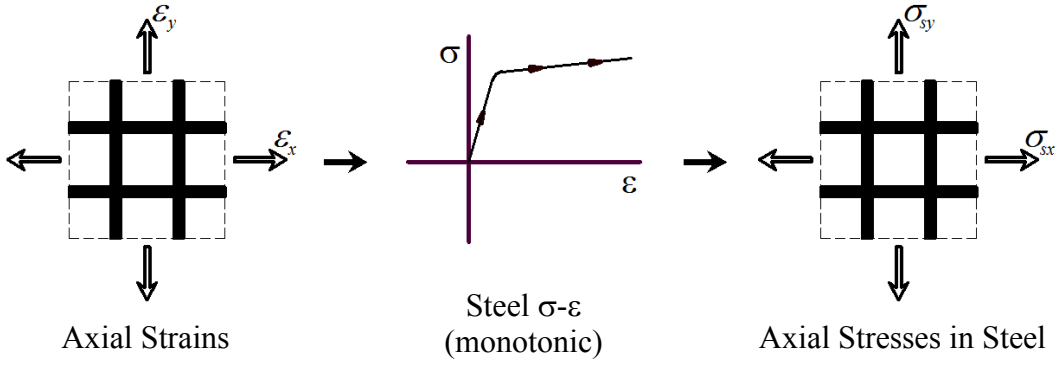

Figure 3-9 Calculation of Stresses in Steel Using Monotonic Constitutive Model

The resulting state of stress in a RC panel element is obtained by superposition of the panel stress fields for concrete and reinforcing steel as shown on Figure 3-10 according to following expressions:

$$\sigma_x = \sigma_{cx} + \rho_{sx} \cdot \sigma_{sx} \tag{3-38}$$

$$\sigma_y = \sigma_{cy} + \rho_{sy} \cdot \sigma_{sy} \tag{3-39}$$

$$\tau_x = \tau_{cxy} \tag{3-40}$$

where ρ_{sx} and ρ_{sy} are the steel reinforcing ratio in x and y direction, respectively.

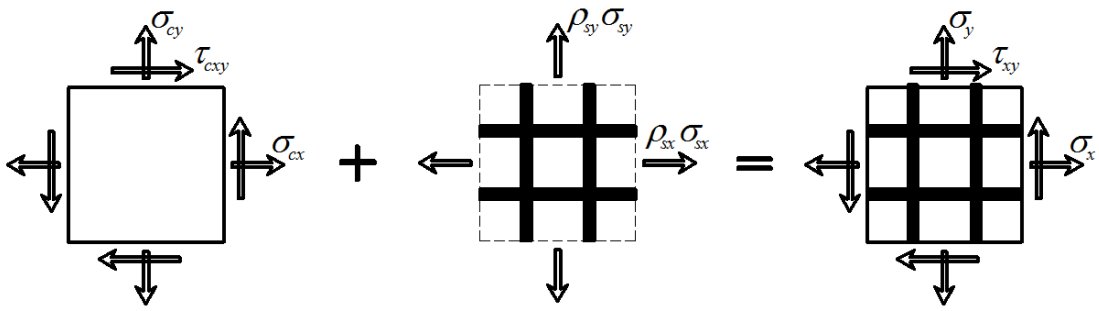

Figure 3-10 Superposition of Stress Fields for Concrete and Steel

3.3.1.2. Panel Behavior after Formation of the First Crack

The first crack is formed when the value of principal tensile strain in concrete exceeds the monotonic cracking strain of concrete for the first time. For the following loading stages, the principal strain direction at the instance of cracking ($\theta = \theta_{crA}$) is assigned as the first "fixed strut" direction for the panel, and it remains unchanged for all of the following loading stages. Direction of the first strut is calculated based on the strain field acting on the panel at the instance of cracking as:

$$\theta_{crA} = \frac{1}{2} \cdot \tan^{-1} \cdot \left(\frac{\gamma_{xy}}{\varepsilon_x - \varepsilon_y} \right) \qquad \text{(at first cracking)} \tag{3-41}$$

In the following loading stages the principal strains ε_1 and ε_2 corresponding to applied strain field (ε_x, ε_y, γ_{xy}), which in the general case deviate from the direction of first fixed strut θ_{crA}, are now transformed into directions parallel and perpendicular to the first strut direction at an angle θ_{crA} ($\varepsilon_{x'}$ and $\varepsilon_{y'}$) as shown on Figure 3-11(a). Axial strains along and perpendicular to the direction of the fixed strut $\varepsilon_{x'}$ and $\varepsilon_{y'}$, and shear slip along the crack surface $\gamma_{x'y'}$ are calculated as:

$$\varepsilon_{x'} = \frac{\varepsilon_x + \varepsilon_y}{2} + \frac{\varepsilon_x - \varepsilon_y}{2} \cdot \cos 2\theta_{cr} + \frac{\gamma_{xy}}{2} \cdot \sin 2\theta_{cr} \tag{3-42}$$

$$\varepsilon_{y'} = \frac{\varepsilon_x + \varepsilon_y}{2} + \frac{\varepsilon_x - \varepsilon_y}{2} \cdot \cos 2\theta_{cr-per} + \frac{\gamma_{xy}}{2} \cdot \sin 2\theta_{cr-per} \tag{3-43}$$

$$\gamma_{x'y'} = \gamma_{xy} \cdot \cos 2\theta_{cr} - \left(\varepsilon_x - \varepsilon_y\right) \cdot \sin 2\theta_{cr} \tag{3-44}$$

where, $\theta_{cr-per} = \theta_{cr} \pm \frac{\pi}{2}$.

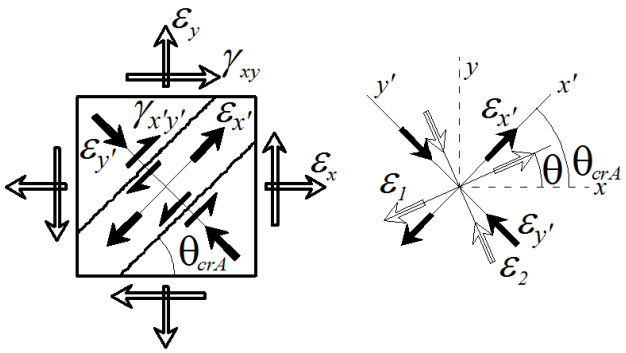

(a) First Fixed Strut, Deviation of Principal Strain Field

Figure 3-11 Panel Behavior after Formation of the First Crack

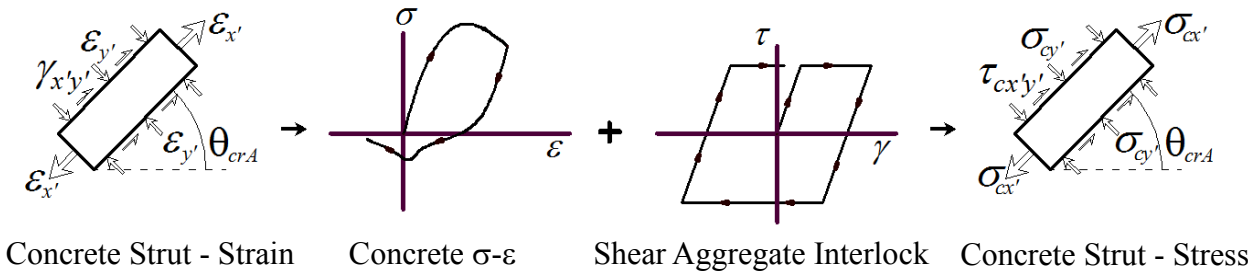

(b) Calculation of Stresses in Concrete using Hysteretic Constitutive Models

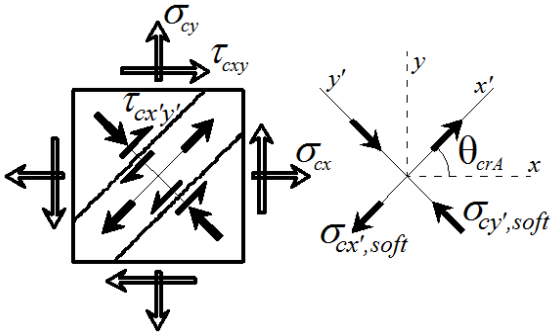

(c) Back-Transformation of Softened and Aggregate Interlock Concrete Stresses

Figure 3-11 (cont.) Panel Behavior after Formation of the First Crack

The concrete stresses along and perpendicular to the first fixed strut direction ($\sigma_{cx'}$ and $\sigma_{cy'}$) are obtained from the cyclic uniaxal material law for concrete based on axial strains applied along these directions ($\varepsilon_{x'}$ and $\varepsilon_{y'}$, Figure 3-11(b)), after which these stresses are reduced by appropriate compression softening and biaxial damage parameters to obtain softened concrete stresses along and perpendicular to first fixed strut direction $\sigma_{cx',soft}$ and $\sigma_{cy',soft}$ (Eq. 3-33 and 3-34). In addition, the shear aggregate interlock stresses along the surface of first fixed crack ($\tau_{cx'y'}$) are obtained based on the magnitude of shear slip along the crack surface ($\gamma_{x'y'}$, Eq. 3-

44) and the normal stress perpendicular to the crack ($\sigma_{cy',soft}$) according to the implemented shear aggregate interlock model as described in Section 3.3.2.1 (Figure 3-11(b)).

Softened concrete stress values ($\sigma_{cx',soft}$ and $\sigma_{cy',soft}$) and the shear aggregate interlock stress along the crack surface ($\tau_{cx'y'}$) are back-transformed into the *x*-*y* coordinate system and superimposed to obtain the resulting concrete stress state in the *x*-*y* coordinates (σ_{cx}, σ_{cy}, and τ_{cxy}) as shown in Figure 3-11(c)).

$$\sigma_{cx} = \frac{\sigma_{cx'soft} + \sigma_{cy'soft}}{2} + \frac{\sigma_{cx'soft} - \sigma_{cy'soft}}{2} \cdot \cos 2\theta_{cr} - \tau_{cx'y'} \cdot \sin 2\theta_{cr} \tag{3-45}$$

$$\sigma_{cy} = \frac{\sigma_{cx'soft} + \sigma_{cy'soft}}{2} - \frac{\sigma_{cx'soft} - \sigma_{cy'soft}}{2} \cdot \cos 2\theta_{cr} + \tau_{cx'y'} \cdot \sin 2\theta_{cr} \tag{3-46}$$

$$\tau_{cxy} = \frac{\sigma_{c1soft} - \sigma_{c2soft}}{2} \cdot \sin 2\theta + \tau_{cx'y'} \cdot \sin 2\theta_{cr} \tag{3-47}$$

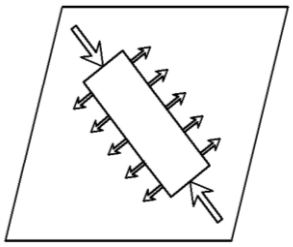

Figure 3-12 Fixed Strut Mechanism after the Formation of the First Crack (Uluğtekin, 2010)

In this stage of concrete behavior (after first cracking), since the direction of the first strut is fixed, a uniaxial hysteretic stress-strain relationship for concrete is applied in principal stress

directions, and history variables in the concrete stress-strain relationship are easily tracked and stored in the two fixed perpendicular directions (Figure 3-12).

The stress field on reinforcing steel is obtained based on axial strains in horizontal *x*-direction and vertical *y*-direction (ε_x and ε_y) by applying a cyclic uniaxial stress-strain relationship for steel along *x* and *y* directions to obtain steel stresses in horizontal and vertical reinforcement (σ_{sx} and σ_{sy}) as illustrated in Figure 3-13. In addition, the shear stress perpendicular to the vertical reinforcement (τ_{sxy}) is calculated based on a shear strain acting on the panel (γ_{xy}) according to implemented dowel action model (as described in Section 3.3.2.2).

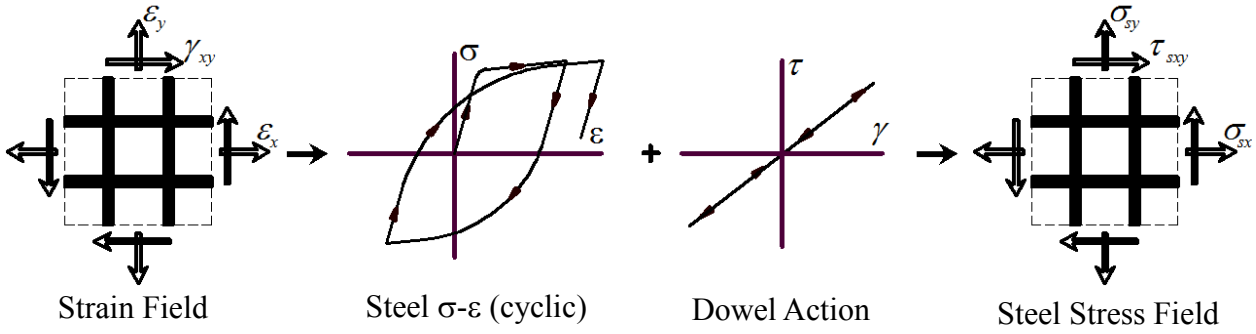

Figure 3-13 Calculation of Stresses in Steel Using Cyclic Constitutive Model and Dowel Action

Finally, the stress fields for concrete and reinforcing steel are superimposed to obtain the resulting state of stress in the panel corresponding to the applied strain field (Figure 3-14).

$$\sigma_x = \sigma_{cx} + \rho_{sx} \cdot \sigma_{sx} \tag{3-48}$$

$$\sigma_y = \sigma_{cy} + \rho_{sy} \cdot \sigma_{sy} \tag{3-49}$$

$$\tau_x = \tau_{cxy} + \tau_{sxy} \tag{3-50}$$

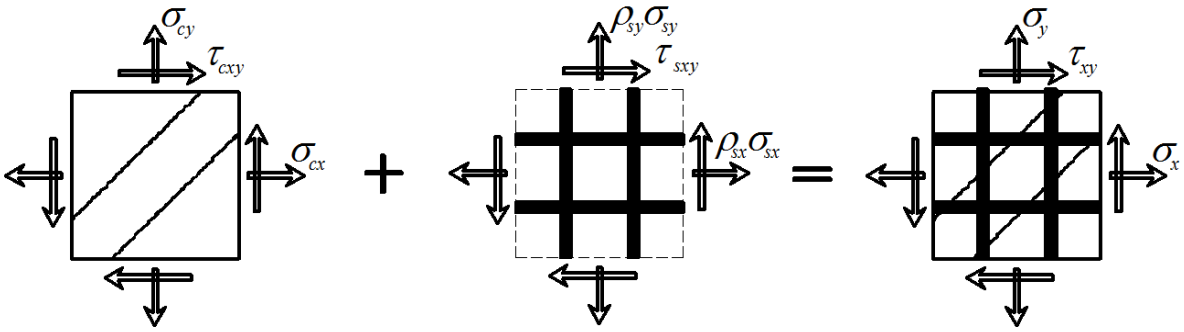

Figure 3-14 Superposition of Stress Fields for Concrete and Steel

3.3.1.3. Panel Behavior after Formation of the Second Crack

The analysis is continued in the form of a single fixed strut mechanism until the formation of the second crack, after which the second strut will develop in the panel model. During the first fixed strut stage of the analysis, the model tracks the concrete stress–strain behavior along the first strut direction, and when the strain along the first strut direction first exceeds the cyclic cracking strain, which depends on both the monotonic cracking strain and the plastic strain upon reversal from a compressive stress state, the second crack is formed. The direction of the second crack is assumed to be perpendicular to the first crack, which is in the case of zero aggregate interlock assumption (the original FSAM formulation) in agreement with a stress-based cracking criterion, since the first strut direction is a principal stress direction and the concrete stress–strain relationship is assumed to be uniaxial along the first strut direction. In the modified FSAM (implemented in this study), the direction of the principal stresses in concrete (i.e. second fixed-strut) can deviate from the direction perpendicular to the first fixed-strut due to the presence of shear aggregate interlock, and an alternative cracking criterion for defining the direction of the second crack was investigated in which the formation and direction of the second crack was

associated with the direction of concrete principal stress. It was found that analytical results obtained by the use of this cracking criterion for the cases investigated (test wall configurations described in Chapter 5) were not significantly different from the original assumption of perpendicular concrete struts. Therefore, for the sake of simplicity and mechanical consistency, the panel model formulation in which the second strut direction forms perpendicular to the first strut is adopted here for the SFI-MVLEM. Hence, the direction of the second "fixed strut" (direction of the second crack) is calculated based on the direction of the first strut as:

$$\theta_{crB} = \theta_{crA} \pm \frac{\pi}{2} \tag{3-51}$$

The principal strains ε_1 and ε_2 corresponding to the applied strain field (ε_x, ε_y and γ_{xy}), which are not aligned with directions of concrete struts in general, are transformed into directions parallel to the first and second strut directions at an angle θ_{crA} and θ_{crB} (Figure 3-15(a)), respectively, by calculating the axial strains along these directions $\varepsilon_{x'}$ and $\varepsilon_{y'}$, as well as the slips along the first and second crack surfaces $\gamma_{x'y'A}$ and $\gamma_{x'y'B}$ according to following expressions:

$$\varepsilon_{x'} = \frac{\varepsilon_x + \varepsilon_y}{2} + \frac{\varepsilon_x - \varepsilon_y}{2} \cdot \cos 2\theta_{crA} + \frac{\gamma_{xy}}{2} \cdot \sin 2\theta_{crA} \tag{3-52}$$

$$\varepsilon_{y'} = \frac{\varepsilon_x + \varepsilon_y}{2} + \frac{\varepsilon_x - \varepsilon_y}{2} \cdot \cos 2\theta_{crB} + \frac{\gamma_{xy}}{2} \cdot \sin 2\theta_{crB} \tag{3-53}$$

$$\gamma_{xy'A} = \gamma_{xy} \cdot \cos 2\theta_{crA} - \left(\varepsilon_x - \varepsilon_y\right) \cdot \sin 2\theta_{crA} \tag{3-54}$$

$$\gamma_{xy'B} = \gamma_{xy} \cdot \cos 2\theta_{crB} - \left(\varepsilon_x - \varepsilon_y\right) \cdot \sin 2\theta_{crB} \tag{3-55}$$

The concrete stresses along the first and second fixed strut directions ($\sigma_{cx'}$ and $\sigma_{cy'}$) are then obtained from the concrete cyclic uniaxal constitutive law (Figure 3-15(b)), after which these stresses are reduced by appropriate compression softening and biaxial damage parameters to obtain softened (final) concrete stresses along the first and second fixed strut directions, $\sigma_{cx'soft}$ and $\sigma_{cy'soft}$ (Eq. 3-33 and 3-34). Similar to the single crack mechanism, the resultant concrete shear stresses along the first and second crack surfaces ($\tau_{x'y'A}$ and $\tau_{x'y'B}$) are obtained from the shear aggregate interlock constitutive model (described in Section 3.3.2.1) given the magnitude of shear slip along these crack surfaces ($\gamma_{x'y'A}$ and $\gamma_{x'y'B}$, Eq. 3-54 and 3-55) and the normal stress perpendicular to the cracks *A* and *B*, $\sigma_{y'soft}$ and $\sigma_{x'soft}$, respectively (Figure 3-15(b)).

The softened axial stresses along the first and second concrete struts ($\sigma_{cx'soft}$ and $\sigma_{cy'soft}$) and shear stresses coming from the aggregate interlock ($\tau_{x'y'A}$ and $\tau_{x'y'B}$) are back-transformed into the *x*-*y* coordinate system (Figure 3-15(c)) according to following stress transformation formulas:

$$\sigma_{cxA} = \frac{\sigma_{cx'soft} + 0}{2} + \frac{\sigma_{cx'soft} - 0}{2} \cdot \cos 2\theta_{crA} - \tau_{xy'A} \cdot \sin 2\theta_{crA} \tag{3-56}$$

$$\sigma_{cyA} = \frac{\sigma_{cx'soft} + 0}{2} - \frac{\sigma_{cx'soft} - 0}{2} \cdot \cos 2\theta_{crA} + \tau_{xy'A} \cdot \sin 2\theta_{crA} \tag{3-57}$$

$$\tau_{cxyA} = \frac{0 - \sigma_{cx'soft}}{2} \cdot \sin 2\theta_{crA} + \tau_{xy'A} \cdot \sin 2\theta_{crA} \tag{3-58}$$

$$\sigma_{cxB} = \frac{0+\sigma_{cy'soft}}{2} + \frac{0-\sigma_{cy'soft}}{2} \cdot \cos 2\theta_{crB} - \tau_{xy'B} \cdot \sin 2\theta_{crB} \tag{3-59}$$

$$\sigma_{cyB} = \frac{0+\sigma_{cy'soft}}{2} - \frac{0-\sigma_{cy'soft}}{2} \cdot \cos 2\theta_{crB} + \tau_{xy'B} \cdot \sin 2\theta_{crB} \tag{3-60}$$

$$\tau_{cxyB} = \frac{0-\sigma_{c2soft}}{2} \cdot \sin 2\theta_{crB} + \tau_{xy'B} \cdot \sin 2\theta_{crB} \tag{3-61}$$

Similar to the single strut mechanism, stresses in horizontal and vertical reinforcement (σ_{sx} and σ_{sy}) are obtained by the use of cyclic uniaxial stress-strain relationship for reinforcing steel applied along *x* and *y* directions, and the dowel stress on the reinforcement (τ_{sxy}) is obtained based on a shear strain acting on the panel (γ_{xy}) by using the simple dowel action model described in Section 3.3.2.2 (Figure 3-13).

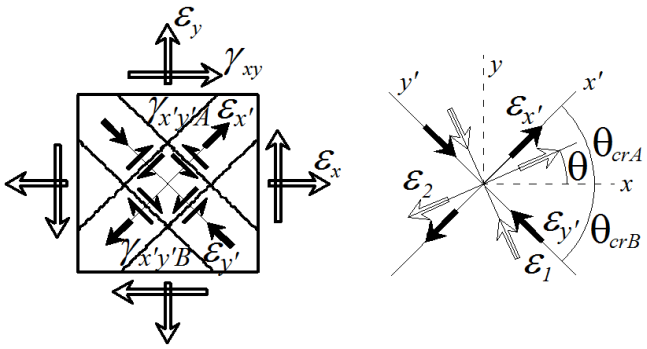

(a) Deviation of principal strain field, fixed strut directions

Figure 3-15 Panel behavior after formation of the second crack

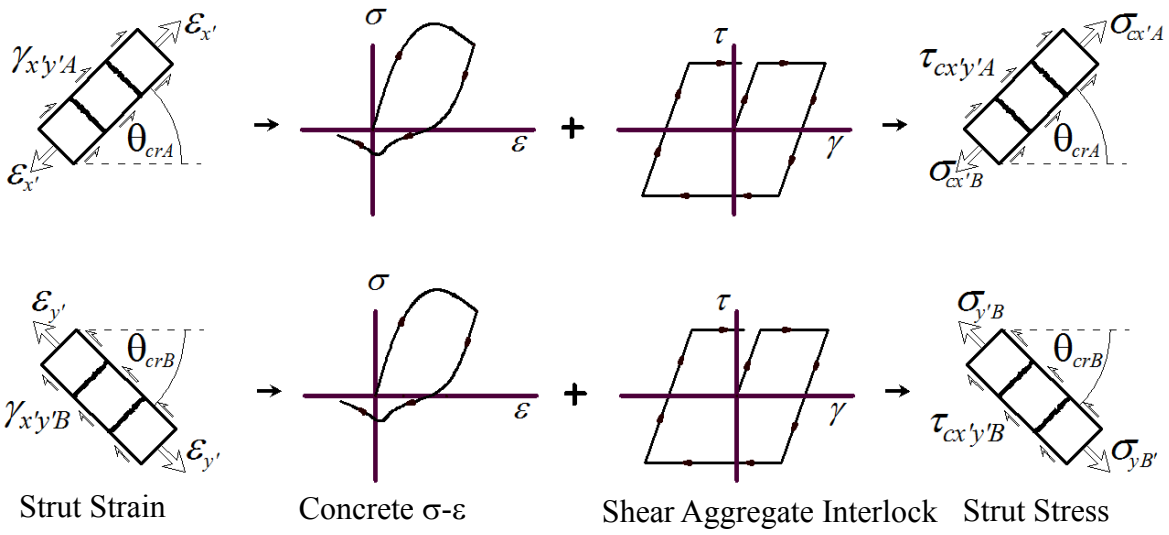

(b) Calculation of stresses in concrete using hysteretic constitutive model

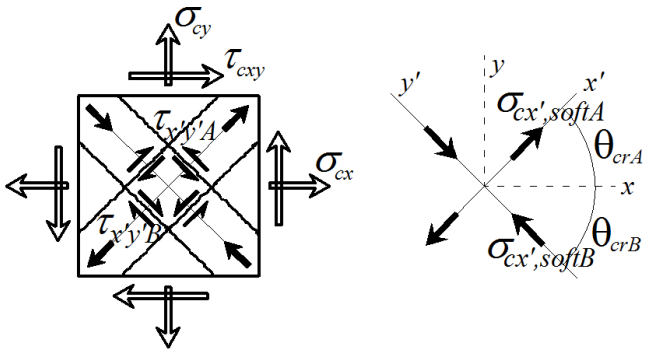

(c) Back-transformation of softened concrete stresses and stress superposition

Figure 3-15(cont.) Panel behavior after formation of the second crack

Finally, the concrete stress fields corresponding to Strut A and Strut B are superimposed to obtain the complete concrete stress state in the *x*-*y* coordinates (Figure 3-15(c)) as:

$$\sigma_{cx} = \sigma_{cxA} + \sigma_{cxB} \tag{3-62}$$

$$\sigma_{cy} = \sigma_{cyA} + \sigma_{cyB} \tag{3-63}$$

$$\tau_{cxy} = \tau_{cxyA} + \tau_{cxyB} \tag{3-64}$$

Finally, the stress fields for concrete and reinforcing steel are superimposed to obtain the resulting state of stress in the panel (Figure 3-16) that corresponds to the applied strain field as:

$$\sigma_x = \sigma_{cx} + \rho_{sx} \cdot \sigma_{sx} \tag{3-65}$$

$$\sigma_y = \sigma_{cy} + \rho_{sy} \cdot \sigma_{sy} \tag{3-66}$$

$$\tau_x = \tau_{cxy} + \tau_{sxy} \tag{3-67}$$

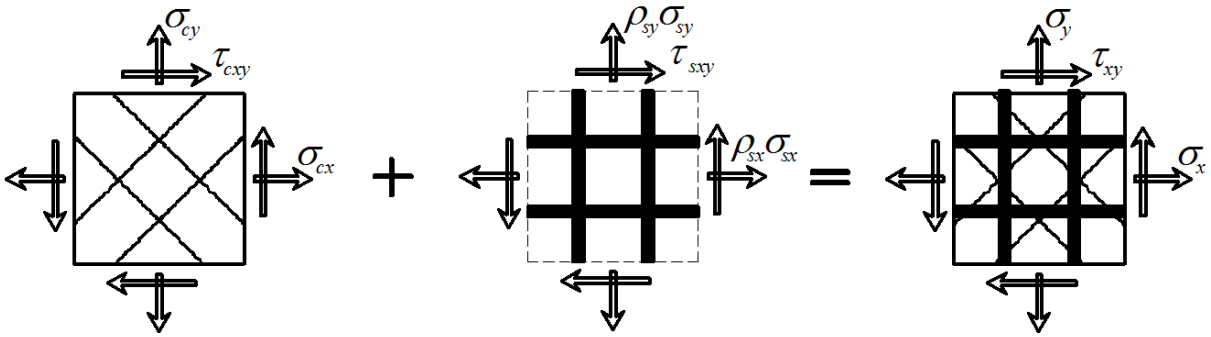

Figure 3-16 Superposition of Stress Fields for Concrete and Steel

For further loading stages, the concrete mechanism consists of two independent struts, working as interchanging compression and tension struts in the two fixed strut directions (Figure 3-17), based on the applied strain field, and history variables in the concrete stress-strain relationship can be tracked and stored in the two fixed directions.

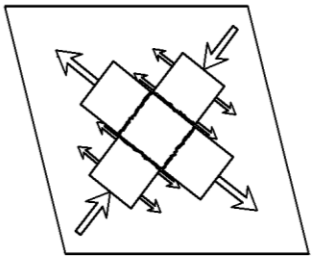

Figure 3-17 Representation of the two-fixed-strut mechanism after formation of the second crack (Uluğtekin, 2010)

3.3.2. Modeling of Shear Resisting Mechanism

As described above, the main inherent assumption underlying the original FSAM is that the principal stress directions in concrete coincide with crack directions, implying that shear strains along crack surfaces (shear slip or sliding), developed due to the deviation between principal strain directions and the principal stress directions in concrete, do not develop shear stresses due to aggregate interlocking along crack surfaces. This inherent assumption of the model is based on interpretation of existing panel tests in the literature, which typically indicate that for a RC panel after formation of cracks the principal stress direction in concrete does not change significantly with loading, although the principal strain direction on a panel may undergo significant variation (e.g., Stevens et al., 1991). The principal stress directions in concrete being insensitive to loading may imply that after formation of cracks, the principal stress directions in concrete follow approximately the fixed crack directions, indicating that shear stresses along a crack (and thus shear aggregate interlocking along a crack) has marginal influence on the panel behavior.

However, in a RC panel, sliding along crack surfaces is known to develop due to aggregate interlock, resulting in shear stress along the crack, the magnitude of which is affected by the crack surface roughness and width, the magnitude of normal stress perpendicular to the crack, as well as the amount of slip deformation along the crack. As discussed in Chapter 4 (Section 4.4.1.1), the zero-aggregate interlock assumption generally results in significant overestimation of sliding shear strains along panel crack surfaces leading to overestimation of shear deformations in RC wall specimens and underestimation of wall strength. Since the original formulation of FSAM allows calculation of shear strains along a crack, it is possible to incorporate a suitable cyclic shear aggregate interlock constitutive model (shear stress versus shear strain along crack surfaces). In addition, the original FSAM formulation (Ulugteking, 2010) does not consider dowel action on the reinforcement, which may also contribute to shear resistance of RC panel elements. Therefore, in order to improve the analytical predictions for RC wall specimens, the original formulation of the FSAM is modified here to incorporate two shear resisting mechanisms across a concrete crack: (1) friction-based shear aggregate interlock model (Orakcal et al., 2012), and (2) linear-elastic reinforcement dowel action. Although this approach is conceptually similarly to shear-friction approach presented in ACI 318-11 (Section 11.6.4), in which shear aggregate interlock and dowel action of reinforcement are combined into one shear resisting mechanism, in the implemented RC panel model these effects are described with two independent models, which provides more flexibility in calibration of model results with experimentally observed behavior. Details about implemented shear aggregate interlock and dowel action model are provided in the following sub-sections.

3.3.2.1. Modeling of Shear Aggregate Interlock

Orakcal et al. (2012) modified the original formulation of FSAM, with zero shear aggregate interlock, by incorporating simple friction-based constitutive model to represent the effects of shear aggregate interlock. The proposed cyclic shear aggregate interlock model starts with linear loading/unloading behavior to relate sliding shear strain along a crack to resultant shear stress along the crack surface. The shear stress is set to zero when the concrete normal stress perpendicular to the crack is tensile (crack open); and is bounded by the product of a friction coefficient η and the concrete normal stress perpendicular to the crack $\sigma_{\perp c}$, when the concrete normal stress is compressive (crack closed). The linear unloading/reloading slope of the shear stress versus sliding strain relationship was taken as a fraction of the concrete elastic modulus; a value $0.4Ec$ was adopted, representing the elastic shear modulus of concrete. The friction coefficient η is considered between 0.6 and 1.4 based on previous research conducted on transfer of shear force in reinforced concrete through shear-friction mechanism (e.g., Chorzepa et al., 2011; Wood, 1990; Hofbeck et al., 1969, Mattock, 1974), and represents a parameter that can be calibrated against test data. As shown on Figure 3-18, under constant compressive stress in concrete perpendicular to the crack ($\sigma_{\perp c}$ = *const*), this model produces elasto-plastic aggregate interlock behavior under cyclic loading, similar to the cyclic stress-strain behavior of reinforcing steel.

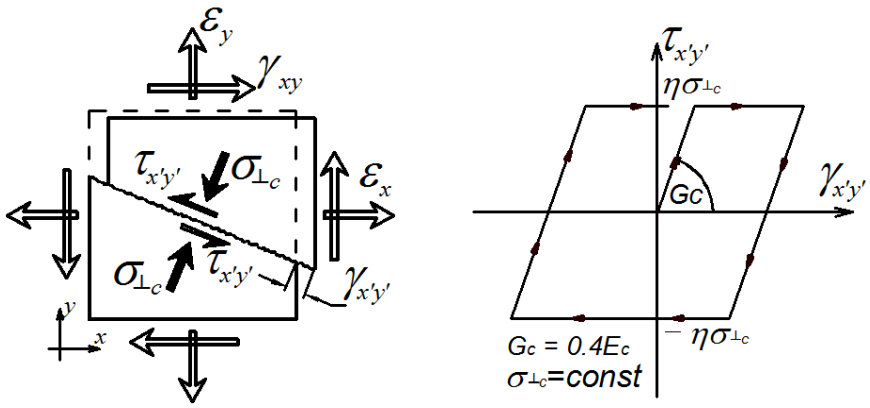

Figure 3-18 Shear aggregate interlock model

3.3.2.2. Modeling of Dowel Action

As discussed in Chapter 4 (Section 4.4.1.1), the use of a RC panel model with described shear aggregate interlock model provided analytical predictions for RC shear wall tests in which shear deformations and pinching of force-deformation response were overestimated in addition to producing a negative stiffness in the unloading branch around zero lateral deformation; detailed review suggested that this is the result of zero shear resistance along the cracks under tension (crack open). However, dowel resistance of vertical reinforcement can provide shear resistance along a crack of a RC panel under shear deformation in the horizontal plane of the wall, even when the crack surface is in tension; therefore, a simple linear-elastic constitutive model is implemented in the RC panel model to simulate the contribution of reinforcement dowel action to shear resistance as:

$$\tau_{sxy} = \alpha \cdot E_s \cdot \gamma_{xy} \tag{3-68}$$

Equation 3-68 relates resulting shear stress on the RC panel due to dowel action of vertical reinforcement (τ_{sxy}) to the shear strain acting on the panel in horizontal plane of the wall (γ_{xy}) using an elastic modulus taken as a fraction (α) of the elastic steel modulus (E_s) (Figure 3-14).

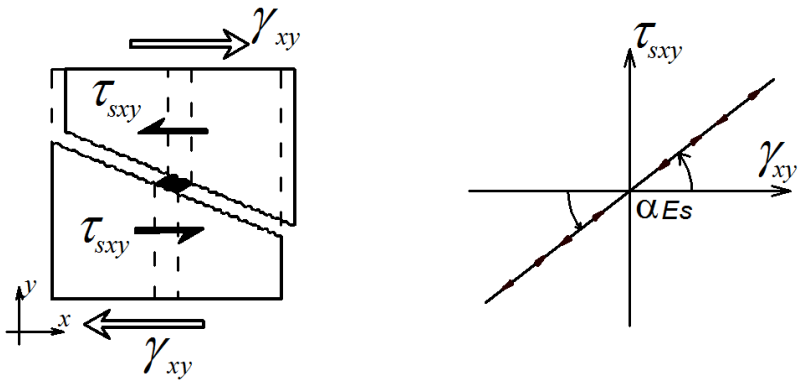

Figure 3-19 Dowel action on reinforcement

More realistic models to represent shear resistance of reinforcement along the crack of a RC panel can be found in literature (eg. Dulacska, 1972); Vintzeleou and Tassios, 1987); their implementation and calibration is not considered here.

Constitutive models incorporated in the original formulation of FSAM to represent shear aggregate interlock and dowel action are phenomenological models (based on physically observed behaviors) that improve comparisons between model and test wall responses. Two parameters in the formulations of the implemented panel model require calibration: (1) friction coefficient of shear aggregate interlock model η, and (2) stiffness of shear resisting mechanism coming from the reinforcement defined as a fraction of Young's modulus for reinforcing steel through coefficient α. Detailed sensitivity studies of model predictions with respect to these

parameters and their calibration with test results are represented in Chapter 4 and Chapter 5, respectively.

3.4 Material Constitutive Models

Advanced state-of-the-art uniaxial hysteretic material constitutive stress-strain relationships for concrete and reinforcing steel were implemented into SFI-MVLEM since the constitutive RC panel model incorporated into the model formulation relates the panel responses directly to uniaxial constitutive stress-strain behavior of concrete and steel reinforcement. Therefore, responses obtained using the present wall model are governed by the properties and parameters of the adopted material constitutive relationships since the stiffness and force-deformation properties of the model sub-elements are derived from panel partial stiffness, which are directly related to stress-strain behavior of materials. The following sub-sections summarize the material presented by Orakcal (2004) and Ulugtekin (2010) and describe the uniaxial constitutive models used to represent the hysteretic behavior of steel and concrete, as well as compression softening of concrete, the effect of tension stiffening on concrete and steel, and concrete biaxial damage; these section are included here for the sake of completeness.

3.4.1. Constitutive Model for Reinforcing Steel

The uniaxial constitutive stress-strain relationship implemented in the wall model for reinforcing steel is the well-known nonlinear hysteretic model of Menegotto and Pinto (1973), as extended by Filippou et al. (1983) to include isotropic strain hardening effects. The model is computationally efficient and capable of reproducing experimental results with accuracy. A typical stress-strain curve with model parameters is presented on Figure 3-20. As shown on the

figure, the stress-strain ($\sigma - \varepsilon$) relationship is in the form of curved transitions each from a straight-line asymptote with slope E_0 (modulus of elasticity) to another straight-line asymptote with slope $E_1 = bE_0$ (yield modulus), where the parameter b is the strain hardening ratio. The curvature of the transition curve between the two asymptotes is governed by a cyclic curvature parameter R, which permits the Bauschinger effect to be represented.

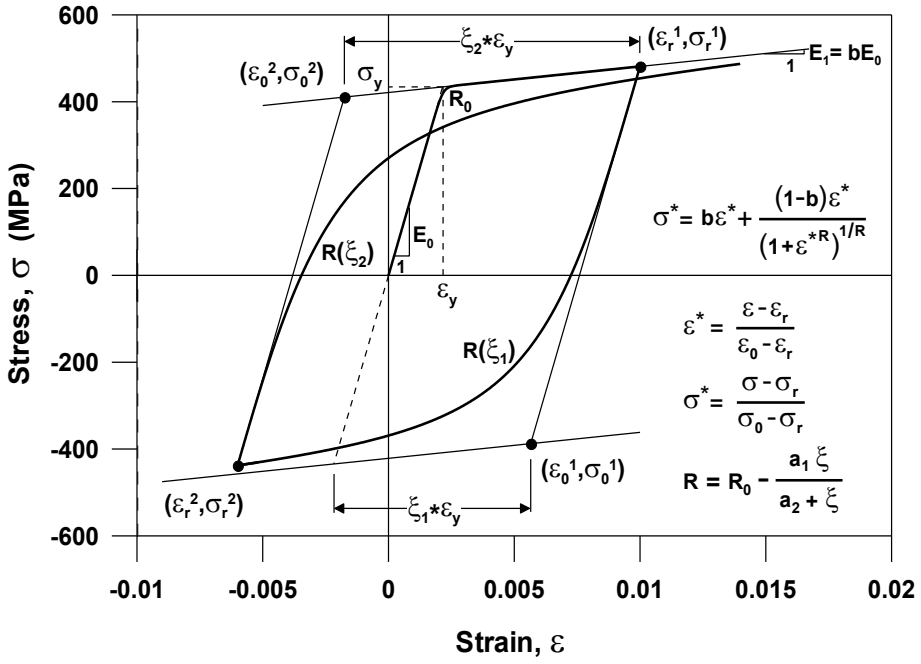

Figure 3-20 Constitutive Model for Steel (Menegotto and Pinto, 1973)

The uniaxial hysteretic stress-strain relationship takes form:

$$\sigma^* = b\varepsilon^* + \frac{(1-b)\varepsilon^*}{\left(1+\varepsilon^{*R}\right)^{1/R}} \tag{3-69}$$

where

$$\xi^* = \frac{\varepsilon - \varepsilon_r}{\varepsilon_0 - \varepsilon_r} \tag{3-70}$$

and

$$\sigma^* = \frac{\sigma - \sigma_r}{\sigma_0 - \sigma_r} \tag{3-71}$$

Parameters σ_r and ε_r are the stress and strain at the point of strain reversal, which also forms the origin of the asymptote with slope E_0, and parameters σ_0 and ε_0 are the stress and strain at the point of intersection of the two asymptotes. The stress-strain pairs $(\sigma_r, \varepsilon_r)$ and $(\sigma_0, \varepsilon_0)$ are updated after each strain reversal (Figure 3-20). The curvature parameter *R* is dependent on the absolute strain difference between the current asymptote intersection point and the previous maximum or minimum strain reversal point depending on whether the current strain is increasing or decreasing, respectively. Menegotto and Pinto suggested the following form of expression for parameter *R*:

$$R = R_0 - \frac{a_1 \xi}{a_2 + \xi} \tag{3-72}$$

where R_0 is the value assigned to the parameter *R* for initial (or monotonic) loading, and a_1 and a_2 are experimentally determined parameters that represent the degradation of the curvature within subsequent cycles. Two sets of values for parameters R_0, a_1, a_2 considered in this study, as suggested by prior researchers based on results of cyclic tests on reinforcing bars, are: (1) $R_0, a_1,$

a_2 = 20, 18.5, 0.15 by Menegotto and Pinto (1973), and (2) R_0, a_1, a_2 = 20, 18.5, 0.0015 by Elmorsi et al. (1998).

The parameters of the constitutive model for steel can be controlled and calibrated based on specific experimental results to model the cyclic behavior of reinforcing steel including the tension stiffening effect (e.g., by calibrating the value of yield stress σ_y and the strain hardening ratio *b*). The calibration of constitutive relationship for steel against experimentally determined stress-strain laws for reinforcing bars used in modeled wall specimens is described in Chapter 5.

3.4.2. Constitutive Model for Concrete

The uniaxial hysteretic constitutive model developed by Chang and Mander (1994) was adopted in the present wall model as the basis for the stress-strain relationship for concrete. The constitutive model by Chang and Mander is a detailed, rule-based, generalized, and non-dimensional model that simulates the hysteretic behavior of confined and unconfined, ordinary and high-strength concrete in both cyclic compression and tension. The model addresses important behavioral issues such as the hysteretic behavior in both cyclic compression and tension, the progressive degradation of stiffness of the unloading and reloading curves for increasing value of strain, gradual crack closure and tension stiffening behavior. Minor modifications to the original formulation of the Chang and Mander model were required to represent behavioral features of concrete under biaxial loading, such as inclusion of parameters to represent compression softening, tension stiffening and hysteretic biaxial damage; these parameters are discussed in Sections 3.4.3, 3.4.4., and 3.4.5, respectively, while details are provided by Ulugtekin (2010).

In the model by Chang and Mander, the monotonic curve forms the envelope for the hysteretic stress-strain relationship. The model envelopes for compression and tension (Figure 3-21) have control on the slope of the stress-strain behavior at the origin and the shape of both the ascending and descending (i.e., pre-peak and post-peak) branches of the stress-strain behavior. Concrete in tension is modeled with a cyclic behavior similar to that in compression. In order to define the compression and tension envelopes, the model by Chang and Mander uses the Tsai's equation (Tsai, 1988), which has proven to be very useful in describing the monotonic compressive stress-strain curve for concrete.

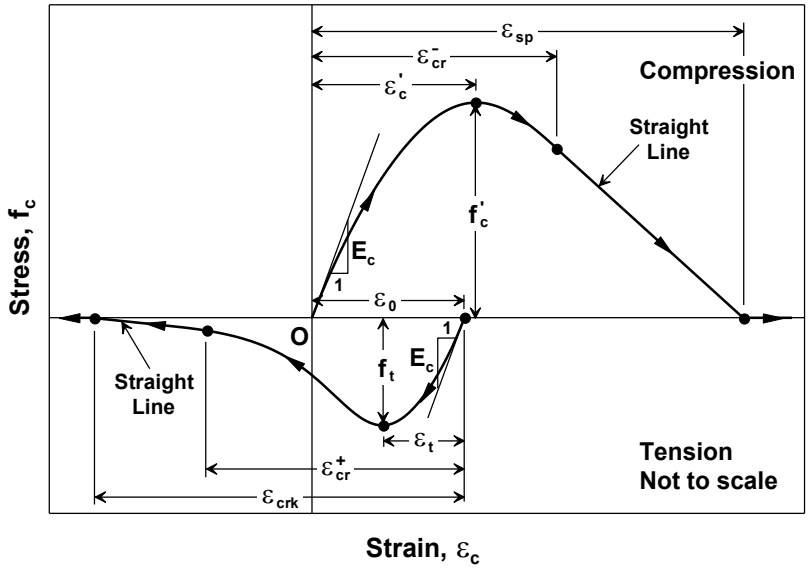

Figure 3-21 Compression and Tension Envelopes of the Model by Chang and Mander (1994)

The compression envelope curve of the model by Chang and Mander is defined by the initial slope E_c, the peak coordinate (ε'_c, f'_c), a parameter ε_{cr}^{-} strain on the compression envelope curve used to define a tangent line up to the spalling strain, a parameter ε_{sp}^{-} to define the spalling strain, and a parameter *r* from Tsai's (1988) equation defining the shape of the envelope

curve (Figure 3-21). All of mentioned parameters can be controlled and manipulated based on specific experimental results for a refined calibration of the compression envelope. The parameters E_c, ε'_c and r, used to generate the unconfined compression envelope, can be calculated as a function of unconfined compression strength f'_c (MPa) of concrete according to following empirical relationships derived by Chang and Mander (1994):

Initial modulus of elasticity: $E_c = 8200 \cdot \left(f'_c\right)^{3/8}$ MPa (3-73)

Strain at peak stress: $\varepsilon'_c = \dfrac{\left(f'_c \,\mathrm{MPa}\right)^{1/4}}{1150}$ (3-74)

Shape parameter: $r = \dfrac{f'_c}{5.2} - 1.9$ (3-75)

The generalized confinement model developed by Mander et al. (1988), applicable to RC members with either circular or rectangular cross-sections and any general type and configuration of reinforcement, is incorporated in the model formulation (e.g., Orakcal et al., 2004) to obtain the compressive envelope of the model by Chang and Mander (1994) for confined concrete, typically located in boundary elements of RC walls.

The shape of the tension envelope curve in the model by Chang and Mander is the same as that of the compression envelope curve, but the curve is shifted to a new origin by the use of parameter ε_0 (Figure 3-21). The parameters associated with the tension envelope curve include: the concrete tensile strength f_t, the strain at peak tensile stress ε_t, the parameter r defining the

shape of the tension envelope curve, and the critical strain on the tension envelope curve ε_{cr}^{+} (where the envelope curve starts following a straight line). These parameters can also be controlled and calibrated based on specific experimental results or empirical relations proposed by other researchers (e.g., Collins and Mitchell, 1991; Belarbi and Hsu, 1994) to model the behavior of concrete in tension and the tension stiffening phenomenon (e.g., by defining a large value of ε_{cr}^{+}).

The hysteretic behavior of concrete in compression and tension is defined by the use of several key hysteretic parameters that are developed empirically by Chang and Mander (1994) by performing regression on an extensive experimental database. The hysteretic parameters for cyclic compression are presented on Figure 3-22 and include the following: secant stiffness (E_{sec}) and plastic stiffness (E_{pl}) upon unloading from, stress and strain offsets (Δf and $\Delta\varepsilon$) upon return to the compression envelope, plastic (residual) strain upon unloading (ε_{pl}), new stress (f_{new}) and tangent modulus (E_{new}) upon return to unloading strain from the envelope curve (ε_{un}), and the strain (ε_{re}), stress (f_{re}) and tangent modulus (E_{re}) at the point of return to the envelope curve.

In terms of modeling generalized hysteretic behavior, the constitutive model uses smooth "connecting" curves for unloading and reloading between the compression and tension envelope curves, and smooth "transition" curves for partial unloading and reloading between the connecting curves (Figure 3-23). The connecting and transition curves are geometrically defined such that they commence at the prescribed starting point (e.g., ε_{un}, f_{un} in Figure 3-22) with a

prescribed initial slope (e.g., E_c), and end up at a prescribed final (target) point (e.g., $\varepsilon_{pl}, 0$) with a prescribed final slope (e.g., E_{pl}). Both connecting and transition curves have slope continuity with uniform sign of curvature (second strain derivative of the curve equation) in between the starting and final points.

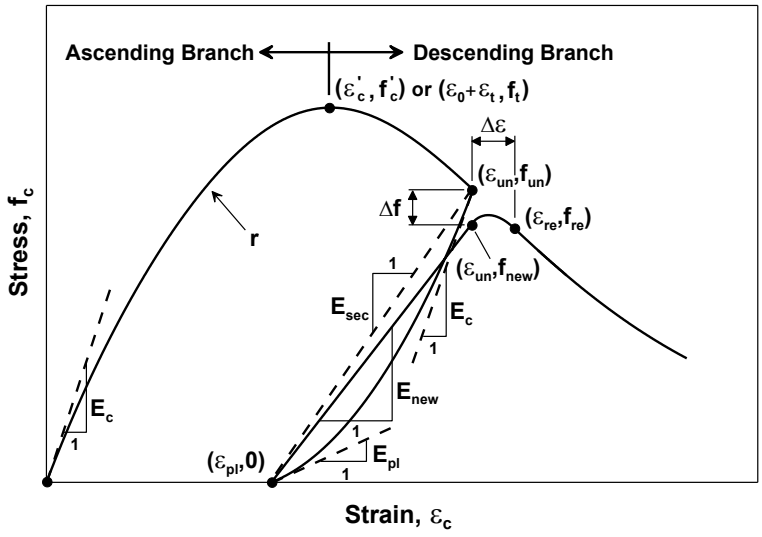

Figure 3-22 Hysteretic Parameters of the Model by Chang and Mander (1994)

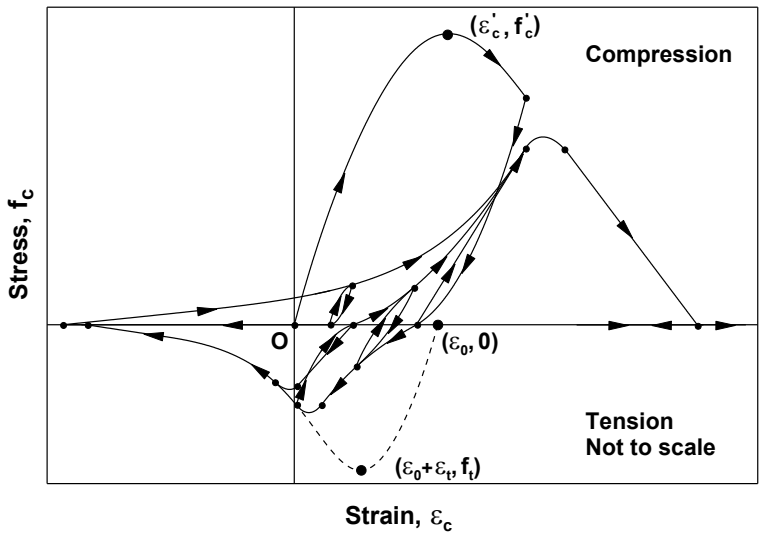

Figure 3-23 Continuous Hysteresis in Compression and Tension

Further details of the model can be found in the referenced report (Chang and Mander, 1994).

3.4.3. Compression Softening of Concrete

An important consideration in modeling the behavior of a RC panel element under membrane actions is incorporating the compression softening effect. The softening effect has been experimentally observed by many researchers (e.g., Vecchio and Collins, 1986), and it is typically represented by analytical models mainly in the form of reduction (softening) in the compressive stresses in concrete along the principal compression direction of RC panels due to presence of tensile strains in the perpendicular principal direction. Some compression softening models have included softening in the compressive strain (e.g., Belarbi and Hsu, 1995; Vecchio and Collins, 1993) by reducing the strain at the peak compressive stress for concrete in addition to softening of compressive stress. Although all of these compression softening models were formulated for the case of monotonic loading, many of them were implemented into cyclic analysis methods (Belarbi and Hsu 1995, Vecchio and Collins 1993).

Vecchio and Collins (1993) used a large experimental database from tests on RC panels to propose two different models to represent compression softening behavior, one considering compression softening in both stresses and strains (Model A), and the second considering softening effect only in stresses (Model B). In this study, the so-called Model B by Vecchio and Collins (1993), which considers only a reduction of peak compressive stress (providing a simpler model implementation), was implemented in the formulation of constitutive RC panel model used in SFI-MVLEM. Vecchio and Collins (1993) observed that more complicated models (including also reduction in the strain at peak stress) are only marginally better for incorporating

the compression softening effect. In this approach, compressive stress along the principal compression direction (concrete-strut) is reduced by the β_m coefficient defined as:

$$\beta_m = \frac{1}{1+K_c} \tag{3-76}$$

where $K_c = 0.27 \cdot \left(\frac{\varepsilon_1}{\varepsilon_0} - 0.37 \right) \geq 1.0$, and ε_1 is the tensile strain in the principal tensile stress direction and ε_0 is the strain corresponding to peak stress of concrete in compression.

3.4.4. Tension Stiffening on Concrete and Steel

The contribution of cracked concrete to the tensile resistance of RC members is known as the effect of tension stiffening. The concrete between the cracks, which is still bonded to the reinforcing steel bars, contributes to the tensile resistance of the member. The tension stiffening phenomenon plays a significant role in reducing the post-cracking deformations of reinforced concrete structures, and has been proven by researchers (e.g., Vecchio and Collins, 1988; Collins and Mitchell, 1991; Belarbi and Hsu, 1994; Pang and Hsu, 1995; Hsu and Zhang, 1996; Mansour et al., 2002; Hsu and Zhu, 2002) to influence considerably the post-cracking stiffness, yield capacity and shear behavior of reinforced concrete members.

A model proposed by Belarbi and Hsu (1994) is incorporated in the formulation of implemented constitutive RC panel model to represent the tensions stiffening effect. As investigated in detail by Belarbi and Hsu (1994), modeling of the tension stiffening phenomenon must consider two effects simultaneously: (1) an average (smeared) tensile stress-strain curve must be considered

for cracked concrete and (2) the stress-strain curve of bare mild steel bars must be replaced by an average (smeared) stress-strain curve for steel bars stiffened by concrete between cracks.

In the Belarbi and Hsu model, the tensile stress-strain behavior of concrete is considered as linear up to cracking and a descending curve is defined for the post-cracked stress-strain region, as shown on Figure 3-24. The average stress-strain relationship proposed by Belarbi and Hsu for concrete in tension takes the following form:

$$\text{If} \quad \varepsilon_c \le \varepsilon_{cr} \quad \text{then} \quad \sigma_c = E_c \varepsilon_c \tag{4-77}$$

$$\text{If} \quad \varepsilon_c > \varepsilon_{cr} \quad \text{then} \quad \sigma_c = f_{cr}\left(\frac{\varepsilon_{cr}}{\varepsilon_c}\right)^{0.4} \tag{3-78}$$

where:

$$E_c = 3875\sqrt{f_c'(MPa)} \tag{3-79}$$

$$f_{cr} = 0.31\sqrt{f_c'(MPa)} \tag{3-80}$$

$$\varepsilon_{cr} = 0.00008 \tag{3-81}$$

In the equations above, ε_c is the average concrete tensile strain, σ_c is the average concrete tensile stress, E_c is the initial Young's modulus of the average stress-strain relationship, f_{cr} is the concrete tensile cracking stress, and ε_{cr} is the concrete strain at cracking.

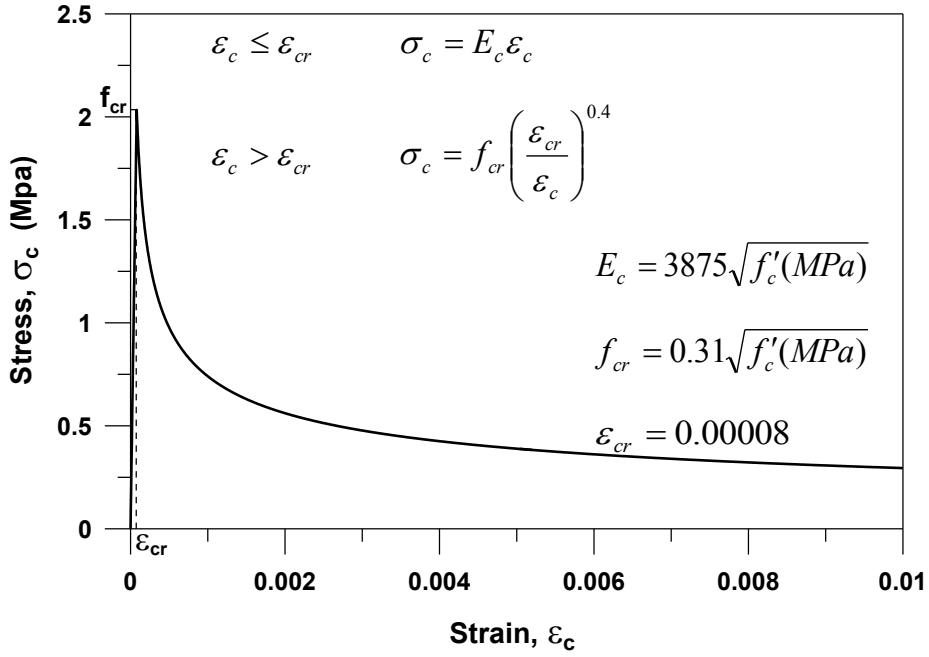

Figure 3-24 Average Stress-Strain Relationship by Belarbi and Hsu (1994) for Concrete in Tension

Belarbi and Hsu (1994) also identified how the average stress-strain relationship of reinforcing steel bars surrounded by concrete is different than the stress-strain relationship of bare steel bars. The most important difference was found to be the lowering of the yield stress f_y, as yielding of a reinforced concrete element occurs when the steel stress at the cracked section reaches the yield strength of the bare bar. At the same time, the average steel stress smeared along the length of the element reaches a level lower than that of the yield stress of the bare bar. Based on experimental data from the RC panels, the effective (reduced) yield stress of bars embedded in concrete (f_{yeff}) was found to be dependent on the cross-sectional area, ratio of the longitudinal steel in the panel (ρ), the ratio of concrete cracking stress (f_{cr}) to the steel yield stress (f_y), and the elastic modulus ratio *n* (E_s / E_c) as:

$$f_{yeff} = f_y \cdot \left[1 - 1.314 \cdot \frac{n^{0.434}}{\rho^{1.084}} \cdot \left(\frac{f_{cr}}{f_y} \right)^{1.517} \right] \tag{3-82}$$

3.4.5. Biaxial Damage on Concrete

Another important consideration in modeling the behavior of a RC panel element under membrane actions is incorporating the cyclic damage effects on concrete subjected to biaxial loading. This cyclic damage of concrete is represented via a damage coefficient. Unlike compression softening and tension stiffening parameters, the damage coefficient is a cyclic-strain-history-dependent parameter, and is not considered in analysis of concrete under monotonic loading.

The damage coefficient depends on the history of concrete strains perpendicular to the direction of the specific concrete compressive stress direction considered (e.g., perpendicular to a compression strut). The damage coefficient is therefore defined for biaxial loading, and does not apply for uniaxial concrete stress-strain behavior. The damage coefficient, similar to the compression softening coefficient, is applied as a multiplier to the concrete compressive stress that softens the stress-strain behavior of concrete in compression.

The empirically-developed damage coefficient proposed by Mansour and Hsu (2005) is used in this study. According to this model, the biaxial damage coefficient (β_{damage}) is calculated based on the ratio of the maximum value of the compressive strain experienced in the direction perpendicular to the compressive (strut) direction considered ($\varepsilon_{\perp \max}$), to the peak compressive strain (ε'_c) in concrete, as:

$$\beta_{damage} = \left(1 - 0.4 \cdot \frac{\varepsilon_{\perp \max}}{\varepsilon'_c} \right) \tag{3-83}$$

The final softening parameter used in this study, to consider both compression softening and biaxial damage, is based on the Mansour and Hsu (2005) formulation for biaxial damage as:

$$\beta = \beta_m \cdot \beta_{damage} \tag{3-84}$$

where β_m is the compression softening coefficient defined by Eq. 3-76 (Vecchio and Collins, 1993) and β_{damage} is the biaxial damage coefficient given by Eq. 3-83.

3.5 Nonlinear Analysis Strategy

Nonlinear analysis solution strategy for conducting nonlinear quasi-static analysis (monotonic or cyclic) of RC walls was implemented in Matlab ("Matlab") along with the formulation of the proposed SFI-MVLEM, the force and stiffness assembly procedure, and the material constitutive relationships described earlier in this chapter. Details of the analysis solution strategy are described in this section, which is adopted from dissertation by Orakcal (2004) and included here for the sake of completeness.

3.5.1. Nonlinear Quasi-Static Problem

Quasi-static response is generated when the externally applied cyclic loads or displacements are applied with a sufficiently slow loading rate that they do not induce dynamic effects. The nonlinear equilibrium equation associated with the quasi-static response can be expressed as:

$$\{F_{\text{int}}(\delta)\} = \{F_{ext}\} \tag{3-85}$$

where $\{F_{\text{int}}(\delta)\}$ is the internal resisting force vector, being a nonlinear function of system (nodal degree of freedom) displacements and the external force vector $\{F_{ext}\}$, representing the externally applied forces at the nodal degrees of freedom. In the case of a linear elastic system, the static problem would reduce to the linear equation:

$$[K]\{\delta\} = \{F_{ext}\} \tag{3-86}$$

where $[K]$ denotes the stiffness matrix and $\{\delta\}$ is the vector of nodal displacements. In the case of a nonlinear system, Eq. 3-86 is a nonlinear algebraic equation in $\{\delta\}$ due to the nonlinear relationship between the resisting force vector $\{F_{\text{int}}\}$ and the vector of nodal displacements $\{\delta\}$.

3.5.2. Applied Nonlinear Analysis Solution Strategy

The hysteretic constitutive material relations in the present SFI-MVLEM formulation were used to determine global non-linear hysteretic structural response based on satisfying both equilibrium conditions and force-deformation relationships at each load step. The solution method implemented is based on a modified Newton-Raphson approach, that is, the tangent stiffness matrix is computed at the beginning of each load step and held constant for each load step. An iterative strategy, based on the incrementation of selected displacement components (Clarke and Hancock, 1990; Simons and Powell, 1982) was used for the purpose of passing load limit points and to allow comparison with experimental results.

According to this strategy, each load step consists of two main stages, the "incrementation stage" and the "equilibrium stage". During the incrementation stage, a suitable external load increment $\Delta\lambda_i^1$ is selected for the first iteration cycle ($j=1$), referred to as the "initial load increment", by the use of the particular "load incrementation strategy". During the equilibrium stage, an "iterative strategy" is used in subsequent iterative cycles ($j \geq 2$) to perform iterations on the load parameter $\Delta\lambda_i^j$ as well as the nodal displacements $\{\delta\}_i^j$ in order to satisfy the equilibrium between external and internal forces for the imposed conditions.

3.5.2.1. Incrementation Cycle (First Iteration Cycle)

Each load step in the analysis starts with an incrementation cycle. Each incrementation cycle, starts with the computation of the tangent stiffness matrix $[K_I]_i$ for the whole system based on known displacements (strains) and loads (stresses) at the conclusion of the previous load step. The tangent stiffness matrix is a $N \times N$ matrix (N defined by Eq. 3-29) assembled from element stiffness matrices as explained in Section 3.2.5. The "tangent" nodal displacements at the model degrees of freedom $\{\delta_I\}_i$ for this load step are then computed as the solution of:

$$[K_I]_i \{\delta_I\}_i = \{F_I\}_i \tag{3-87}$$

in which $\{F_I\}_i$ is the reference external load vector, typically specified in the input data for the problem. The magnitude of the tangent displacements is arbitrary, only their direction is important. Next, the value of the initial load increment $\Delta\lambda_i^1$ is calculated as:

$$\Delta\lambda_i^{j=1} = \frac{-\{b_n\}^T \{\Delta\delta_R\}_i^{j=1}}{\{b_n\}^T \{\delta_I\}_i} \tag{3-88}$$

where b_n is a vector with a unity term along the degree-of-freedom to be incremented for the displacement-controlled analysis, and zero along other degrees of freedom. The numerator of this expression represents the applied nodal displacement increment along the controlled degree of freedom of the model (given by Eq. 3-89) in the case of displacement controlled analysis where the applied nodal displacement increment of the controlled degree of freedom is controlled.

$$\Delta\delta_n = \{b_n\}^T \{\Delta\delta_R\}_i^{j=1} \tag{3-89}$$

Therefore, the initial load increment can be expressed as:

$$\Delta\lambda_i^{j=1} = \frac{(\Delta\delta_n)_i}{\{b_n\}^T \{\delta_I\}_i} \tag{3-90}$$

The incremental displacements are then evaluated by scaling the tangent displacements as:

$$\{\Delta\delta\}_i^{j=1} = \Delta\lambda_i^{j=1} \{\delta_I\}_i \tag{3-91}$$

The total displacements and load level are updated from those existing at the conclusion of the previous load step as:

$$\{\delta\}_i^{j=1} = \{\delta\}_{i-1} + \{\Delta\delta\}_i^{j=1} \tag{3-92}$$

$$\lambda_i^{j=1} = \lambda_{i-1} + \Delta\lambda_i^{j=1} \tag{3-93}$$

where $\{\delta\}$ represents the nodal displacement vector, *i* denotes the current load step, *j=1* denotes the first iteration (incrementation), and λ is a scalar to be multiplied with the reference external load vector to obtain the external force vector $\{F_{ext}\}$. The internal force vector is calculated using the stresses developed on each RC panel element of the wall model for the applied displacement field at degrees of freedom, while the external force vector is calculated as:

$$\{F_{ext}\}_i^{j=1} = \lambda_i^{j=1}\{F_I\}_i \tag{3-94}$$

The difference between the internal and external force vectors is defined as the residual force vector $\{R\}$ for the incrementation cycle:

$$\{R\}_i^{j=1} = \{F_{\text{int}}\}_i^{j=1} - \{F_{ext}\}_i^{j=1} \tag{3-95}$$

At this stage the residual force vector does not satisfy total equilibrium within the specified tolerance, hence additional iterative cycles are required to restore equilibrium.

3.5.2.2. Equilibrium Iteration Cycles

Since the residual force vector is known at the end of the "incrementation" cycle, the residual displacement increment can be calculated as the solution of the following equation:

$$[K_I]_i\{\Delta\delta_R\}_i^j = \{R\}_i^{j-1} \tag{3-96}$$

The incremental external force multiplier and nodal displacement vector can now be calculated from the residual displacement vector as:

$$\Delta\lambda_i^j = \frac{-\{b_n\}^T \{\Delta\delta_R\}_i^j}{\{b_n\}^T \{\delta_I\}_i} \tag{3-97}$$

$$\{\Delta\delta\}_i^j = \Delta\lambda_i^j \{\delta_I\}_i + \{\Delta\delta_R\}_i^j \tag{3-98}$$

After the calculation of load and displacement increments, the nodal displacement vector and external force multiplier at the end of the current iteration cycle can be calculated as:

$$\{\delta\}_i^j = \{\delta\}_i^{j-1} + \{\Delta\delta\}_i^j \tag{3-99}$$

$$\lambda_i^j = \lambda_i^{j-1} + \Delta\lambda_i^j \tag{3-100}$$

Subsequently, the external force vector $\{F_{ext}\}$ and the internal force vector $\{F_{\text{int}}\}$ are calculated as done in the "incrementation" stage, and the residual force vector is defined as the difference between these two vectors:

$$\{F_{ext}\}_i^j = \lambda_i^j \{F_I\}_i \tag{3-101}$$

$$\{R\}_i^j = \{F_{\text{int}}\}_i^j - \{F_{ext}\}_i^j \tag{3-102}$$

Iteration cycles are continued until a convergence criterion based on either the structure forces or displacements is satisfied. If convergence is not achieved within a specified number of cycles, or if divergence of the solution is detected, a re-solution strategy may be adopted. Graphical representations of the nonlinear analysis solution strategy described are illustrated in Figure 3-25

and Figure 3-26. Further information on the solution strategy can be found in Clarke and Hancock (1990) and Powell and Simons (1982).

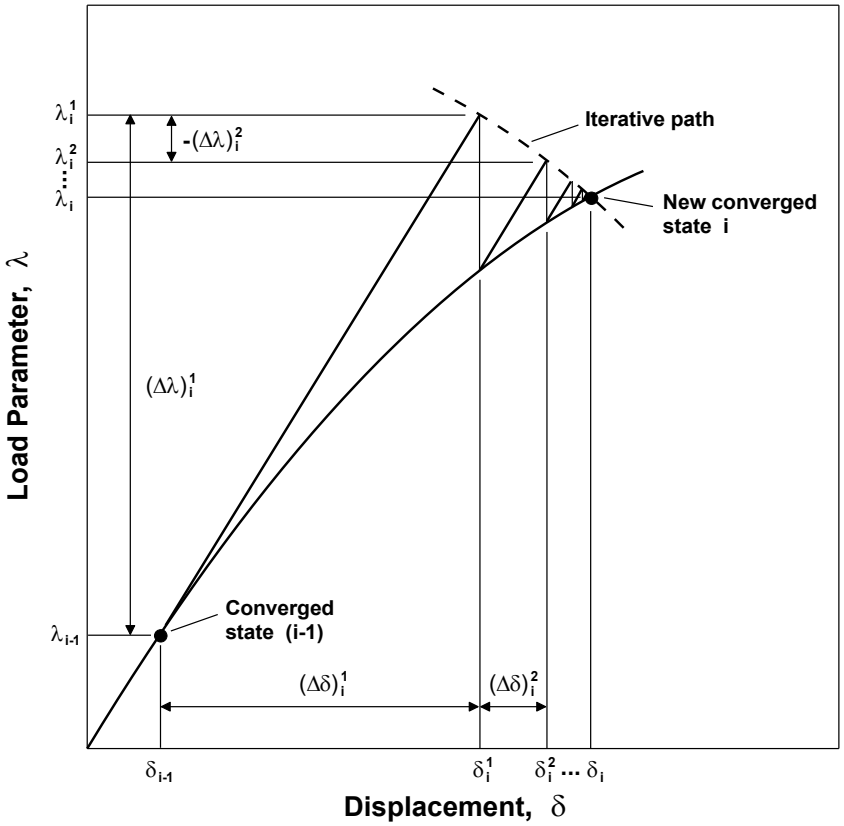

Figure 3-25 Nonlinear Analysis Solution Scheme for a Single Degree of Freedom System (Orakcal, 2004)

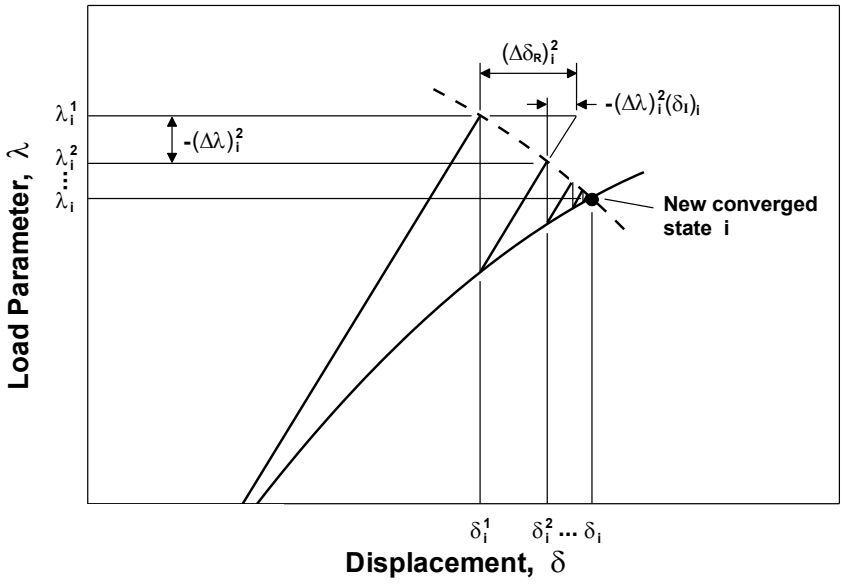

Figure 3-26 Iterative Strategy and Residual Displacements (Orakcal, 2004)

3.5.2.3. Convergence Criteria and Re-Solution Strategy

Within the analysis, iteration cycles are continued until a convergence criterion based on structure displacements is satisfied at the end of each load step. In this study, a convergence criterion based on the incremental displacements is used. The stringent maximum norm is adopted in the present study to test for convergence, that is:

$$\text{Maximum norm:} \qquad \|\varepsilon\|_\infty = \max_k \left| \frac{\Delta\delta_k}{\delta_k} \right| \tag{3-103}$$

where $\Delta\delta_k$ is the change in the displacement component *k* during the current iteration cycle and δ_k is the value of that displacement component updated at the end of the previous iteration. Convergence is achieved when:

$$\|\varepsilon\|_{\infty} < \zeta_c \tag{3-104}$$

where the tolerance ζ_c used in this study is 10^{-3} (typically between 10^{-2} to 10^{-5}).

In the solution technique described above, a re-solution strategy was incorporated. A re-solution is necessary if convergence is not attained at each load step within the maximum specified number of iterative cycles, or if the solution appears to be diverging. The re-solution is facilitated by recovering the previous converged load step at displacement level $\{\delta\}_{i-1}$, and starting the current load step over using the initial stiffness matrix of the first load step (undeformed configuration). If convergence is still not attained within the number of specified iterations, the value of the prescribed displacement increment $\Delta\delta_n$ is changed (usually decreased), and the current step is repeated until an increment that satisfies convergence and complies with the applied displacement history is found.

CHAPTER 4

ANALYTICAL MODEL RESULTS AND PARAMETRIC SENSITIVITY STUDIES

4.1. General

The proposed SFI-MVLEM elements, with implemented constitutive panel behavior and material stress-strain relationships, are assembled into a complete wall model using a direct stiffness assembly procedure, and an incremental-iterative numerical scheme (all described in Chapter 3) is used to perform nonlinear quasi-static analysis (monotonic or cyclic) of wall models using Matlab ("Matlab"). This chapter provides detailed discussion about the attributes of the analytical model response, the capability of model to capture important response features for walls with various modes of behavior and failure mechanisms, and the sensitivity of model results to variations in wall configurations and model parameters.

To provide context to above mentioned studies, specimen RW-A15-P10-S78 tested by Tran and Wallace (2012), is used to assess model capabilities and sensitivity to mentioned parameters. Test specimen RW-A15-P10-S78 had rectangular cross-section (RW), aspect ratio of 1.5 (A15) with height of 183 cm (72 in) and length of 122 cm (48 in), thickness of 15.2 cm (6 in), applied constant axial load of approximately 10% of the axial load capacity of the wall specimen (P10), and design web shear stress of $0.65\sqrt{f_c'}$ MPa ($7.8\sqrt{f_c'}$ psi, S78). In addition, the specimen had

web reinforcing ratio of 0.73% and boundary longitudinal reinforcing ratio of 6.06%, resulting in a shear demand at nominal moment capacity corresponding to 85% of the nominal shear capacity. The behavior of the specimen was characterized with significant contribution of nonlinear shear deformations, contributing up to 35% of total top lateral deformations, and shear-flexure interaction (Tran, 2012). The analysis results were obtained using five SFI-MVLEM elements along the height of the wall (n = 5) and five RC panel elements (macro-fibers) along the wall length (m = 5) as shown on Figure 4-1; Figure 4-1(a) displays wall discretization in vertical and horizontal directions, whereas Figure 4-1(b) shows the reinforcement configuration and discretization of wall cross-section.

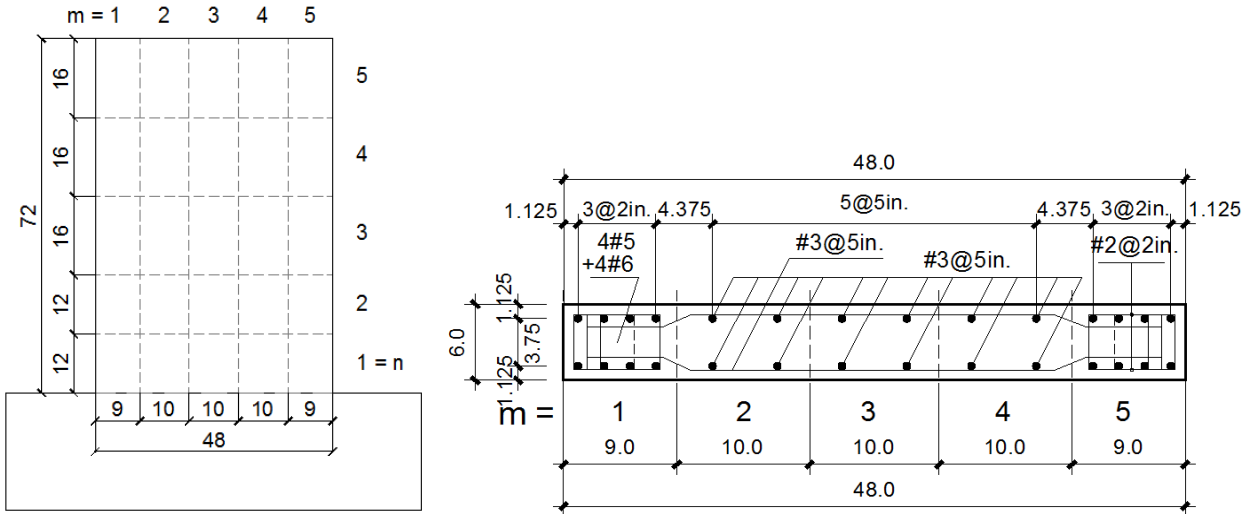

(a) Plane View (b) Cross-Section (with reinforcement)

Figure 4-1 Wall Model Discretization

Material models for concrete and reinforcing steel were calibrated to match the material properties of tested RC wall specimen as described in Chapter 5. Analytical results are obtained by applying a displacement history at the top of the wall model consisting of one loading cycle

for each drift level of 0.1%, 0.25%, 0.5%, 0.75%, 1.0%, 1.5%, 2.0%, and 3.0%, which corresponded to drift levels used in the test program (where multiple cycles were used). More details about experimental test program are presented in Chapter 5.

4.2. Analytical Model Results

Analytical prediction of the lateral load versus wall top displacement response of specimen RW-A15-P10-S78 under cyclic loading applied at the top is presented in Figure 4-2. It can be observed from the figure that characteristics of the overall cyclic wall behavior are clearly reflected by the model, including the overall hysteretic shape of the lateral load versus top displacement behavior, degradation of unloading/reloading stiffness, plastic (residual) displacements at zero load level, and moderate pinching behavior.

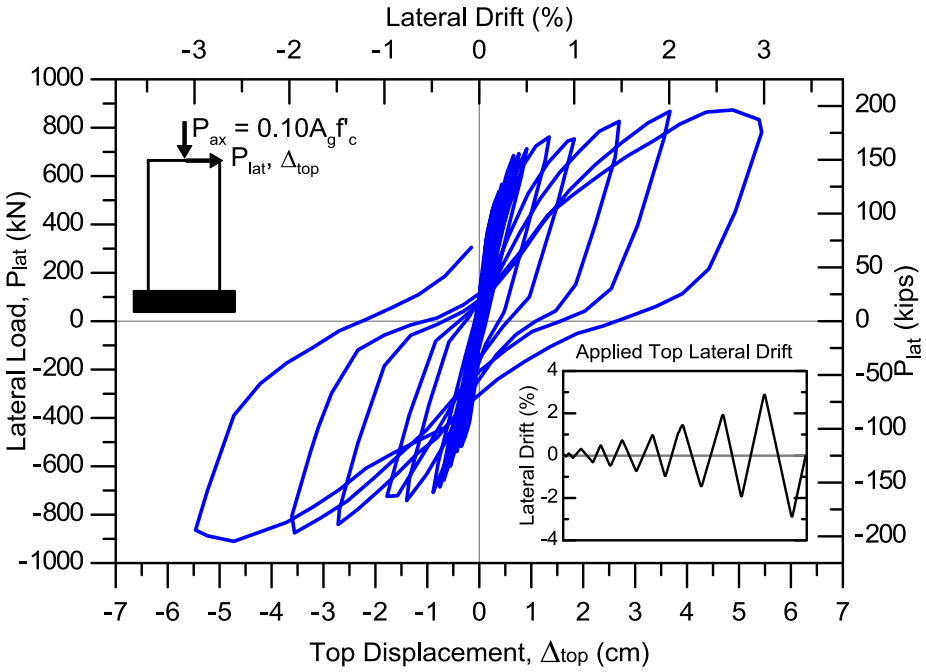

Figure 4-2 Lateral load versus top wall displacement predicted by the model

Analytical results presented in Figure 4-3 and Figure 4-4 show corresponding lateral load versus shear and flexural deformation components of the top displacement, respectively. It can be observed from the figures that model successfully captures nonlinear shear and flexural deformations, as well as their coupling through the entire cyclic loading history, since flexural and shear yielding occur near-simultaneously at lateral load of approximately 700 kN (157 kips). In addition, it can be observed from Figure 4-3 that hysteretic response in shear is characterized by highly pinched behavior, whereas Figure 4-4 shows the shape of hysteretic loops for flexural behavior shows no pinching behavior; therefore, the pinching behavior observed in overall load-displacement response is associated with shear behavior. Figure 4-3 also indicates that the relative contributions of shear deformations at the top is approximately 45%, while Figure 4-4 shows that flexural deformations at the top contribute by roughly 55% to the top lateral displacement of the wall throughout the entire cyclic loading history.

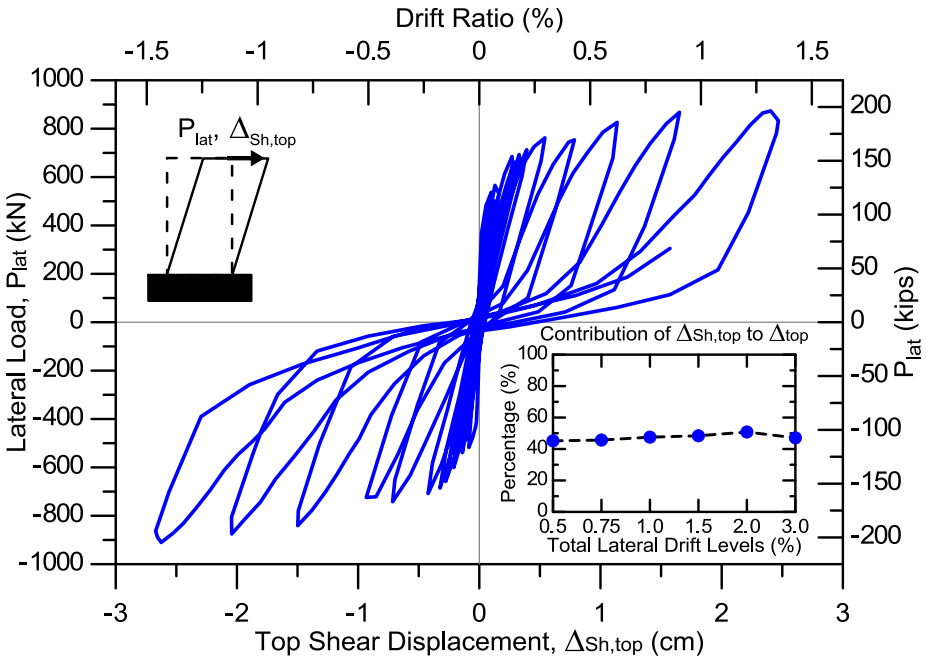

Figure 4-3 Load versus Shear Wall-Top Displacement Response Predicted by the Model

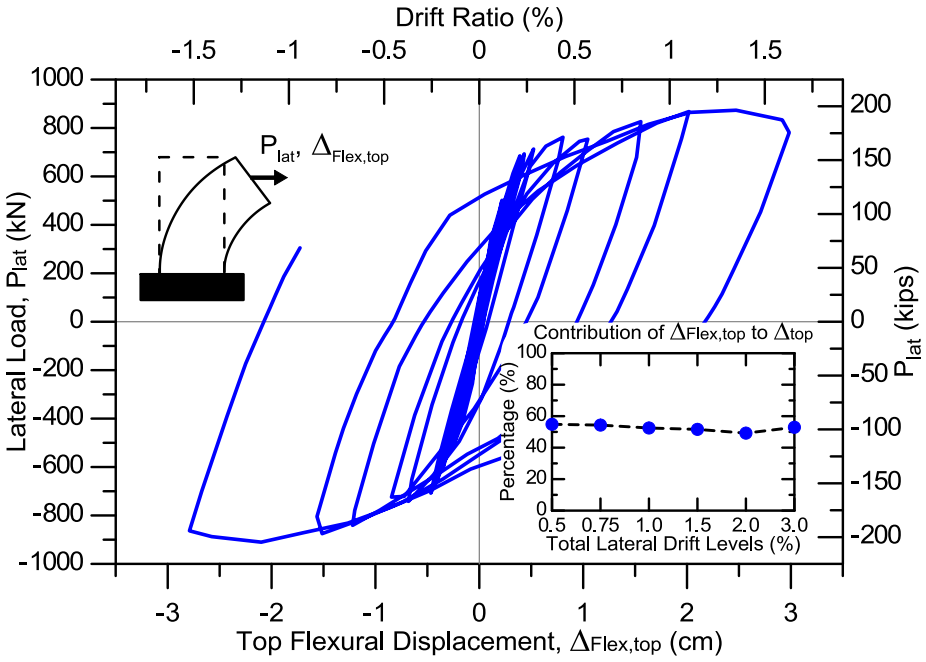

Figure 4-4 Load versus Flexural Wall-Top Displacement Response Predicted by the Model

Figure 4-5 illustrates profiles of total lateral displacements over the wall height determined at maximum applied lateral drifts of 0.5%, 0.75%, 1.0%, 1.5%, 2.0% and 3.0%, whereas corresponding shear and flexural displacement profiles and their contributions to total lateral displacements are displayed in Figure 4-6. Displacement profiles were obtained at height levels of 30.5 cm (12 in.), 61.0 cm (24 in.), 101.6 cm (40 in.), 142.2 cm (56 in.), and 243.8 cm (96 in.), which correspond to the height of model elements used in the wall model shown on Figure 4-1.

It can be observed from Figure 4-5 that total displacement profiles are almost linear over the wall height for drift levels lower and equal than 1.0%, whereas for larger drift levels total displacements are higher at the bottom of the wall up to the height of approximately $l_w/2$. This concentration of nonlinear deformations can be also observed on Figure 4-6, which reveals that

profiles of shear and flexural deformations are also nonlinear up to the wall height of about $l_w/2$, where for the rest of the wall these profiles are almost linear.

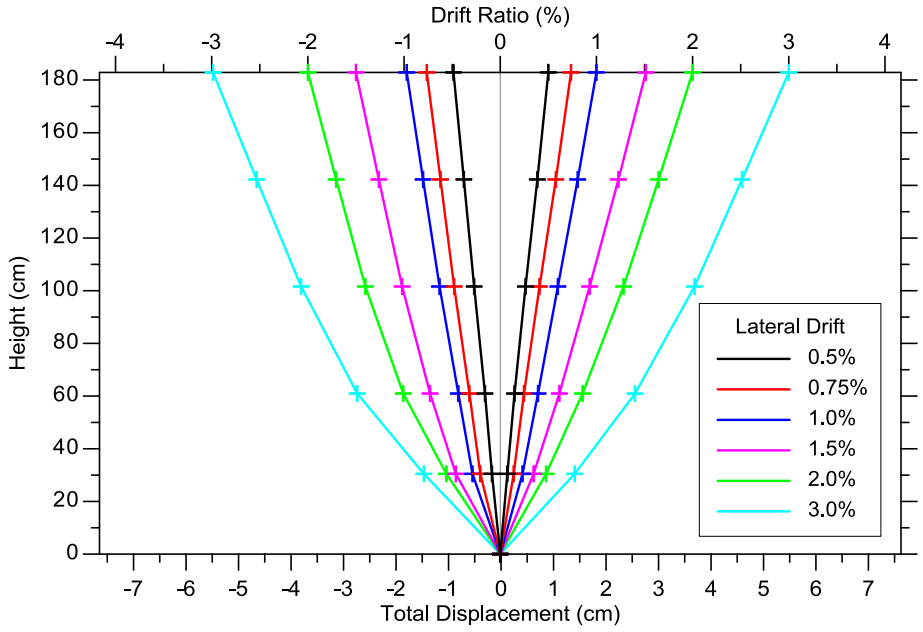

Figure 4-5 Total Displacement Profiles

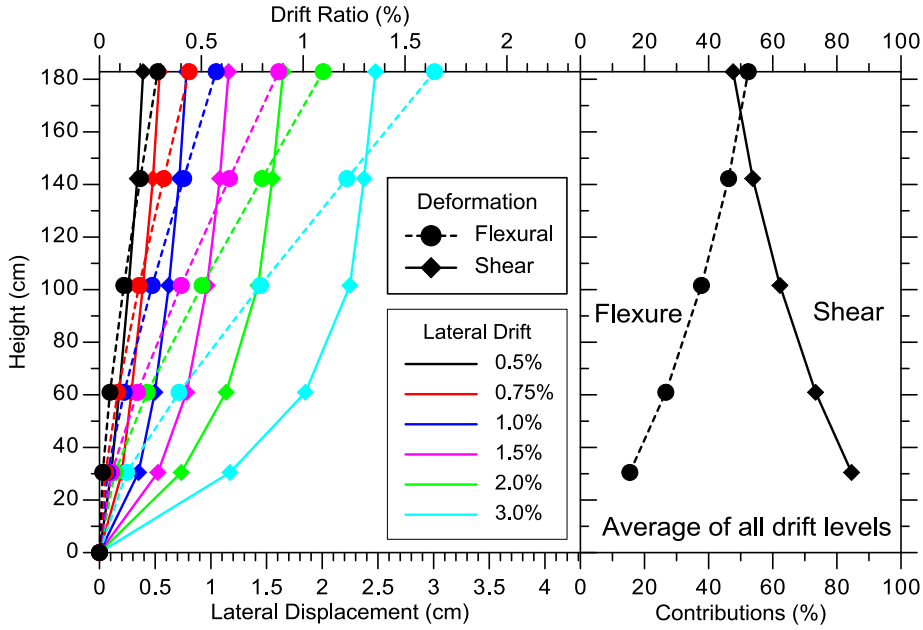

Figure 4-6 Shear and Flexural Displacement Profiles with Contributions to Total Displacement

It can be also observed from Figure 4-6 that relative contributions of shear deformations are dominant along the wall height, except at the top of the wall, and that their predicted average contributions to the total lateral displacements range from 85% at the wall bottom to 45% at the wall top, indicating larger nonlinear shear deformations at the bottom of the wall where nonlinear flexural deformations are concentrated.

The relationship between vertical growth and lateral displacement at the top of the wall model is shown in Figure 4-7, which reveals that model predicts approximately constant vertical growth of the wall throughout the loading history. In addition, analytical results are characterized with residual vertical growth at zero lateral displacement that is approximately 80% of the vertical growth at the previously experienced peak of lateral displacmenet, which results in generally higher predicted vertical growth in negative versus positive loading cycles.

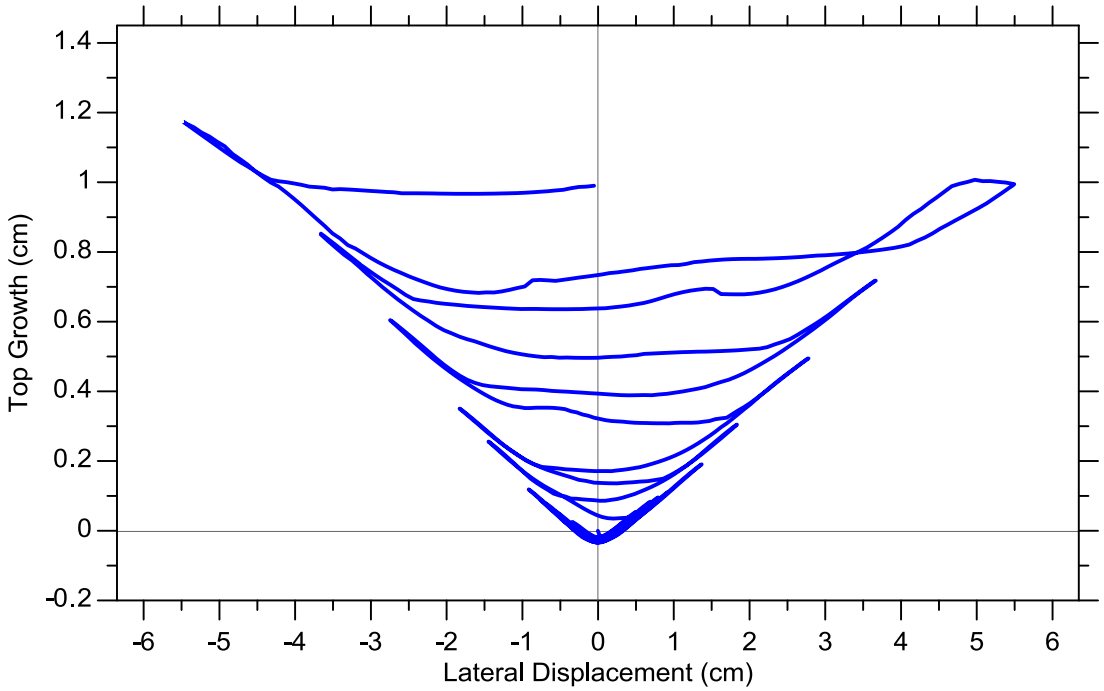

Figure 4-7 Vertical Growth versus Lateral Displacement

Similar to displacement profiles presented in Figure 4-5 and Figure 4-6, profiles of vertical growth over the wall height presented in Figure 4-8 are determined at maximum applied lateral drifts of 0.5%, 0.75%, 1.0%, 1.5%, 2.0% and 3.0%, and at height levels of 30.5 cm (12 in.), 61.0 cm (24 in.), 101.6 cm (40 in.), 142.2 cm (56 in.), and 243.8 cm (96 in.). The figure reveals that distributions of vertical growth are almost linear at low drift levels, and that the vertical growth profiles become nonlinear after yielding of the vertical boundary reinforcement; large contributions of the vertical growth can be observed over the wall height of approximately $l_w/2$ from the bottom of the wall model, i.e. within the so-called plastic hinge region.

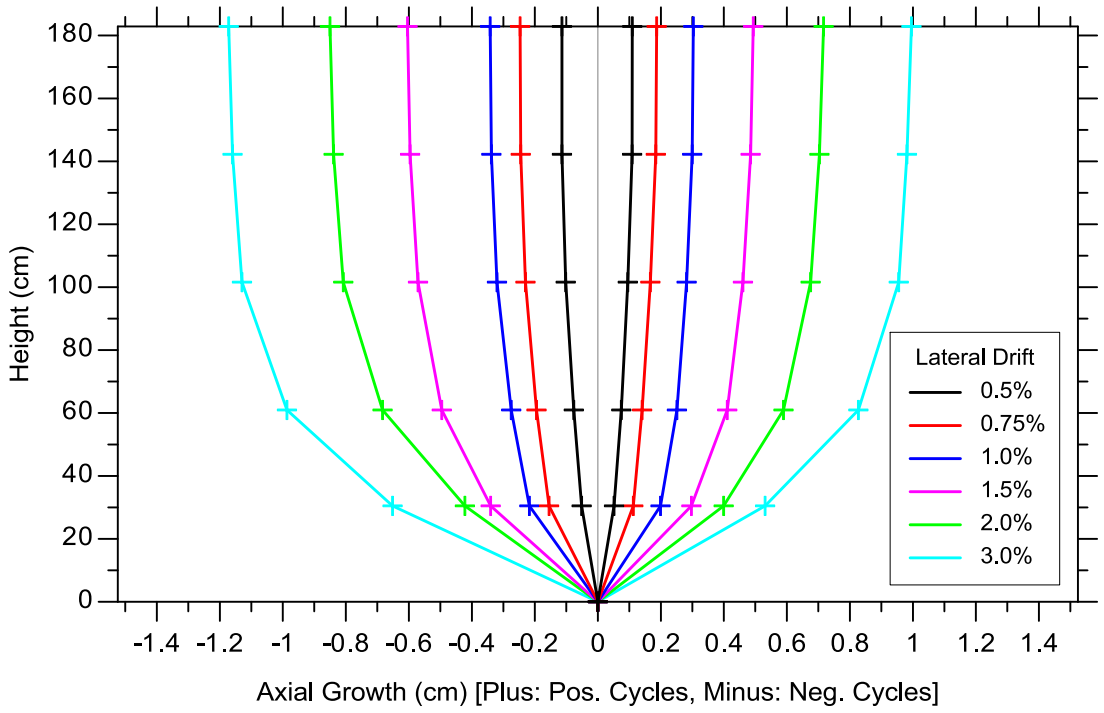

Figure 4-8 Axial Growth Profiles

Figure 4-9 displays the cracking pattern predicted by the model at the end of the applied cyclic loading history along with schematics showing, conceptually, the distributions of vertical axial

strains ε_y (calculated from the plane section assumption) and shear strains γ_{xy} (assumed to be constant over a wall cross-section) along the length and height of the wall; horizontal axial strains ε_x are not presented because the analysis results indicated that they are small compared to ε_y and γ_{xy}.

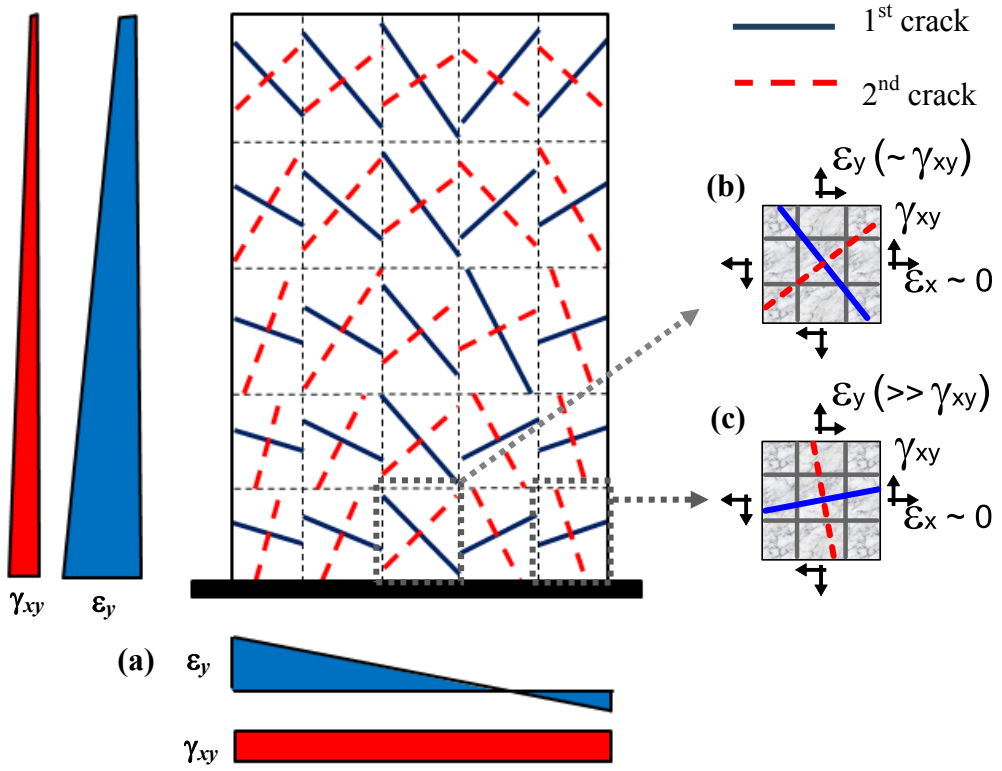

Figure 4-9 Predicted Cracking Pattern and Strain Distributions

As shown on the figure, two perpendicular cracks (i.e., concrete struts) are formed in all RC panel elements of the wall model at the end of the applied loading history. As described in Section 3.3, the initiation and the orientations of cracks in each RC panel element are determined based on the magnitudes and directions of principal strains, which directly depend on the relative magnitudes of axial and shear strains, according to implemented RC panel model. Analytically

predicted cracking pattern shown on Figure 4-9(a) reveals that flexural (more horizontal) cracks are located at the wall boundaries where vertical axial strains are dominant (Figure 4-9(b)), whereas shear (inclined) cracks are located towards the middle of the wall (wall web) where shear strains dominate over the vertical axial strains that are close to zero (Figure 4-9(c)). Furthermore, the magnitudes of vertical axial and shear strains decrease towards the top of the wall resulting in a more inclined orientation of cracks for panels and elements located closer to the top of the wall, as also illustrated on Figure 4-9(a).

Figure 4-10 compares the average vertical strains ε_y and maximal principal strains ε_1 (along the concrete strut) for boundary and central RC panel macro-fibers in the bottom wall-model element, as well as the shear strain γ_{xy} in that element under applied loading history. It can be observed from the figure that shear strains are slightly larger (almost symmetrical around the zero-strain axis) in the negative cycles due to the cyclic degradation of shear stiffness (loading is first applied in the positive direction). In contrast, the longitudinal strains are not symmetric with respect to zero-strain axis, and the vertical strains predicted at the centroid are tensile for almost the entire loading history (except for a range of small displacements due to presence of axial load). Furthermore, principal strains in tension are almost identical to vertical strains for the boundary macro-fiber, due to the almost vertical orientation of the principal strain direction (i.e. compression strut), whereas in the central macro-fiber the orientation of principal strains is approximately 45 degrees from horizontal direction, resulting in a significant difference between vertical and principal strains.

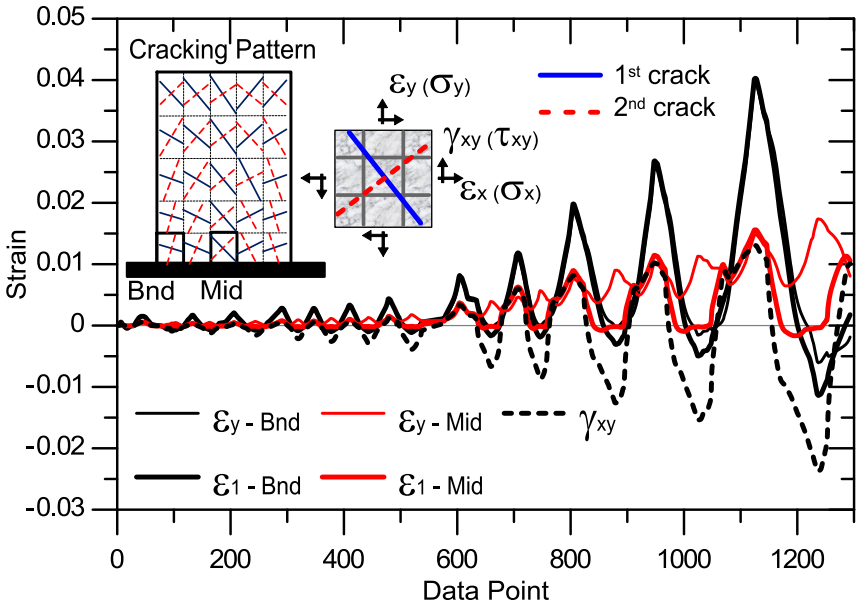

Figure 4-10 Vertical, principal and shear strain histories in wall boundary and center

Figure 4-11 shows the distribution of average vertical normal strains and average shear stresses in unconfined concrete along the wall length at the bottom of the wall obtained at peak drift levels of 0.5%, 1.0%, 2.0% and 3.0%. It can be observed from the figure that the neutral axis depth does not significantly change with increasing drift ratios, and that the shear force on the wall is resisted primarily by the concrete panels subjected to vertical (axial/flexural) compressive strain, whereas panels under vertical tensile strain resist very low or no shear stress, demonstrating the interaction between axial/flexural and shear responses at the element level of the SFI-MVLEM. Results presented in Figure 4-11 also indicate that at drift levels of 0.5% and 1.0%, panels subjected to higher levels of vertical compression develop higher shear stress, whereas at a drift level of 2.0%, the shear stresses at the wall boundary decreases due to degradation in concrete compressive stresses associated with crushing of unconfined concrete in the boundary zone. Furthermore, at the 3.0%drift level, the shear stress migrates from the wall

boundary to the web due to further strength degradation in the stress-strain behavior of concrete at the wall boundary. Overall, Figure 4-11 illustrates that the SFI-MVLEM initially imposes more shear stress demand on the boundary zone in compression, and the shear stresses migrate towards the wall web with increasing nonlinear compression behavior at the boundary.

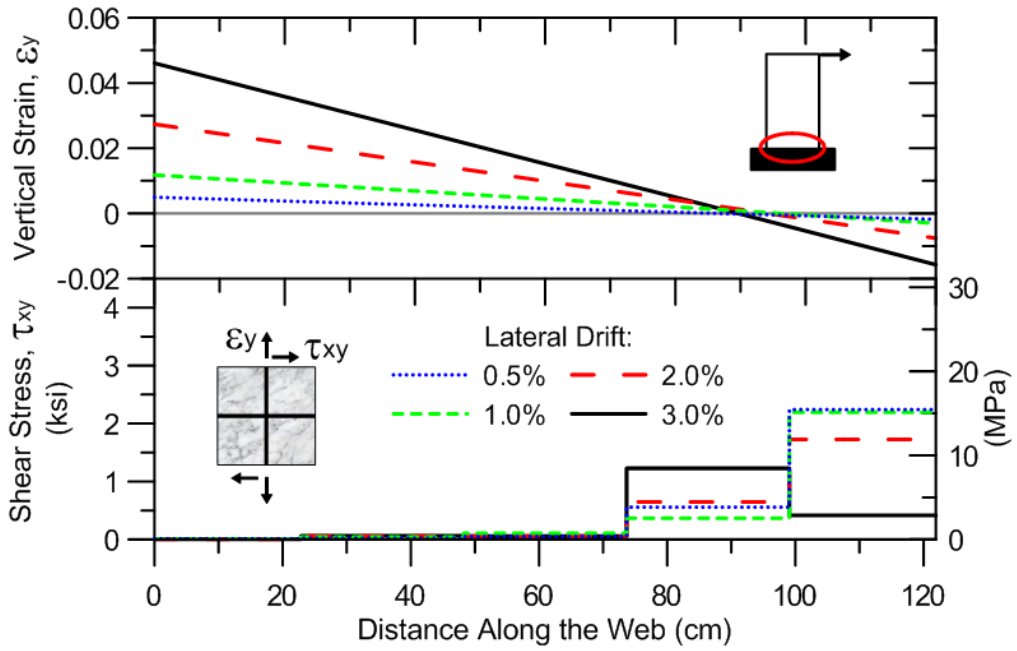

Figure 4-11 Axial-shear coupling at the wall base along the length of the wall

4.3. Sensitivity of Model Response to Wall Configurations

The sensitivity of analytical results to different wall aspect ratios, ratios of nominal shear and flexural strengths, and levels of axial load are presented to illustrate the capabilities of the analytical model to predict behavior of RC walls with various behavior modes and failure mechanisms. As mentioned earlier, specimen RW-A15-P10-S78 (Tran and Wallace, 2012) is used as the baseline model for these studies in which the considered parameters of the wall model are

manipulated; detailed calibration of wall geometry, materials, and parameters of shear resisting mechanism is presented in Chapter 5.

4.3.1. Wall Aspect Ratio

In order to investigate the sensitivity of model predictions to wall aspect ratio, the wall configuration used for previous analyses (representing specimen RW-A15-P10-S78, with aspect ratio of 1.5) was "elongated" to an aspect ratio of 2.0, and "shortened" to an aspect ratio of 1.0, while keeping the same cross-sectional dimensions and reinforcement configurations. Each wall configuration was analyzed under cyclic loading at the top of the wall with a target drift of 3.0%, to peak drift levels of 0.25%, 0.5%, 0.75%, 1.0%, 1.5%, 2.0%, and 3.0% (only one cycle per drift level is applied). Figure 4-12 compares the model results obtained for the three considered aspect ratios of 1.0, 1.5, and 2.0. Predicted wall load-deformation responses can be distinguished by the lateral load capacity prediction, the shape of the overall lateral load versus top displacement response, and the contribution of shear deformation to wall top displacement. For the short wall with aspect ratio of 1.0 (Figure 4-12(a)), the overall lateral load versus displacement response is characterized with shear-dominated (pinched) hysteretic loops, similar in shape to the pure shear response shown previously on Figure 4-3, which is consistent with the large contribution of shear deformation to wall lateral displacements (more than 70%), as shown on Figure 4-12(d). In contrast, for the more slender wall with aspect ratio of 2.0 (Figure 4-12(c)), the shape of the overall response shows wide hysteretic loops and almost no pinching, similar to the shape of the flexural load–displacement response shown on Figure 4-4, implying that flexural deformation contributes significantly to lateral displacements, and the contribution of shear deformations is small (limited to approximately 20% as shown on Figure 4-12(d)). The predicted response of the

wall with the intermediate aspect ratio of 1.5 (baseline wall model, Figure 4-12(b)) falls between the walls with aspect ratios of 1.0 and 2.0 in terms of the pinching characteristics of the response and contribution of shear deformations to wall lateral displacement, as moderately pinched hysteresis loops are obtained and the contribution of shear deformations is approximately 45%. Finally, as expected, the lateral load capacities predicted for the three walls decrease with increasing aspect ratios.

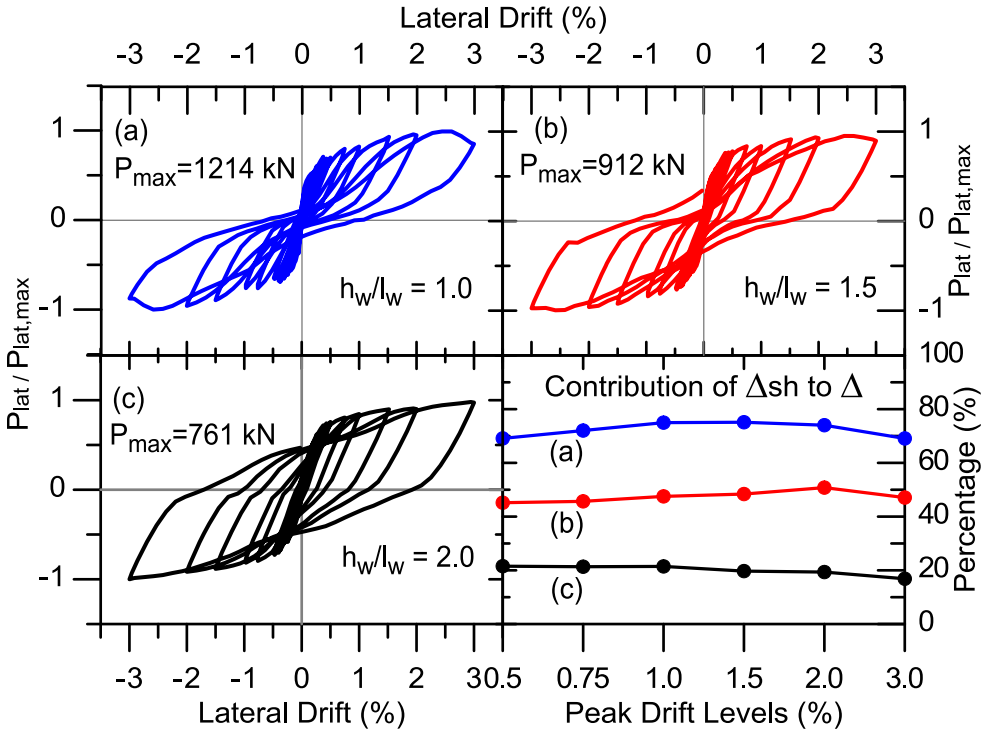

Figure 4-12 Sensitivity of predicted response to wall aspect ratio (h_w/l_w)

4.3.2. Reinforcement Ratio

The sensitivity of the model response to the web reinforcement ratio (ρ_{web}) of the wall was also investigated in order to evaluate whether the model can capture different modes of behavior and

different flexural and shear deformation contributions to the response, depending on relative nominal flexural and shear capacities of the wall. For this purpose, the web reinforcement ratio of the wall configuration was reduced to half of its original value (0.73% to 0.36%). The original wall specimen had a nominal flexural lateral load capacity of 809 kN (182 kips) and a nominal shear capacity of 947 kN (213 kips), resulting in a shear demand at flexural capacity corresponding to 85% of the nominal shear capacity. When the web reinforcement ratio is reduced to half, the nominal flexural lateral load capacity of the wall decreases to 761 kN (171 kips), whereas the nominal shear capacity decreases to 645 kN (145 kips), resulting in shear demand at flexural capacity corresponding to 118% of the nominal shear capacity. Figure 4-13 depicts the lateral load versus top displacement responses obtained for the original wall and the wall configuration with reduced web reinforcement, as well as contributions of shear deformation to the lateral displacement at the top of each wall. It can be observed from the figure that when the flexural capacity of the wall is lower than its nominal shear capacity ($V@M_n/V_n$=0.85), the model predicts a more flexure-dominated behavior, characterized by only moderate pinching in load-displacement response, and shear deformations contribute approximately 45% to wall lateral displacement. In contrast, when the flexural capacity of the wall is higher than its nominal shear capacity ($V@Mn/Vn$=1.18), the model predicts a more shear-dominated behavior, with more pinched load-displacement loops, higher contribution of shear deformations (approximately 55% of wall displacement), and reduced ductility due to initiation of strength degradation in the load-displacement response before reaching the target drift level of 3%, For both cases, the model yields a lateral load capacity which is slightly larger

(approximately 15-20%) than the "controlling" capacity of the wall (smaller of flexural and nominal shear capacities).

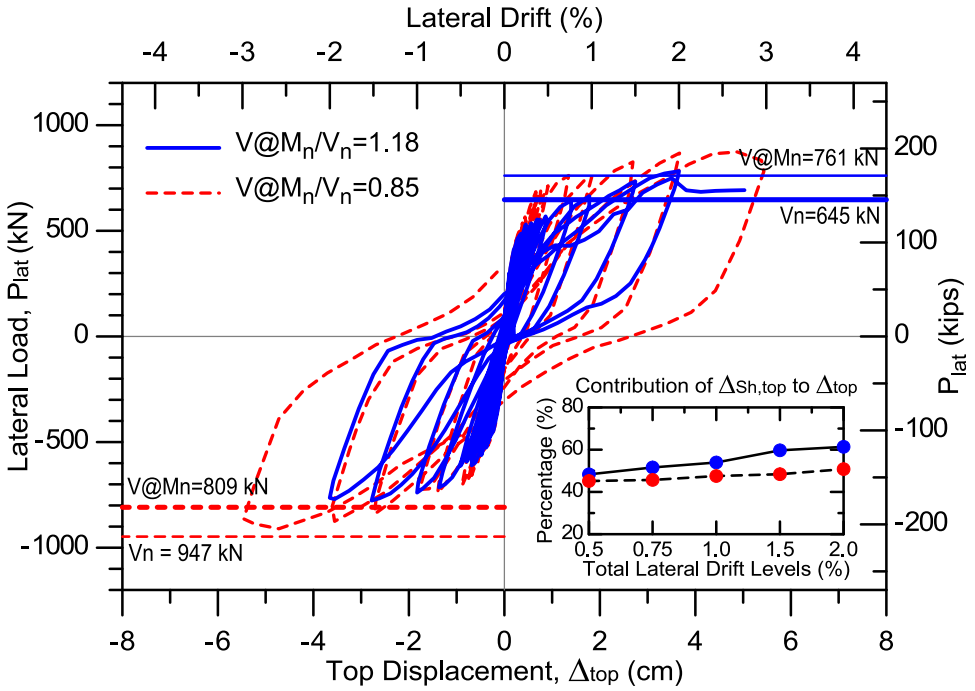

Figure 4-13 Sensitivity of predicted response to wall reinforcement ratio

4.3.3. Axial Load

The influence of the axial load level on predicted wall response is further investigated by subjecting the baseline wall model of specimen RW-A15-P10-S78 to monotonic lateral loading at the top of the wall and axial load levels of 0%, 5%, 10% (original axial load), 15%, and 20% of the wall axial capacity ($A_g f'_c$). The influence of axial load was studied on the effective secant flexural stiffness corresponding to yielding of the longitudinal boundary reinforcement (flexural yielding), effective secant shear stiffness corresponding to shear cracking, and effective secant shear stiffness corresponding to flexural yielding. Secant stiffness (flexural and shear)

corresponding to flexural yielding were determined at the point when axial strain in the boundary reinforcement reaches value of 0.002, while shear cracking is associated with the point at which abrupt change of shear stiffness was observed.

Effective secant flexural stiffness (EI_{eff}), normalized by the concrete gross section flexural stiffness (EI_g), is determined according to the following expression proposed by Tran (2012):

$$\frac{I_{eff}}{I_g} = \frac{h_w^3}{3E_c I_g}\left(\frac{P_{lat}}{\Delta_{flex}}\right) \tag{4-1}$$

where P_{lat} is the lateral load, Δ_{flex} is the flexural displacement at the top of the wall, E_c is Young's modulus of concrete determined using ACI 318 requirements, and h_w is the height of the wall. Similarly, effective secant stiffness of a wall (GA_{eff}), normalized by $E_c A_w$, is calculated according to the following expression derived by Tran (2012):

$$\frac{GA_{eff}}{E_c A_w} = \frac{h_w}{E_c A_w}\left(\frac{P_{lat}}{\Delta_{sh}}\right) \tag{4-2}$$

where Δ_{sh} is the shear displacement at the top of the wall, and A_w is the wall cross-section area.

Figure 4-14(a) displays lateral-load-versus-top-flexural-displacement relationships with points of yielding of longitudinal boundary reinforcement (marked with square), whereas Figure 4-14(b) shows lateral-load-versus-top-shear-displacement relationships with points of yielding of flexural yielding (marked with square) and shear cracking (marked with circle) for all considered levels of axial load.

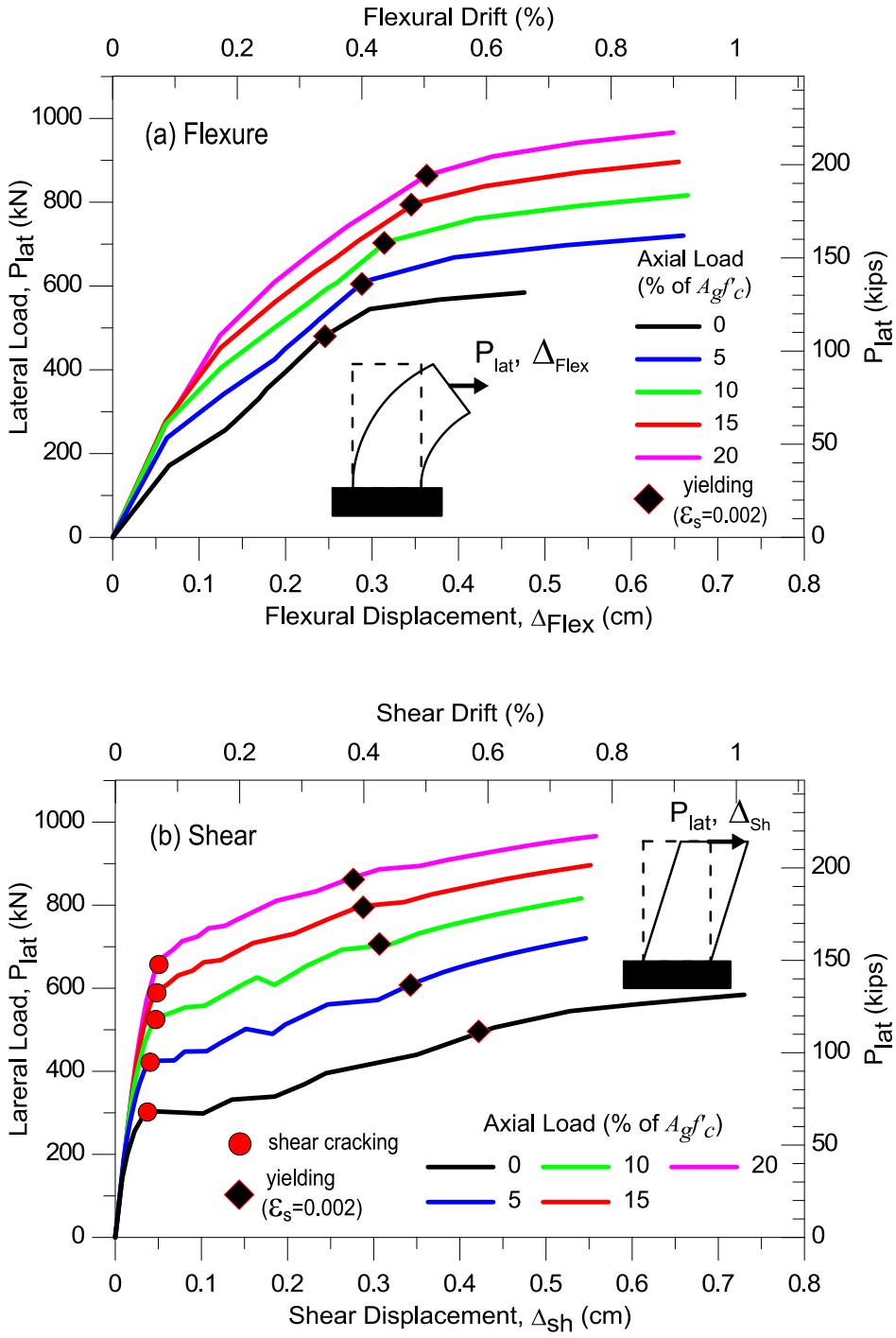

Figure 4-14 Sensitivity to Axial Load of Load-Displacement Relations in: (a) flexure, (b) shear

Lateral loads (P_{lat}), lateral flexural displacements (Δ_{flex}) and lateral shear displacements (Δ_{sh}) corresponding to flexural yielding and shear cracking for all considered levels of axial load, displayed on flexural and shear force-deformation relationships shown on Figure 4-14, are used to calculate effective secant flexural and shear stiffness according to Eq. 4-1 and 4-2; results are summarized in Table 4-1.

Table 4-1 Overview of Analytical Results for Specimen RW-A20-P10-S63

RW-A15-P10-S78	Parameter	Axial Load Level $P_{ax} / A_g f'_c$ (%)				
		0	5	10	15	20
@ yielding	$P_{lat,Flex}$ (kips)	113.5	137.2	158	180	194
	Δ_{Flex} (in)	0.102	0.115	0.125	0.110	0.106
	Δ_{Sh} (in)	0.173	0.135	0.125	0.110	0.106
	I_{eff} / I_g*	**0.46**	**0.50**	**0.53**	**0.54**	**0.56**
	$GA_{eff} / E_c A_w$**	**0.03**	**0.05**	**0.06**	**0.08**	**0.08**
@ shear cracking	$P_{lat,Sh}$ (kips)	68.46	95.54	117.74	132.91	151.26
	Δ_{Sh} (in)	0.0141	0.0162	0.0188	0.0199	0.0213
	$GA_{eff} / E_c A_w$**	**0.22**	**0.27**	**0.29**	**0.33**	**0.34**

* According to Eq. 4-1
** According to Eq. 4-2

Based on results presented in Table 4-1, the relationships between axial load level and effective secant flexural stiffness (normalized by I_g , i.e., I_{eff} / I_g) associated with flexural yielding, as well as effective secant shear stiffness (normalized by $E_c A_w$, i.e., $GA_{eff} / E_c A_w$) corresponding to flexural yielding and shear cracking, are derived and presented in Figure 4-15. It can be

observed from the figure that flexural and shear secant stiffness increase almost linearly with the increase of axial load. The increase of axial load from 0% to 20% results in the increase of effective secant flexural stiffness at flexural yielding from 0.46 to 0.56 of gross flexural stiffenss EI_g (by approximately 20%), whereas the effective secant shear stiffness at flexural yielding and shear cracking increase from 0.03 to 0.08 of $E_c A_w$ (by approximately 50%) and from 0.22 to 0.33 of $E_c A_w$ (also by approximately 50%), respectively.

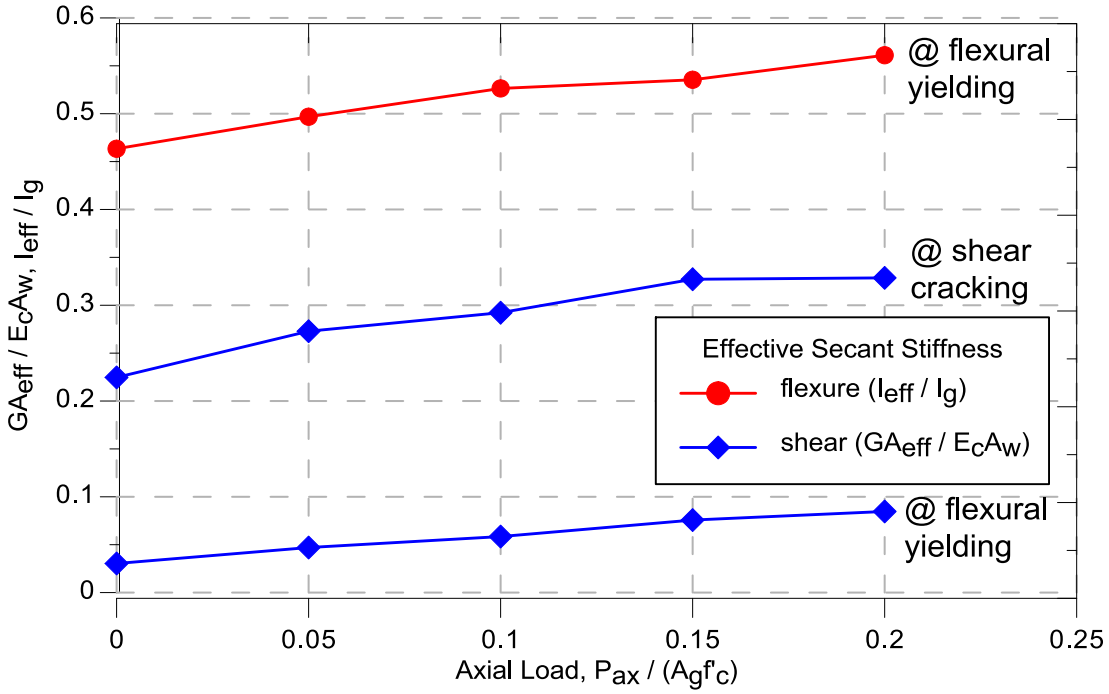

Figure 4-15 Axial Load versus Normalized Effective Secant Stiffness

4.4. Model Parameters

The proposed analytical model includes various parameters, such as the parameters associated with discretizing the model, such as the number of RC panel elements used along the wall length (m) and the number of SFI-MVLEM elements stacked on top of each other along the height of

the wall (n), parameters associated with shear resisting mechanism in a RC panel model, including the friction coefficient of the shear aggregate interlock (η) and stiffness of shear resisting mechanism provided by reinforcement (αE_s), as well as the parameter defining the location of the centroid of rotation along the height of each SFI-MVLEM element (c). This section discusses the sensitivity of model predictions to these model parameters, except for parameter c, where a value of 0.4 was adopted based on prior studies by Vulcano et al. (1988) and Orakcal and Wallace (2006).

4.4.1. Shear Resisting Mechanism of RC Panel Model

Prior to discussion of the sensitivity of analytical predictions to parameters of shear aggregate interlock model (i.e. friction coefficient η) and dowel action (i.e. stiffness parameter α), the sensitivity of model predictions to implementation of these mechanisms in constitutive RC panel model incorporated in SFI-MVLEM is presented.

4.4.1.1. Shear Aggregate Interlock and Dowel Action

The SFI-MVLEM is used to generate analytical predictions for test specimen RW-A15-P10-S78 (Tran and Wallace, 2012) with three different RC panel model formulations: (1) the original RC panel model (FSAM, Ulugtekin, 2010) without shear aggregate interlock and dowel actions implemented, (2) the modified formulation of the FSAM that incorporates the shear aggregate interlock behavior only (Orakcal, 2012), and (3) the formulation of the RC panel model that includes the shear aggregate interlock behavior and dowel action; lateral load versus wall top displacement relations are presented for all three cases considered in Figure 4-16.

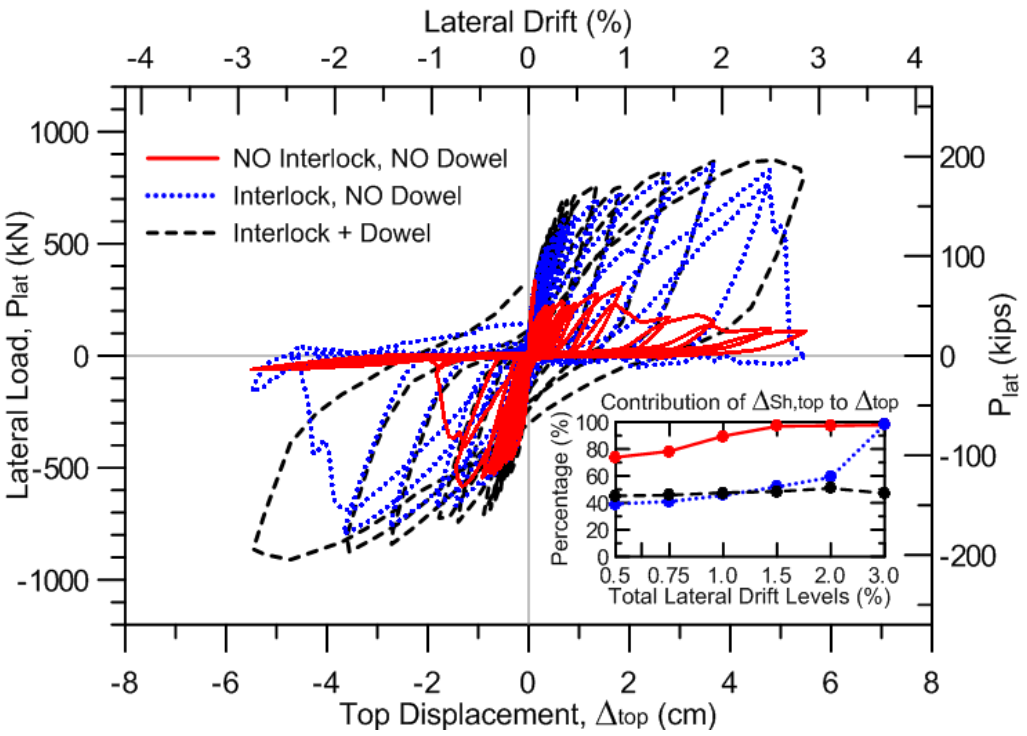

Figure 4-16 Sensitivity to Shear Resisting Mechanism in RC Panel Model

It can be observed from the figure that, if there are no shear resisting mechanisms implemented along cracks of a RC panel model (i.e., no shear aggregate interlock and no dowel action), then the analytical predictions significantly underestimate the wall strength due to shear sliding along the cracks of RC panel macro-fibers. This behavior is characterized by very large percentage contributions of shear deformations to the total lateral wall displacement (larger than 70% at low drift levels and larger than 95% at high drift levels), resulting in highly pinched load-deformation response.

Figure 4-16 further reveals that incorporating shear aggregate interlock mechanism into the formulation of original FSAM stabilizes the load-deformation responses until relatively large lateral drift levels are reached. For this case, predicted wall response is characterized by much

higher lateral strength and stiffness, and much lower contributions of shear deformation at low and moderate drift rations (approximately 40-60%); however, strength degradation is still present at large drift levels, due to shear sliding along the cracks of RC panel elements (which results in the greater than 95% contribution of shear deformations to top lateral displacement at the 3.0% drift level). Although incorporating shear aggregate interlock along the cracks of RC panel model improve the predicted load-deformation response, the analytical predictions of RC wall behavior are still characterized with high contributions of shear deformations at larger drift levels, pronounced pinching of force-deformation response, as well as the negative stiffness in the unloading branch around zero lateral deformation. Detailed investigation of the analytical results suggested that the negative stiffness is caused by zero shear resistance along the cracks under tension (crack open), which is characteristic of implemented shear aggregate interlock model, as described in Section 3.3.2.1.

Since dowel resistance of vertical reinforcement can provide shear resistance along the cracks of a RC panel, even when the crack surface is in tension, a simple linear-elastic constitutive model (described in Section 3.3.2.2) is implemented in RC panel model to simulate the contribution of reinforcement to shear transferring mechanism. As it can be observed in Figure 4-16, when both shear aggregate interlock and dowel action are incorporated into the formulation of FSAM, the overall load-deformation response is characterized with stable hysteretic loops characterized with moderate pinching throughout the entire cyclic loading history. In addition, predicted wall strength is approximately 10-20% higher than for the case with shear aggregate interlock only, and the wall response is characterized with almost constant contributions of shear deformations of approximately 45% throughout the loading history. These analytical results agree reasonably

well with experimental results in terms of both load-deformation response and contributions of shear deformations as shown in Sections 6.3.4 and 6.6.3, respectively.

Based on previous discussion, the formulation of a RC panel model with incorporated shear aggregate interlock behavior and dowel action is implemented into a SFI-MVLEM to obtain improved predictions of RC walls. As discussed in Sections 3.3.2.1 and 3.3.2.2, models used to represent the shear aggregate interlock and dowel action are characterized with two parameters that need to be calibrated against experimental results: (1) friction coefficient of shear aggregate interlock η, and (2) stiffness parameter of dowel action α. The sensitivity of analytical results to these parameters is presented in the following section.

4.4.1.2. Shear Friction Coefficient (η) and Stiffness of Dowel Action (αE_s)

In order to investigate the sensitivity of model predictions to parameters of shear resisting mechanism, analytical results are obtained for specimen RW-A15-P10-S78 (Tran and Wallace, 2012) using friction coefficient of aggregate interlock η = 0.6, 1.0 and 1.5, and stiffness coefficient of dowel action α = 0.002, 0.005, 0.01 and 0.02. Lateral-load-versus-total-top-displacement and lateral-load-versus-shear-top-displacement responses for considered values of parameters η and α are compared on Figure 4-17 and Figure 4-18, respectively.

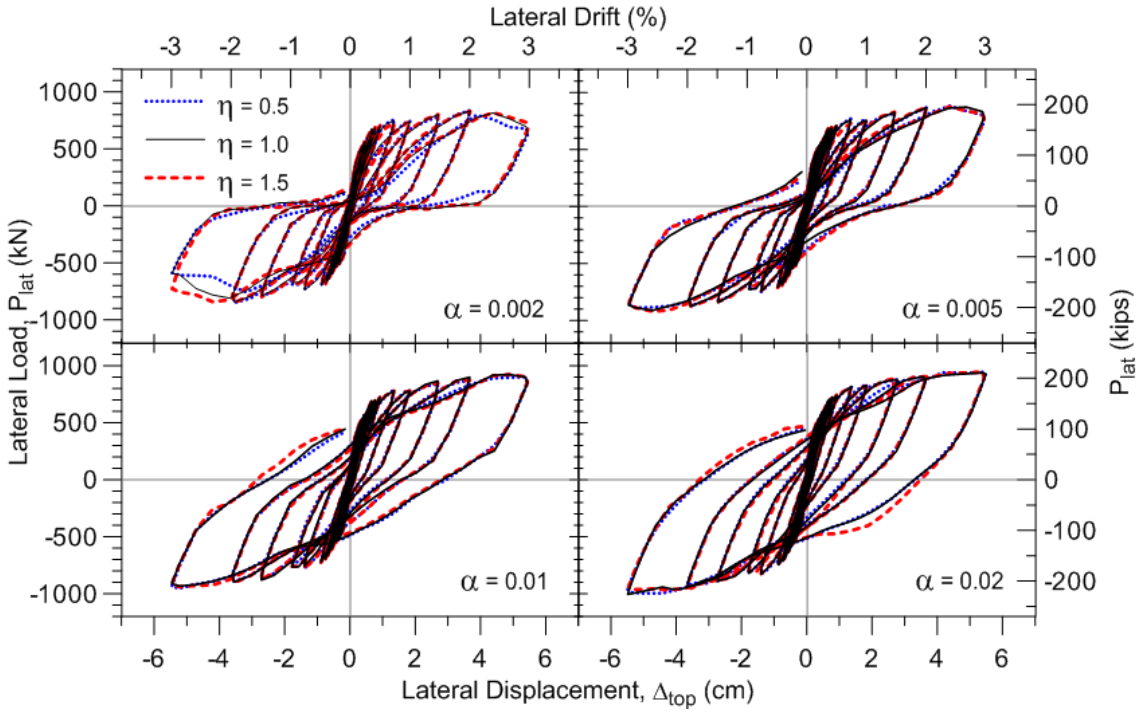

Figure 4-17 Sensitivity of Load-versus-Total-Top-Displacement Response to Parameters α and η

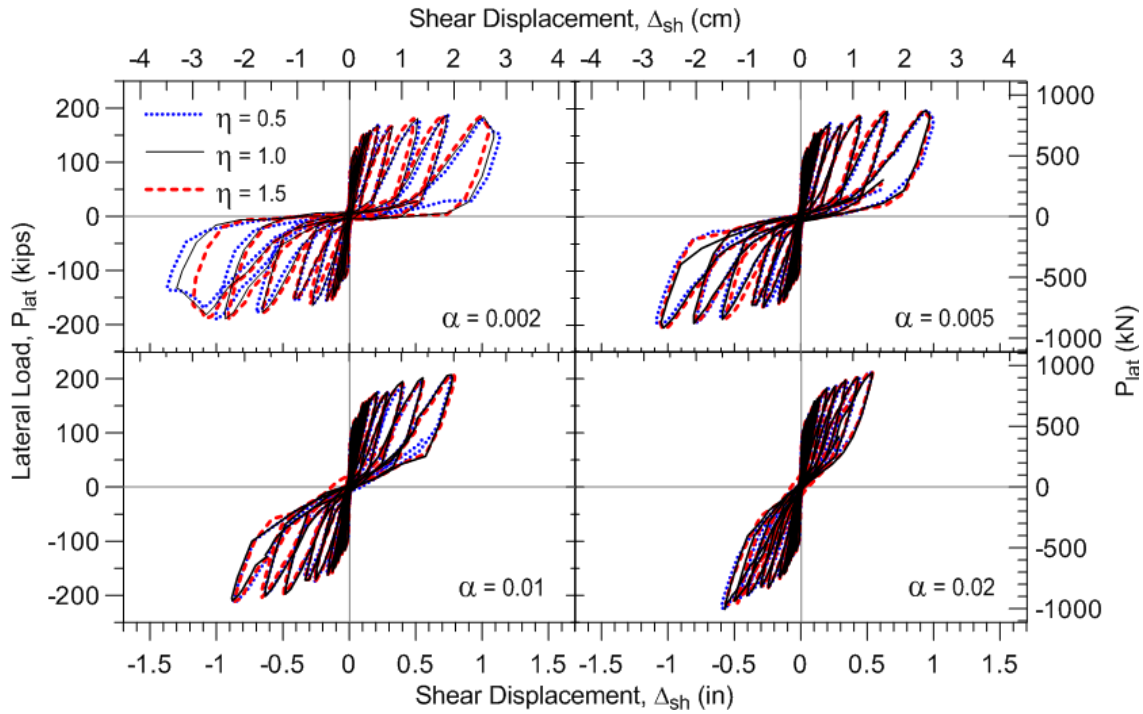

Figure 4-18 Sensitivity of Load-versus-Shear-Top-Displ. Response to Parameters α and η

Results presented on Figure 4-17 indicate that for a fixed value of parameter α, lateral-load-versus-total-top-displacement relations are marginally sensitive to variations in parameter η in terms of stiffness, lateral load capacity, and pinching. Similarly, Figure 4-18 reveals that given the value of parameter α, predicted nonlinear shear deformations are only slightly larger when lower values of friction coefficient is used; the most drastic increase of nonlinear shear deformations can be observed for $\alpha = 0.002$, where the decrease of friction coefficient from 1.4 to 0.6 results in the increase of shear deformations of about 15%. In contrast, it can be observed from Figure 4-17 and Figure 4-18 that the predicted wall behavior is considerably more sensitive to the stiffness parameter of dowel action (α) in terms of total and shear load-deformation responses. Although the wall stiffness and capacity are similar for all considered values of parameter α, higher values of this parameter yield less pinched total load-deformation response and smaller magnitudes of predicted nonlinear shear deformations, e.g. the increase of parameter α from 0.002 to 0.02 reduces the magnitude of shear deformations to about 50%.

In summary, presented results suggest that model predictions are more sensitive to stiffness coefficient of dowel action α then to friction coefficient of shear aggregate interlock η in terms of load-deformation response and contributions of shear deformations. The increase of shear resistance along the cracks (shear stress) in RC panels, which can be achieved by increasing the dowel action stiffness coefficient or the shear friction coefficient, will result in the decrease in the amount of shear deformations and shear slip along the cracks of RC panels predicted by the model, which provides less pinching in the overall load-deformation response.

4.4.2. Model Discretization

Sensitivity of simulated wall response to variations in the number of SFI-MVLEM elements along the wall height (n) and the number of RC panel macro-fibers along the wall length (m) is further investigated. Results for different wall discretizations are compared in terms of overall load-deformation response, contributions of shear deformations to wall top lateral displacement and local responses (e.g. vertical and principal strains).

4.4.2.1. Strain Localization

In displacement-based beam-column elements with distributed plasticity and strain softening material laws, such as for the proposed SFI-MVLEM element, there is a potential for strain localization to occur. This phenomenon can lead to numerical results that are sensitive to the element length in which the plastic strain is localized. To avoid this problem, Coleman and Spacone (2001) proposed a methodology, so-called regularization, to modify stress-strain relationships of material laws (e.g. concrete and steel material laws) according to the element size in order to maintain constant fracture energy dissipation, which ensures that the numerical solution will be objective and not sensitive to element size. The effect of material regularization on analytical results of SFI-MVLEM is investigated.

According to this methodology, the envelope of the stress-strain relationship for concrete was modified based on the element size by calculating a value of strain at which descending (post-peak) branch of concrete stress-strain relationship reaches zero (ε_r) to maintain constant fracture

energy (Figure 4-19). Given the implemented constitutive law for concrete (Chang and Mander, 1988), the following expression for ε_r is derived:

$$\varepsilon_r = \frac{G_{f,c}}{f_c^{'} L_e} - \frac{f_c^{'}}{E_c} + \varepsilon_p \tag{4-2}$$

where $f_c^{'}$ is the concrete compressive strength (confined or unconfined), ε_p is the strain corresponding to the peak stress, E_c is the initial modulus of elasticity assumed to remain the same during loading and unloading (adopted as $E_c = 8200 f'_c$ (MPa) as suggested by Chang and Mander, 1988), L_e is the model element length, and $G_{f,c}$ is the fracture energy in compression for concrete. The fracture energy $G_{f,c}$ of concrete can be calculated based on the area under post-peak branch of experimental concrete stress-strain curve (Figure 4-19) as:

$$G_c^f = \left(\frac{f_c^{'}}{E_c} + \left(\varepsilon_r - \varepsilon_p \right) \right) \cdot f_c^{'} \cdot L_p \tag{4-3}$$

where L_p is the plastic length, i.e. the length along which concrete strength degradation occurs.

In this study, the reference value of concrete fracture energy $G_{c,f}$ is calculated according to Eq. 4-3 for the plastic length (L_p) equal to 12 in., which corresponds to the length of concrete test cylinder used to obtain concrete stress-strain relationship used in wall specimens. Since the post peak slope of concrete stress-strain relationship determined from the cylinder test was not reliable (due to instability of test specimen after the initiation of crushing), the strain value ε_r

was calibrated such that the post-peak slope of the concrete stress-strain relationship agrees with the post-peak slope of the Saatcioglu and Razvi (1992) model for both confined and unconfined concrete; details about calibration of stress-strain relationship for concrete against experimental data are provided in Section 5.2.2.2. Finally, the value of strain ε_r corresponding to the element size (L_e) in the model was calculated according to Eq. 4-2.

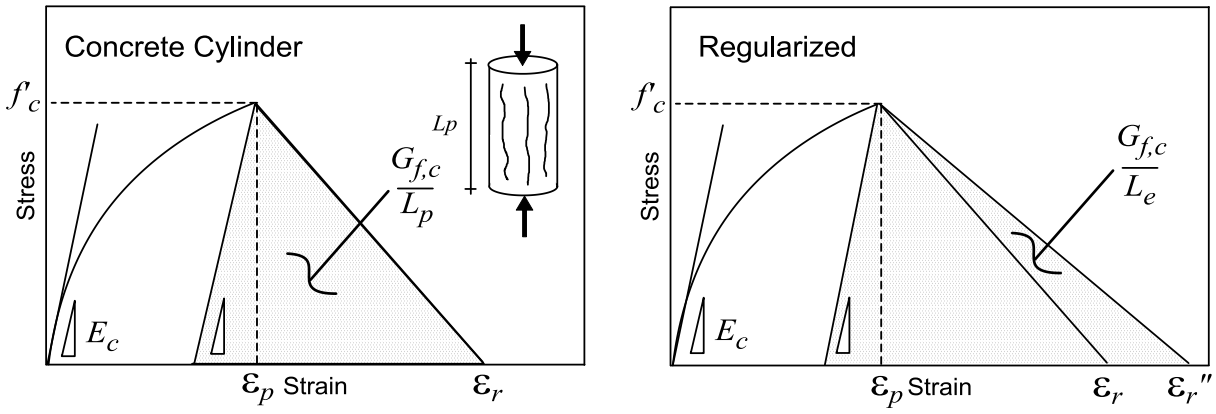

Figure 4-19 Chang and Mander (1988) Stress-Strain Law and Compression Fracture Energy

Similarly, the constitutive model for steel was manipulated by adjusting the slope of post-yielding branch of the stress-strain curve via parameter ε_u, which represents strain corresponding to the ultimate stress in steel (f_u), based on the length of the model element (L_e), such that the strain energy of steel ($G_{s,f}$, Figure 4-20) remains constant. Parameter ε_u can be calculated according to stress-strain relationship for reinforcing steel represented by the Menegotto and Pinto (1973) model by the use of following expression:

$$\varepsilon_u = 0.002 + \frac{2G_{s,f}}{(f_u + f_y)L_e} \tag{4-4}$$

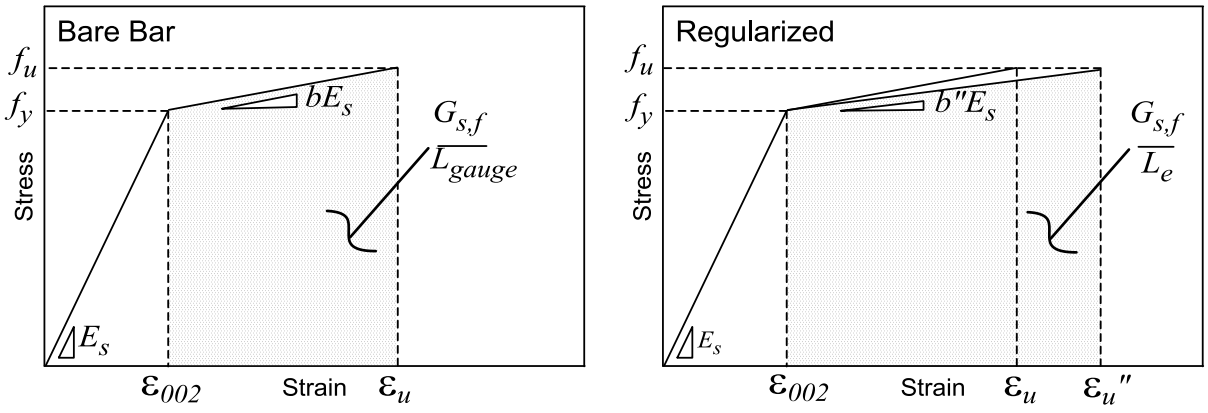

Figure 4-20 Regularization of Stress-Strain Relationship for Steel

Furthermore, the strain energy $G_{s,f}$ of steel can be calculated based on the area under post-yielding branch of experimental steel stress-strain curve (Figure 4-20) as:

$$G_{s,f} = \frac{\left(f_u + f_y\right)}{2} \cdot \left(\varepsilon_u - 0.002\right) \cdot L_{gauge} \tag{4-5}$$

In this study, the reference strain energy $G_{s,f}$ is obtained according to Eq. 4-5 using L_{gauge} equal to 8 in., which corresponds to the strain gauge length used in tension test on 24 in. long steel rebar samples used in wall specimens; calibration of stress-strain relationship for steel is described in Section 5.2.2.1.

In order to investigate the sensitivity of analytical results to the effects of strain localization and material regularization when the element size is varied, two model discretizations were considered: (1) the model discretization with 5 SFI-MVLEM elements stacked along the height of the wall (n = 5) and 5 RC panel fibers (macro-fibers) along the wall length (m = 5) shown on Figure 4-21(a), and (2) the model with 3 SFI-MVLEM elements stacked along the height of the

wall (n = 3) and 5 RC panel fibers (macro-fibers) along the wall length (m = 5) shown on Figure 4-21(b). Tran and Wallace (2012) reported that the height of the wall specimen RW-A15-P10-S78 along which inelastic deformations were observed (the so-called plastic hinge region) was approximately 24 in. from the bottom of the wall (i.e. l_w/2), which is represented with 2 (Figure 4-21(a)) and 1 (Figure 4-21(b)) SFI-MVLEM elements for the wall discretizations considered; therefore, the element lengths for which regularization was performed are 12 in. and 24 in.

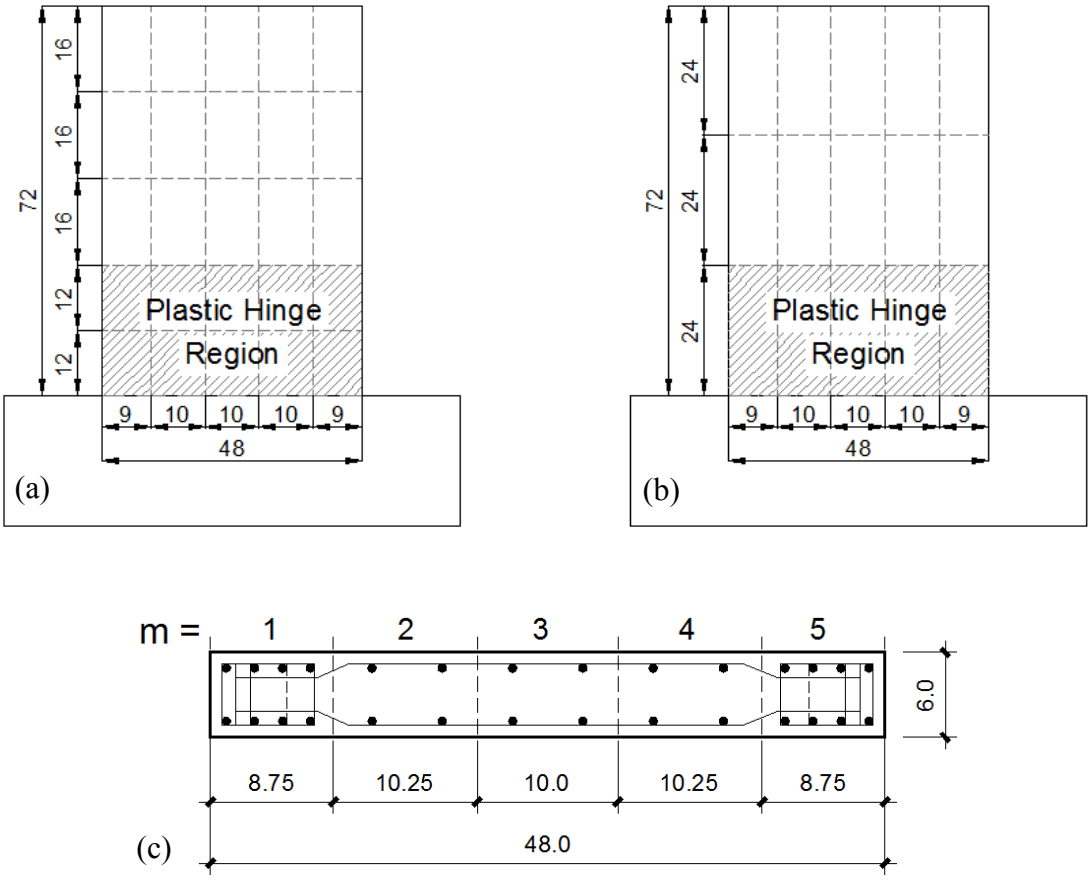

Figure 4-21 Considered Wall Discretizations: (a) n = 5, m = 5, (b) n = 3, m = 5, (c) wall-cross section

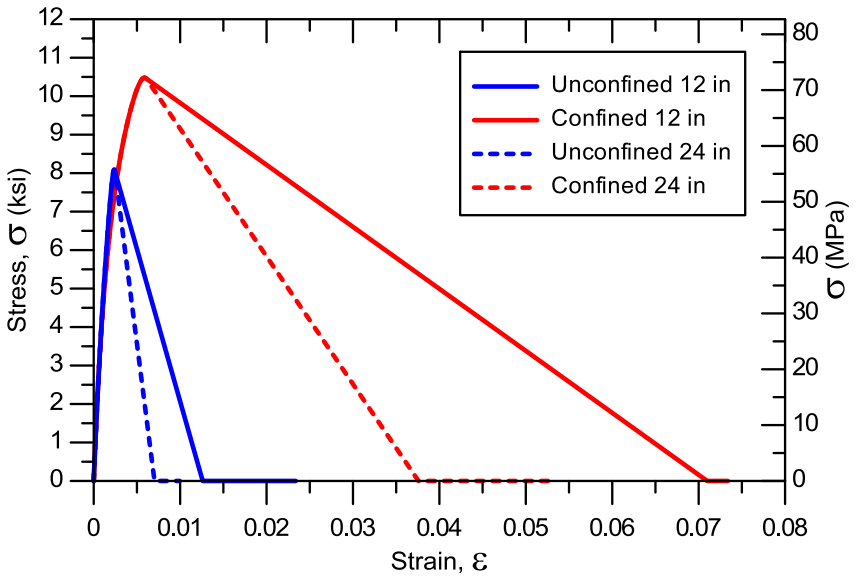

Figure 4-22 Stress-Strain Concrete Material Law for 12 in and 24 in Element Length

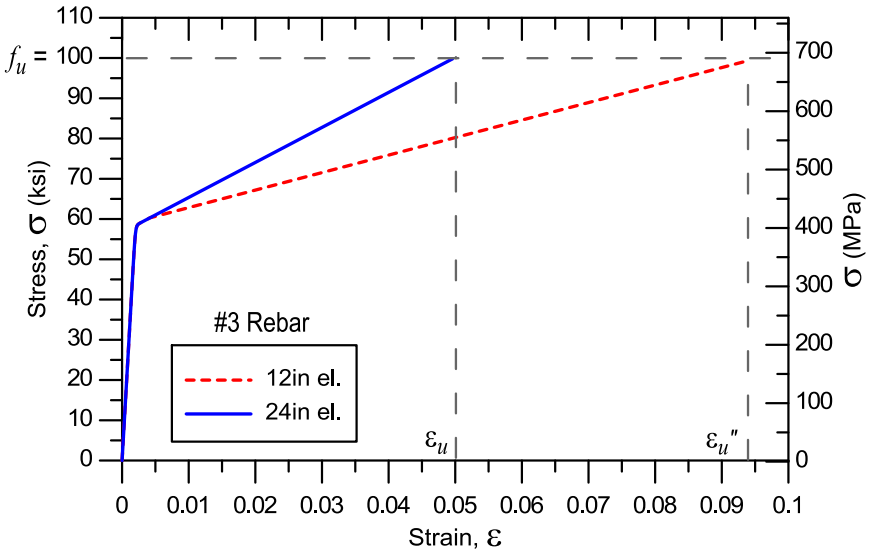

Figure 4-23 Stress-Strain Steel Material Law for 12 in and 24 in Element Length

The reference strain energies of concrete ($G_{c,f}$) and steel ($G_{s,f}$) were first determined based on experimentally measured stress-strain relationships of these materials, according to Eq. 4-3 and Eq. 4-5, respectively. The regularization of concrete and steel material laws was then performed

by calculating values of parameters ε_r (Eq. 4-2) and ε_u (Eq. 4-4), respectively, according to 12 in. and 24 in. element lengths; the envelopes of stress-strain relationships for concrete (confined and unconfined) and reinforcing steel (#3 bars only) corresponding to 12 in and 24 in element are shown on Figure 4-23 and Figure 4-23, respectively.

In order to investigate the influence of material regularization (i.e., concrete post-peak slope and steel post-yielding slope) on analytical results, the predicted load-deformation behavior of specimen RW-A15-P10-S78 (Tran and Wallace, 2012) is compared for three combinations of two considered element lengths and two concrete and steel material laws: (1) element lengths of 12 in. with material laws corresponding to 12 in. long elements, (2) elements lengths of 24 in. with material laws corresponding to 24 in. long elements, and (3) element lengths of 12 in. with material laws corresponding to 24 in. long elements. Since the concrete stress-strain law degrades after its compressive strength is reached (concrete crushing), whereas material law for steel does not account for any form of strength degradation (e.g., bar buckling in compression and/or bar fracture in tension), stress-strain relationships for concrete along the principal directions of confined-boundary RC panel elements were monitored during analyses, and occurrence of two events in concrete constitutive behavior were recorded for the sake of discussion: (a) "initiation of concrete strength degradation", defined when stress in confined concrete in the boundary RC panel element reaches the compressive strength of confined concrete (marked with triangle on Figure 4-24), and (b) "concrete crushing", defined when the concrete strength along the compression strut in boundary RC panel element reaches zero (marked with circle on Figure 4-24); the lateral-load-versus-top-wall-deformation responses for three considered cases are compared on Figure 4-24.

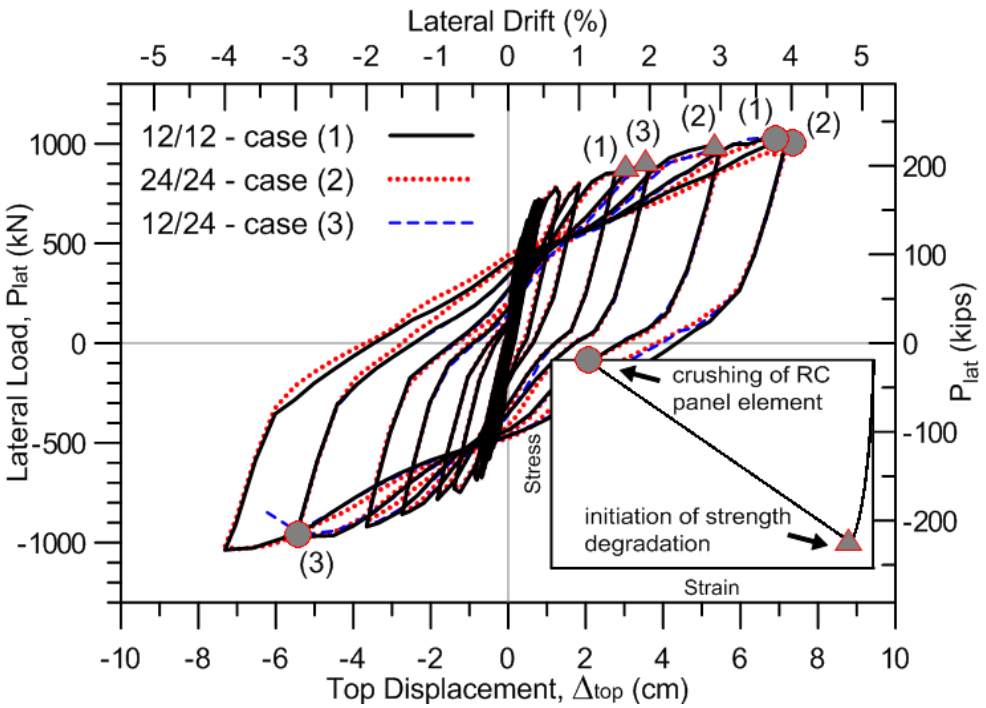

Figure 4-24 Effect of material regularization on predicted global load-deformation response

It can be observed from Figure 4-24 that the "initiation of concrete strength degradation" for cases (1) and (3) (cases with same element lengths but different material plastic behavior) occurs at approximately same positive drift level of roughly 2%, whereas for case (2) (case with larger element length) the "initiation of concrete strength degradation" occurs at the positive drift level of 3%. These results suggest that predicted average concrete strains are dependent on the element size, i.e. the model with larger elements predict smaller average strains over the same height of the wall, which is consistent with the concept of smeared strains. After the peak compressive strength of concrete is reached, the strength degradation of concrete in case (3) occurs along the post-peak branch with the steeper slope than in case (1), which results in faster degradation of wall strength and ultimately earlier point of "concrete crushing" when comparing to case (1). As well, for case (3), the "initiation of concrete strength degradation" of the wall occurs at negative

3% drift level, whereas in case (1) “concrete crushing” occurs at positive 4% drift level. In case (2) “concrete crushing” of the wall occurs at the same drift level as in case (1) suggesting that even when different element lengths are used, which initiates the crushing of concrete at different levels of lateral deformation, after the regularization of the material stress-strain relationships, predicted wall capacities are very close. It can be also observed from Figure 4-24 that overall load-deformation responses for cases (1) and (2) do not differ significantly before the “initiation of concrete strength degradation”, suggesting that sensitivity of analytical predictions to model discretization is small, which is investigated in more detail in following section.

Based on previous discussion, the need for material regularization is important only when strength degradation in concrete is expected since it affects only the degrading part of the stress-strain relationship. Test specimens tested by Tran and Wallace (2012) experienced various failure modes that, although initiated with concrete crushing, are governed by various failure mechanisms (e.g. instability of compression zone due to buckling of boundary reinforcement, diagonal tension, shear sliding). Thus, the effect of material regularization does not play significant role in modeling experimental specimens considered in this study.

4.4.2.2. Model Discretization

As mentioned earlier, the baseline wall model of specimen RW-A15-P10-S78 (Tran and Wallace, 2012) is generated by using 5 SFI-MVLEM elements stacked along the height of the wall and 5 RC panel fibers (macro-fibers) along the wall length (n = 5, m = 5), as shown on Figure 4-1. In order to investigate the sensitivity of analytical predictions to model discretization, three wall models were considered with different levels of element sizes: (1) the baseline model

discretization (moderate-size discretization, Figure 4-1), (2) wall model with 3 SFI-MVLEM elements stacked along the height of the wall and 4 RC panel fibers (macro-fibers) along the wall length (n = 3, m = 4, sparse discretization, Figure 4-25(a.1,b.1)), and (3) wall model with 10 SFI-MVLEM elements stacked along the height of the wall and 10 RC panel fibers (macro-fibers) along the wall length (n = 10, m = 10, dense discretization Figure 4-25(a.2,b.2)). It should be mentioned that inelastic deformations are observed in the experiment over the bottom 24 in. of the wall (i.e., $0.5l_w$, as discussed earlier), which is represented with 1, 2 and 3 SFI-MVLEM elements for the case of sparse, moderate-size, and dense wall discretization, respectively. Hence, material laws for steel and concrete were adapted to the element sizes in these model elements according to regularization procedure described in previous section.

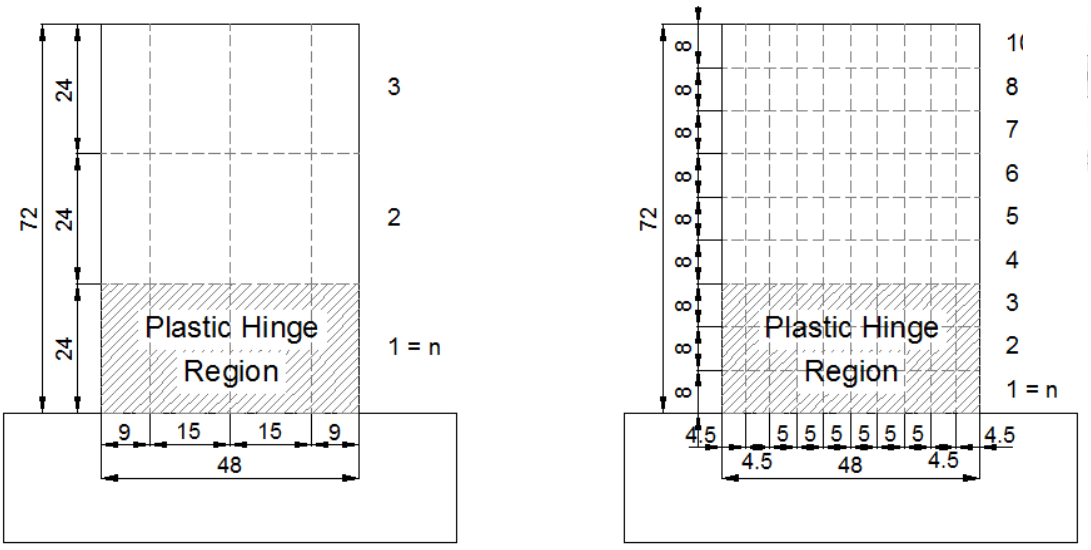

(a.1) n = 3, m = 4 (a.2) n = 9, m = 10

(a) Plane View

Figure 4-25 Considered Wall Discretizations

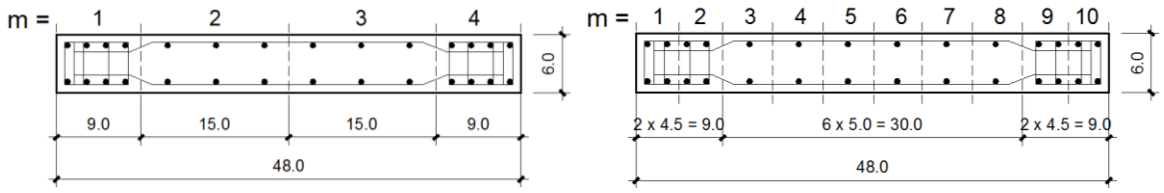

(b.1) $n = 3$, $m = 4$ (b.2) $n = 9$, $m = 10$

(b) Cross-Section

Figure 4-25 (cont.) Considered Wall Discretizations

The comparison of lateral load versus top-displacement response and the contributions of shear deformations to the total lateral displacement at the top of the wall obtained with three considered wall discretizations are presented on Figure 4-27. The comparison indicates that increasing or decreasing the number of RC panel elements in the wall cross-section or the number of SFI-MVLEM elements along the wall height does not change significantly the prediction of the lateral-load-versus-top-displacement response or the contributions of shear deformations to the total lateral displacement. Results shown in Figure 4-27, which compare principal strain histories at boundary and centroidal concrete fiber in the base SFI-MVLEM element for three considered model configurations (i.e., $n = 5$, $m = 5$; $n = 3$, $m = 4$; and $n = 9$, $m = 10$), indicate that the use of more elements is valuable in terms of obtaining more detailed information on local behavior, such as the state of strain at a given location. Since the panel model is based on the concept of smeared (average) strains, using more SFI-MVLEs over the height of the wall may allow for an improved local prediction of the strains; results illustrated on Figure 4-27 indicate that larger model elements predict generally smaller strains. In addition,

using more RC panel elements along the wall length allows a more refined description of the wall cross section in terms of distribution and location of the reinforcement (Figure 4-25(b)).

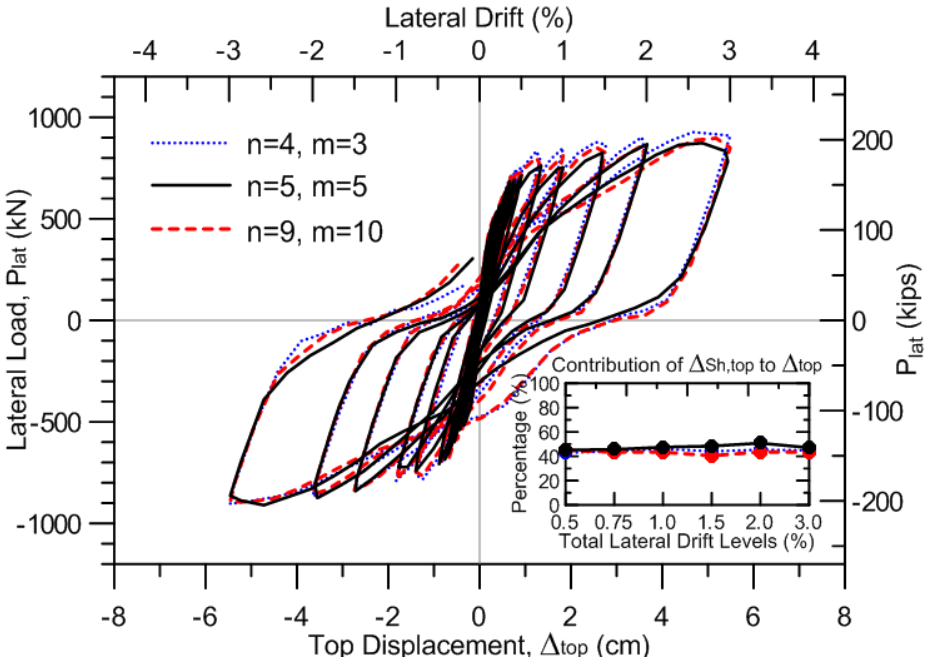

Figure 4-26 Sensitivity of Load-versus-Top-Displacement Response to Wall Discretization

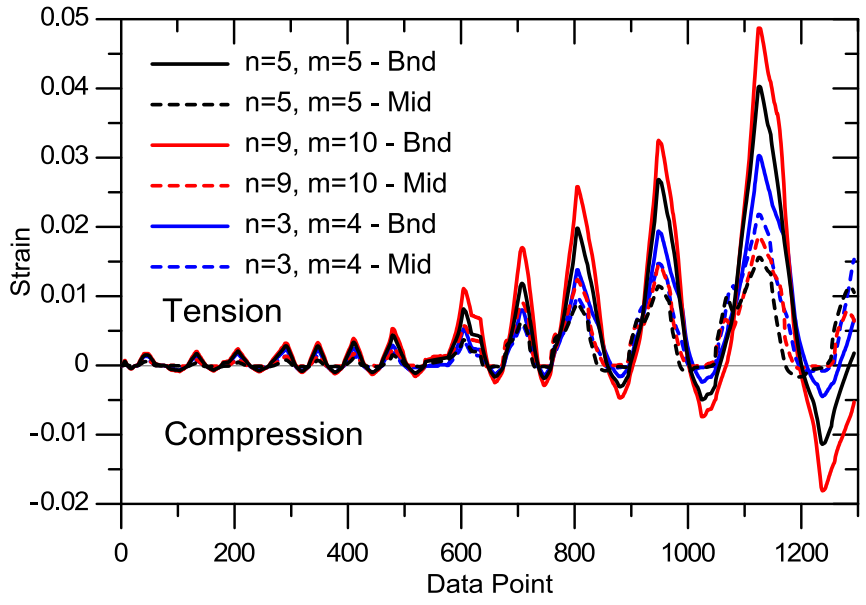

Figure 4-27 Sensitivity of Principal Strains to Wall Discretization

CHAPTER 5

EXPERIMENTAL MODEL CALIBRATION

This chapter presents detailed information on the calibration of the analytical macro-model described in Chapter 3 using test results for reverse cyclic loading of moderate-aspect ratio walls; calibration studies for a slender RC wall specimen are provided in Chapter 7. Extensive experimental data for five rectangular RC wall specimens tested by Tran and Wallace (2012) that experienced significant shear-flexure interaction and nonlinear shear deformations were used to validate and calibrate the proposed modeling approach. An overview of these experimental studies, calibration of model geometry, materials, and parameters for shear resisting mechanisms implemented in the RC panel model (Section 3.3.2) are presented in following sections.

5.1. Overview of Experimental Studies

Experimental studies conducted by Tran and Wallace (2012) included five one-third scale cantilever RC wall specimens subjected to combination of constant axial load and reversed-cyclic lateral loading applied at the top of the walls. Specimens were designed and tested in the Structural/Earthquake Engineering Research Laboratory (SEERL) at the University of California Los Angeles (UCLA). The primary objectives of the test program were to investigate the impact of level of axial stress and average shear stress on the wall failure modes and lateral deformation capacity, as well as to assess the distribution and magnitude of lateral deformations associated with shear and flexure. The primary test variables included wall aspect ratio (1.5 and 2.0), axial

load level ($0.025\,A_g f'_c$ and $0.10\,A_g f'_c$), and wall shear stress level (between approximately 0.33 and $0.66\sqrt{f'_c}$ MPa or 4 and $8\sqrt{f'_c}$ psi). An overview of specimen design, materials, test setup and instrumentation is presented in the following paragraphs, while detail information can be found in PhD dissertation by Tran (2012).

5.1.1. Test Specimen Information

Five RC wall specimens were 15 cm (6 in.) thick and 122 cm (48 in.) long, with lateral load applied at either 183 cm (72 in.) or 244 cm (96 in.) above the wall-foundation block interface. Axial load levels of $0.10\,A_g f'_c$ were applied to the first four specimens and the axial load of $0.025\,A_g f'_c$ is applied to the fifth specimen, where A_g is the gross cross-section area of shear walls and f'_c is the specified concrete compressive strength. The ratios of horizontal and vertical web reinforcement are the same and higher than the minimum requirement from Chapter 21 of ACI 318-11 (0.0025). Specimens were designed to yield in flexure before reaching the ACI 318-11 nominal shear strength. Test matrix is presented in Table 5-1, a typical wall cross-section is shown on Figure 5-1 and wall reinforcement details are summarized in Table 5-2. The minimum and maximum ratios of vertical boundary reinforcement ρ_b for the five test specimens are 3.23% and 7.11%.

Table 5-1 Test matrix (Tran, 2012)

Test No.	Specimen code	$\frac{h_w}{l_w}$	$\frac{P_{ax}}{A_g f'_c}$		Web Reinforcement		Boundary Reinf.		$\frac{V@M_n}{V_n}$		$\frac{V@M_n}{A_{cv}\sqrt{f'_c}}$	
			des.	*act.*	ρ_t=ρ_l (%)	*configuration*	ρ_b (%)	*conf.*	*des.*	*act.*	*des.*	*act.*
1	RW-A20-P10-S38	2.0	0.10	0.073	0.27	6D6@140 mm	3.23	8#4	0.80	0.81	3.8	3.6
2	RW-A20-P10-S63		0.10	0.073	0.61	5#3@152 mm	7.11	8#6	0.88	0.91	6.3	6.1
3	RW-A15-P10-S51	1.5	0.10	0.077	0.32	7D6@114 mm	3.23	8#4	0.80	0.83	5.1	4.9
4	RW-A15-P10-S78		0.10	0.064	0.73	6#3@127 mm	6.06	4#6+4#5	0.84	0.85	7.8	7.0
5	RW-A15-P2.5-S64		0.025	0.016	0.61	5#3@152 mm	6.06	4#6+4#5	0.79	0.79	6.4	5.8

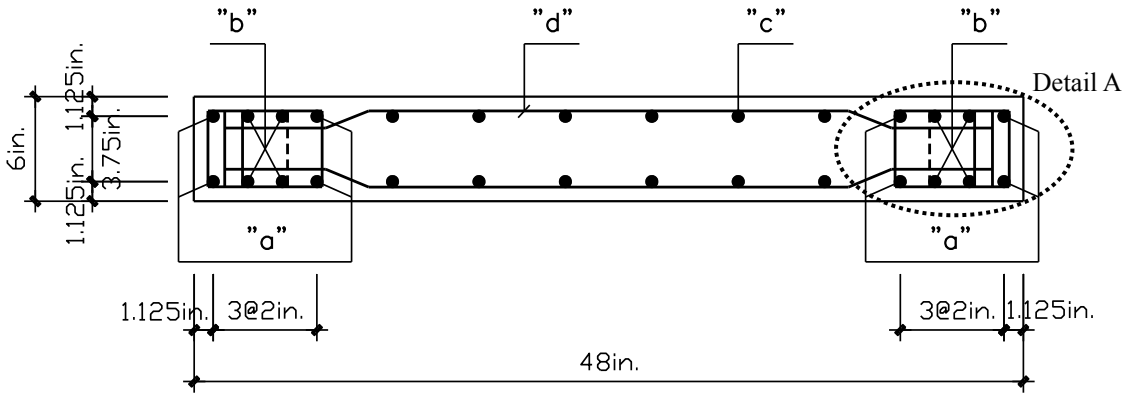

Figure 5-1 Typical Wall Cross-Section

Table 5-2 Wall Reinforcement Details

Wall specimen	"a"	"b"	"c"	"d"
RW-A20-P10-S38	4#4	4#4	6D6a @140 mm (@5.5in.)	D6b @140 mm (@5.5in.)
RW-A20-P10-S63	4#6	4#6	5#3 @152 mm (@6in.)	#3 @152 mm (@6in.)
RW-A15-P10-S51	4#4	4#4	7D6a @114 mm (@4.5in.)	D6b @114 mm (@4.5in.)
RW-A15-P10-S78	4#6	4#5	6#3 @127 mm (@5in.)	#3 @127 mm (@5in.)
RW-A15-P2.5-S64	4#6	4#5	5#3 @152 mm (@6in.)	#3 @152 mm (@6in.)

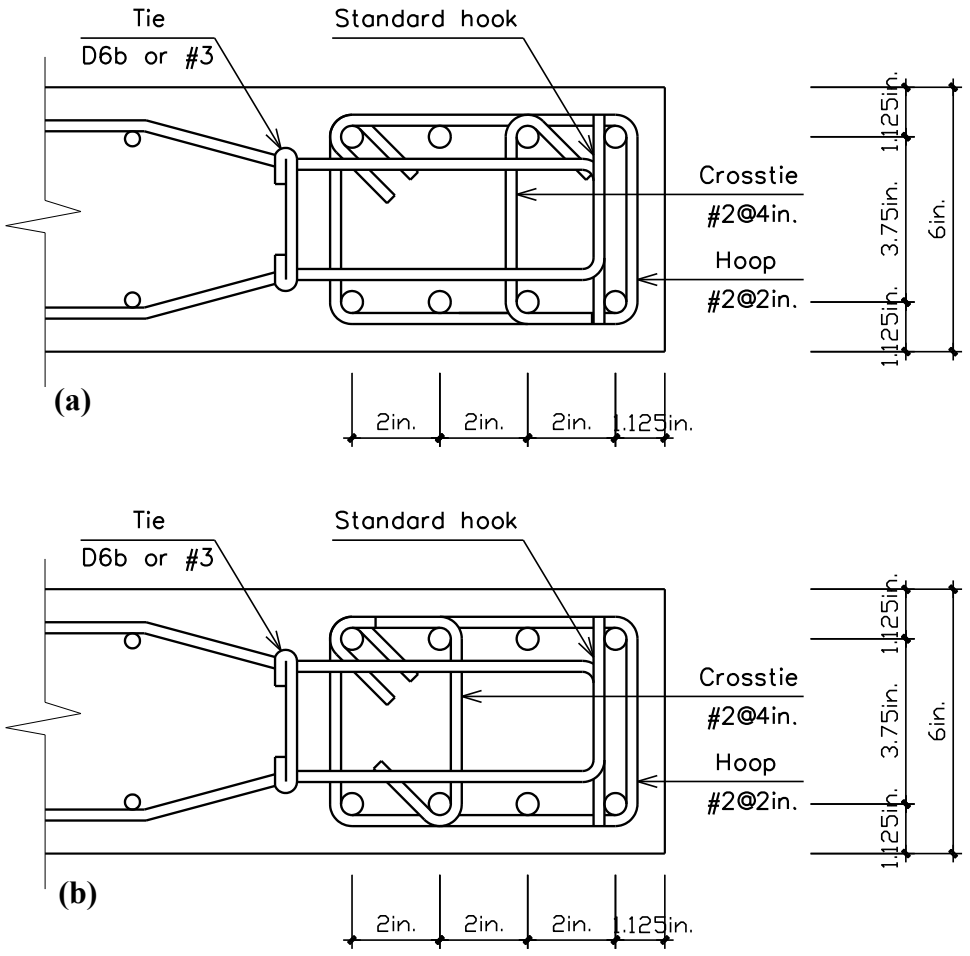

Figure 5-2 Wall Boundary Zone Detailing, Detail A (Tran 2012)

Based on the displacement-based detailing assessment of ACI 318-11 S21.9.6, all specimens needed special boundary elements (Figure 5-1, Detail A); therefore, boundary transverse reinforcement was designed and detailed to satisfy ACI 318-11 S21.9.6.4 requirements for special boundary element. Figure 5-2 shows a typical detail of the special boundary elements used in the test specimens. A hoop and a single crosstie (both #2 bars, d_b = 0.25 in. = 6.35 mm) were used at each level of all wall special boundary elements; the crosstie was alternated between pairs of boundary longitudinal reinforcement over the height of the special boundary

element as shown in Figure 5-2(a) and (b). Each crosstie ends with a 90-degree hook at one side and with a 135-degree hook at the other side, with the 90- and 135-degree hooks alternated (end-to-end), as required ACI 318-11 Section 21.6.4.2 (Figure 5-2).

5.1.2. Test Setup

The cantilever wall specimens were tested in an upright position. The reversed cyclic lateral load is applied by a 200 kips (890 kN) hydraulic actuator at the top of the wall specimens, while the vertical load was applied to the specimens using two 100 ton (224 kip) hollow cylinders. The lateral load was applied using a friction mechanism to ensure the lateral load was distributed across the top of the specimen. Testing was continued until the loss of lateral and axial load capacity was observed. A schematic of test setup is presented in Figure 5-3.

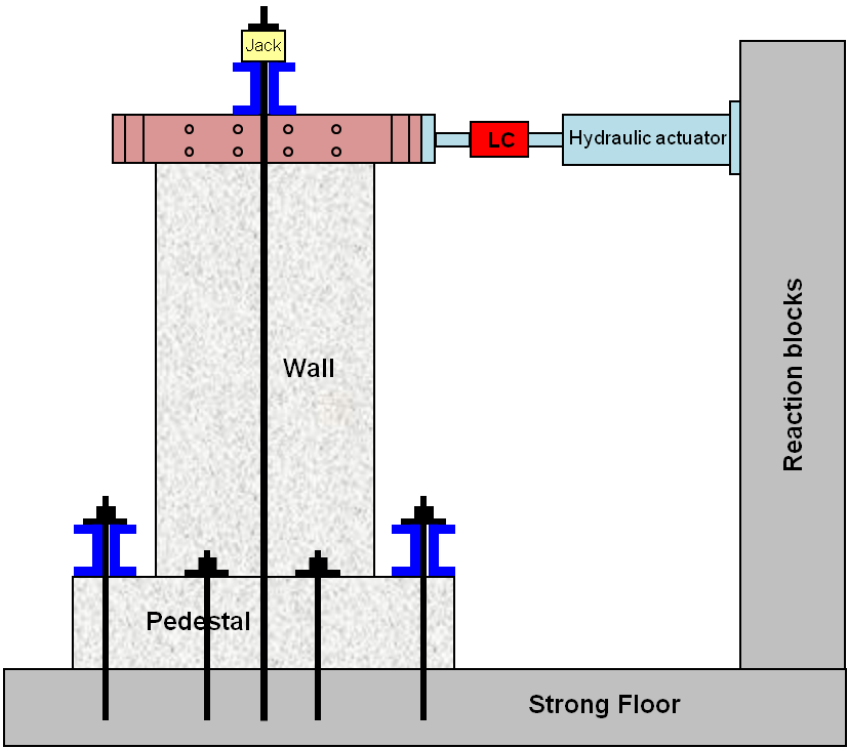

Figure 5-3 Scheme of Test Setup (Tran, 2012)

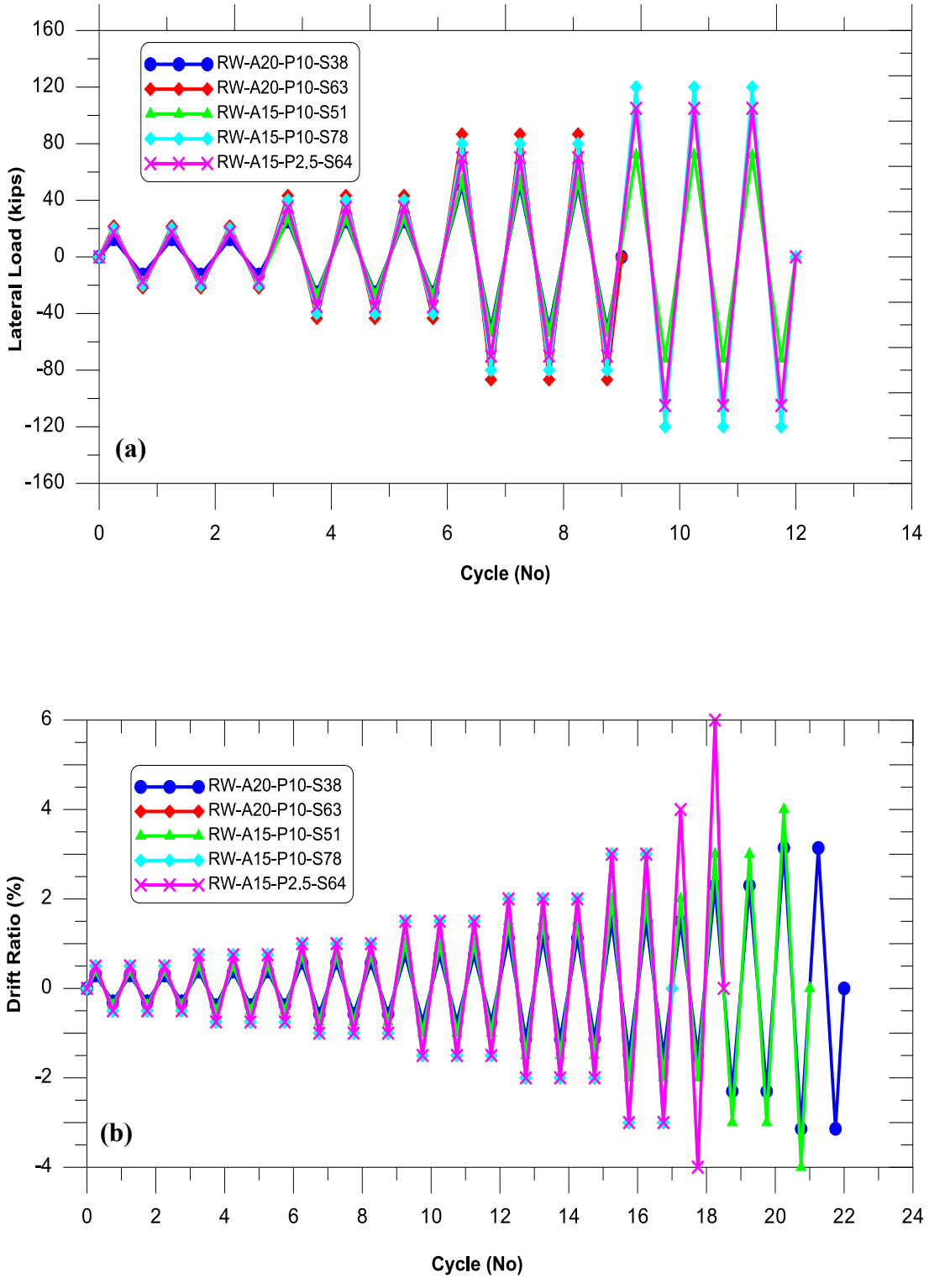

Figure 5-4 Loading Protocols (Tran, 2012): (a) Force Controlled, (b) Drift Controlled

The testing protocol consisted of load-controlled cycles followed by displacement-controlled cycles. Load-controlled cycles generally consisted of cycles at 1/8, 1/4, 1/2, and 3/4 of the expected yield force (Figure 5-4(a)), after which the testing protocol was switched to displacement-controlled cycles for the rest of the test. Displacement-controlled cycles were typically performed at lateral drift ratios of 0.5%, 0.75%, 1.0%, 1.5%, 2.0%, 3.0%, and 4.0% (Figure 5-4(b)), with slight differences in the applied drift history for drift levels beyond 3.0%. Force and drift controlled loading protocols for all five tested RC wall specimens are presented on Figure 5-4.

5.1.3. Instrumentation and Data Acquisition

Wall specimens were heavily instrumented to obtain detailed response data. Linear Variable Differential Transformers (LVDTs) were used to obtain data for calculation of wall foundation sliding and uplift, lateral wall displacements at various height levels (including flexural, shear, and sliding shear components), as well as wall average concrete strains over specified gauge lengths. Figure 5-5 and Figure 5-6 show the sensor configuration used for specimens #1 and #2, and #3, #4, and #5, respectively.

Reinforcement strains were measured at numerous locations using 30 strain gauges affixed to boundary longitudinal and transverse reinforcement, and web vertical and horizontal reinforcement, concentrated over a height of approximately $l_w/2$ from the wall-foundation block interface. Figure 5-7 describes the strain gauge layout on boundary transverse reinforcement (hoops and cross-ties) for the five tested wall specimens, whereas Figure 5-8 shows the strain

gauge layout on boundary longitudinal reinforcement and web vertical and horizontal reinforcement.

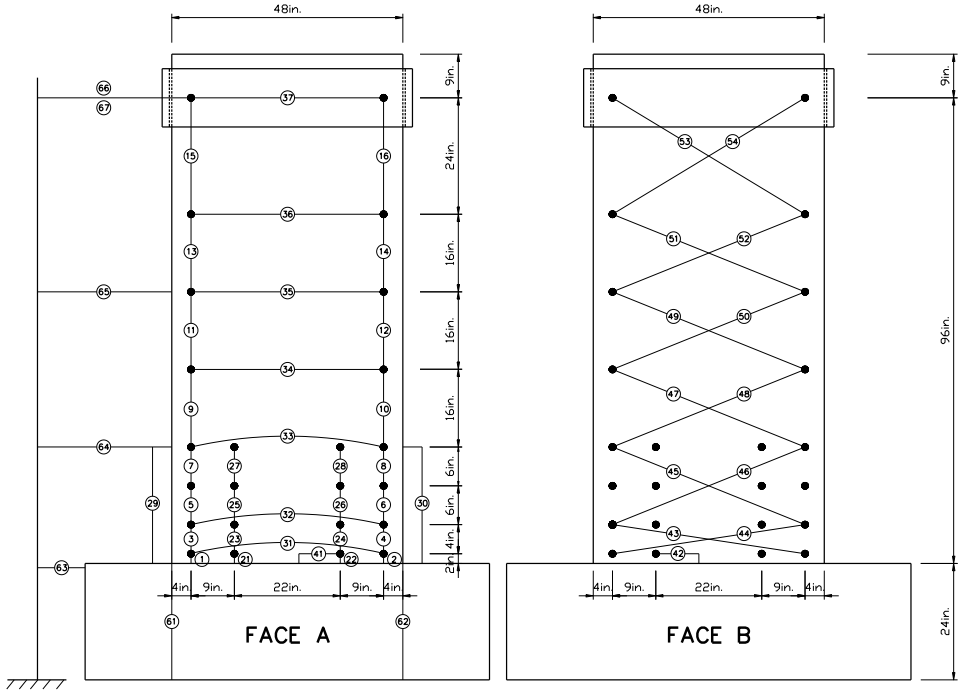

Figure 5-5 Sensor Configuration for Specimens #1 and #2 (Tran, 2012)

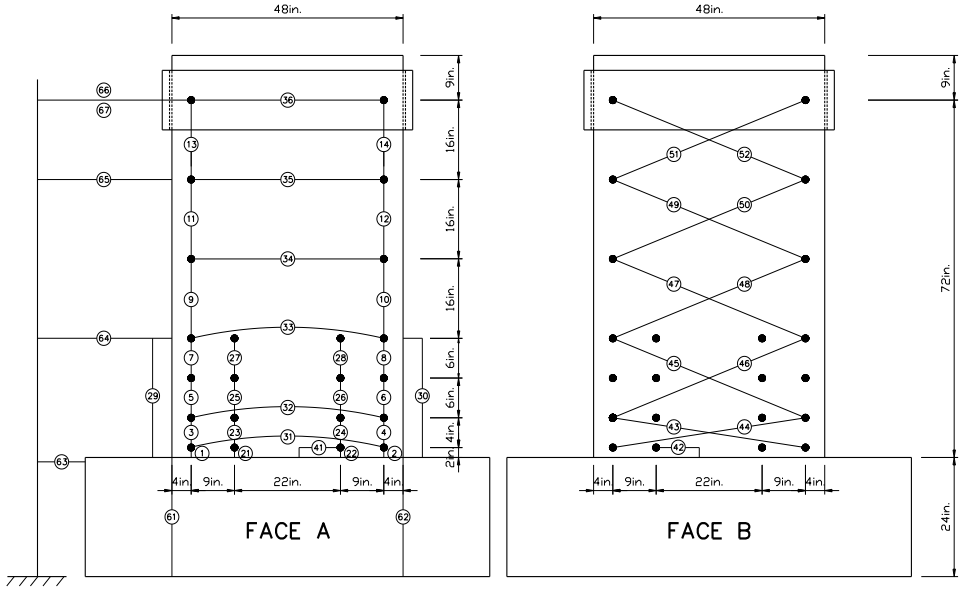

Figure 5-6 Sensor Configuration for Specimens #3, #4, and #5 (Tran, 2012)

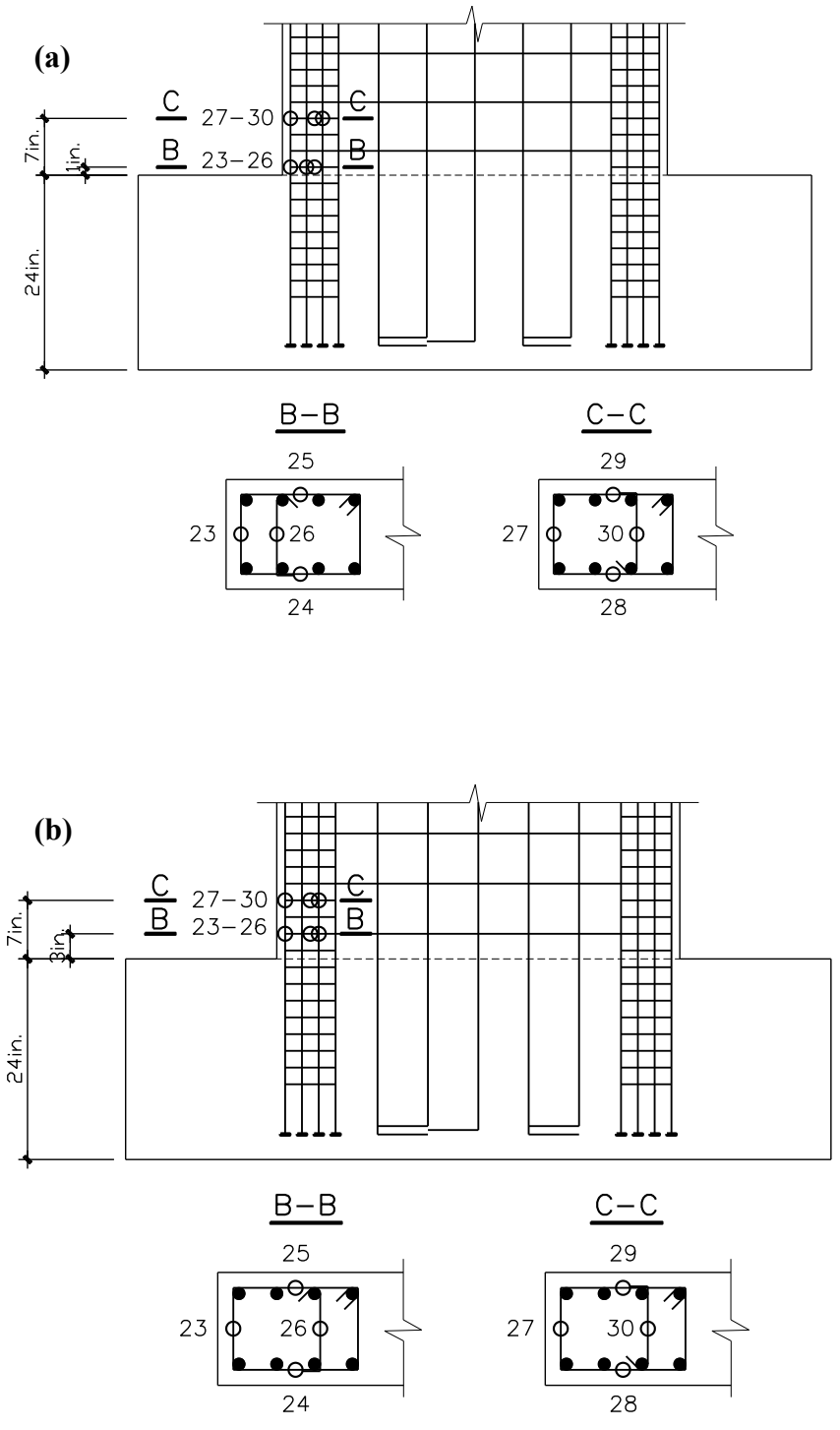

Figure 5-7 Strain Gage Location in Boundary Transverse Reinforcement: (a) Tests 1 and 3, (b) Tests 2, 4, and 5 (Tran, 2012)

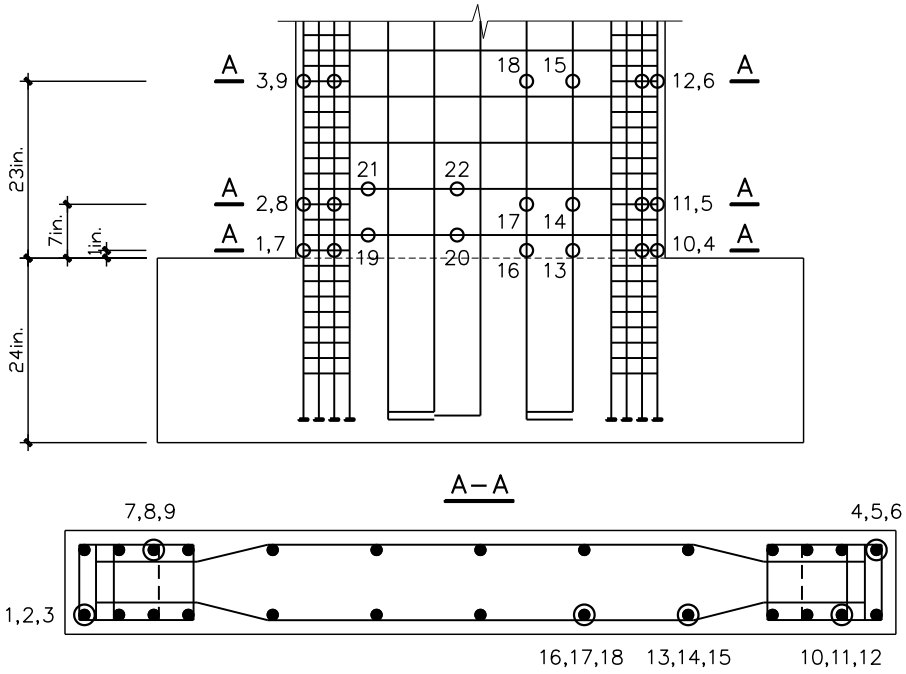

Figure 5-8 Strain Gage Location in Vertical and Horizontal Reinforcement (Tran, 2012)

5.1.4. Material properties

The concrete mix for the test specimens was designed to have a specified concrete compressive strength of 5,000 psi (34.5 MPa). For each wall specimen, three 15.2× 30.5 cm (6 × 12 in.) concrete cylinders were tested at the UCLA material testing laboratory at/or closed to the test day. Figure 5-9 plots the stress-strain relationships obtained from cylinder tests for all five RC wall specimens along with the average values of peak concrete stress (f'_c) and corresponding concrete strain (ε'_c); stress-strain relationships are presented only up to peak concrete stress because the post-peak behavior was not recorded properly due to instability of concrete test cylinders after the initiation of concrete strength degradation. Average compressive strength of concrete and strain at the peak stress at test date, as well as wall test date and cylinder test date for all five specimens are summarized in Table 5-3.

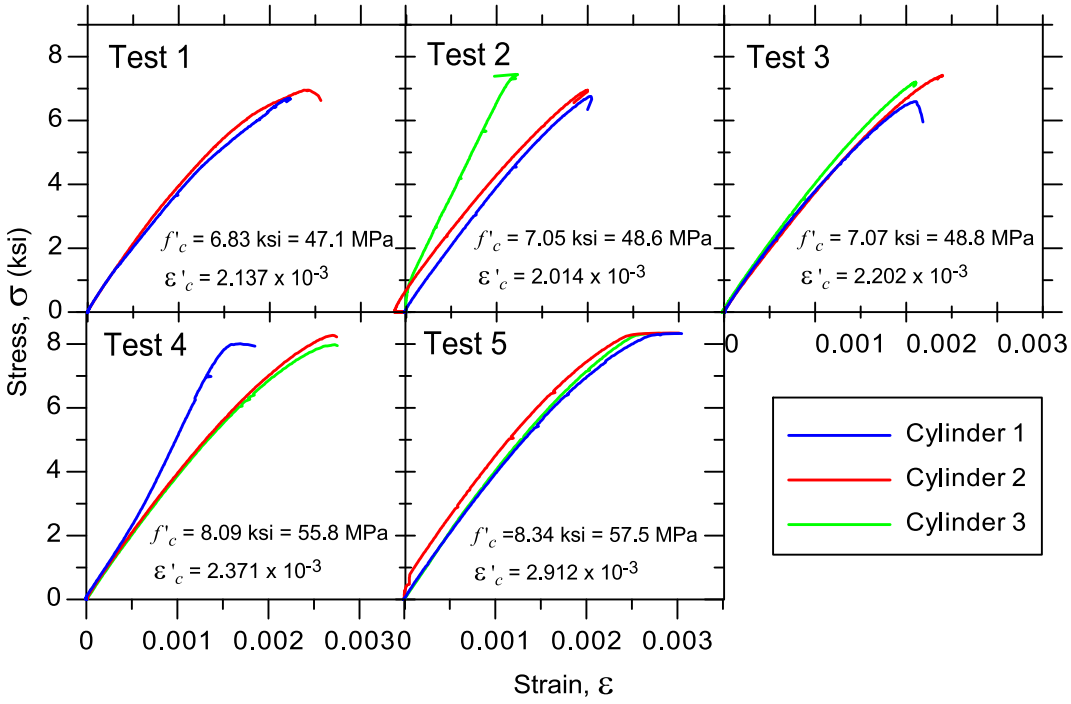

Figure 5-9 Concrete Cylinder Stress-Strain Relationships for Tests 1 to 5

Table 5-3 Average Compressive Strength of Concrete at the Day of Testing (Tran, 2012)

No.	Specimen	Wall test date	Cylinder test date	Cylinder maturity days	Compressive strength ksi (MPa)	Strain at peak stress ($x10^3$)
Test 1	RW-A20-P10-S38	07/11/2011 to 07/12/2011	07/06/2011	216	6.83 (47.1)	2.317
Test 2	RW-A20-P10-S64	07/27/2011 to 08/04/2011	08/10/2011	232	7.05 (48.6)	2.014
Test 3	RW-A15-P10-S51	08/19/2011	08/23/2011	255	7.07 (48.8)	2.202
Test 4	RW-A15-P10-S78	10/07/2011	10/10/2011	304	8.09 (55.8)	2.371
Test 5	RW-A15-P2.5-S65	10/24/2011	10/26/2011	321	8.34 (57.5)	2.912

Boundary longitudinal reinforcement for each wall specimen consisted of eight, A706 Grade 60 (yield strength of 414 MPa or 60 ksi), vertical bars (either #4, #5, or #6) that were continuous over the wall height and with heads at both ends. Headed bars were used to help avoid congestion of reinforcement and to reduce anchorage lengths at the top of specimens. Vertical and horizontal web reinforcement for Tests #2, #4, and #5 were Grade 60 deformed #3 bars, except deformed D6 (6 mm - diameter) bars are used for vertical and horizontal web reinforcement for Tests #1 and #3. Smooth Grade 40 #2 bars (yield strength of 310 MPa or 45 ksi) were used for transverse reinforcement in the boundary regions, i,e., hoops and crossties. At least three rebar coupons with the length of 610 mm (24 in.) were tested in tension for D6, #2, and #3 bars to obtain stress-strain relationships shown on Figure 5-10. For headed bars, consisting of #4, #5, and #6 bars, material strengths were specified based on mill certificates (without testing) because no extra bars were leftover to conduct material testing. Yield and ultimate strengths, along with diameter and cross-sectional areas, of all reinforcement used in wall specimens are summarized in Table 5-4 and Figure 5-10.

Table 5-4 Yield and ultimate strengths of reinforcement

Bar	#2	#3	#4	#5	#6	D6a	D6b
Diameter, in. (mm)	0.25 (6.4)	0.375 (9.5)	0.5 (12.7)	0.625 (15.9)	0.75 (19.1)	0.236 (6.0)	0.236 (6.0)
Cross-sectional area, $in.^2$ (mm^2)	0.049 (31.7)	0.11 (71.3)	0.20 (126.7)	0.31 (197.9)	0.44 (285.0)	0.044 (28.3)	0.044 (28.3)
Yield strength, ksi (MPa)	61.4 (423)	64.2 (443)	68.4 (472)	68.7 (474)	69.2 (477)	65.3 (450)	74.9 (516)
Ultimate strength, ksi (MPa)	71.3 (492)	102.6 (707)	88.9 (613)	89.9 (620)	92.4 (637)	95.9 (661)	84.2 (580)

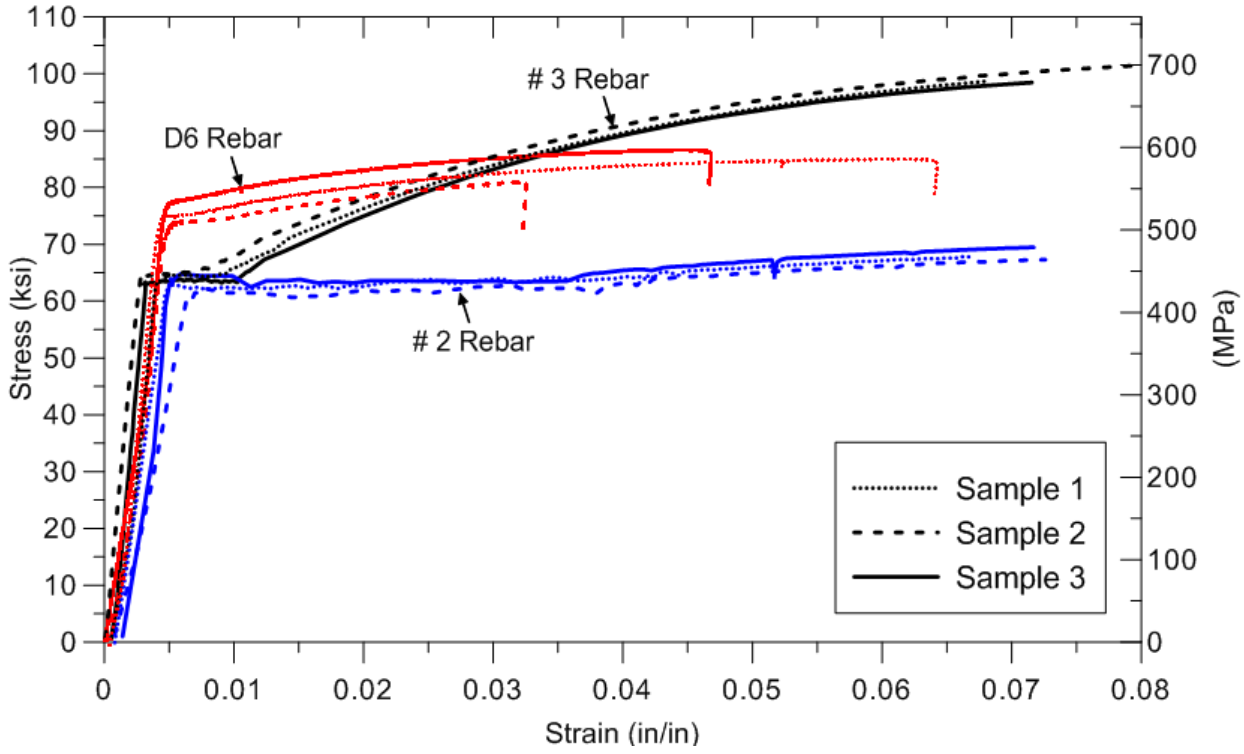

Figure 5-10 Experimental Stress-Strain Relationships for Reinforcement

5.2. Calibration of Wall Specimens

This section describes calibration of analytical models used to predict experimentally observed behavior of five RC wall specimens described in the preceding sections. Model calibration is performed with respect to specimen geometry and material properties, as well as the parameters of shear resisting mechanisms of the constitutive RC panel model incorporated in the formulation of SFI-MVLEM.

5.2.1. Calibration for Model Geometry

As mentioned earlier, the analytical model of a RC wall consists of *n* SFI-MVLEM elements stacked on top of each other. The heights and number of model elements over the height, i.e. the

vertical model discretization, was selected in this study to agree with locations of sensors installed on the wall specimens to measure wall responses (i.e. locations of LVDTs shown in Figure 5-5 and Figure 5-6). Use of this discretization allows for direct comparisons between analytically predicted and experimentally measured responses at various locations over the wall height. Vertical discretizations of analytical models of wall specimens with aspect ratios 2.0 and 1.5, along with locations of LVDTs installed in "X" configuration on one side of the wall specimens, are presented in Figure 5-11.

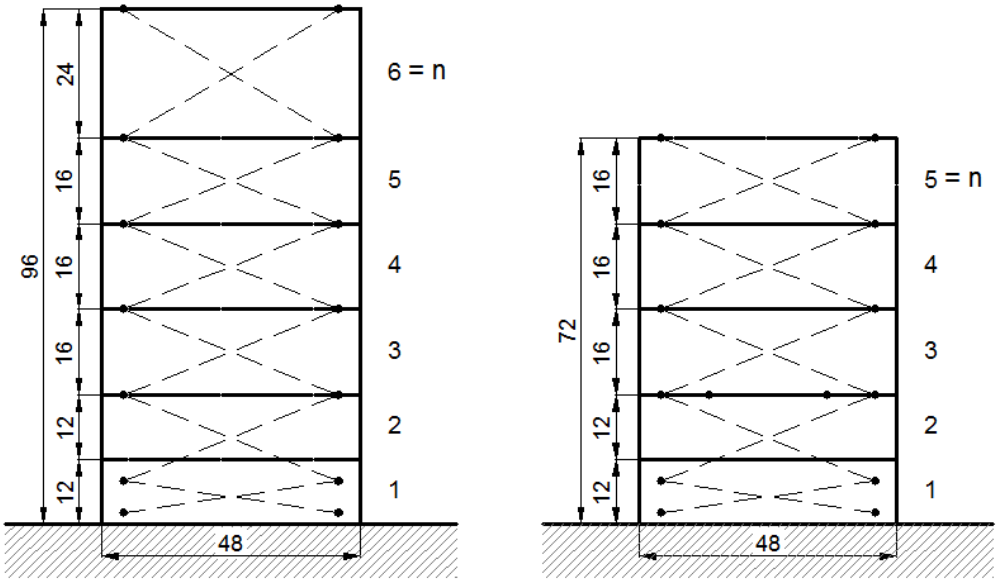

Figure 5-11 Discretization of Wall Models over the Wall Height and Locations of LVDTs

Discretization of wall models in the horizontal direction was based on the distribution of vertical boundary and web reinforcement within the wall cross-section (e.g., wall). All five RC wall specimens had the same cross-section dimensions (l_w = 1.22 m = 48 in, t_w = 0.152 m = 6 in), the same special boundary elements dimensions at wall edges, and uniformly distributed web reinforcement; therefore, it was convenient to use five RC panel elements along the wall length

(*m*=5) to describe the cross-section (Figure 5-12). Two external RC panels were used to represent the behavior of the boundary elements (both confined and unconfined cover concrete and concentrated boundary longitudinal reinforcement) and three inner panel elements were used to model the behavior of wall web (unconfined concrete and uniformly distributed web reinforcement).

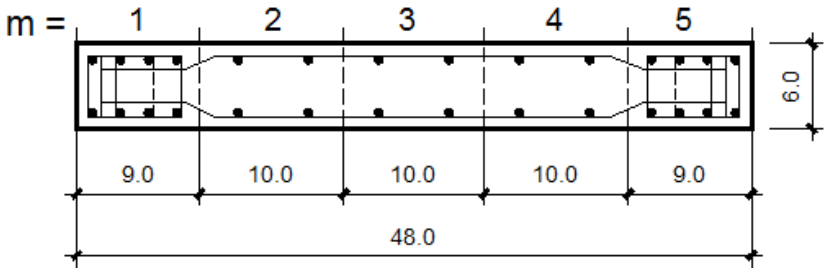

(a) Tests 1 and 4

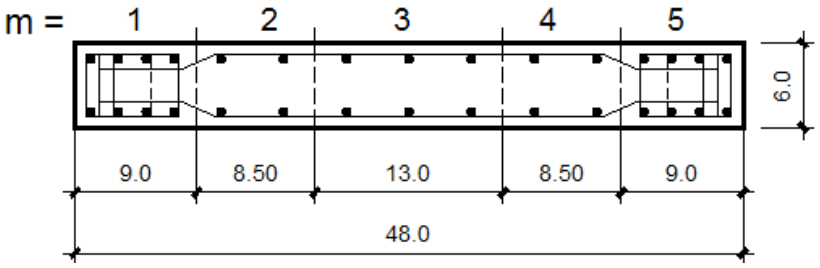

(b) Tests 3

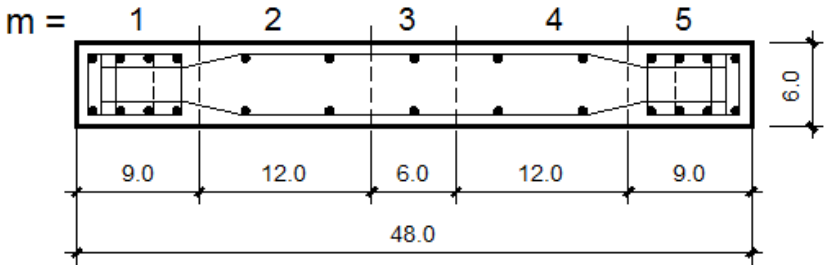

(c) Tests 2 and 5

Figure 5-12 Model Discretization and Tributary Area Assignment

Typical discretization in both vertical and horizontal directions of wall models used to predict the nonlinear behavior of RC wall specimens with aspect ratios of 2.0 and 1.5 is displayed in Figure 5-13. As shown in Figure 5-13, two SFI-MVLEs were used along the height of the region where nonlinear deformations are expected to be concentrated (so-called plastic hinge region), with height of approximately 24 in. from the base of the wall for all specimens (i.e., $h_w/4$ and $h_w/3$ for specimens with aspect ratio of 2.0 and 1.5, respectively) according to information reported by Tran (2012).

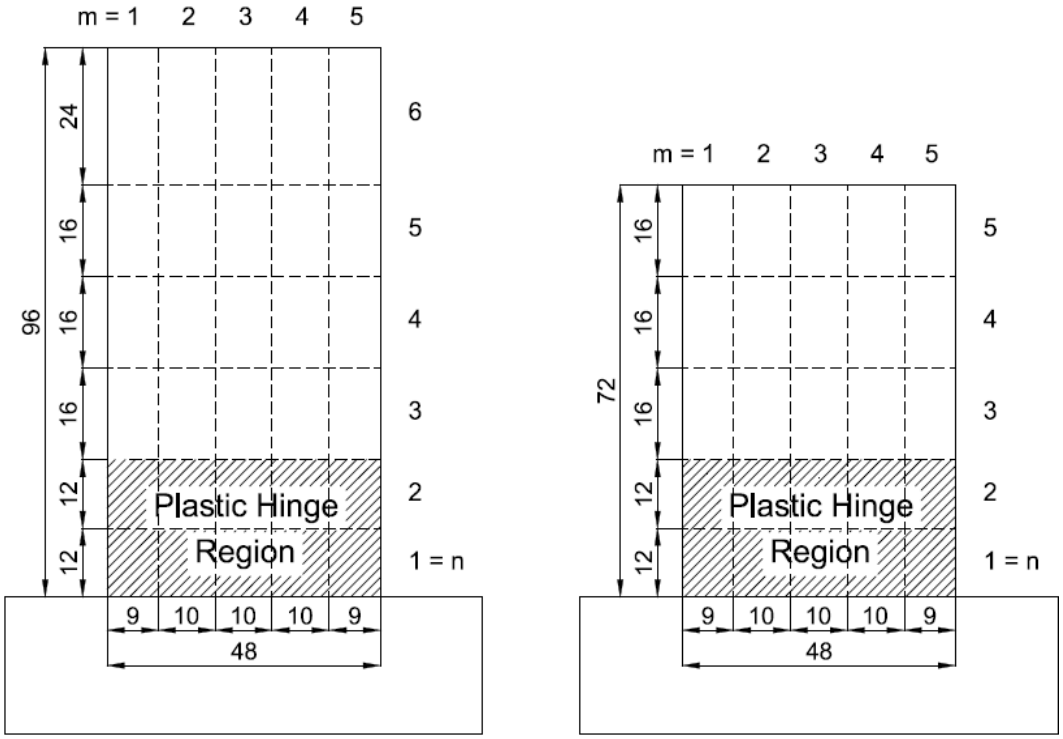

(a) Aspect Ratio 2.0 (b) Aspect Ratio 1.5

Figure 5-13 Adopted Discretization of Wall Models

5.2.2. Calibration for Constitutive Material Parameters

5.2.2.1. Steel Stress-Strain Relationships

The constitutive behavior for reinforcing steel is described by the Menegotto and Pinto (1977) model (extended by Filippou et al., 1983) whose typical stress-strain relationship is illustrated on Figure 5-14.

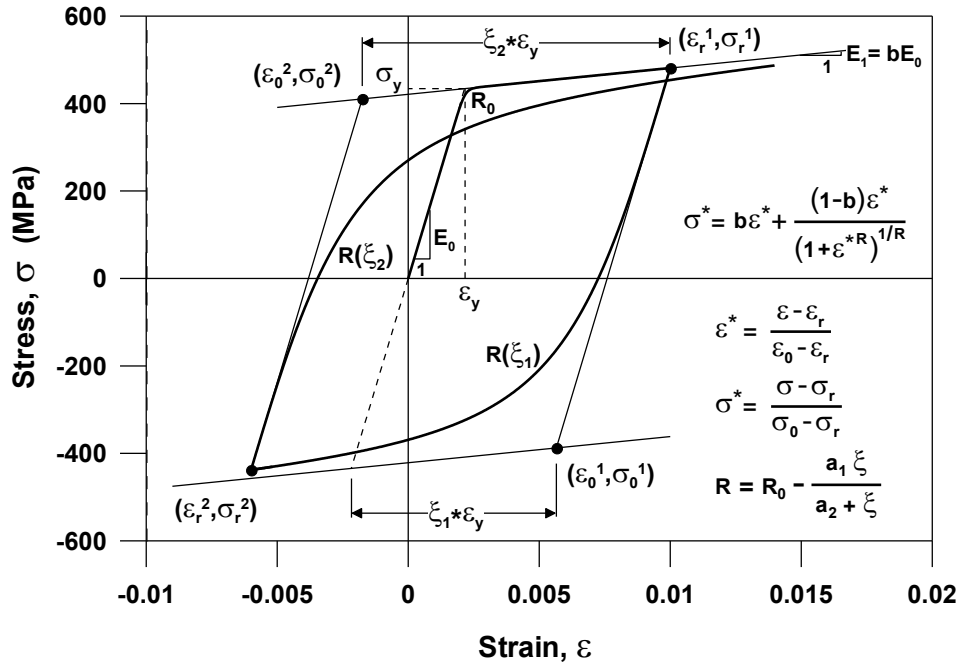

Figure 5-14 Constitutive Model for Reinforcing Steel and Associated Parameters

The analytical model was calibrated to reasonably represent the experimentally observed properties of the longitudinal and horizontal reinforcement used in the experimental study. An elastic modulus of E_0 = 200 GPa (29000 ksi) was assigned to all reinforcing bars used in the test specimens. Calibration of the steel stress-strain model for D6 (d_b = 6mm; 0.24 in), #2 (d_b = 6.35 mm; 0.25 in) and #3 (d_b = 9.53 mm; 0.375 in) reinforcing bars was based on selecting values of

yield strength (σ_y) and strain hardening ratio (b) to match experimental results obtained from monotonic stress-strain tensile tests on 61 cm (24 in.) long rebar samples. Calibration of stress-strain relationships for #4 (d_b = 12.25 mm; 0.50 in), #5 (d_b = 15.31 mm; 0.625 in), and #6 (d_b = 18.37 mm; 0.75 in) reinforcing bars was based on selecting values of tensile yielding strength (σ_y) and ultimate strength (σ_u) to match values specified in mill certificates because no additional coupons were available to use for tensile tests. The yield strength and strain-hardening parameters for the bare bars in tension were modified according to the empirical relations proposed by Belarbi and Hsu (1994) to include the effect of tension stiffening on steel bars embedded in concrete, as described in Section 3.4.4.

Figure 5-15 shows comparisons of experimental stress-strain relationships for steel reinforcement obtained from monotonic tensile tests on D6, #2 and #3 bars (the average of 3 samples) against the analytical stress-strain relationships for these bars after calibration with tensile tests, as well as analytical stress-strain laws used for #4, #5, and #6 bars calibrated using information provided in mill certificates. Corresponding parameters of the stress-strain relationships for reinforcing steel, including yield stress (σ_y), Young's modulus (E_s), and strain hardening ratio (b) are provided in Table 5-5. The stress-strain relationships of reinforcing bars in tension were used to represent the constitutive behavior of reinforcing bars in compression; therefore, the steel stress-strain law for reinforcing steel does not account for reduction of stress due to rebar buckling in compression.

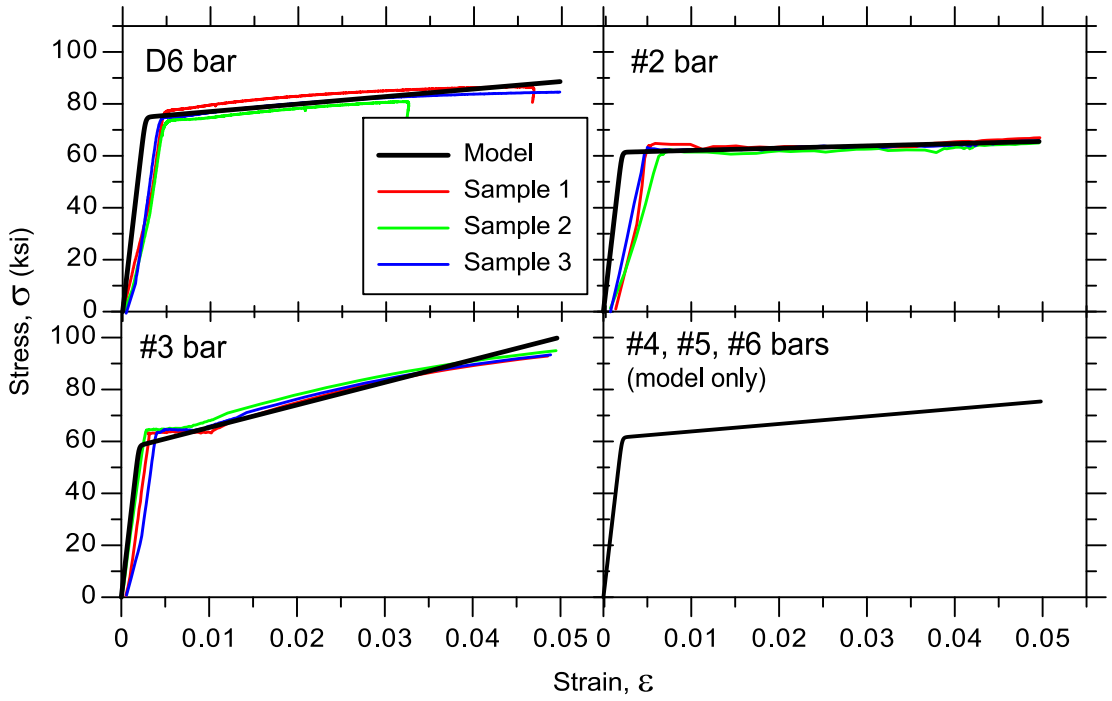

Figure 5-15 Calibration of Stress-Strain Relationships of Reinforcing Bars

Table 5-5 Calibrated Parameters of Steel Material Law

Parameter	Reinforcement bar					
	D6a	#2	#3	#4	#5	#6
f_y, MPa (ksi)	450 (65.3)	423 (61.4)	443 (64.2)	471 (68.4)	474 (68.7)	477 (69.2)
E_0, GPa (ksi $\times 10^3$)	200 (290)	200 (290)	200 (290)	200 (290)	200 (290)	200 (290)
b	0.02	0.003	0.02	0.01	0.01	0.01

Calibration of parameters R_0, a_1 and a_2 (accounting for the cyclic degradation of the curvature coefficient R and the Bauschinger effect) requires cyclic test results, which are not available. The following values of these parameters, suggested by Menegotto and Pinto (1973), are used in this

study to describe cyclic properties of steel constitutive model: R_0, a_1, a_2 = 20, 18.5, 0.15. Additional information on calibration of these parameters is presented by Orakcal (2004).

5.2.2.2. Concrete Stress-Strain Relationships

Monotonic envelope relations for the implemented concrete stress-strain relations in compression and tension allow control on the shape of both the ascending and descending (i.e., pre-peak and post-peak) branches of the stress-strain behavior. The curves can be calibrated for selected values of peak stress (f'_c), strain at peak stress (ε'_c), elastic modulus (E_c), strain at zero concrete stress (ε_r), and also via the parameter *r* defining the shape of the envelope curve, allowing for model refinement. The envelope curve used in the analytical model for concrete in compression (Figure 5-16) was calibrated for unconfined concrete using stress-strain relationships obtained from the monotonic compression tests conducted at time of testing on standard 152.4 mm x 304.8 mm (6 in. × 12 in.) cylinder specimens of the concrete used in the construction of the walls. Calibrated monotonic stress-strain relationships for unconfined concrete against results from test cylinders used for wall specimens in Tests 1 to 5 are plotted on Figure 5-17. The compressive strength value (f'_c) and the strain at peak compressive stress (ε'_c) were assigned in accordance with the average compressive strength from test cylinders for each test specimen (Table 5-3). The initial tangent modulus (elastic modulus) of concrete was determined as $E_c = 8200 f'_c \; MPa$, as proposed by Chang and Mander (1994).

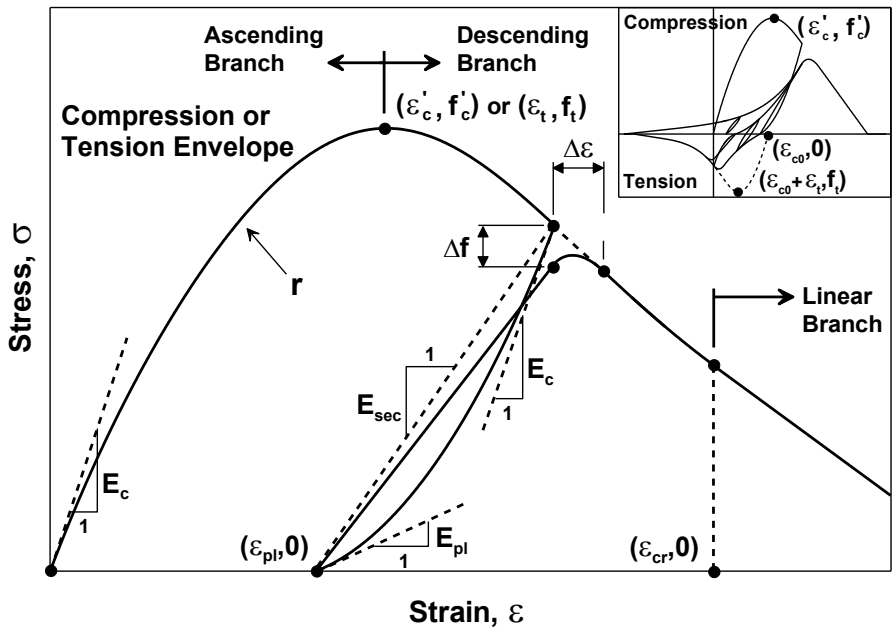

Figure 5-16 Constitutive Model for Concrete and Associated Parameters

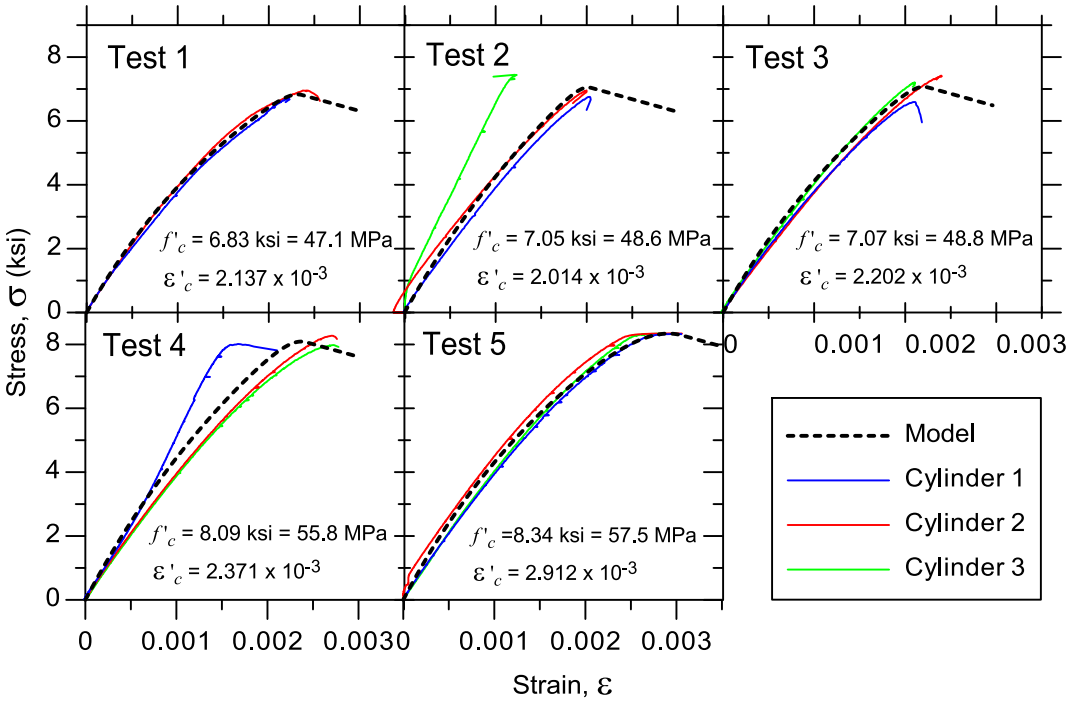

Figure 5-17 Calibration of Concrete Envelop Curve in Compression

The compression envelope used in the analytical model to represent the behavior of confined concrete, located in confined wall boundary regions of wall models, was calibrated via empirical relations proposed by Mander et al. (1988) for the peak compressive stress (f'_{cc}) and the strain at peak compressive stress (ε'_{cc}) based on the area, configuration, spacing, and yield stress of the transverse reinforcement in the confined boundary regions of walls.

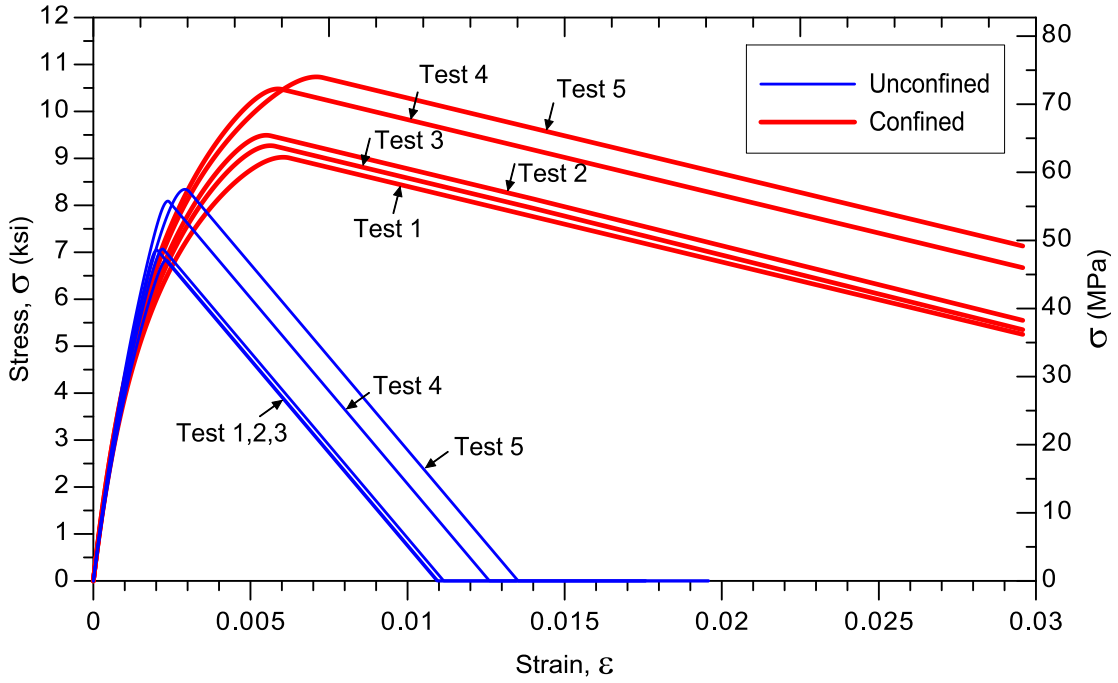

Figure 5-18 Calibrated Concrete Material Stress-Strain Relationships in Compression

The post-peak behavior of the stress-strain relationship of both confined and unconfined concrete was calibrated by the use of parameter ε_{cr}, which defines the strain where the descending (linear) branch of the monotonic concrete stress-strain relation reaches zero stress, such that the post-peak slope of the concrete stress-strain model agrees with the post-peak slope of the Saatcioglu and Razvi (1992) model for confined and unconfined concrete. Figure 5-18 shows the

concrete stress-strain relations used to describe the behavior of confined and unconfined concrete in compression for Tests 1 to 5, whereas calibrated parameters of monotonic (envelope) stress-strain material models for confined and unconfined concrete in compression are presented in Table 5-6.

Table 5-6 Parameters of confined and unconfined concrete in compression

Material	Parameter	RW-A20-P10-S38		RW-A20-P10-S63		RW-A15-P10-S51		RW-A15-P10-S78		RW-A15-P2.5-S64	
		Boundary (confined)	Web (unconf.)	Boundary (confined)	Web (unconf.)	Boundary (confined)	Web (unconf.)	Boundary (confined)	Web (unconf.)	Boundary (confined)	Web (unconf.)
Concrete in compressoin	f'_c, MPa (ksi)	62.2 (9.02)	47.1 (6.83)	65.4 (9.49)	48.6 (7.05)	63.9 (9.27)	48.7 (7.07)	72.2 (10.48)	55.8 (8.09)	74.0 (10.74)	57.5 (8.34)
	ε'_c	0.006	0.00232	0.0055	0.00201	0.0056	0.00220	0.0059	0.00237	0.0071	0.00291
	E_c, GPa (ksi)	38.8 (5629)	34.9 (5071)	39.5 (5737)	35.4 (5131)	39.2 (5686)	35.4 (5137)	41.0 (5954)	37.2 (5403)	41.4 (6008)	37.7 (5465)
	ε_r	0.062	0.0111	0.063	0.0112	0.062	0.0113	0.071	0.0126	0.074	0.0135
	R	10.2	20	10.8	20	10.5	20	12.2	15	12.4	9

As suggested by Belarbi and Hsu (1994), the concrete strength in tension for each specimen was determined using concrete compressive strength as:

$$f_t = 0.31\sqrt{f'_c} \text{ (MPa)} \tag{5-1}$$

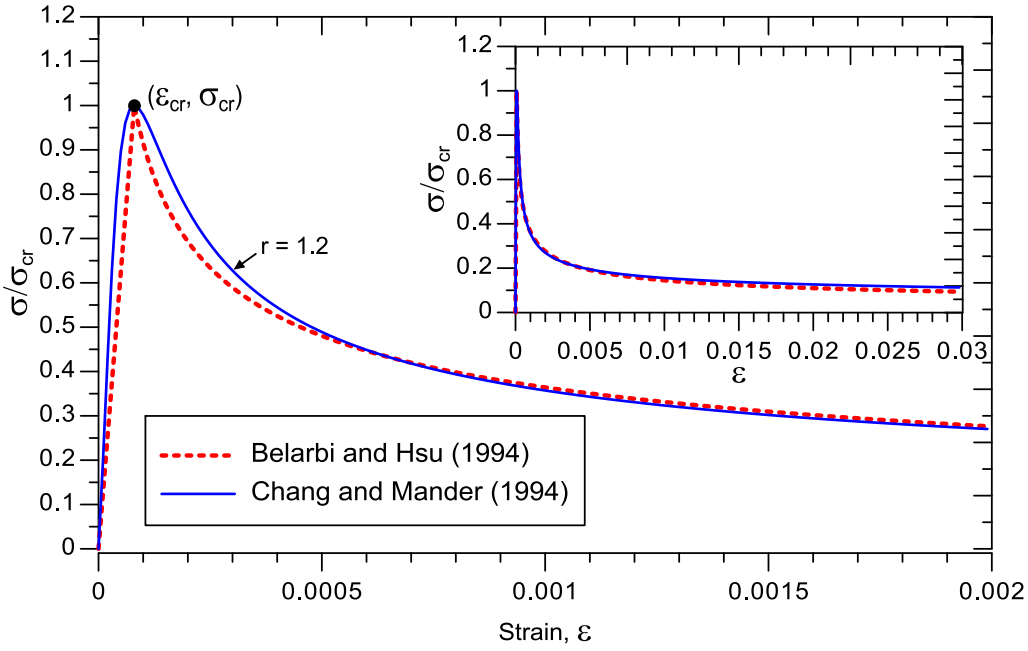

Figure 5-19 Calibration of Stress-Strain Relationship for Concrete in Tension

Table 5-7 Parameters of confined and unconfined concrete in tension

Material	Parameter	RW-A20-P10-S38	RW-A20-P10-S63	RW-A15-P10-S51	RW-A15-P10-S78	RW-A15-P2.5-S64
Concrete in tension	f'_c, MPa (ksi)	47.1 (6.83)	48.6 (7.05)	48.7 (7.07)	55.8 (8.09)	57.5 (8.34)
	f_t, MPa (ksi)	2.1 (0.3085)	2.2 (0.3135)	2.2 (0.3139)	2.3 (0.3358)	2.3 (0.3409)
	ε_t	0.00008	0.00008	0.00008	0.00008	0.00008
	E_c, MPa (ksi)	34.9 (5071)	35.4 (5131)	35.4 (5137)	37.2 (5403)	37.7 (5465)
	ε_{cr}	∞	∞	∞	∞	∞
	r	1.2	1.2	1.2	1.2	1.2

A value of 0.00008 was selected for the strain (ε_t) at peak monotonic tensile stress for all specimens, whereas an *r*-value of 1.2 was used to define the shape of the monotonic tension

envelope so that it reasonably agreed with the average post-crack stress-strain relation proposed by Belarbi and Hsu (1994). Resulting stress-strain relations are plotted in Figure 5-19 and the parameters used to model the constitutive behavior for concrete in tension are presented in Table 5-7.

5.2.3. Calibration of Shear Resisting Mechanism of RC Panel Model

As described in Section 3.3.2, the shear resisting mechanism along inclined cracks of implemented RC panel model consists of a friction-based shear aggregate interlock model (Figure 5-20(a)), and a linear elastic model representing dowel action of reinforcing bars (Figure 5-20(b)). Two parameters associated with the shear resisting mechanisms require calibration: (1) friction coefficient of shear aggregate interlock model η, and (2) stiffness parameter of dowel action α. Results of the calibration studies, which were accomplished by comparing analytical and experimental results for these two parameters, are presented in this section.

Calibration studies were performed by comparing analytically predicted lateral-load-versus-wall-top-displacement relations obtained using different values of parameters η and α with experimentally measured load-deformation behavior; in specific, the lateral load (P_{lat}) corresponding to peak values of applied lateral drift at the top of the wall, as well the area of hysteretic loops of the lateral-load-versus-wall-top-displacement relationship (A_{hys}) were used as criteria for model calibration. For calibration purposes only, in order to reduce computational effort, one loading cycle per each drift level was applied in the analysis, as oppose to the multiple loading cycles at each drift level that were performed in the experiment. Analytical predictions of

P_{lat} and A_{hys} are compared with experimental values corresponding to the first loading cycle for each of the applied drift levels conducted in the tests.

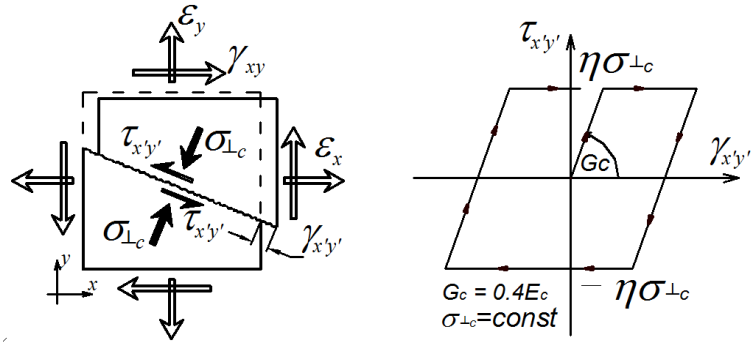

(a) Shear Aggregate Interlock Model

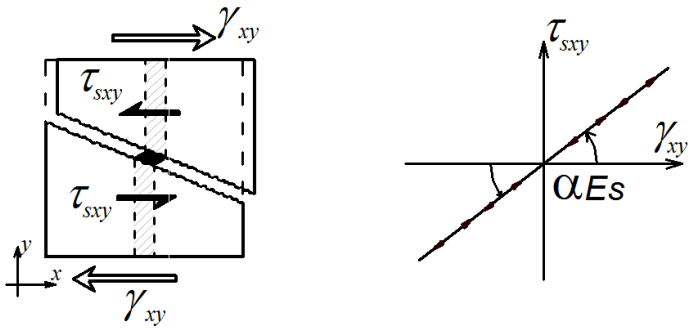

(b) Dowel Action Model

Figure 5-20 Shear Resisting Mechanisms of RC Panel Model with Parameters

5.2.3.1.Criteria for Model Calibrations

The first criterion used to assess the accuracy of analytical predictions was the prediction of the lateral load corresponding to peak applied lateral drift, for each level of applied lateral drift. If vectors $\{P\}_{\text{exp}}$ and $\{P\}_{\text{mod}}^{\alpha,\eta}$ consist of the experimentally measured and analytically predicted

values (for a given combination of model parameters α and η) of lateral forces at peak applied drift levels, respectively, then analysis error for the i-th applied peak drift level is calculated as:

$$\{e_P\}_i^{\alpha,\eta} = \left| \frac{P_{\text{exp},i} - P_{\text{mod},i}^{\alpha,\eta}}{P_{\text{exp},i}} \right| \cdot 100 \quad (\%) \tag{5-3}$$

Total analytical error, in terms of the lateral load at peak drift levels, was then determined by applying the *L2* error norm to the vector of relative lateral force errors $\{e_P\}_i^{\alpha,\eta}$ as:

$$e_P^{\alpha,\eta} = \sqrt{\sum_{i=1}^{n} \left(\{e_P\}_i^{\alpha,\eta} \right)^2} \tag{5-4}$$

where n is the number of drift cycles at which analytical and experimental results are compared.

The second criterion used to assess the accuracy of analytical predictions was the area of hysteretic loops of the lateral load versus total top displacement relationship. If A_{exp} and $A_{\text{mod}}^{\alpha,\eta}$ are total areas of hysteretic loops (of all applied drift levels) obtained experimentally and analytically, respectively, the error of predicted area of hysteretic loops for the given parameters α and η is calculated as:

$$e_A^{\alpha,\eta} = \left| \frac{A_{\text{exp}} - A_{\text{mod}}^{\alpha,\eta}}{A_{\text{exp}}} \right| \cdot 100 \ (\%) \tag{5-5}$$

The calibrations of shear friction coefficient η and dowel stiffness parameter α are performed based on analytical errors $e_P^{\alpha,\eta}$ and $e_A^{\alpha,\eta}$ obtained for a range of these parameters.

5.2.3.2. Calibration of Parameters η and α

Results presented in this section provide comparisons of experimental and analytical load-deformation responses obtained for a range of parameters η (shear friction coefficient) and α (dowel stiffness parameter) for specimen RW-A15-P10-S78 (Tran and Wallace, 2012). As discussed in Section 4.5.1.2, the analytical results are not very sensitive to the value of friction coefficient η; therefore, the objective here is to confirm that analytical errors $e_P^{\alpha,\eta}$ and $e_A^{\alpha,\eta}$ are also insensitive to friction coefficient η and potentially reduce computational effort. The friction coefficient η was assigned values between 0.6 and 1.4 based on previous research conducted on transfer of shear force in RC walls and membrane elements through shear-friction mechanism (e.g., Chorzepa et al., 2011; Wood, 1990; Hofbeck et al., 1969; Mattock, 1974); these values are similar to values given in Section 11.6.4.3 of ACI 318-11 for shear-friction design. The range of values considered for parameter α (between 0.002 and 0.02) is shown to be reasonable based on the results presented; therefore, analytical predictions of the wall responses are obtained for the following values: η = 0.6, 1.0, 1.4, and α = 0.002, 0.005, 0.01, 0.02. Comparisons of experimental and analytical lateral-load-versus-total-top displacement relations of specimen RW-A15-P10-S78 for the considered values of parameters α and η are shown on Figure 5-21, whereas the corresponding analytical errors $e_A^{\alpha,\eta}$ and $e_P^{\alpha,\eta}$ are presented in Table 5-8.

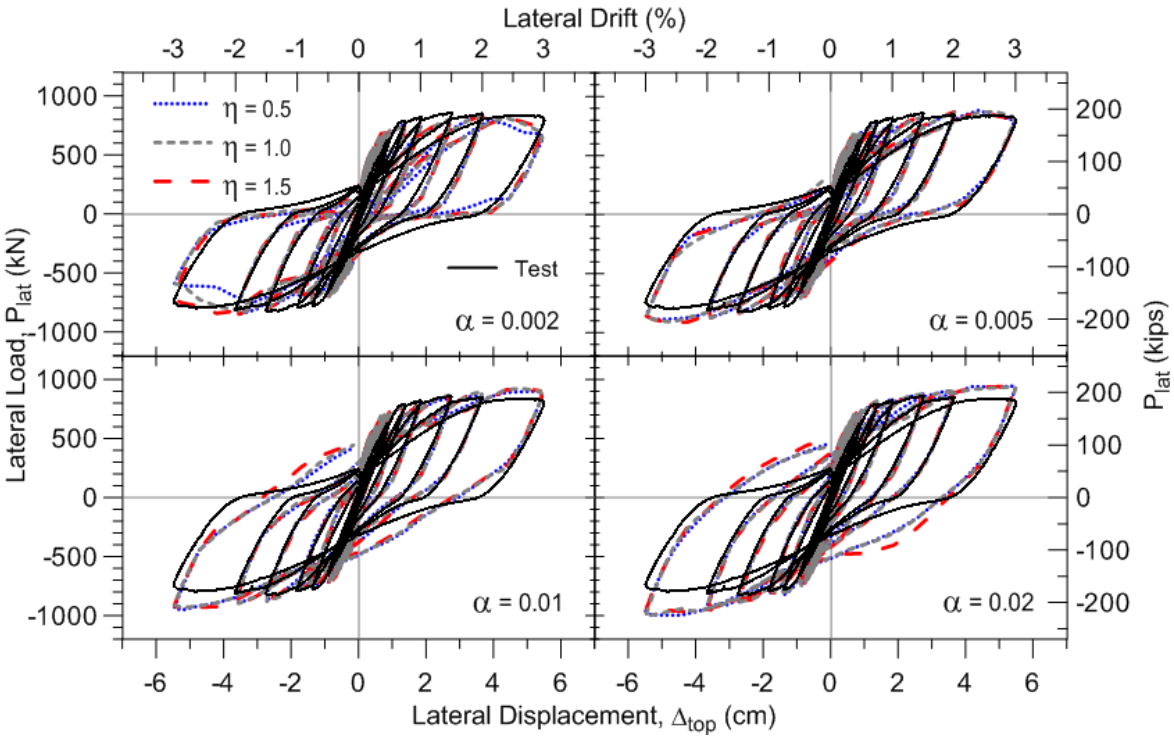

Figure 5-21 Calibration of Load-Deformation Response Against Parameters α and η

Table 5-8 Errors $e_A^{\alpha,\eta}$ and $e_P^{\alpha,\eta}$ for a Range of Parameters α and η

RW-A15-P10-S78	Friction coefficient, η					
	0.6		1.0		1.4	
α	$e_A^{\alpha,\eta}$ (%)	$e_P^{\alpha,\eta}$ (%)	$e_A^{\alpha,\eta}$ (%)	$e_P^{\alpha,\eta}$ (%)	$e_A^{\alpha,\eta}$ (%)	$e_P^{\alpha,\eta}$ (%)
0.002	16.7	48.5	15.6	49.9	14.2	44.2
0.005	**3.8**	**40.5**	4.4	44.7	3.9	46.2
0.01	7.4	48.8	7.9	52.7	8.9	53.7
0.02	18.0	60.7	17.0	65.3	19.5	64.9

It is clear from Figure 5-21 that the analytical predictions obtained with $\alpha = 0.005$ are in very close agreement with experimental results in terms of both the lateral load at peak drift levels and the area of hysteretic loops, whereas Table 5-8 reveals that analytical errors $e_A^{\alpha,\eta}$ and $e_P^{\alpha,\eta}$ are lowest for $\alpha = 0.005$ and $\eta = 0.6$. Also, it can be observed from Figure 5-21 and Table 5-8, that the predicted load-deformation response and the analytical errors do not vary significantly with changes in friction coefficient η when the value of parameter α is fixed. Further calibration of the friction coefficient produces only marginally improvements; therefore, the primary parameter that requires calibration against test results is the stiffness coefficient of dowel action α. Hence, in order to significantly reduce computational effort without considerably affecting the accuracy of analytical results, the calibration of proposed wall model with respect to parameters of shear resisting mechanism in RC panel model focuses on calibration of dowel action stiffness parameter α, whereas the value of friction coefficient η is set equal to 1.0 for all cases. This approach for selecting a value of friction coefficient has been adopted by other researchers (e.g., Wood, 1990; Valluvan et al., 1999; Chorzepa et al., 2011).

In summary, the calibration of the analytical model with respect to parameters of shear resisting mechanism in RC panel model should be performed for a large set of parameters α and η to obtain a broad set of analytical results to compare with experimental results at various response levels. It is noted that other criteria could be employed to assess errors associated with analytical results, e.g. distribution of shear (or flexural) deformations or strains. Thus, the calibration of parameters α and η presented here is only preliminary, since it considers limited set of analytical results.

5.2.3.3. Calibration of Parameter α (η = 1.0)

Based on the discussion presented in previous section, the calibration of analytical model against experimental results for the five wall specimens tested by Tran and Wallace (2012) is performed using the values of α = 0.001, 0.002, 0.005, 0.01, 0.02 and η = 1.0. Load-deformation responses and corresponding analytical errors ($e_A^{\alpha,\eta}$ and $e_P^{\alpha,\eta}$) for the considered values of parameter α are presented on Figure 5-22 to Figure 5-26 for Tests 1 to 5, respectively. For the sake of brevity, without influencing the validity of conclusions, the analytical results for α = 0.002, 0.005, 0.01, 0.02 are presented for Tests 1 to 4, whereas results for α = 0.001, 0.002, 0.005, 0.01 are presented for Test 5.

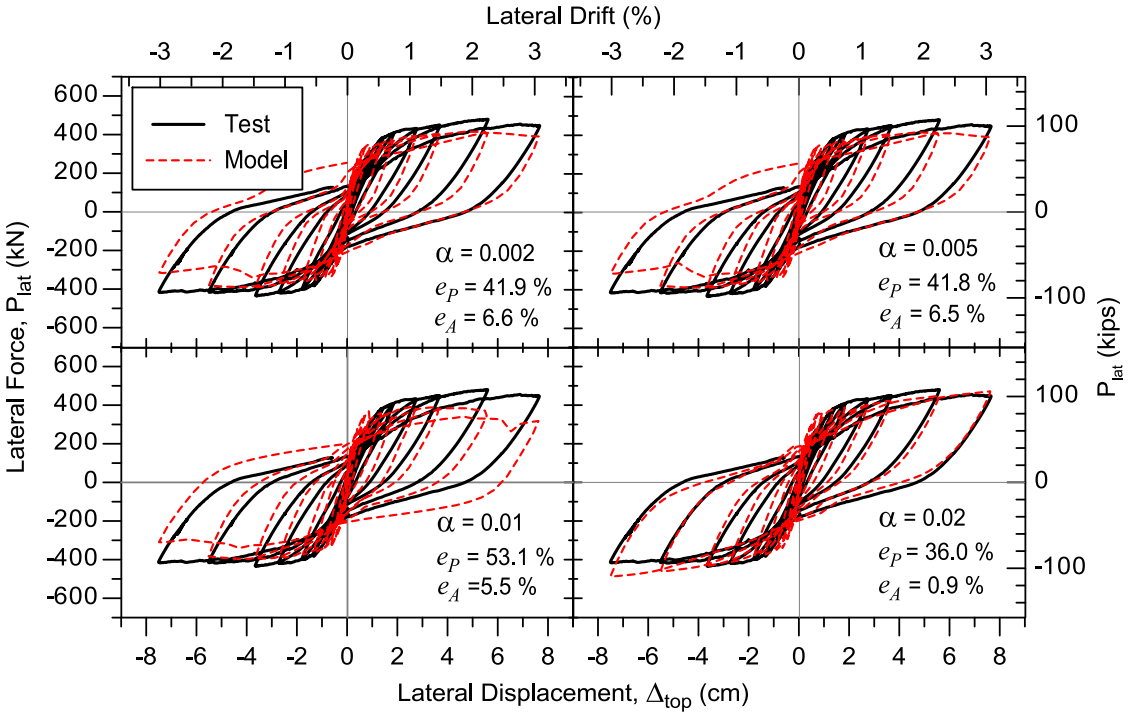

Figure 5-22 Calibration of Parameter α for Specimen RW-A20-P10-S38, Test 1

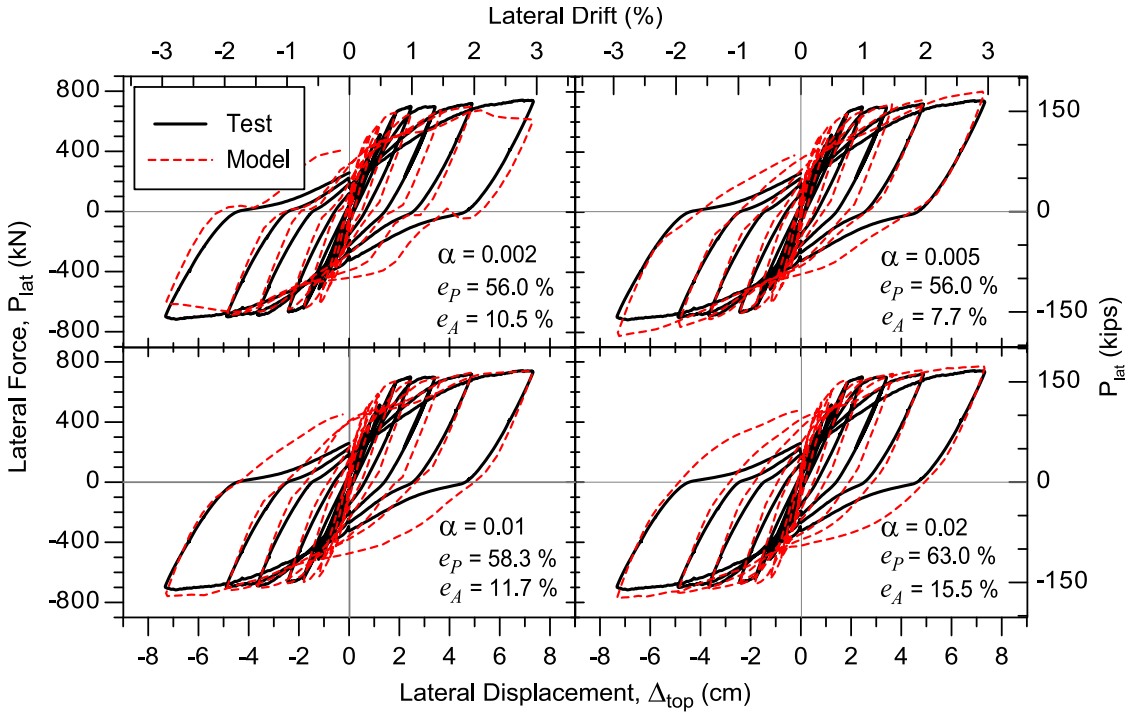

Figure 5-23 Calibration of Parameter α for Specimen RW-A20-P10-S63, Test 2

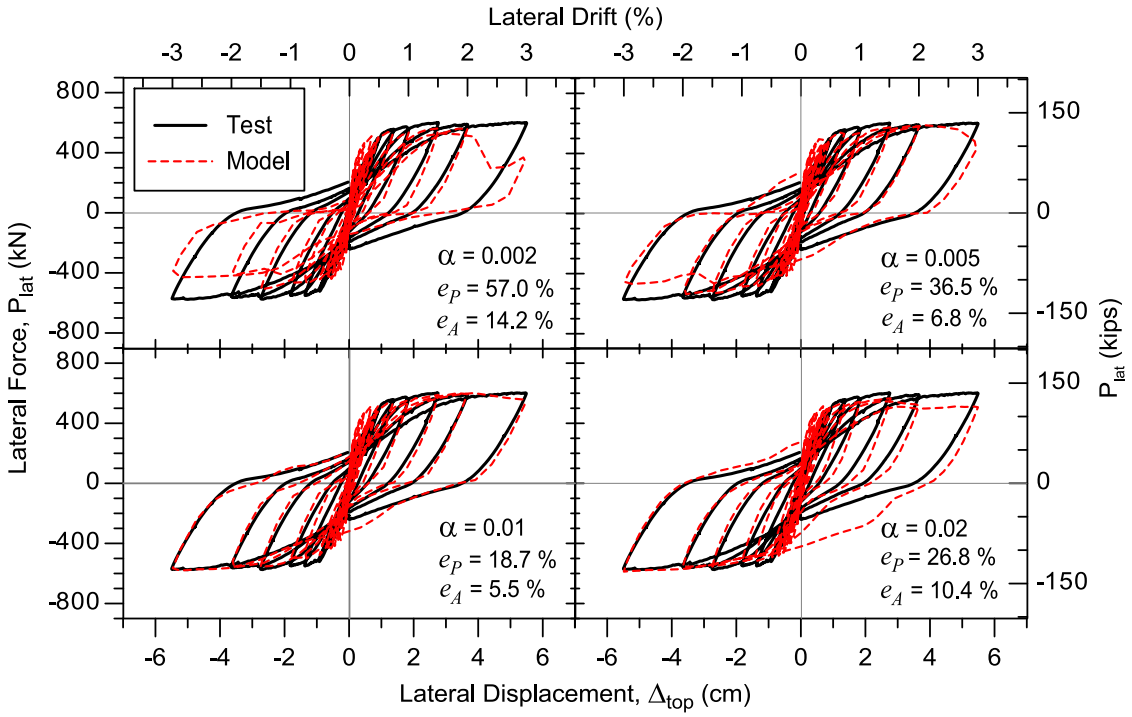

Figure 5-24 Calibration of Parameter α for Specimen RW-A15-P10-S51, Test 3

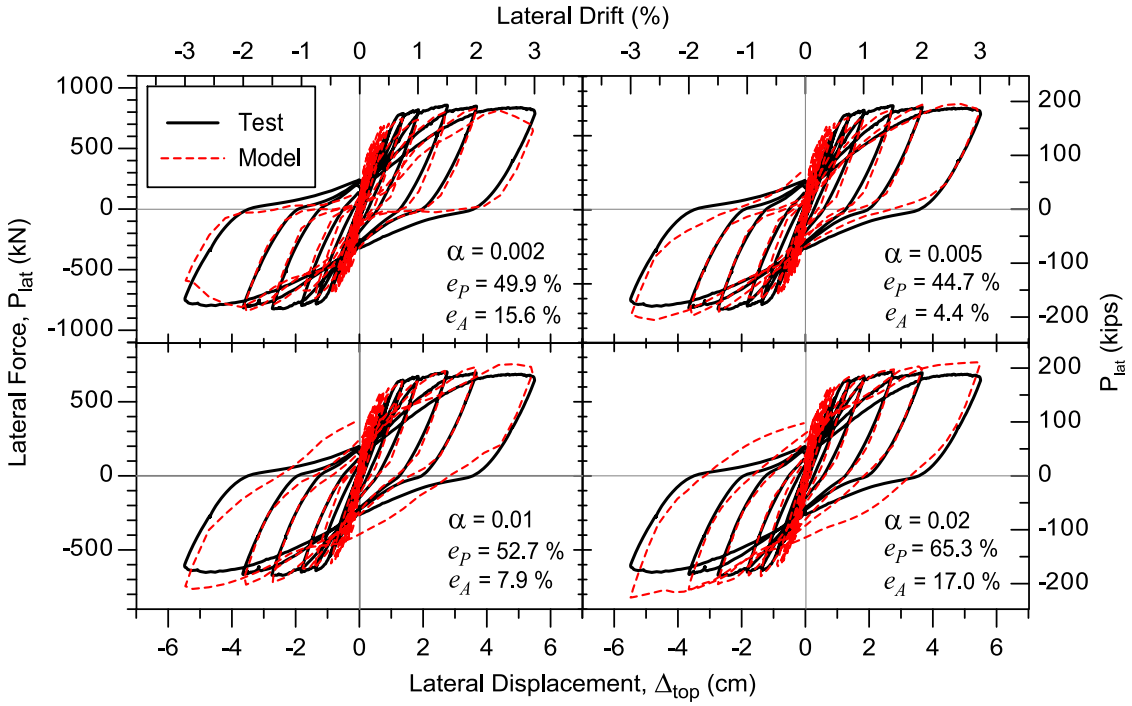

Figure 5-25 Calibration of Parameter α for Specimen RW-A15-P10-S78, Test 4

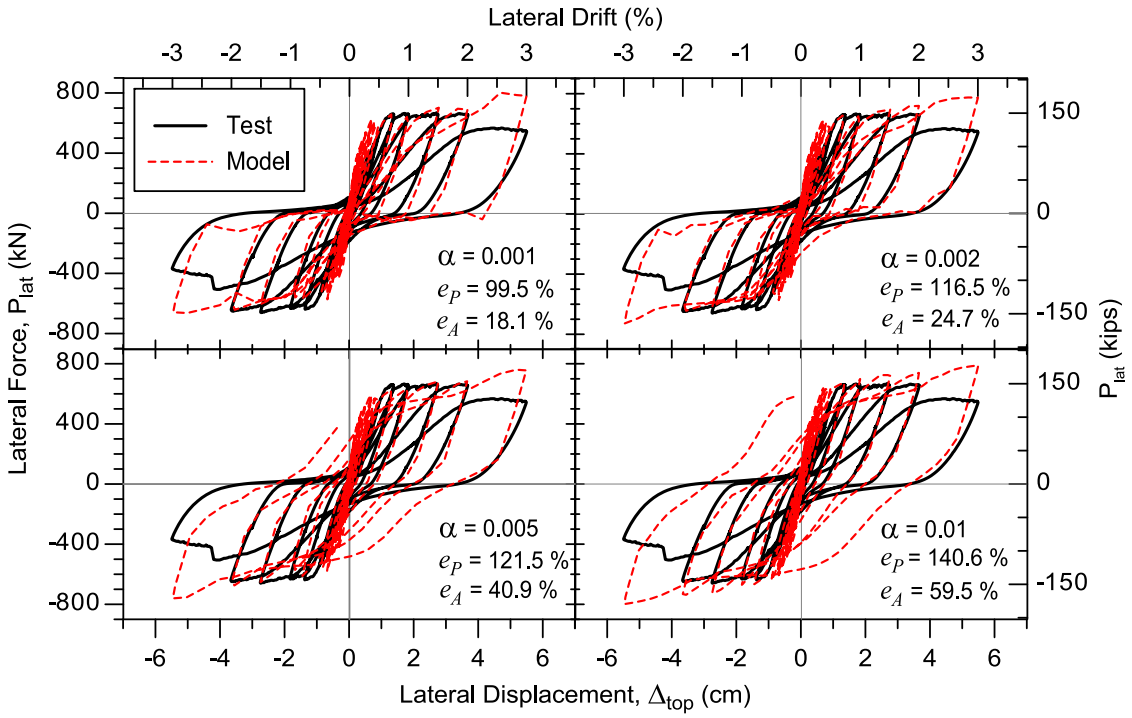

Figure 5-26 Calibration of Parameter α for Specimen RW-A15-P2.5-S64, Test 5

Using error criteria $e_A^{\alpha,\eta}$ and $e_P^{\alpha,\eta}$ calculated from analytical results presented on Figure 5-22 to Figure 5-26, values of parameter α that produce the closest agreement between analytically predicted and experimentally measured load-deformation relations are determined for all five considered wall specimens and summarized in Table 5-9.

Table 5-9 Calibrated Values of Parameter α

Test No.	Specimen code	Parameter α
1	RW-A20-P10-S38	0.02
2	RW-A20-P10-S63	0.005
3	RW-A15-P10-S51	0.01
4	RW-A15-P10-S78	0.005
5	RW-A15-P2.5-S64	0.001

Figure 5-27 plots the final (calibrated) values of parameter α for five RC wall specimens tested by Tran and Wallace (2012) against peak value of wall shear stress (normalized by $\sqrt{f'_c}$) for walls with aspect ratio of 1.5 and 2.0), whereas numbers in prentices represent the ratio between the applied axial load and wall axial load capacity (e.g., 0.10 stands for $P_{ax} = 0.10 A_g f'_c$).

Although the relationships presented on Figure 5-27 are obtained for a very limited set of experimental data (only five wall specimens), two general trends can be observed: (1) the parameter α decreases with increasing shear stress, and (2) parameter α is lower for the one case with lower level of axial load; the relationship between parameter α and wall aspect ratio (h_W / l_w) is not very clear from the figure.

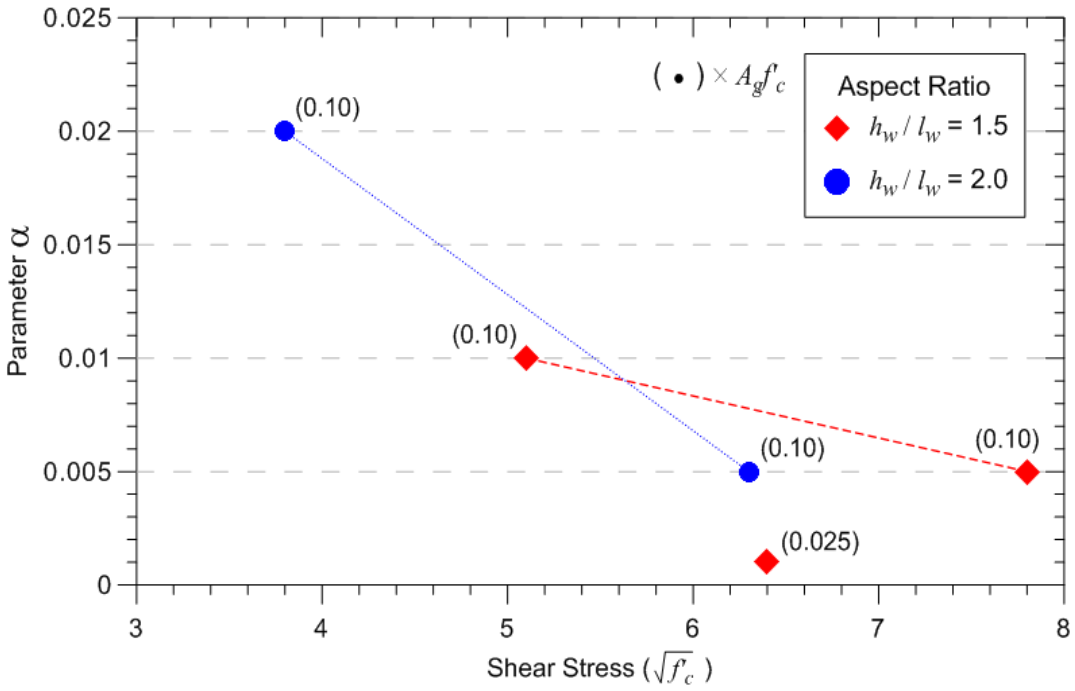

Figure 5-27 Parameter α as a Function of Wall Shear Stress, Aspect Ratio and Axial Load

The decrease of parameter α with increasing shear stress is obvious from results presented on Figure 5-27. For walls with aspect ratio of 2.0, an increase in shear stress from 0.32 $\sqrt{f'_c}$ MPa (3.8 $\sqrt{f'_c}$ psi) to 0.53 $\sqrt{f'_c}$ MPa (6.3 $\sqrt{f'_c}$ psi), by approximately 65%, results in a decrease in the α parameter from 0.02 to 0.005 Similarly, for walls with aspect ratio equal to 1.5, an increase in shear stress from 0.42 $\sqrt{f'_c}$ MPa (5.1 $\sqrt{f'_c}$ psi) to 0.65 $\sqrt{f'_c}$ MPa (7.8 $\sqrt{f'_c}$ psi), by approximately 50%, a decrease in the α parameter from 0.01 to 0.005. Based on these results, parameter α is more sensitive for walls with higher aspect ratios and at lower values of shear stress.

Furthermore, it can be observed from results for walls with aspect ratio of 1.5 (Figure 5-27), that for low level of axial load (P = 0.025 $A_g f'_c$) and moderately high shear stress of 0.53 $\sqrt{f'_c}$ MPa (6.4 $\sqrt{f'_c}$ psi), the optimum value of parameter α is 0.001, whereas for walls with higher level of axial load of 0.10 $A_g f'_c$ and moderate shear stress of 0.43 $\sqrt{f'_c}$ MPa (5.1 $\sqrt{f'_c}$ psi) and high shear stress of 0.65 $\sqrt{f'_c}$ MPa (7.8 $\sqrt{f'_c}$ psi), or average shear stress of 0.54 $\sqrt{f'_c}$ MPa (6.45 $\sqrt{f'_c}$ psi), the optimal values of parameter α are 0.01 and 0.005, respectively (or an average values of 0.0075)). These results suggest that lower axial load levels require use of lower value of parameter α.

Although some trends can be observed between parameter α and the test variables for the wall tests, additional experimental data from heavily instrumented wall specimens with different values of shear stress, axial load, and aspect ratio are needed to verify these trends and to develop detailed recommendations (or relationships) for calibration of parameters of the shear resisting mechanisms. The calibration of analytical model results against experimental data available in the literature (e.g. Thomsen and Wallace, 1995, 2004; Brueggen and French, 2009; Johnson, 2010) could be performed as a part of future studies.

CHAPTER 6

COMPARISON OF ANALYTICAL AND EXPERIEMNTAL RESULTS

This chapter presents comprehensive correlation studies conducted to compare experimentally measured and analytically predicted responses of the five rectangular, moderate-aspect ratio RC wall specimens tested by Tran and Wallace (2012). A description of the wall specimens and the experimental program, along with details about the calibration of the analytical model, are described in Chapter 5. Model results are compared with processed test measurements to allow for a direct comparison between predicted and measured responses at various locations and response levels. These comparisons not only allow for a better understanding of the inelastic behavior of RC walls, they also help assess model capabilities as well as ways to improve the model. The following response characteristics of the wall specimens are considered: (1) lateral load versus top total lateral displacement response, (2) propagation of cracking and cracking patterns, (3) profiles of total lateral displacements over the wall height, (4) vertical growth versus top total lateral displacement response, (5) profiles of vertical growth over the wall height, (6) lateral load versus top flexural displacement response, (7) profiles of flexural displacements over the wall height, (8) lateral load versus top shear displacement response, (9) profiles of shear displacements over the wall height, (10) contributions of shear and flexural displacements to total wall top displacement, (11) effective secant flexural and shear stiffness, (12) profiles of

vertical strains at the wall bottom, (13) strain histories at the wall boundary, and (14) rotations over the wall plastic hinge length.

6.1. Lateral Load versus Total Lateral Displacement Relations

This section presents the comparison of experimentally measured and analytically predicted lateral load versus total lateral displacement relations for Tests 1 to 5 of experimental program conducted by Tran and Wallace (2012). The agreement between experimental and analytical results is characterized based on comparisons of wall lateral stiffness, load capacity, and ductility as well as failure mechanisms under cyclic loading history applied at the top of the walls. In addition, an overview of results is provided in terms of comparisons of lateral loads and displacements corresponding to first concrete tensile cracking, yielding of the longitudinal boundary reinforcement and peak lateral load obtained experimentally and analytically.

6.1.1. Lateral Stiffness and Load Capacity

Comparisons between experimental and analytical lateral-load-versus-total-lateral-displacement responses of specimens in Tests 1 to 5 are presented in Figure 6-1 to Figure 6-5, respectively. It can be observed from the figures that model successfully captures the overall shape of the hysteretic loops for all five specimens, i.e. slightly pinched shape for specimens with aspect ratio 2.0 and axial load of 0.10 $A_g f'_c$ (Tests 1 and 3), moderately pinched shape for specimens with aspect ratio 1.5 and axial load of 0.10 $A_g f'_c$ (Tests 3 and 4) and highly pinched shape of specimen with aspect ratio 1.5 and lower axial load of 0.025 $A_g f'_c$ (Test 5). It can be also observed from the figures that model predicts well the cyclic characteristics of the wall load-

deformation responses for all five wall specimens including cyclic degradation of wall stiffness throughout the loading history and plastic (residual) deformation at zero lateral load.

The lateral stiffness is typically well predicted by the model for moderate and high drift levels, whereas overestimation of wall lateral stiffness by approximately 10-20% can be observed at drift levels lower than 0.75% for specimens with aspect ratio 2.0 (Tests 1 and 2) and drift levels lower than 0.5% for specimens with aspect ratio 1.5 (Tests 3, 4, and 5). At intermediate drift levels, between approximately 0.75% and 2.0%, the lateral load and stiffness are reasonably well predicted by the model for all five wall specimens. In addition, at drift levels larger than 2.0% the predicted lateral load is less accurate due to significant strength degradation observed in the experimental data typically around 3.0% drift (as discussed in more details in the following section).

For Test 1 (Figure 6-1) the lateral load is underestimated by approximately 5-10% at drift levels between 0.75% and 2.0% in the positive loading direction, and overestimated by approximately 5-15% at the lateral drifts larger than 2% in the negative loading direction, whereas generally good agreement between experimental and analytical results can be observed for the rest of applied lateral drifts. For Test 2 (Figure 6-2) analytical model underestimates wall lateral load capacity by less than 10% at drift levels between 0.75% and 2.0%, and predicts closely the lateral load at drift level of 3.0%. Furthermore, Figure 6-3 reveals that for Test 3 at drift levels higher than 0.75%, the lateral load is generally underestimated in the analytical results by approximately 5-10%. For Test 4, the wall lateral stiffness is reasonably well predicted at drift levels between 0.5% and 2.0%, and analytically obtained lateral loads at peak lateral displacements are within 5% of the experimentally measured values, as shown on Figure 6-4. As

well, at drift levels of 2.0% and 3.0%, the analytical model overestimates lateral load by 5% and 10% for positive and negative loading directions, respectively. Finally, for Test 5 (Figure 6-5), the lateral load corresponding to peak applied lateral displacements is reasonably well predicted for drift levels between 0.50% and 2.0% in both loading directions, except at negative 0.75% drift where the wall capacity is underestimated by approximately 10%.

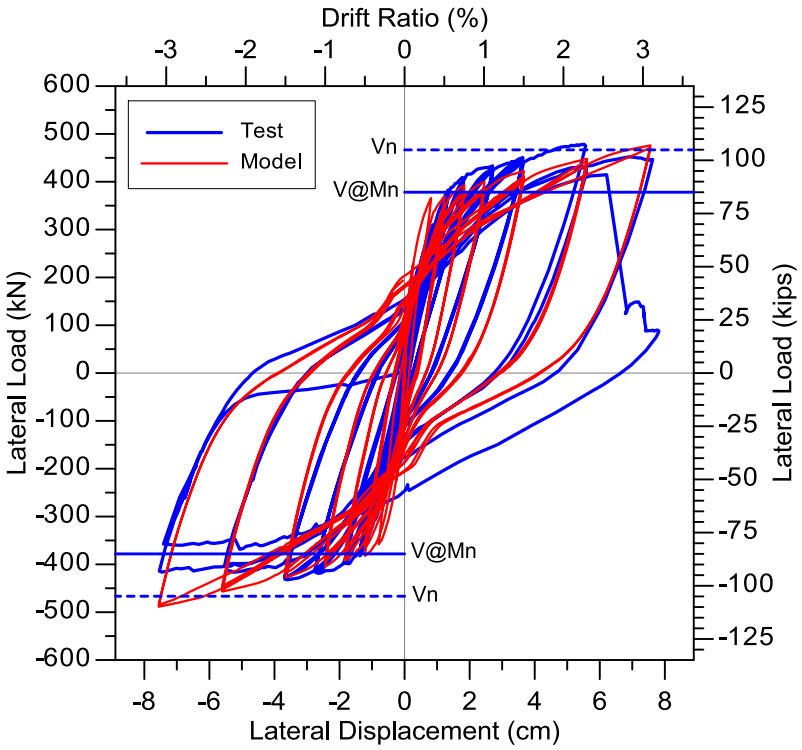

Figure 6-1 Top Lateral Displacements for Specimen RW-A20-P10-S38, Test 1

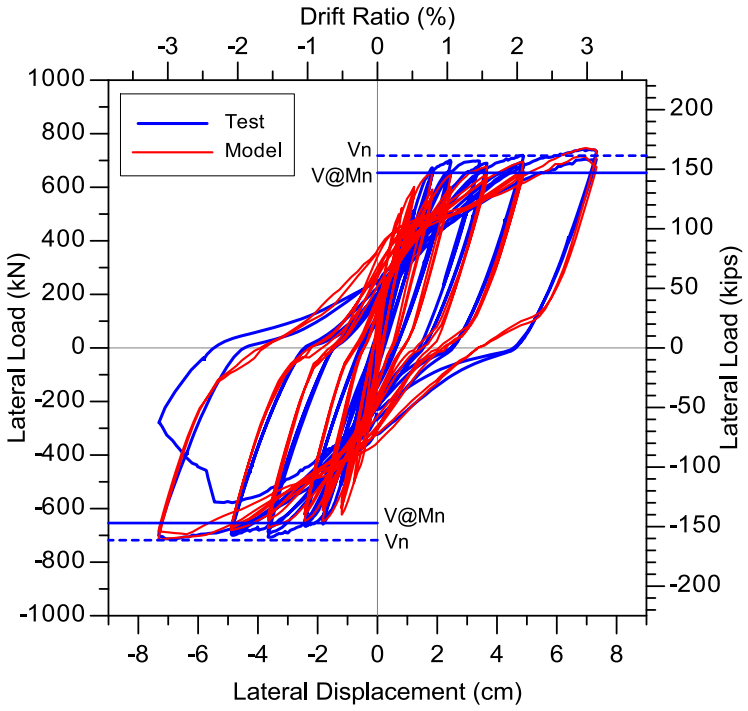

Figure 6-2 Top Lateral Displacements for Specimen RW-A20-P10-S63, Test 2

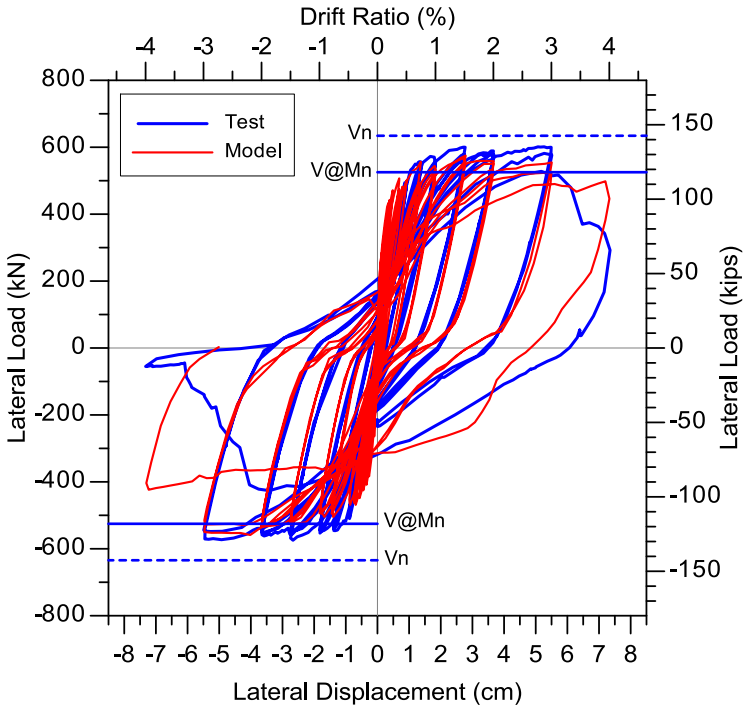

Figure 6-3 Top Lateral Displacements for Specimen RW-A15-P10-S51, Test 3

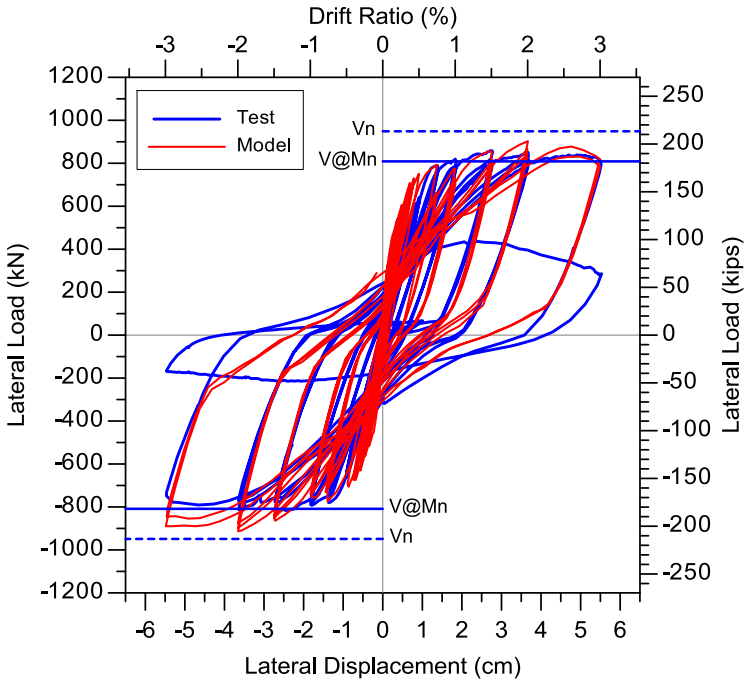

Figure 6-4 Top Lateral Displacements for Specimen RW-A15-P10-S78, Test 4

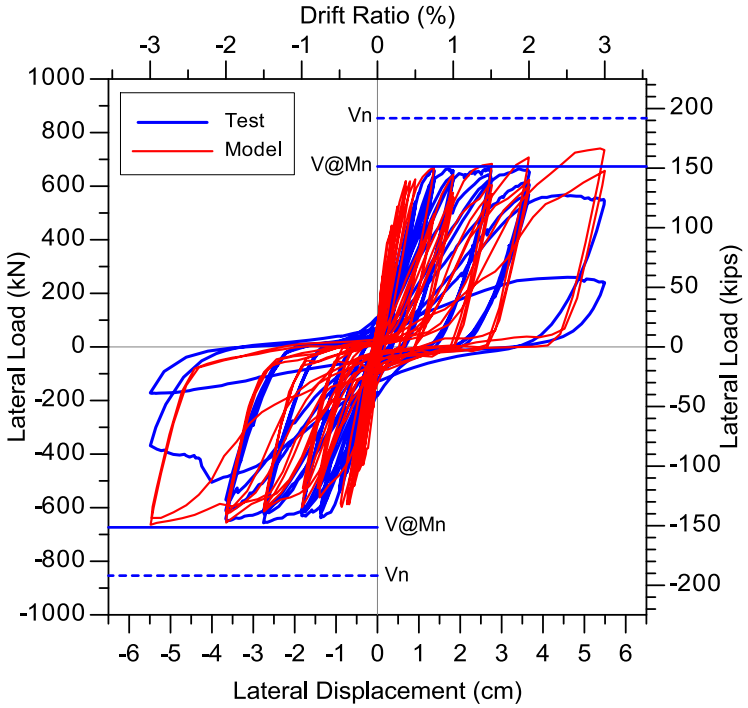

Figure 6-5 Top Lateral Displacements for Specimen RW-A15-P2.5-S64, Test 5

6.1.2. Failure Mechanisms

Specimen RW-A20-P10-S38 (Test 1) - Observations from the test indicated that, at the second cycle of lateral drift of 3.0%, concrete in the core boundary element crushed and boundary longitudinal reinforcement buckled causing sudden diagonal tension failure with fracture of horizontal web bars along a diagonal crack, which resulted in drop to wall lateral strength to only about 30% of its peak value (Figure 6-1). Although the analytical model predicts the initiation of concrete crushing in wall boundaries at the drift level of 3.0%, the significant strength degradation observed in the experiment is not predicted by the model due to inability of the implemented stress-strain relationship for reinforcing steel to capture buckling of longitudinal reinforcement observed in test. Therefore, the analytical model does not describe appropriately the failure mechanism observed during the test.

Specimen RW-A20-P10-S63 (Test 2) - The loss of wall strength in the experiment was caused by concrete crushing and bar buckling in wall boundary of the test specimen under negative loading during the second cycle of applied lateral drift of 3.0%, which caused lateral instability of the boundary zone (out-of-plane buckling) and resulted in drop of wall strength to 39% of its peak value (Figure 6-2). Similarly as for the previous wall specimen, the analytical model is not able to capture experimentally observed sudden strength drop because the buckling of reinforcing bars is not incorporated in the steel stress-strain relationship used in the model.

Specimen RW-A15-P10-S51 (Test 3) - When the wall test specimen was loaded in positive direction to 4.0% drift in the experiment, crushing of core concrete of the south wall boundary and buckling of vertical boundary reinforcement occurred, which initiated diagonal tension failure along a major

crack with fracture of several horizontal web bars crossing the diagonal crack. As a result, the wall was able to resist only 41% of the peak strength at 4.0% drift (Figure 6-3). When reversed loading was applied, fracture of two longitudinal bars at the south wall boundary was observed, along with concrete crushing and buckling of longitudinal reinforcement at the north wall boundary causing the lateral load to drop to only 10% of the peak load (Figure 6-3). In the analysis, crushing of concrete in wall boundaries was predicted in both positive and negative loading directions to 4.0% drift, which resulted in drop of predicted lateral wall capacity to approximately 80% and 70% of peak lateral load for positive and negative loading direction, respectively, as shown in Figure 6-3. However, since buckling and fracture of reinforcing bars are not implemented in constitutive material model for steel, the model was not able to predict all failure mechanisms observed during test.

Specimen RW-A15-P10-S78 (Test 4) - During 3.0% lateral drift cycle in the experiment, concrete spalling was observed along the wall base causing lateral load drop to the 90% of the peak value. During second cycle of 3.0% drift, shear sliding occurred near the base of the wall caused residual strength to drop to only 33% of the peak capacity (Figure 6-4), which was followed by out-of-plane buckling. When load was reversed, out-of-plane buckling occurred at the other (opposite) wall boundary and lateral load dropped to 20% of the peak load (Figure 6-4). Although strength degradation can be observed in the analytical results, caused by degradation of spalling of cover concrete and strength degradation of the confined concrete in the wall boundaries, the analytical results do not describe appropriately failure mechanism observed in the experiment due to inability of the model to capture shear sliding near the wall base.

Specimen RW-A15-P2.5-S64 (Test 5) - Similarly to RW-A15-P10-S78, during the first cycle to 3.0% drift, modest spalling of cover concrete was observed along diagonal compressive concrete struts near the wall-foundation interface at the wall boundaries, leading to relatively significant strength degradation in both loading directions. Shear sliding was observed during the subsequent cycle, causing a substantial reduction of the wall lateral strength, followed by in-plane buckling of boundary longitudinal reinforcement, which caused the wall capacity to drop to 55% of the peak value at negative 3.0% drift (Figure 6-5). As mentioned earlier, the analytical model does not capture shear sliding at or near the base of the wall, nor buckling of wall reinforcement. Although degradation of wall stiffness is present in the analytical results, the failure mechanism observed in the experiment was not captured by the model.

Overall, the analytical model captures successfully the initiation of strength degradation of confined concrete as well as spalling of unconfined concrete in the wall boundaries. However, complex failure mechanisms observed in the experiments that occurred after the initiation of wall strength degradation, i.e. rebar buckling and fracture, shear sliding along the base of the wall and lateral instability of the wall boundary, were not implemented in the current model formulation. Therefore, analytical results do not describe appropriately failure mechanisms observed during experiments, and therefore typically do not capture significant strength degradation observed in the experimental load-deformation relationships.

6.1.3. Overview of Results

The comparisons of experimentally measured and analytically predicted lateral load and top lateral displacement in both positive and negative loading directions at tensile cracking of

concrete, yielding of boundary longitudinal reinforcement, and peak lateral load for all five wall specimens are presented in Figure 6-6 and summarized in Table 6-1.

Table 6-1 Overview of comparisons of analytical versus experimental results

Test no.	Wall code	Loading Direction	Cracking				Yielding				Peak load			
			F, kN (kips)		Δ_{top}, mm (in)		F, kN (kips)		Δ_{top}, mm (in)		F, kN (kips)		Δ_{top}, mm (in)	
			test	model	test	model	test	model	test	model	test	model	test	model
1	RW-A20-P10-S38	Positive	148 (33.3)	145 (32.5)	2.0 (0.079)	1.0 (0.04)	379 (85.28)	367 (82.4)	13 (0.53)	8 (0.33)	481 (108.03)	472 (106.1)	56 (2.20)	76 (3.01)
		Negative	-143 (-32.2)	-144 (-32.4)	-1.8 (-0.069)	-1.0 (-0.04)	-374 (-84.12)	-349 (-78.5)	-14 (-0.54)	-9 (-0.35)	-436 (-97.98)	-489 (-109.9)	-36 (-1.42)	75 (-2.96)
2	RW-A20-P10-S63	Positive	169 (38.0)	167 (37.47)	2.1 (0.084)	1.0 (0.04)	630 (141.57)	590 (132.6)	16 (0.63)	12 (0.48)	742 (166.91)	747 (167.85)	69 (2.72)	70 (2.74)
		Negative	-165 (-37.1)	-166 (-37.39)	-2.0 (-0.080)	-1.0 (-0.04)	-597 (-134.26)	-591 (-132.9)	-15 (-0.59)	-12 (-0.48)	-717 (-161.14)	716 (-160.91)	-69 (-2.72)	-73 (-2.88)
3	RW-A15-P10-S51	Positive	190 (42.8)	175 (39.3)	1.3 (0.051)	0.5 (0.02)	527 (117.46)	523 (117.5)	10 (0.40)	6 (0.25)	603 (135.45)	575 (129.3)	52 (2.05)	28 (1.09)
		Negative	-189 (-42.6)	-229 (-51.5)	-1.1 (-0.045)	-0.8 (-0.03)	-506 (-113.69)	-503 (-113.1)	-9 (-0.37)	-6 (-0.25)	-575 (-129.31)	-559 (-125.7)	-50 (-1.97)	45 (-1.78)
4	RW-A15-P10-S78	Positive	201 (45.2)	190 (42.65)	1.5 (0.060)	0.5 (0.02)	776 (174.38)	753 (169.2)	12 (0.48)	9 (0.36)	859 (193.15)	902 (202.9)	27 (1.08)	37 (1.44)
		Negative	-198 (-44.5)	-258 (-58.03)	-1.1 (-0.044)	-0.8 (-0.03)	-727 (-163.48)	-723 (-162.5)	-11 (-0.42)	-9 (-0.36)	-823 (-184.91)	-917 (-206.1)	-27 (-1.06)	-37 (-1.44)
5	RW-A15-P2.5-S64	Positive	142 (31.9)	166 (37.4)	1.3 (0.052)	0.5 (0.02)	627 (140.97)	601 (135)	11 (0.44)	7 (0.27)	670 (150.62)	748 (168.1)	27 (1.06)	55 (2.16)
		Negative	-141 (-31.7)	-161 (-36.2)	-1.1 (-0.044)	-0.76 (-0.03)	-588 (-132.28)	-589 (-132.5)	-10 (-0.40)	-14 (-0.55)	-660 (-148.30)	-664 (-149.2)	-27 (-1.07)	-54 (-2.15)

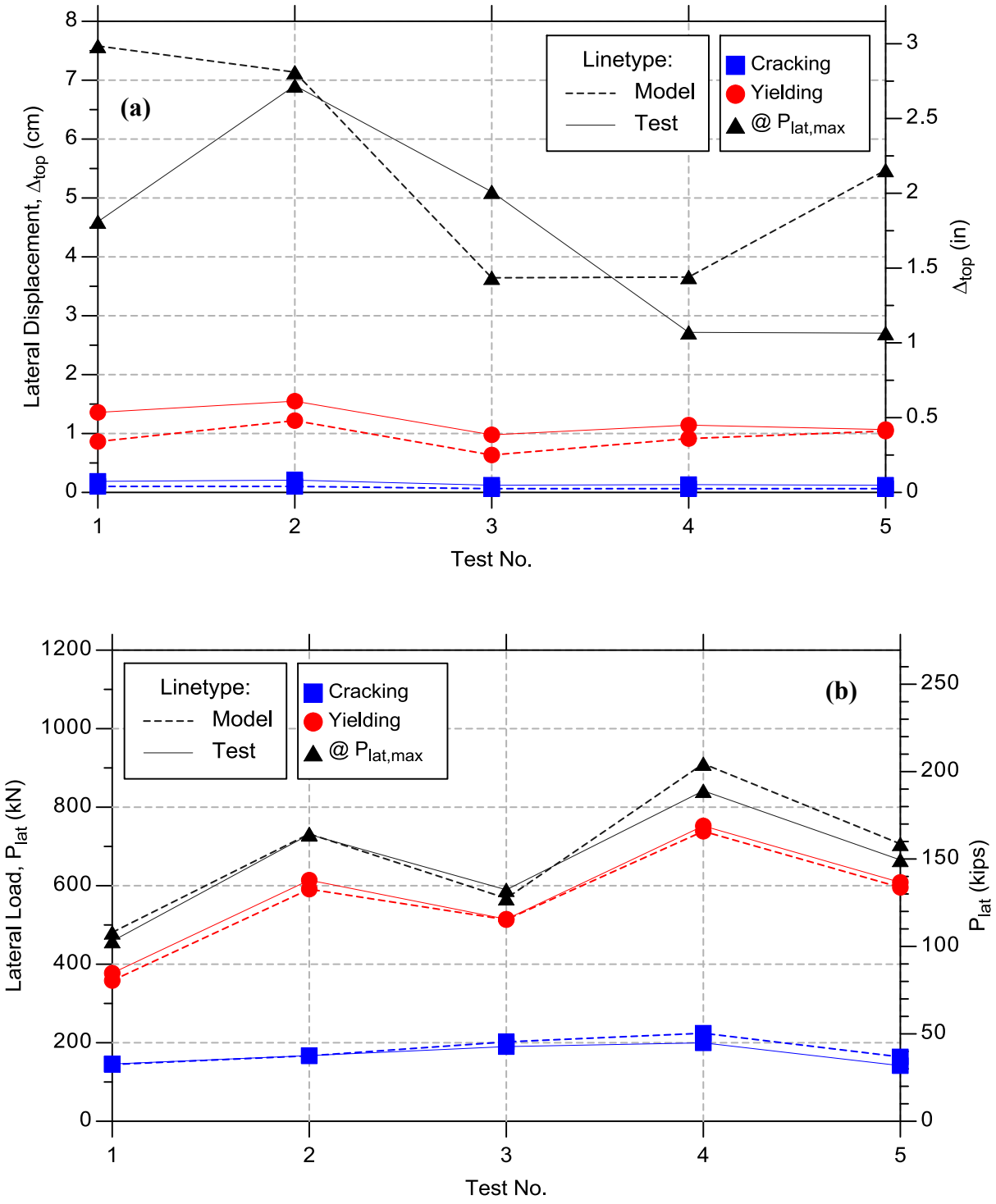

Figure 6-6 Experimental versus Analytical (a) Top Wall Displacement and (b) Lateral Load at Concrete Cracking, Reinforcement Yielding and Maximal Lateral Load ($P_{lat,\ max}$)

As displayed in Figure 6-6(a), the predicted lateral displacement at the top of the wall at cracking of concrete and yielding of longitudinal boundary reinforcement is approximately 50% and 70% of experimentally measured displacement, respectively. In addition, Figure 6-6(b) illustrates that lateral loads at first tensile cracking of concrete and yielding of boundary longitudinal reinforcement are predicted within 5% for all specimens.

Although the peak lateral load is predicted by the analytical model within 10% of experimentally measured load for all specimens, it does not occur at the same drift levels as noted in the experiment (Figure 6-6(b)). Analytical results show very little (or no) strength degradation, i.e., the predicted maximal lateral load generally corresponds to the peak applied lateral drift (e.g., 2.0% drift for Tests 3 and 4, and 3.0% drift for Tests 1, 2, and 5), whereas the experimental results reveal that the peak lateral load is reached prior the ultimate drift level followed by strength degradation. Therefore, top lateral displacement at maximum lateral load is generally overestimated by the analytical model for all specimens, except for specimen RW-A15-P10-S51 (Test 3), as illustrated on Figure 6-6(a).

6.2. Cracking Patterns

Cracking patterns observed during the experiments and predicted by the analytical model for the five RC wall specimens (Tran and Wallace, 2012) are compared at various levels of lateral force and lateral drift in order to investigate the capability of the model to capture propagation and orientation of cracks as lateral load increases.

6.2.1. Specimen RW-A20-P10-S38 – Test 1

This wall specimen had horizontal and vertical web reinforcement ratios of 0.0027, which are slightly larger than ACI 318-11 (Section 21.9.2) minimum requirements for special structural walls of 0.0025. Figure 6-7 compares the experimentally observed and analytically predicted cracking patterns for specimen RW-A20-P10-S38 at lateral load level of 50.0 kips and lateral drift levels of 0.38%, 0.56% and 1.5%. In the experiment, initial cracking occurred during the first cycle of the third force-controlled level (2/3*Vy*; 222 kN or 50 kips) as shown on Figure 6-7(a). It can be observed from Figure 6-7 that horizontal flexural cracks at wall edges and three major inclined (shear) cracks on each side of the wall, which initiated from the boundary zone toward the wall center, occurred over the lower 1.0 m (40 in.) of the wall height. The cracking predicted by the analytical model also is noted over a wall height of 40 in., i.e. in the bottom three SFI-MVLEM elements of heights equal to 12 in., 12 in., and 16 in. The angle of the first (analytical) crack is steeper for the panels closer to the center of the wall indicating that flexural cracks are developed closer to the wall boundaries and shear cracks are developed closer to the wall center, which is in agreement with experimental observations. In the bottom level of SFI-MVLEM elements, all RC panels (except the middle one) develop both perpendicular cracks (as described in Section 3.3), in the second level of SFI-MVLEM elements (from the bottom), most of the panels developed only the first crack and one panel is uncracked, whereas in third level of SFI-MVLEM elements, two panels are uncracked and most of other panels developed only the first crack.

During the subsequent displacement-controlled loading cycles, at a lateral drift level of 0.38%, new flexural and shear cracks tended to form closer to the top of the wall test specimen and

appeared over one half of the wall height prior reaching the yield load (Figure 6-7(b)). During this loading cycle, the analytical model predicts that concrete cracking spreads out over the lower four SFI-MVLEM element levels, whereas only one panel in the fifth model element level developed both cracks, which corresponds to the experimentally observations in terms of distribution of cracks over the wall height. As well, the orientation of newly formed cracks followed the trend observed in the experiment, i.e., flexural cracks at the wall boundary become steeper towards the top of the wall due to decrease in moment demand (axial strain), while cracks in the middle portion of the wall remain were inclined at an angle close to 45 degrees from the horizontal direction.

When lateral drift was increased to 0.56% (Figure 6-7(c)), cracking in both experimental and analytical results propagated towards the top of the wall up to the wall height of $3/4h_w$. However, for larger drift levels, up to a lateral drift ratio of 1.5%, the cracking pattern did not change significantly for both the experimental and the analytical results as shown in Figure 6-7(d). It can be observed from the Figure 6-7(d) that the predicted cracking pattern propagates up to the 5^{th} SFI-MVLEM element level, which agrees reasonably well with the experimentally observed cracking pattern, which extends up to the $3/4h_w$; the orientation of cracks observed in the experiment is predicted reasonably well by the model.

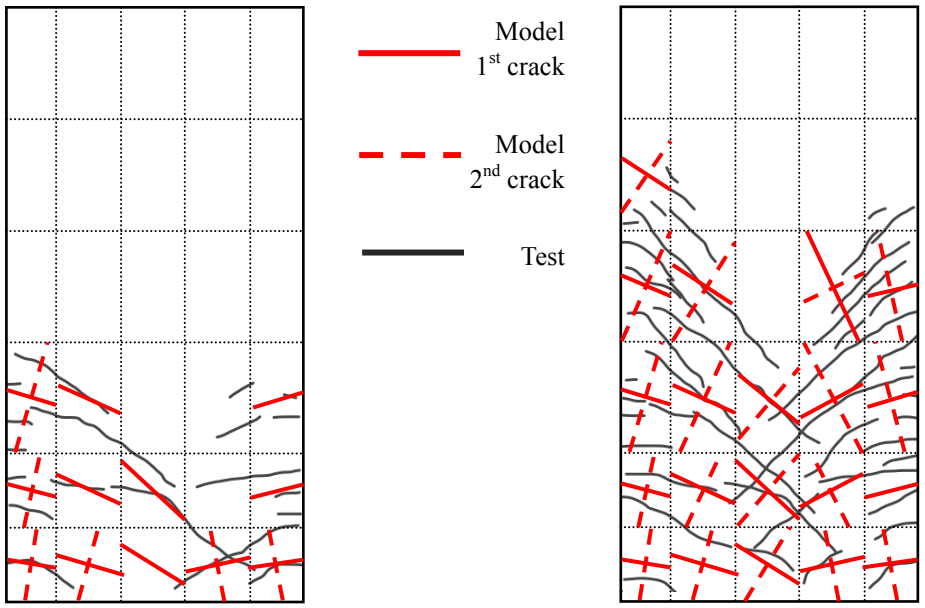

(a) V=50 kips

(b) 0.38% Drift

(c) 0.56% Drift

(d) 1.5% Drift

Figure 6-7 Cracking Patterns for Specimen RW-A20-P10-S38, Test 1

6.2.2. Specimen RW-A20-P10-S63 – Test 2

This specimen was characterized with the higher level of shear stress than the previous specimen ($6.1\sqrt{f'_c}$ psi versus $3.6\sqrt{f'_c}$ psi; $0.51\sqrt{f'_c}$ MPa versus $0.30\sqrt{f'_c}$ MPa), which is achieved by approximately doubling the value of boundary and web reinforcement. Figure 6-8 compares the experimentally observed and analytically predicted cracking patterns for specimen RW-A20-P10-S63 at lateral load level of 389.66 kN or 87.6 kips (yielding of the boundary reinforcement, V_y) and lateral drift levels of 0.75% and 1.5%. The initiation of tensile concrete cracking was observed in the experiment during the first cycle of the second force-controlled level ($V_y/3$; 93 kN or 43.3 kips) including one or two inclined (shear) cracks on each side of the wall up to the wall height of $0.25l_w$. With increasing lateral load (force-controlled levels), horizontal flexural cracks occurred at the boundaries and new inclined cracks occurred over the wall height leading to the cracking pattern at the yielding of the boundary reinforcement shown on Figure 6-8(a). It can be observed from the figure that both analytically predicted and experimentally measured cracking patterns spread approximately up to the wall height of $h_w/2$ (122 cm or 48 in.); the majority of RC panels at the wall model in bottom three SFI-MVLEM elements over the height of 40 in (12 in. + 12 in. + 16 in.) developed two perpendicular cracks, whereas the cracking in the fourth and fifth model element levels (16 in. + 16 in.) is initiated at wall boundaries. At this level of lateral load, the analytically predicted cracking pattern is characterized by flexural cracks at the wall boundaries and shear cracks within the web of the wall, which is consistent with experimentally observed crack patterns and orientations (Figure 6-8(a)).

With increasing lateral load (force-controlled levels) or lateral displacement (displacement-controlled levels), inclined cracks continued to propagate along the wall height in both experimental and analytical results. Experimental and analytical cracking patterns are very similar to that of RW-A20-P10-S38, except that in RW-A20-P10-S63 diagonal cracks formed up to the top of the wall at the lateral drift level of 0.75% as shown on Figure 6-8(b). In addition, it can be observed on Figure 6-8(c) that when increasing lateral drift to 1.5%, the cracking patterns did not change significantly since most of the cracks were formed at lower drift levels, i.e. cracks only open and close without any further propagation. The analytical model captures well the propagation of cracks and their orientation observed during the experiment at lateral drift levels of 0.75% and 1.5% as shown on Figure 6-8(b) and Figure 6-8(c), respectively.

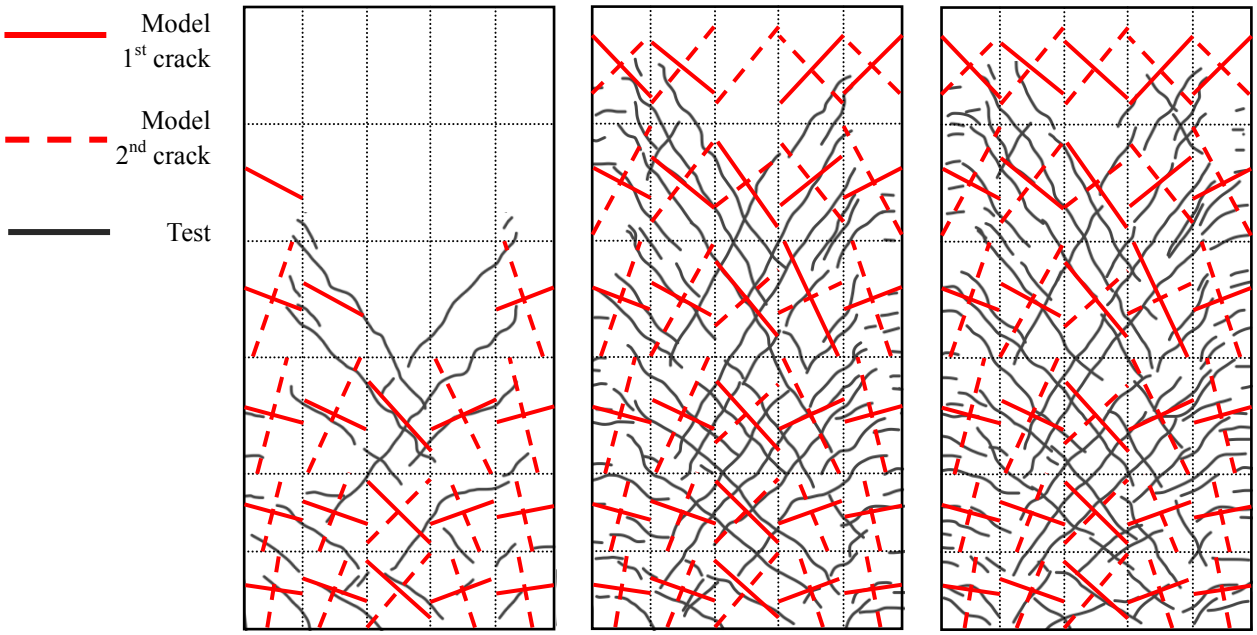

(a) 86.7 kips (b) 0.75 % Drift (c) 1.5 % Drift

Figure 6-8 Cracking Patterns for Specimen RW-A20-P10-S63, Test 2

6.2.3. Specimen RW-A15-P10-S51 – Test 3

The third wall specimen had the same longitudinal boundary reinforcement and axial load level as the first wall specimen (RW-A20-P10-S38), but a lower aspect ratio (1.5 versus 2.0) and a slightly higher web reinforcement ratio (0.0032 versus 0.0027); the lateral load corresponding to the nominal moment capacity was larger, leading to a higher design shear stress than for RW-A20-P10-S38 ($5.1\sqrt{f_c'}$ psi versus $3.8\sqrt{f_c'}$ psi or $0.43\sqrt{f_c'}$ MPa versus $0.32\sqrt{f_c'}$ MPa).

Figure 6-9 compares experimentally observed and analytically predicted cracking patterns for specimen RW-A15-P10-S51 at lateral load level of 320 kN (72 kips) and lateral drift levels of 0.375%, 1.0% and 3.0%. The initiation of cracking in the experiment occurred during the first cycle of the third force-controlled level ($2/3V_y$; 240 kN or 54 kips); Figure 6-9(a) displays the cracking patterns at the subsequent loading cycle at the lateral load level of 320 kN (72 kips). As shown on the figure, the experimental cracking pattern consisted of several horizontal flexural cracks along the wall boundaries and three major inclined (shear) cracks on each side of the wall propagating from the wall boundaries at the wall-foundation interface towards the wall center up to the height of approximately $0.5h_w$ above the wall-foundation interface. Figure 6-9(a) also reveals that the corresponding analytically predicted cracking pattern is in good agreement with the distribution and orientation of cracks observed during the experiment; analytical model predicts horizontal (flexural) cracks at the wall boundaries and diagonal (shear) cracks towards the middle of the wall in two bottom SFI-MVLEM element levels, as well as the initiation of diagonal cracks at the wall boundaries of the third SFI-MVLE.

After increasing lateral drift to 0.375 % (Figure 6-9(b)), the major diagonal cracks propagate from the wall boundaries towards the top of the wall test specimen up to the height of approximately $3/4h_w$ (1.37 m or 54 in.) was observed in the experiment as well as in the analytical results; the model predicts the formation of cracks approximately up to a height of $3/4h_w$, i.e. in lower four model elements (12 in + 12 in + 16 in + 16 in = 56 in) in which the first and second cracks can be observed in all RC panel elements of lower three model element levels and in all RC panels of the fourth model element except in the middle panel.

Further crack propagation in the experiment can be observed at drift level of 1.0% (Figure 6-9(c)), where diagonal cracks extended to the top of the wall specimen leaving a small uncracked portion in the middle of the wall near the wall top. The analytical model predicts very similar behavior with the first and second cracks formed in all RC panel elements in the wall model except the middle panel element at the top of the wall, as shown on Figure 6-9(c). In addition, it can be observed from the figure that the orientation of cracks agrees reasonably well with the experimentally observed cracking pattern at lateral drift of 1.0%.

The experimentally observed cracking pattern at lateral drift of 3.0% (Figure 6-9(d)) does not differ significantly from the cracking patter at lateral drift of 1.0%, i.e. no new cracks form at intermediate drift levels. All RC panel elements in the wall model developed first and second crack, the orientation of which agrees reasonably well with the orientation of cracks for specimen RW-A15-P10-S51 observed in the test.

.

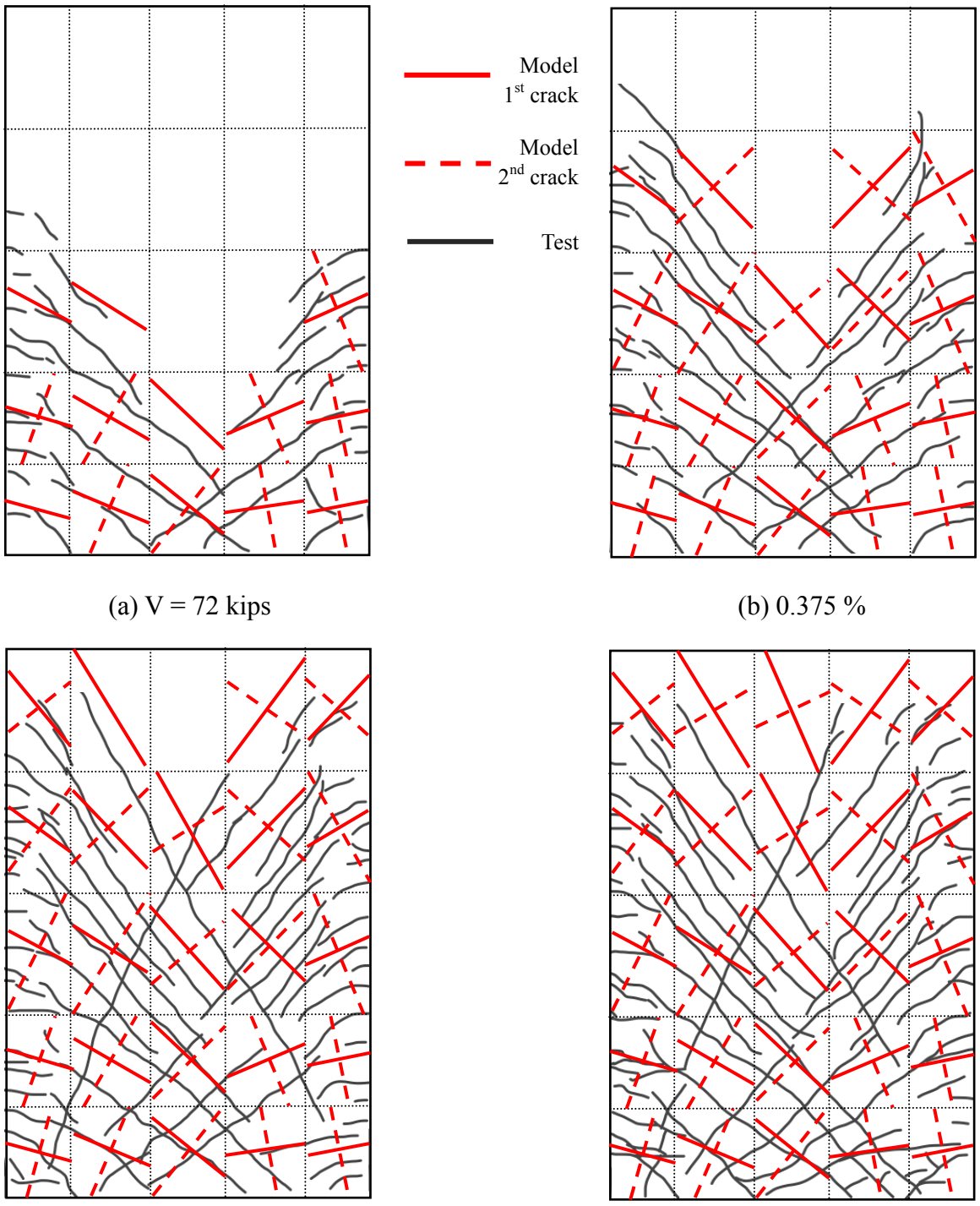

(a) V = 72 kips

(b) 0.375 %

(c) 1.0 % Drift

(d) 3.0 % Drift

Figure 6-9 Cracking Patterns for Specimen RW-A15-P10-S51, Test 3

6.2.4. Specimen RW-A15-P10-S78 – Test 4

Specimen RW-A15-P10-S78 had the same level of axial load and aspect ratio (1.5) as Test 3, but much higher average shear stress ($7.0\sqrt{f'_c}$ psi versus $4.9\sqrt{f'_c}$ psi or $0.58\sqrt{f'_c}$ MPa versus 0.41 $\sqrt{f'_c}$ MPa). Figure 6-10 compares experimentally observed and analytically predicted crack patterns for specimen RW-A15-P10-S78 at lateral load level of 356 kN (80 kips) and lateral drift levels of 0.75% and 2.0%. The initiation of cracking was observed in the experiment during the first cycle of the third force-controlled level, at the level of lateral load of 356 kN (80 kips, Figure 6-10(a)). Experimentally observed cracking pattern included horizontal (flexural) cracks between the wall-foundation interface to a height of approximately l_w (1.22 m or 48 in) at wall edges and three major inclined (shear) cracks on each side of the wall. The corresponding analytically predicted cracking pattern agrees with the experimental observations as shown on Figure 6-10(a); the first and second cracks formed in all RC panel elements of two bottom model element levels (up to height of 0.66 m or 24 in), and cracking was initiated at the wall boundary elements in the third model element level (up to height of 1.0 m or 40 in).

Although the cracking pattern of this wall was similar to that of RW-A15-P10-S51, the propagation of inclined cracks was more extensive in RW-A15-P10-S78. As can be observed in Figure 6-10(b) that, at a lateral drift of 0.75%, the inclined (shear) cracks propagate to the top of the wall specimen; accordingly, the analytical model predicts cracking in all RC panel elements in the wall model. Figure 6-10(c) illustrates that experimental and analytical cracking patterns at drift level of 2.0% are almost identical to that at 0.75%, suggesting that that for increasing levels

of applied lateral drift, the cracking pattern does not change in both experimental and analytical results (crack widths change).

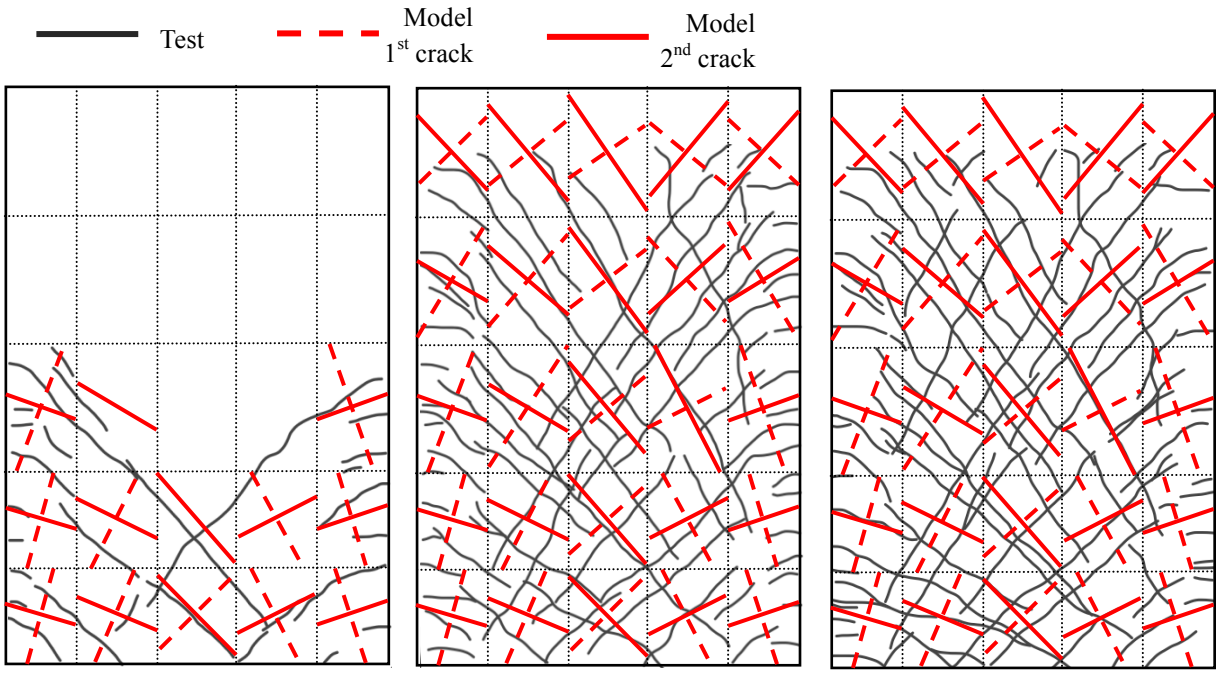

(a) V = 80 kips (b) 0.75 % Drift (c) 2.0 % Drift

Figure 6-10 Cracking Patterns for Specimen RW-A15-P10-S78, Test 4

6.2.5. Specimen RW-A15-P2.5-S64 – Test 5

This test specimen had the same reinforcement configuration as specimen RW-A15-P10-S78, except a slightly smaller web reinforcement ratio. The main difference between these two walls was the axial load ratio $P / A_g f'_c$, i.e., the axial load ratio of RW-A15-P2.5-S64 was only one-fourth of that of RW-A15-P10-S78 (0.016 $A_g f'_c$ versus 0.064 $A_g f'_c$).

The comparison of experimentally observed and analytically predicted cracking patterns at lateral load levels of 156 kN (35 kips), 331 kN (70 kips), and drift levels of 0.5% and 2.0% are presented in Figure 6-11. First cracking in RW-A15-P2.5-S64 in the experiment is formed during the first cycle of the second force-controlled level (V_y/4; 156 kN or 35 kips) and consisted of two short inclined (shear) cracks on each side of the wall (Figure 6-11(a)). At the same level of lateral load the analytical model predicts similar cracking pattern, consisting of slightly inclined cracks in panel elements located at the bottom of the wall at the wall boundaries (Figure 6-11(a)). As it can be observed on Figure 6-11(a), cracks predicted at the level of lateral load equal to 156 kN (35 kips) tend to be shallower than the cracks observed during the experiment.

The propagation of cracks in this wall was similar to that of RW-A15-P10-S78; however, the angle of inclined cracks obtained experimentally and analytically were shallower in RW-A15-P2.5-S64; the inclination of inclined cracks increased when they became closer to the opposite boundary zone. Figure 6-11(b) illustrates that, at applied lateral load of 331 kN (70 kips), cracking propagated approximately up to the height of 3/4h_w above the wall-foundation interface in both experimental and analytical results. In addition, the orientation of cracks is more diagonal at higher levels of the test specimen as well as the wall model suggesting that analytical results describe reasonably well not only propagation of concrete cracking, but also the orientation of concrete cracks along the wall height.

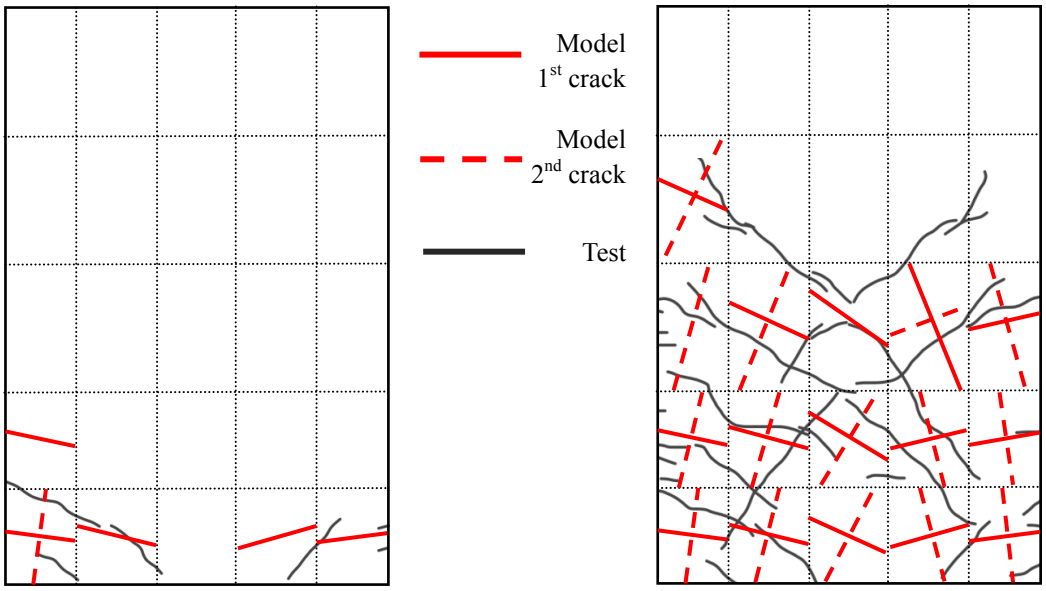

(a) V= 35 kips (b) V = 70 kips

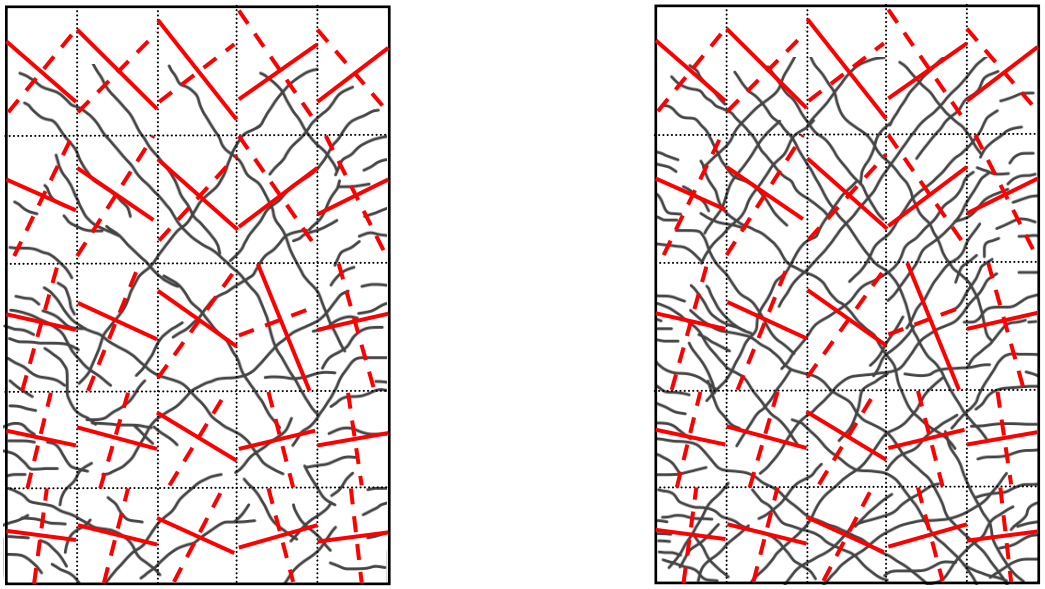

(b) 0.5% Drift (c) 2.0% Drift

Figure 6-11 Cracking Patterns for Specimen RW-A15-P2.5-S64, Test 5

At the applied lateral drift of 0.5% (Figure 6-11(c)), the cracking pattern in the experiment propagated to the top of the wall specimen; similarly, the analytical predictions show that the

first and the second crack developed in all RC panel elements in the wall model. In addition, the model predicts reasonably well the orientation of cracks over the wall height (Figure 6-11(c)). As shown on Figure 6-11(d), experimentally observed cracking pattern at lateral drift of 2.0% is not significantly different from the pattern observed at lateral drift of 0.5% (Figure 6-11(c)) (i.e., cracks are slightly denser, but their orientation remained the same), whereas the cracking pattern predicted by the analytical model at 2.0% drift is identical to that at 0.5% drift.

6.3. Total Displacement Profiles

This section provides comparisons of total lateral displacement profiles measured during the experiments and obtained using the analytical model for the five RC wall specimens tested by Tran and Wallace (2012). Total displacement profiles were determined at maximum displacements during the first cycle under positive and negative loadings for both experimental and analytical results. As described in Section 5.2.1, the discretization of wall models in the vertical direction (along the height of the wall) was selected to agree with locations of sensors placed on wall specimens during experiments to enable direct comparisons between analytically predicted and experimentally measured wall responses, which is at height levels of 24 in. (610 mm), 40 in. (1016 mm), 56 in. (1422 mm), 72 in. (1829 mm), and 96 in. (2438 mm).

From experimental results, total lateral displacements were calculated by the use of external sensors installed in “X” configuration as shown on Figure 6-12.

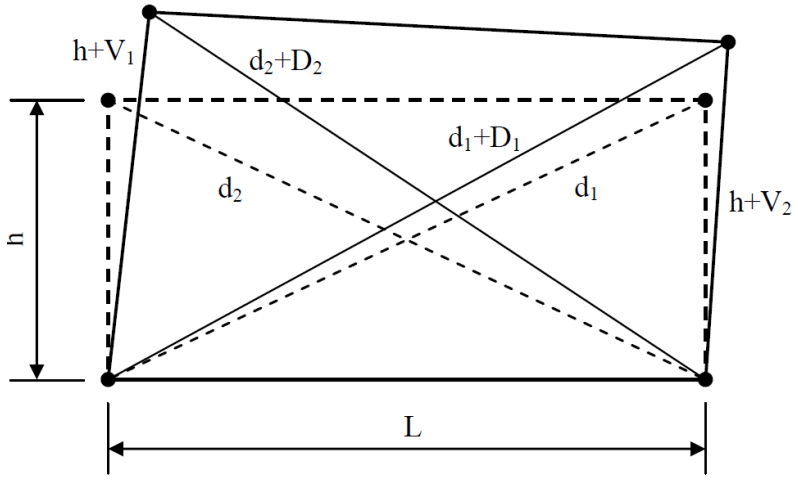

Figure 6-12 Deformation of a wall section (Tran, 2012)

Based on measurements from these sensors, total lateral displacement was obtained as:

$$\Delta_{total} = \frac{\sqrt{(d_1 + D_1)^2 - (h + V_2)^2} - \sqrt{(d_2 + D_2)^2 - (h + V_1)^2}}{2}$$

where d_1 and d_2 are original lengths of the two diagonal sensors, D_1 and D_2 are displacements measured from these diagonal sensors, h is the height of the wall section, and V_1 and V_2 are displacements measured from vertical sensors (Figure 6-12). Analytically predicted profiles of total lateral displacement are obtained from horizontal degrees of freedom of each model element at their top and bottom nodes.

The comparisons of experimentally measured and analytically predicted total lateral displacement profiles for Tests 1 to 5 are presented on Figure 6-13 to Figure 6-17, respectively. Experimentally measured profiles for wall specimens in Tests 1 to 4, which had the same design axial load of $0.10A_g f'_c$, are almost linear over the wall height at all applied lateral drift levels. The analytical model predicts reasonably well the displacement profiles for these wall specimens, i.e.,

the model predicts almost linear displacement profiles for all drift levels except the last drift level of 3.0%. The model underestimates wall lateral displacements over the height of $h_w/2$ from the wall base by approximately 10-15% for Tests 1, 2 and 3, and overestimates by 15% for Test 4. For wall specimen in Test 5, with low design level of axial load equal to $0.025A_g f'_c$, experimentally measured displacement profiles are almost linear at all lateral drift levels except at a lateral drift of 3.0%, at which lateral displacements are larger. For this specimen, the correlation between analytical and experimental lateral displacement profiles is good at lower drift levels of 0.5% and 0.75% as well as a drift level of 3.0%, whereas at the intermediate drift levels (e.g., 1.0%, 1.5% and 2.0%), the analytical model tends to overestimate wall lateral displacements up to the wall height of $h_w/2$ by approximately 20-30%.

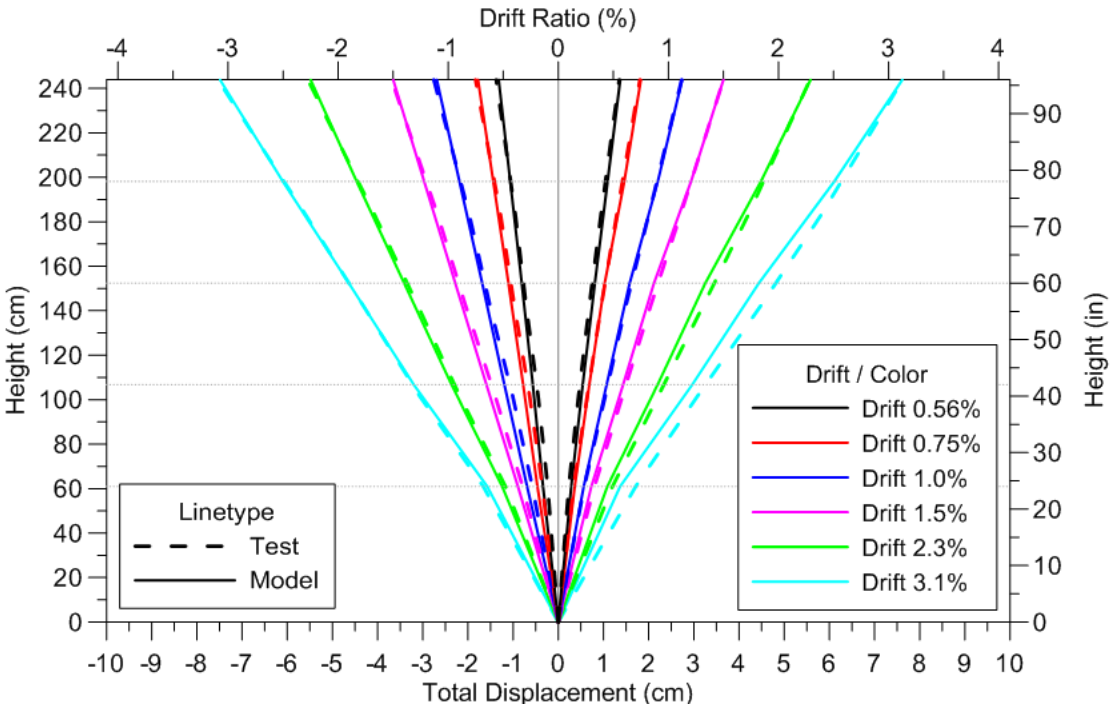

Figure 6-13 Total Displacement Profile Specimen RW-A20-P10-S38, Test 1

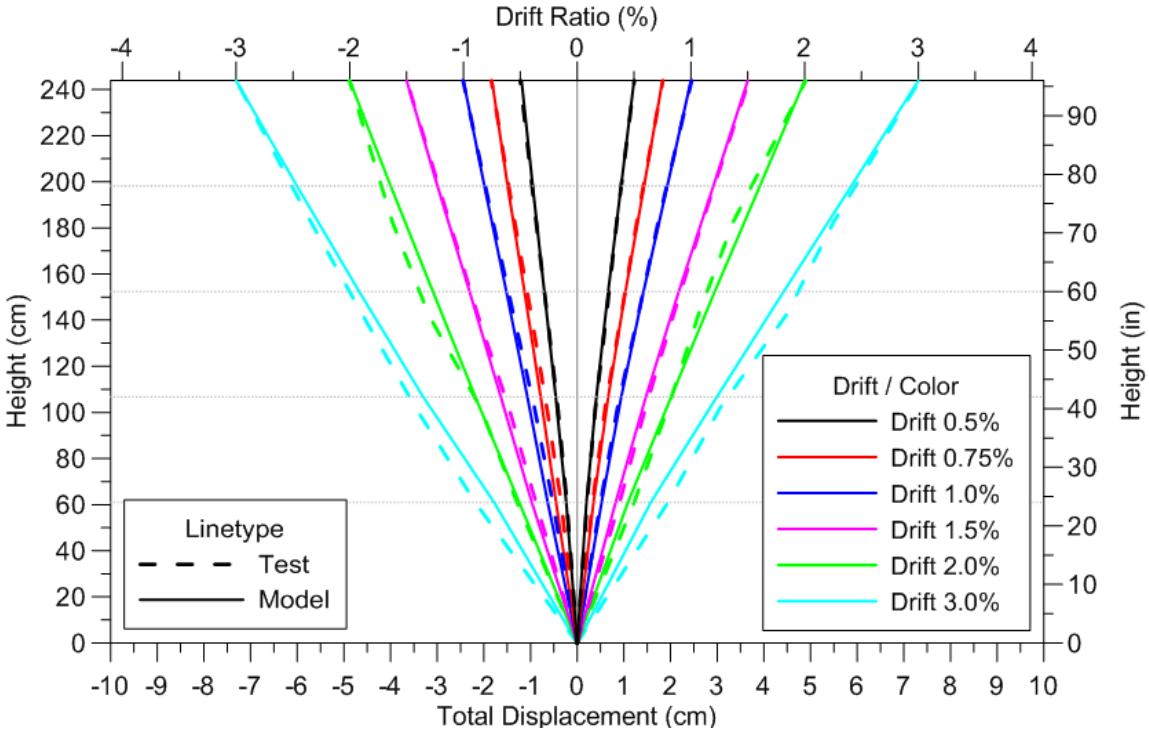

Figure 6-14 Total Displacement Profile for Specimen RW-A20-P10-S63, Test 2

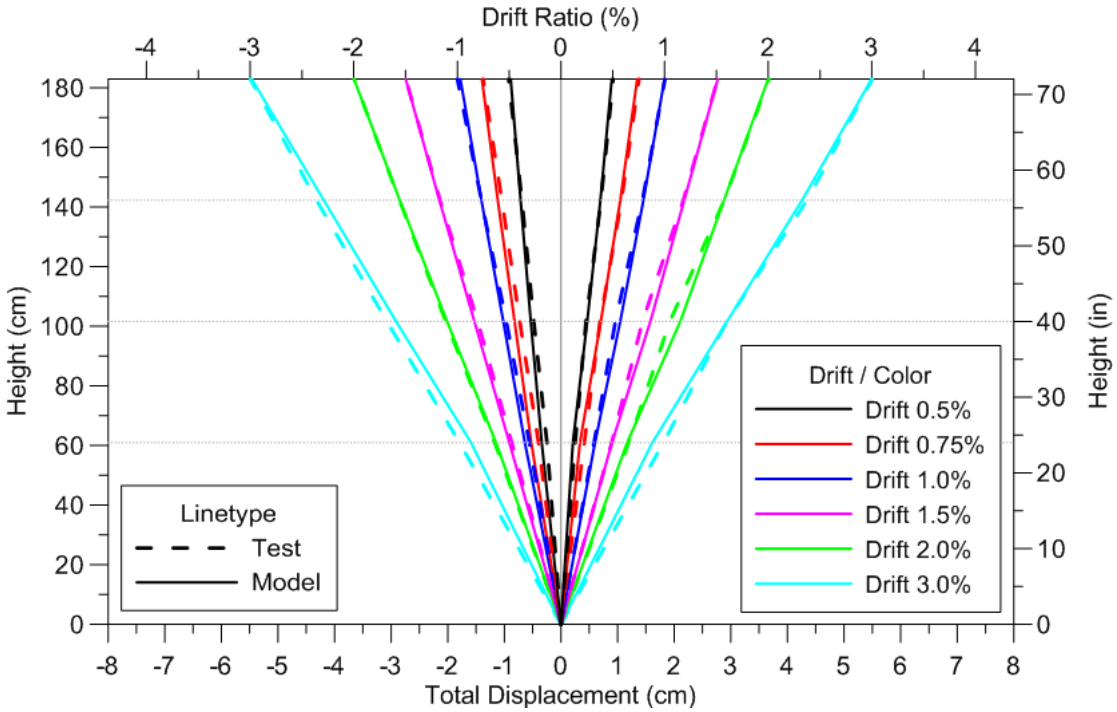

Figure 6-15 Total Displacement Profile for Specimen RW-A15-P10-S51, Test 3

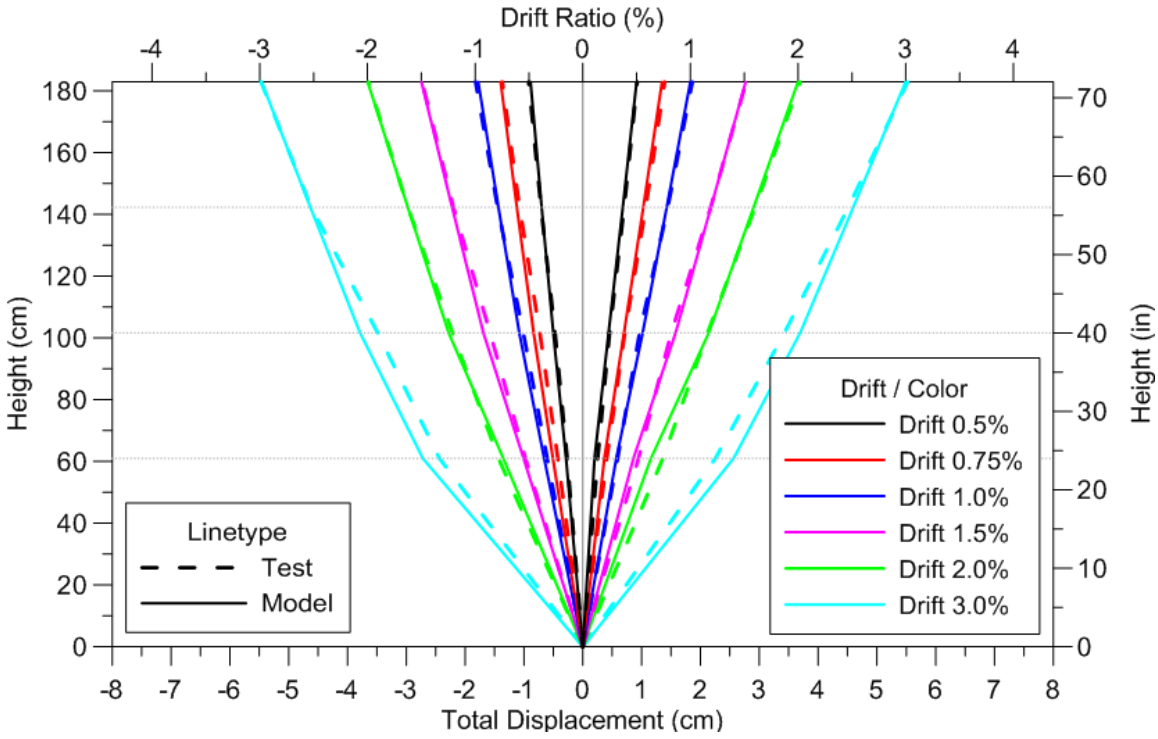

Figure 6-16 Total Displacement Profile for Specimen RW-A15-P10-S78, Test 4

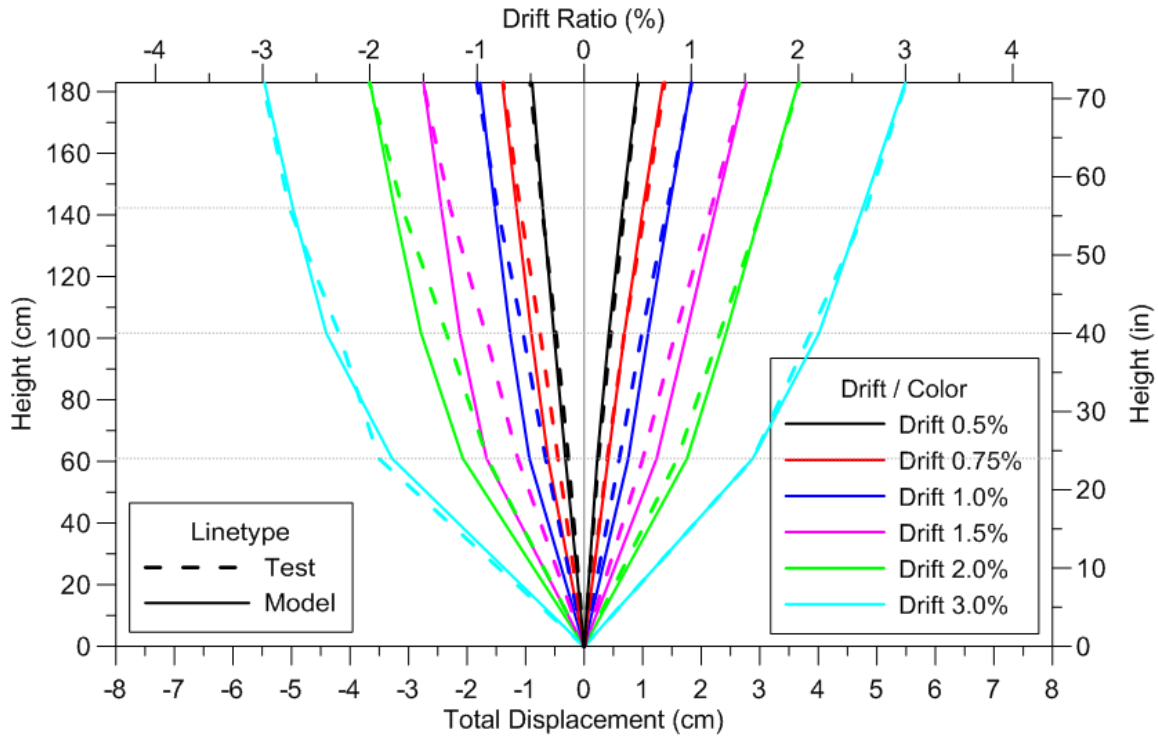

Figure 6-17 Total Displacement Profile for Specimen RW-A15-P2.5-S64, Test 5

6.4. Wall Vertical Growth

6.4.1. Vertical Growth versus Top Lateral Displacement Relations

Comparisons of experimentally measured and analytically predicted vertical-growth versus lateral-displacement relations for Tests 1 to 5 are shown on Figure 6-18 to Figure 6-22, respectively. The experimentally measured relations indicate that vertical growths of Tests 1 to 4, which had the same design axial load of $0.10A_g f'_c$, were very similar for cycles up to 2.0% drift, whereas the vertical growth of the wall with low axial load ratio (Test 5) was larger than that of the other walls for cycles up to 2.0% drift. For Tests 4 and 5, during subsequent cycles at 3.0% drift ratio, wall vertical growth was slower or remained unchanged, due to substantial in-plane buckling of boundary longitudinal reinforcement at both wall boundaries.

It can be observed from the figures that analytical model is able to capture vertical growth at the top of all five RC wall specimens. Presented results reveal that the analytical model underestimates the magnitude of vertical growth at peak lateral drifts by approximately 40% for Tests 1 (Figure 6-23) and Test 5 (Figure 6-27), and 30% for Test 2 (Figure 6-24), whereas for Tests 3 (Figure 6-25) and Test 4 (Figure 6-26) the vertical growth was reasonably well predicted. In addition, the model significantly underestimates the residual vertical growth at zero lateral displacement for specimens with low shear stress (i.e., Tests 1 and 3), whereas for specimens with moderately high and high shear stress (i.e., Tests 2, 4 and 5) the residual vertical growth is captured reasonably well by the model.

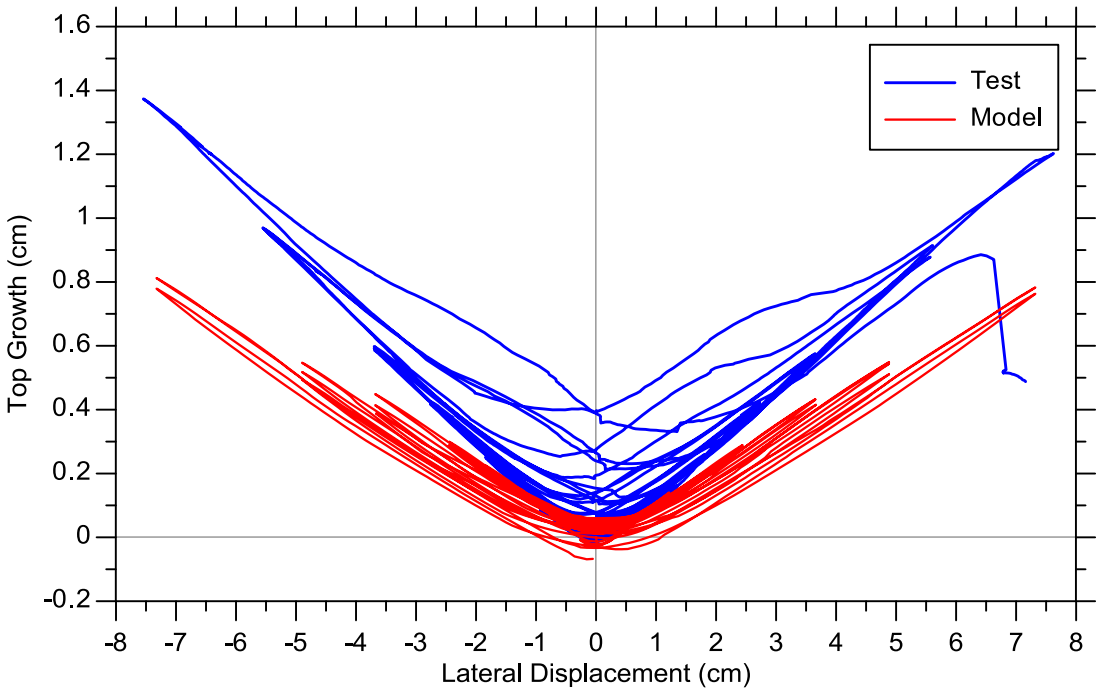

Figure 6-18 Vertical Growth versus Lateral Displacement for RW-A20-P10-S38, Test 1

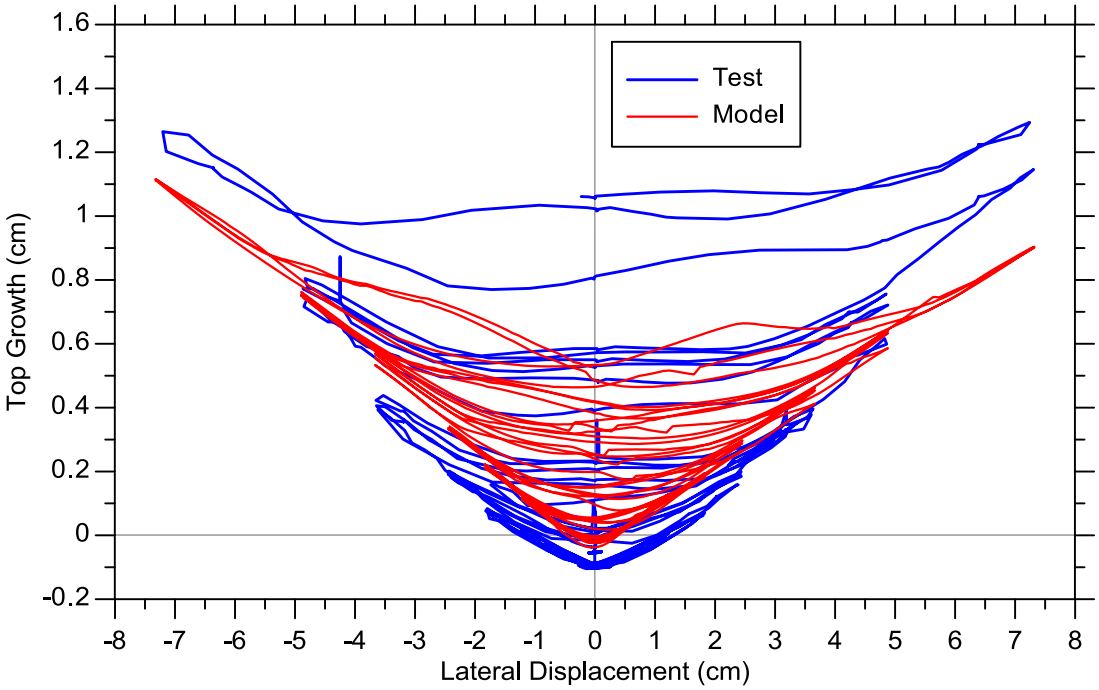

Figure 6-19 Vertical Growth versus Lateral Displacement for RW-A20-P10-S63, Test 2

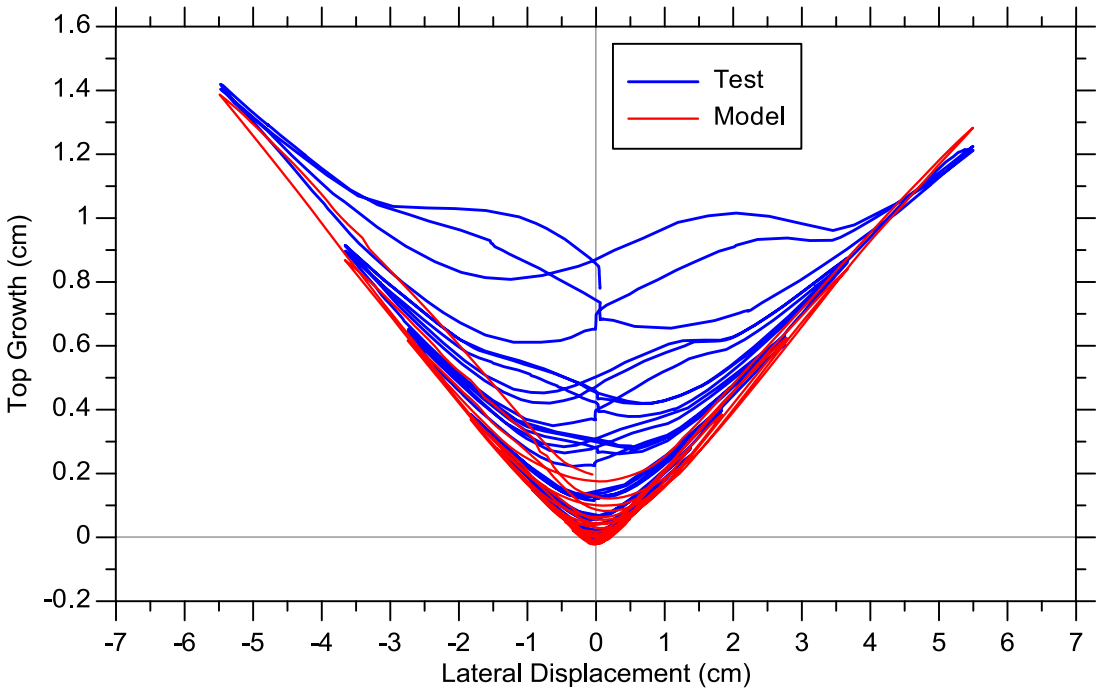

Figure 6-20 Vertical growth versus lateral displacement for RW-A15-P10-S51, Test 3

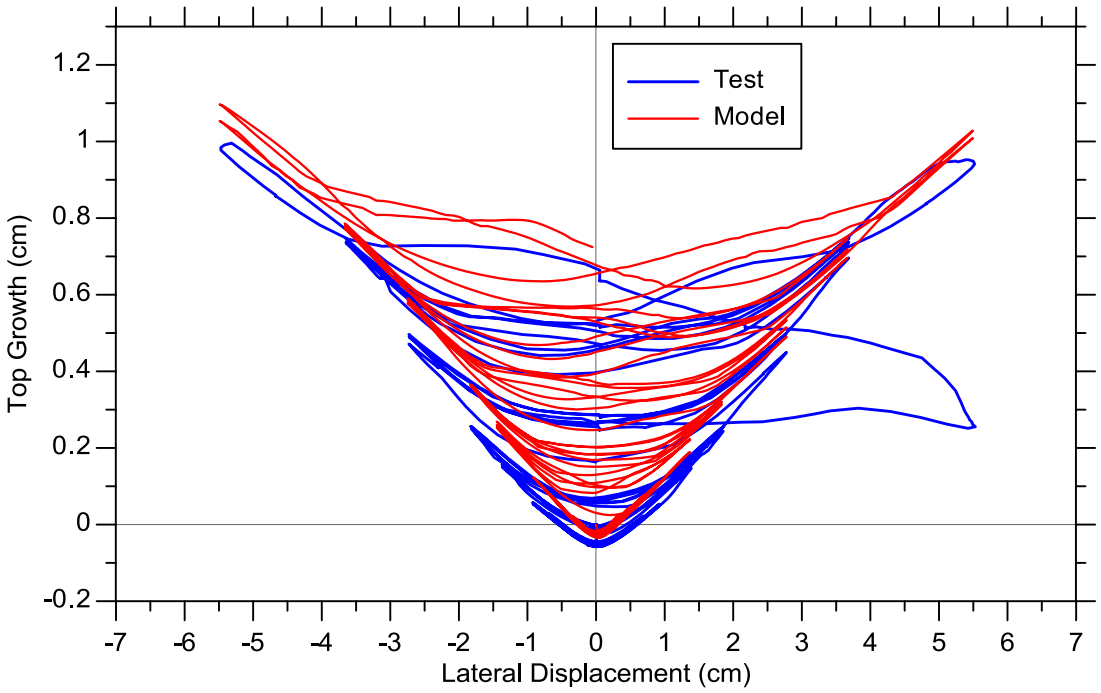

Figure 6-21 Vertical growth versus lateral displacement for Test 4, RW-A15-P10-S78

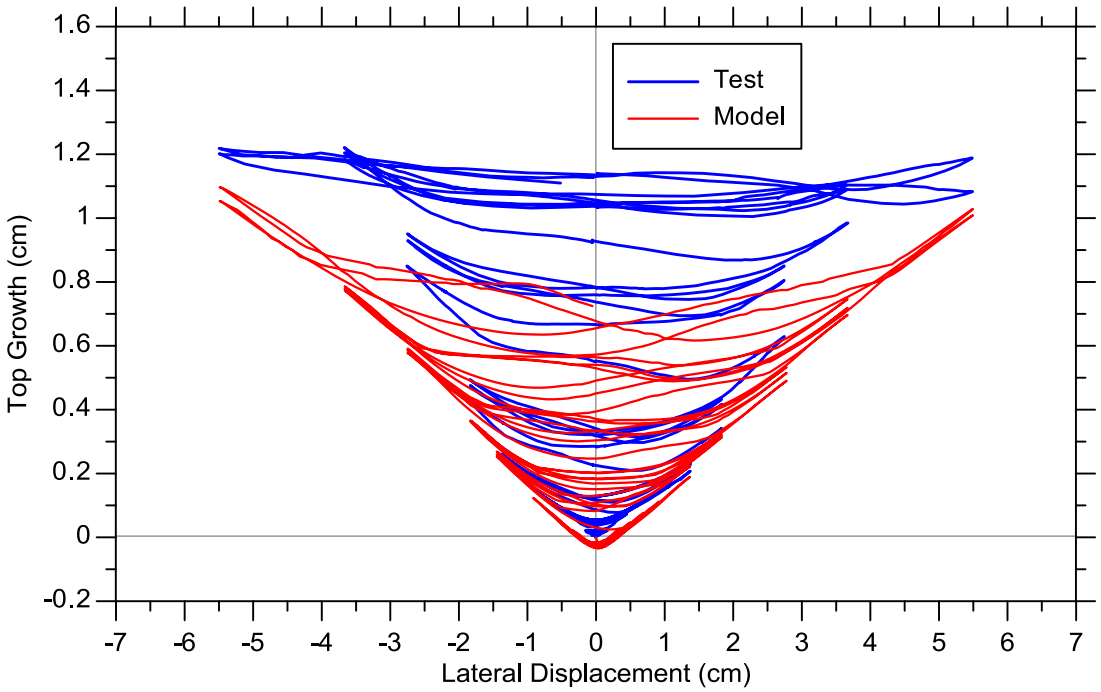

Figure 6-22 Vertical growth versus lateral displacement for Test 5, RW-A15-P2.5-S64

6.4.2. Vertical growth profiles

Experimentally measured and analytically predicted profiles of vertical growth over the wall height for Tests 1 to 5 are presented in Figure 6-23 to Figure 6-27, respectively. In these profiles, vertical growth was determined, both analytically and experimentally, at peak drift levels for the first cycle under both positive and negative loading. As mentioned earlier, the wall discretization is in agreement with the locations of wall instrumentation used to measure vertical growth; therefore, the experimental and analytical vertical growth profiles were obtained at height levels of 24 in (610 mm), 40 in (1016 mm), 56 in (1422 mm), 72 in (1829 mm), and 96 in (2438 mm) above the wall base.

Figure 6-23 to Figure 6-27 show that, at low drift levels (e.g. 0.5% and 0.75%), the experimentally measured distributions of vertical growth are almost linear, whereas the analytical model predicts larger vertical growth closer to the base of the walls, over a wall height of approximately $h_w/2$, resulting in nonlinear vertical growth profiles even at low drift levels; the values of vertical growth at the top of the walls are reasonably well predicted. After yielding of boundary longitudinal reinforcement, vertical growth profiles become considerably nonlinear in both experimental and analytical results, with significant contribution coming from the deformation over a wall height of $l_w / 2$ from the wall base (the plastic hinge region). Overall, the analytical model describes reasonably well the shape of vertical growth profiles and the magnitude of vertical growth along the wall height at most of the drift levels. The most accurate predictions are obtained for Test 3, where the model predicts vertical growth profiles with error less than 10% at all drift levels. For other test specimens (Tests 1, 2, 4 and 5), analytical results are within 10 to 30 % of the experimentally measured vertical growth profiles. The model predictions are generally not accurate at drift level of 3.0% where various failure modes were observed during the experiments (e.g. shear sliding, instability along the wall base) that were not captured in the analysis.

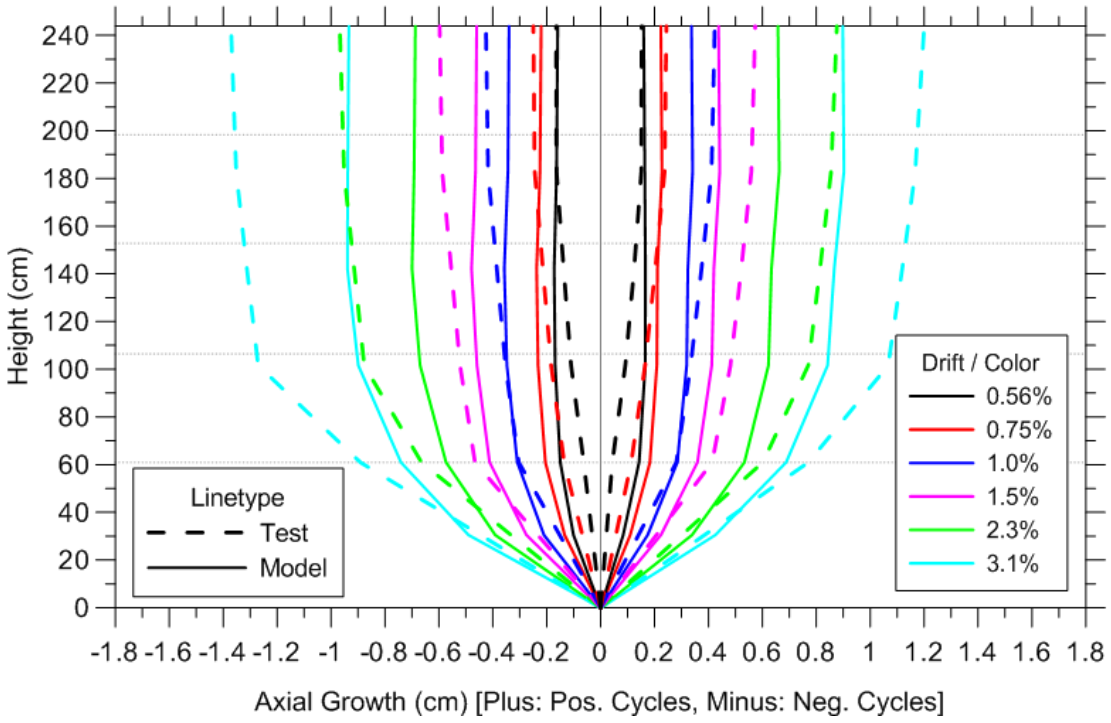

Figure 6-23 Vertical Growth Profile for Specimen RW-A20-P10-S38, Test 1

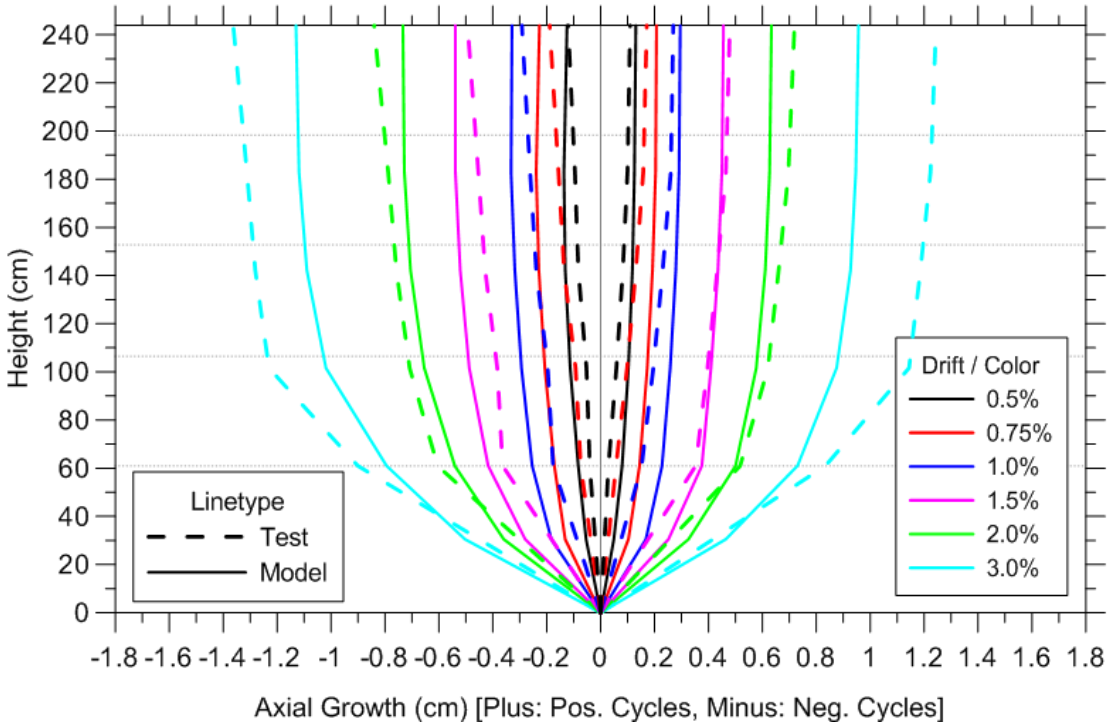

Figure 6-24 Vertical Growth Profile for Specimen RW-A20-P10-S63, Test 2

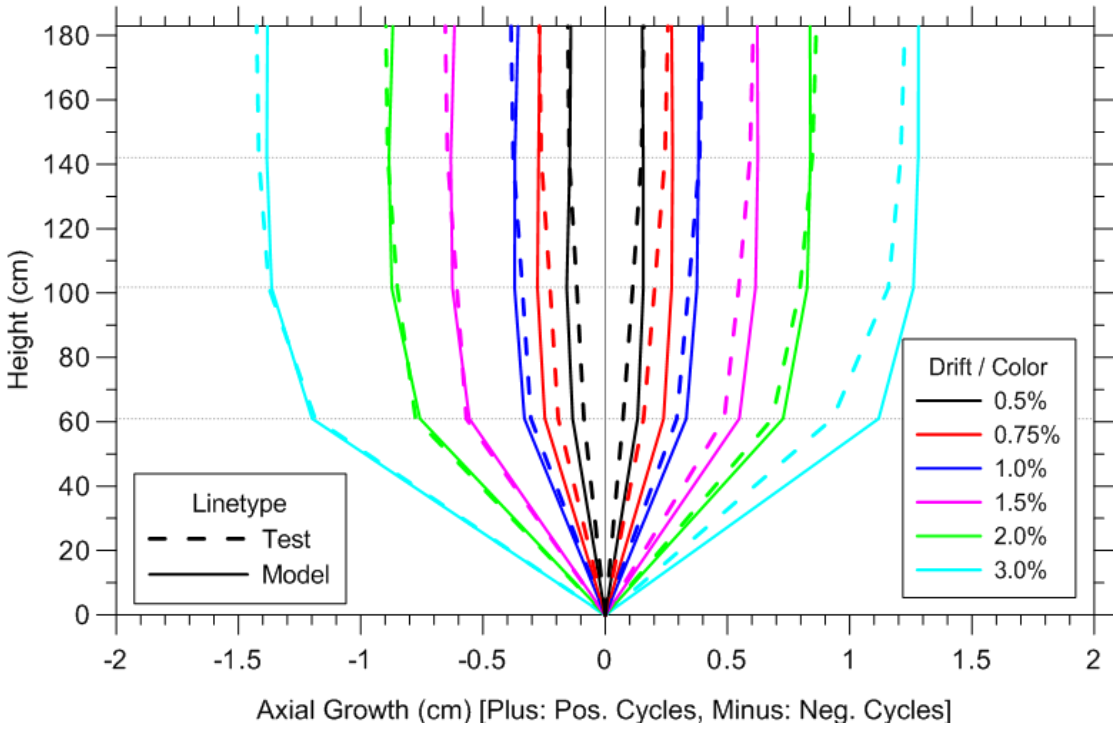

Figure 6-25 Vertical Growth Profile for Specimen RW-A15-P10-S51, Test 3

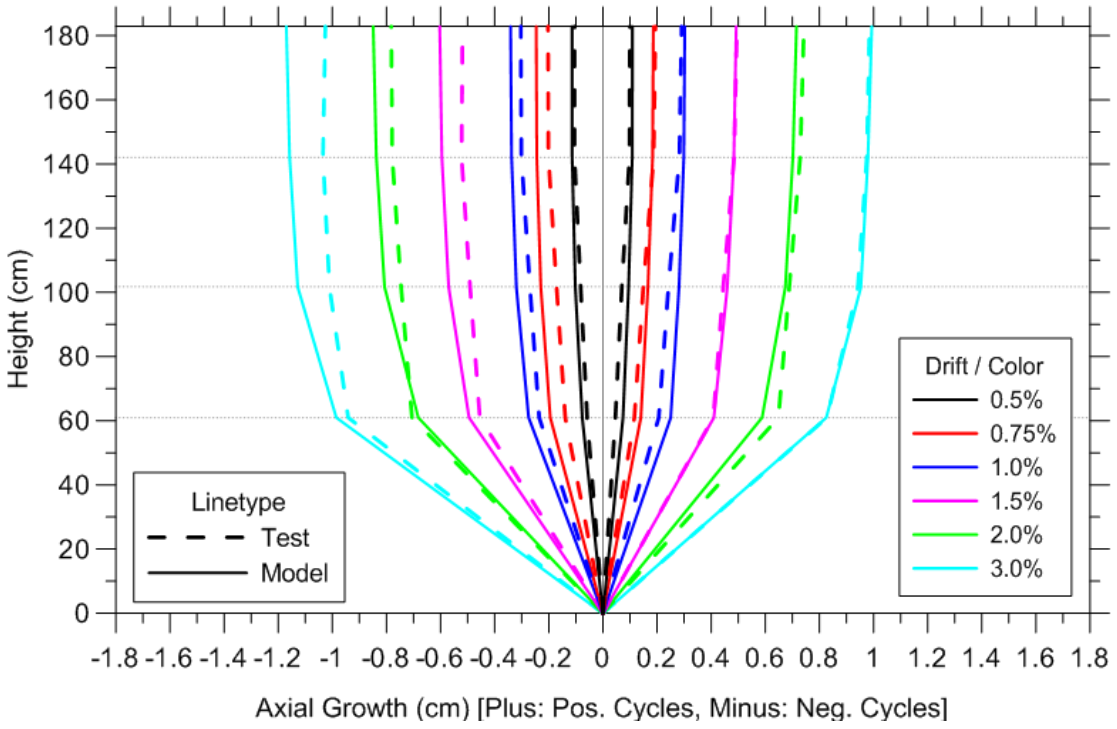

Figure 6-26 Vertical Growth Profile for Specimen RW-A15-P10-S78, Test 4

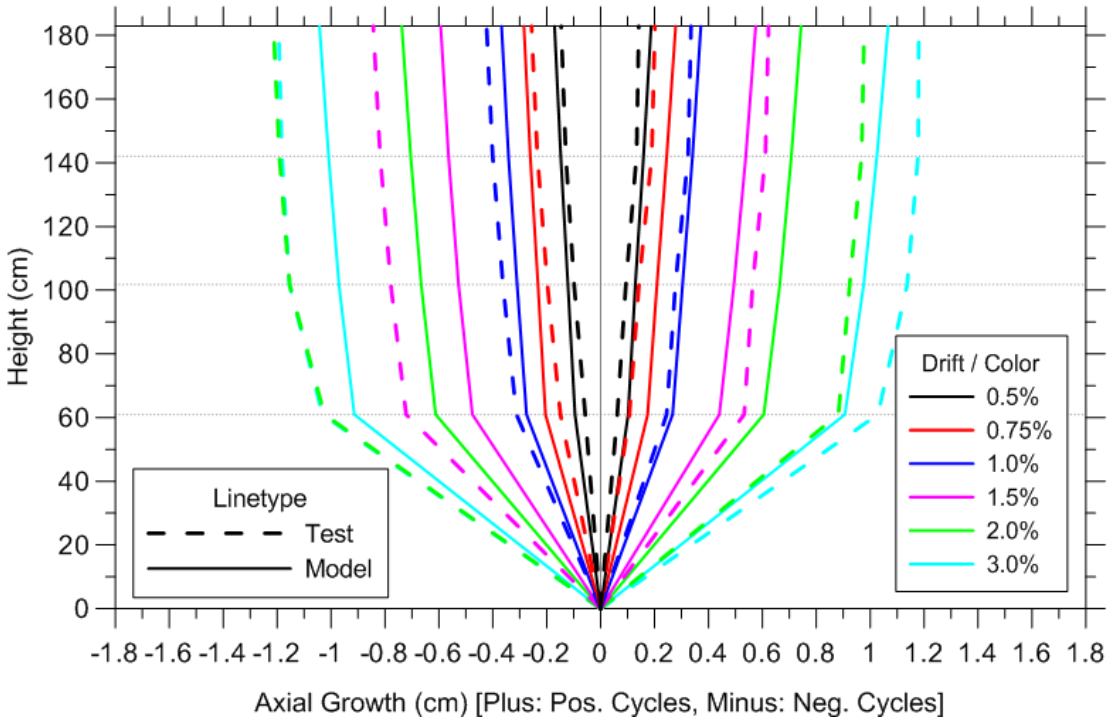

Figure 6-27 Vertical Growth Profile for Specimen RW-A15-P2.5-S64, Test 5

6.5. Components of Lateral Displacement

This section presents a comparison of experimentally measured and analytically predicted flexural and shear deformation components of wall lateral displacement. The results are presented in terms of load-versus-deformation-component relations, deformation profiles along the height of the wall, and contributions of each deformation component to total lateral displacement.

6.5.1. Flexural Component of Lateral Displacement

Flexural displacements of a wall section of height h are derived from the definition of the location of center of curvature distribution (Figure 6-28) as:

$$\alpha h = \frac{\int_0^h \Phi x dx}{\int_0^h \Phi dx} = \frac{\Delta_f}{\theta} \Rightarrow \Delta_f = \alpha \theta h \tag{6-1}$$

where Δ_f is the flexural lateral displacement at the top of the wall section, α is the relative distance from the top of the wall section to the centroid of the curvature diagram, h is the height of the wall section, θ is the rotation at the top of the wall section, and $\Phi = \Phi(x)$ is the curvature of the wall section at location x (Figure 6-28).

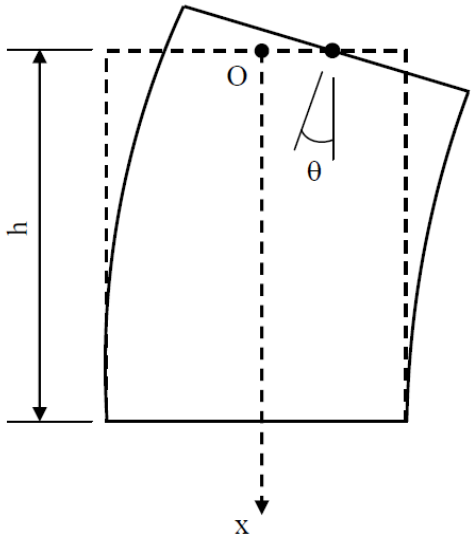

Figure 6-28 Calculation of Flexural Deformation for a Wall Section in Experiment (Tran, 2012)

The rotation θ at the top of the wall section is obtained as:

$$\theta = \frac{V_1 - V_2}{L} \tag{6-2}$$

where V_1 and V_2 are vertical displacements measured from two lines of vertical sensors near the wall edges and L is the horizontal distance between the sensors. Details about the calculation of flexural displacements from experimental data can be found in dissertation by Tran (2012).

For the analytical results, flexural deformations of a wall model element (corresponding to a wall section of experimental wall specimen) can be calculated from the rotation (Φ) at the center of rotation of an element located at the height *ch* (Figure 6-29) as:

$$\Delta_f = \Phi(1-c)h \tag{6-3}$$

where h is the height of the model element, c = 0.4 as suggested by Vulcano et al. (1988) and verified by Orakcal and Wallace (2006).

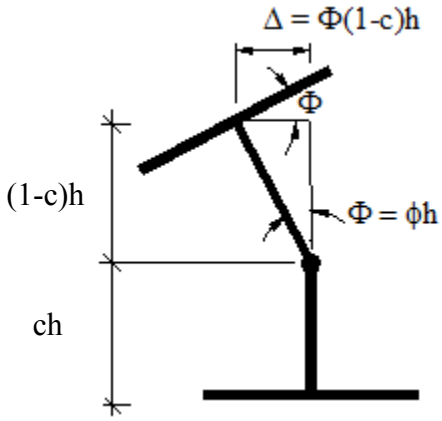

Figure 6-29 Calculation of Flexural Deformation for a Wall Element in the Model

Rotation of the model element (Φ) can then be obtained as:

$$\Phi = \phi h \tag{6-4}$$

assuming that the distribution of curvature (ϕ) along the element height is constant.

However, in this study, the flexural displacements (Δ_f) at the top of a model element are calculated simply by subtracting shear displacement (Δ_s) from the total lateral (Δ_{total}) displacement as:

$$\Delta_f = \Delta_{total} - \Delta_s \tag{6-5}$$

This method for obtaining flexural displacements in the analytical results is very suitable for the given model formulation because shear deformation of each model element ($u_{Sh} = \Delta_s$) is calculated during the analysis from displacements at 6 nodal degrees of freedom at the top and bottom of a model element $\{\delta_N\}$, as described in Section 6.6.2.

6.5.1.1. Lateral Load versus Flexural Displacement Relations

Comparisons of experimental and analytical relations of lateral-load-versus-flexural-displacement at the top of the wall specimens for Tests 1 to 5 are presented on Figure 6-30 to Figure 6-34, respectively. It can be observed from Figure 6-30 and Figure 6-31 that, for specimens with aspect ratio of 2.0, the shapes of load-versus-flexural-displacement diagrams resemble the shape of their load-versus-total-displacement responses shown in Figure 6-1 (Tests 1) and Figure 6-2 (Tests 2), suggesting that flexural deformations are dominant for these wall specimens. The main difference between the two load-flexural-displacement responses is that flexural deformations in RW-A20-P10-S63 (Test 2) were much smaller than those in RW-A20-P10-S38 (Test 1) at large drift ratios, although both of these two specimens reached about the

same drift levels prior to significant loss of lateral strength. Comparison between the relations for Tests 1 and 2 also indicates that the wall with higher shear stress has less pinching, probably due to larger compression and deeper compression zone, which would lead to more pullout, or slip/extension of vertical reinforcement, in the wall with lower shear. For both specimens with aspect ratio 2.0 (RW-A20-P10-S38 and RW-A20-P10-S63), the shape of load-flexural-displacement responses, flexural loading/unloading stiffness, as well as magnitudes of flexural deformations are predicted closely by the analytical model.

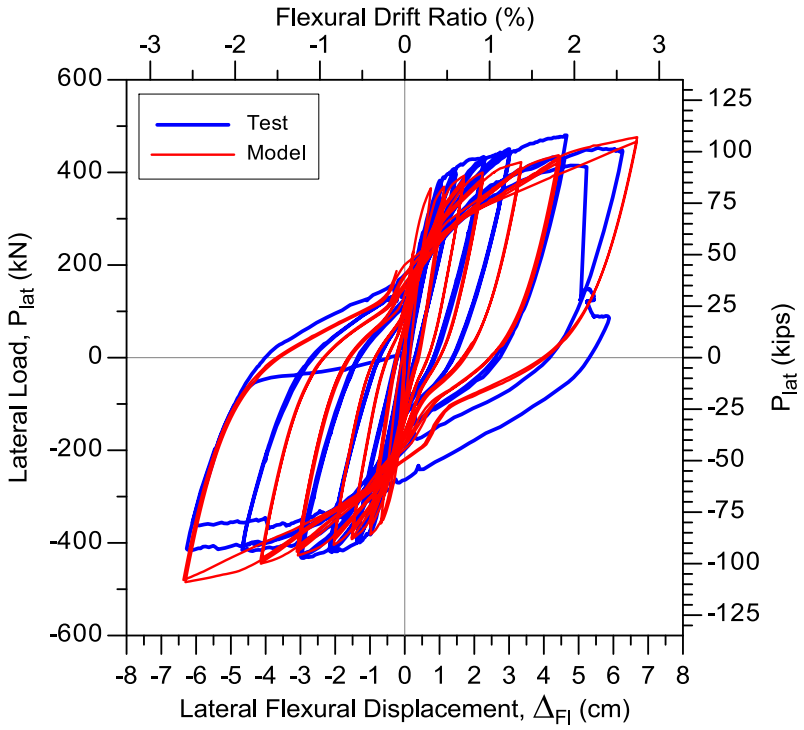

Figure 6-30 Top Flexural Displacement for Specimen RW-A20-P10-S38, Test 1

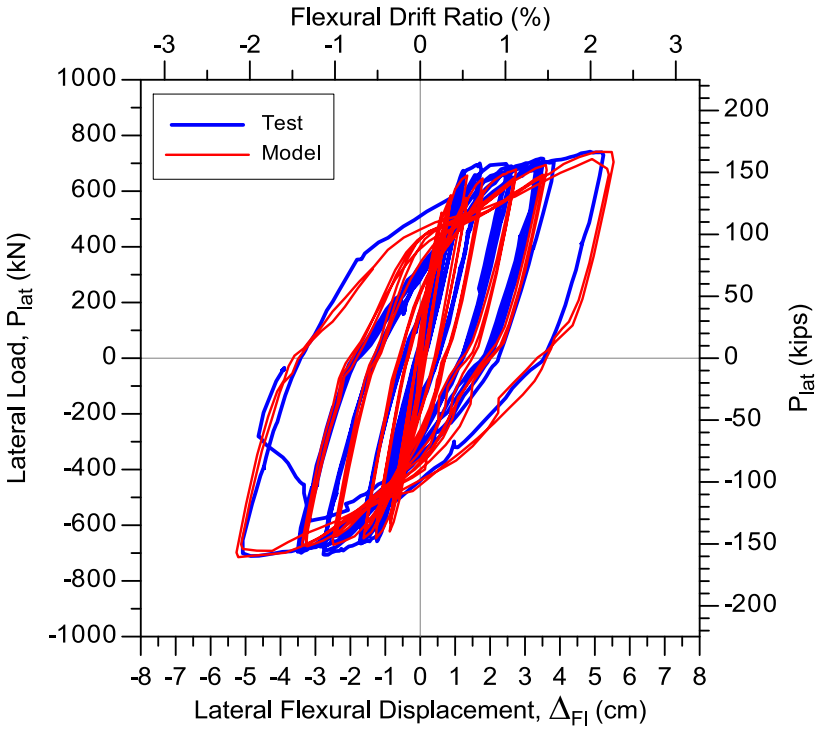

Figure 6-31 Top Flexural Displacement for Specimen RW-A20-P10-S63, Test 2

It can be observed from Figure 6-32 to Figure 6-34 that experimentally measured and analytically predicted load-versus-flexural-displacement diagrams for specimens with aspect ratio of 1.5 are characterized with the absence of pinching, whereas the load-versus-total-displacement diagrams for these specimens (Figure 6-3 to Figure 6-5 for Tests 3 to 5, respectively) are characterized with moderately-to-highly pinched shapes, suggesting that flexural deformations are less pronounced in the aspect ratio 1.5 wall specimens compared to the specimens with aspect ratio 2.0. Experimentally measured flexural displacements of Test 4 tend to be smaller than those of Test 3 during cycles at large drift levels, probably for the same reasons noted in the comparison of Tests 1 and 2. Analytically derived flexural deformations are within 5-10% of experimental results at all drift levels for Tests 3 and 4, except that for Test 4 analytical model overestimates flexural deformations by roughly 20% at lateral drift of 3.0% due

to sliding shear deformations at the base of the test specimen, which are not captured in the analysis, that reduced flexural deformations in experimental results. For Test 5, with relatively low axial load level, experimental results revealed that flexural deformations are much lower than those of Test 4 after yielding in boundary longitudinal reinforcement, which is reasonably well predicted in the analysis; for the same reason as in Test 4, the model overestimates flexural deformations at drift level of 3.0%. The model also predicts reasonably well flexural loading/unloading stiffness of wall specimens in Tests 1 to 3 throughout the entire cyclic history (even at lower drift levels), whereas for Test 5 (with lower level of axial load) the flexural stiffness is slightly overestimated.

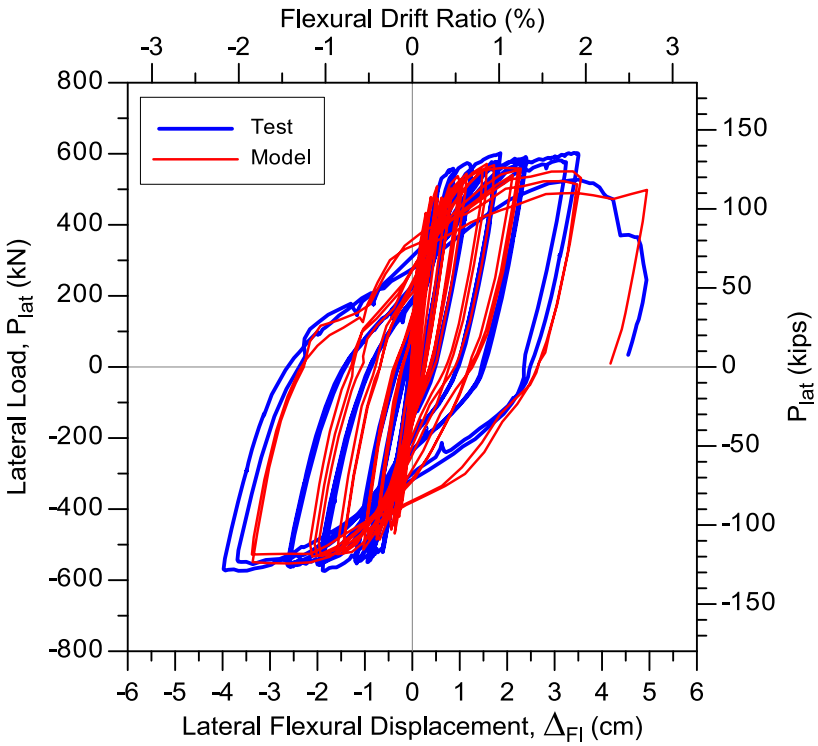

Figure 6-32 Top Flexural Displacement for Specimen RW-A15-P10-S51, Test 3

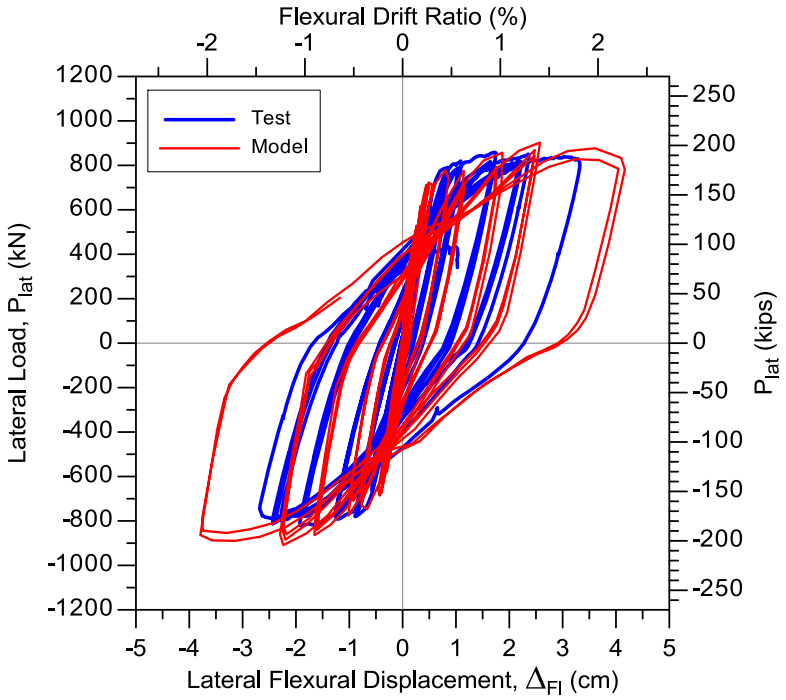

Figure 6-33 Top Flexural Displacement for Specimen RW-A15-P10-S78, Test 4

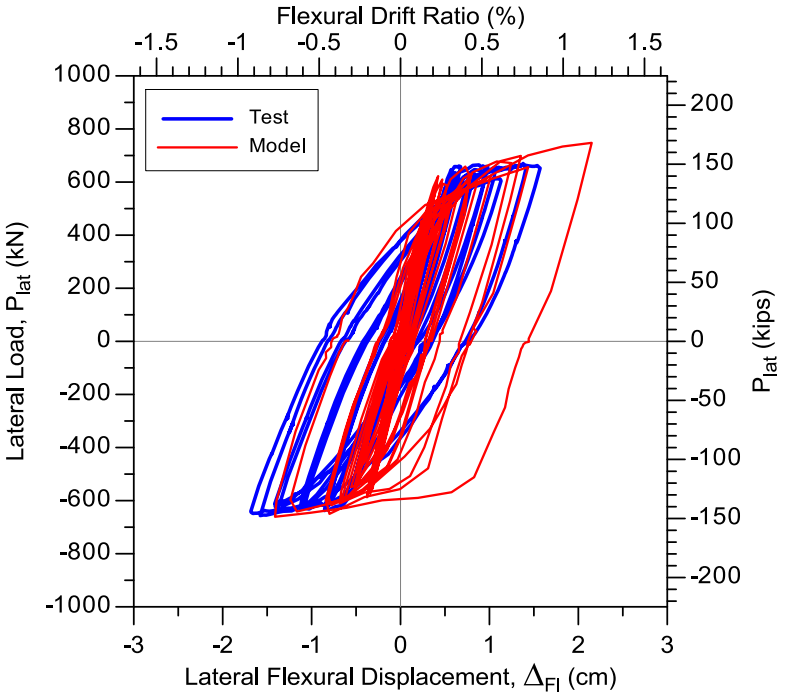

Figure 6-34 Top Flexural Displacement for Specimen RW-A15-P2.5-S64, Test 5

6.5.1.2. Flexural Displacement Profiles

Comparisons between experimental and analytical profiles of flexural displacements over the wall height for Tests 1 to 5 are presented on Figure 6-35 to Figure 6-39, respectively. In these profiles, flexural displacements were determined at the peak displacement during the first cycle to drift levels of 0.5%, 0.75%, 1.0%, 1.5%, 2.0%, and 3.0%, under both positive and negative loadings for experimental and analytical results. Flexural displacements during the test and analysis were obtained at 24 in. (610 mm), 40 in. (1016 mm), 56 in. (1422 mm), 72 in. (1829 mm), and 96 in. (2438 mm) above the wall-foundation block interface.

It can be observed from the figures that experimental and analytical flexural displacement profiles of all five wall specimens are nonlinear within the bottom region within the height of approximately $l_w/2$, whereas for wall sections above this height the flexural displacement profiles are almost linear, indicating that nonlinear flexural deformations were likely relatively small at these locations. Presented profiles of flexural deformations reveal that the model successfully captures the distribution of the nonlinear flexural deformations (i.e., shape of the flexural displacement profiles) along the wall height for all five test specimens.

The most accurate predictions of flexural displacement profiles were obtained for Test 1 (Figure 6-35) where the model captures closely flexural displacements at peak drift levels by overestimating them by only approximately 5-10%. For Test 2 (Figure 6-36) and Test 3 (Figure 6-37) the model predicts flexural displacement profiles with reasonable accuracy in negative and positive directions, respectively, whereas in the opposite loading direction the analytical results overestimate flexural deformations for about 25% on the average of all drift levels. Furthermore,

it can be observed form Figure 6-38 that for Test 4 the analytical model predicts flexural displacement profiles within 15% at all drift levels except at drift level of 3.0% where shear sliding was observed during the test at the wall-base interface; at this loading cycle the flexural displacement profiles predicted by the model are overestimated by approximately 40%. This behavior is even more pronounced in Figure 6-39 which reveals that the experimental flexural displacements for Test 5 are decreased at 3.0% drift in comparison to 2.0% drift, as well as that there is only a slight increase in flexural deformations for this wall between 1.5% and 2.0% drift, indicating that significant sliding deformations were likely initiating between these drift levels, which was not captured in the analysis. Therefore, flexural displacement profiles are not very well predicted by the model for Test 5.

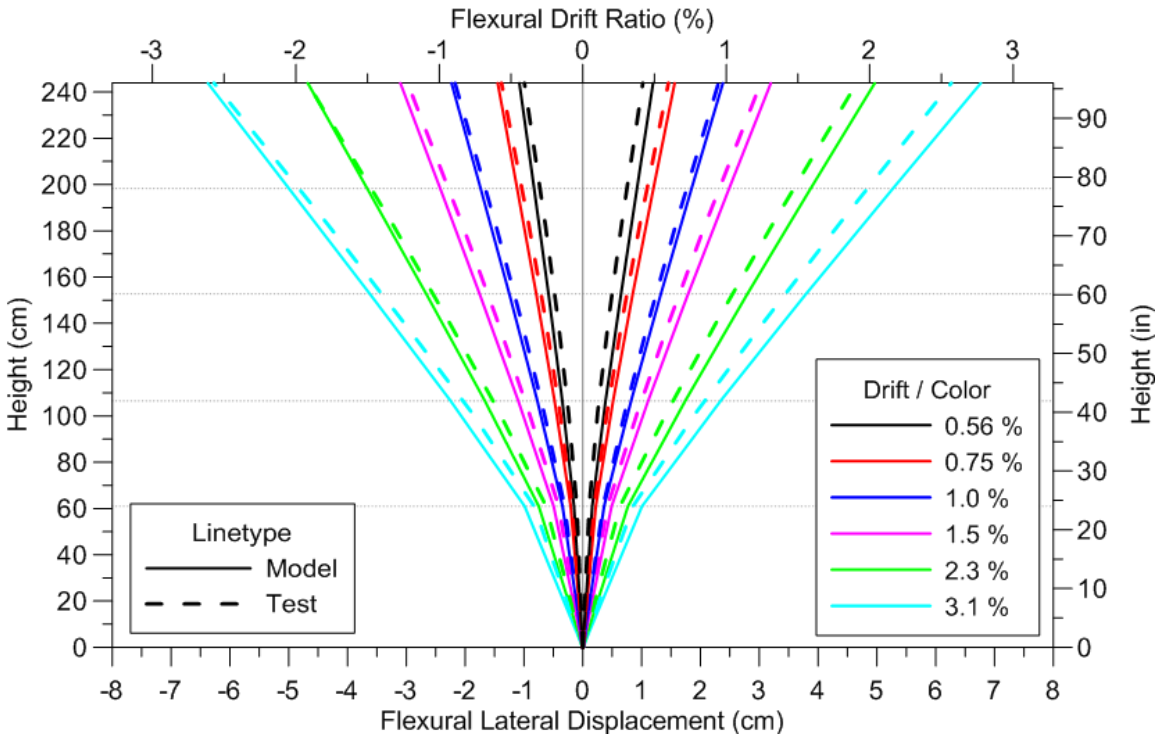

Figure 6-35 Flexural Displacement Profiles for Specimen RW-A20-P10-S38, Test 1

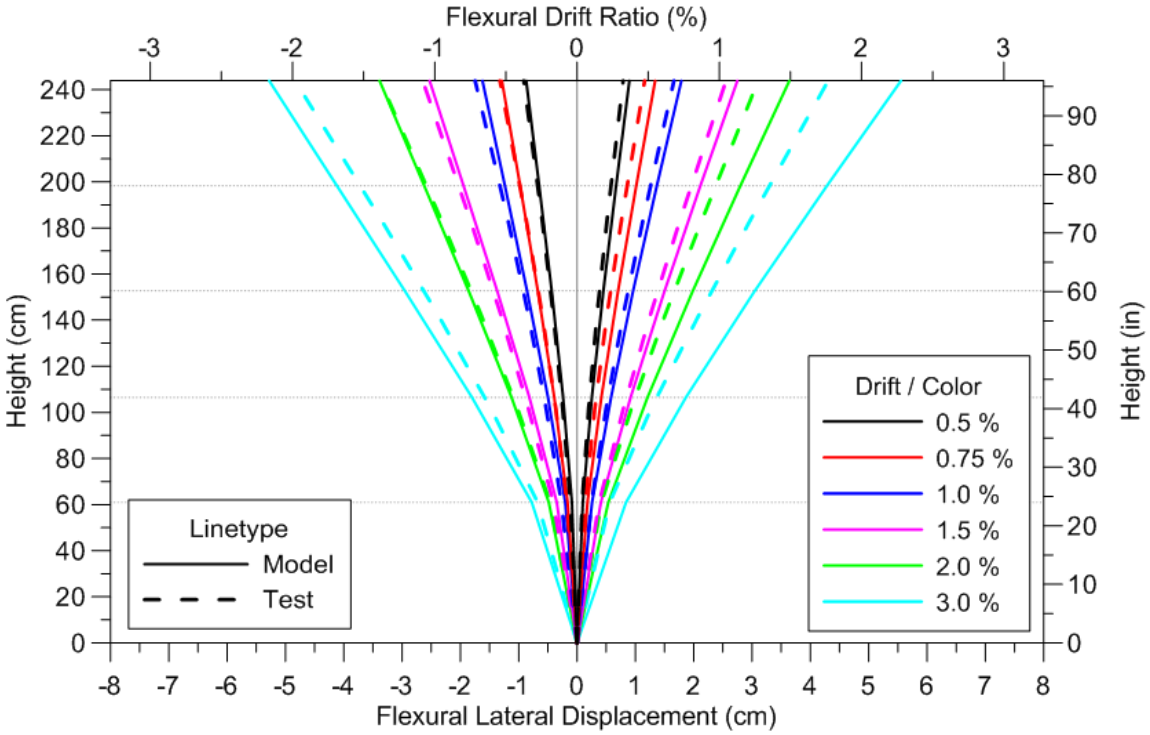

Figure 6-36 Flexural Displacement Profile for Specimen RW-A20-P10-S63, Test 2

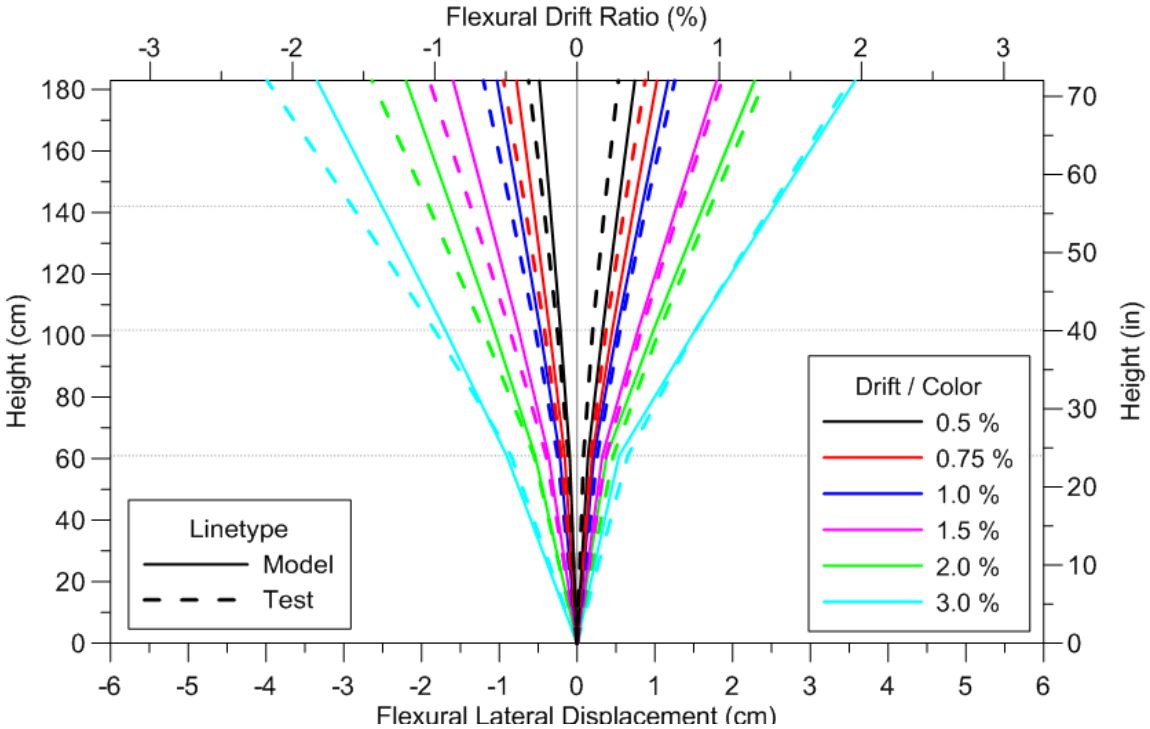

Figure 6-37 Flexural Displacement Profile for Specimen RW-A15-P10-S51, Test 3

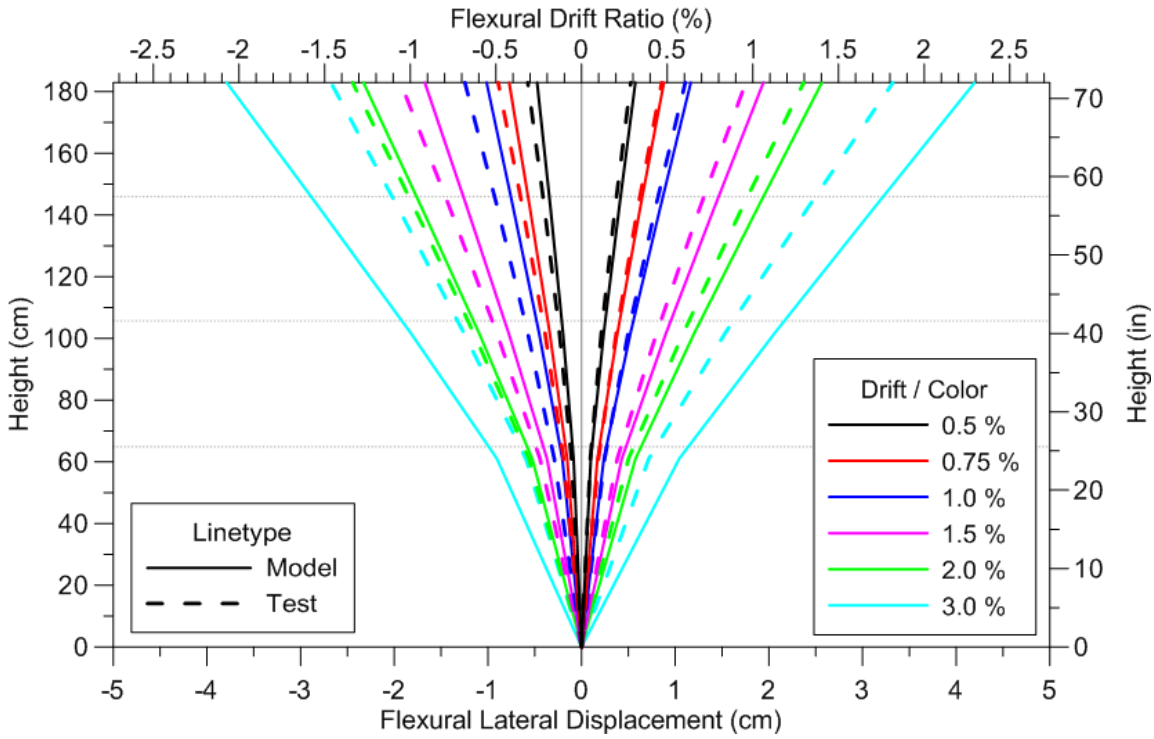

Figure 6-38 Flexural Displacement Profile for Specimen RW-A15-P10-S78, Test 4

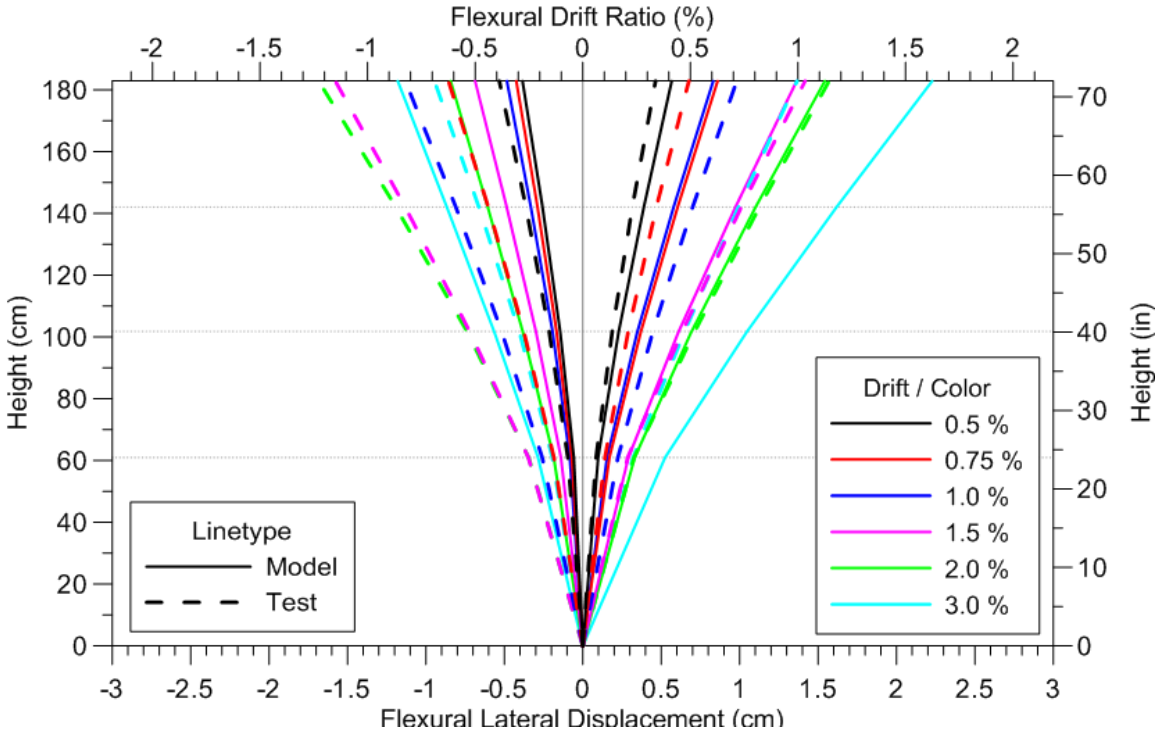

Figure 6-39 Flexural Displacement Profile for Specimen RW-A15-P2.5-S64, Test 5

6.5.2. Shear Component of Lateral Displacement

Two methods were considered to obtain shear deformations from the experimentally measured data. Shear deformations can be obtained directly from an "X" configuration as:

$$\Delta_s = \frac{\sqrt{(d_1 + D_1)^2 - h^2} - \sqrt{(d_2 + D_2)^2 - h^2}}{2} \tag{6-6}$$

where d_1 and d_2 are original lengths of the two diagonal sensors, D_1 and D_2 are displacements measured from these diagonal sensors, h is the height of the wall section, as shown on Figure 6-40.

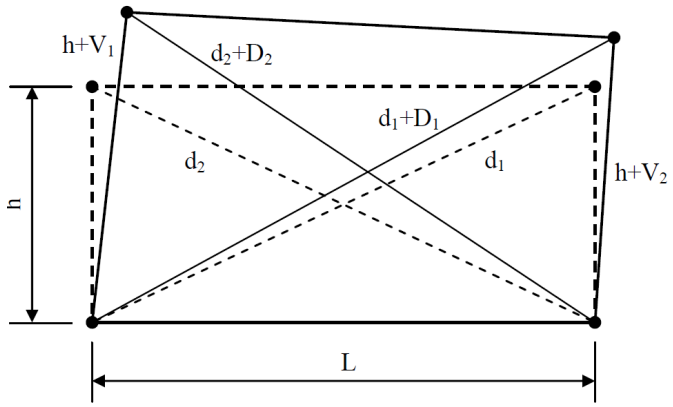

Figure 6-40 Deformations of Wall Section

However, in the experimental study by Tran (2012), shear lateral deformations (Δ_s) were determined by subtracting the flexural (Δ_f, calculated as described in Section 6.6.1) and sliding shear (Δ_{sld}) displacements from total lateral displacement (Δ_{total}) as:

$$\Delta_s = \Delta_{total} - \Delta_f - \Delta_{sld} \tag{6-7}$$

In the analytical results, the shear deformations at the height *ch* in each SFI-MVLEM element (u_{Sh}, Figure 6-41) was directly calculated from the deformations at 6 nodal degrees of freedom $\{\delta_N\}$ as described in Chapter 3 (Section 3.2.3).

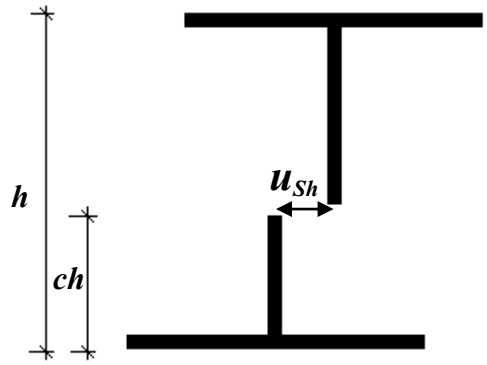

Figure 6-41 Shear Deformation of a Model Wall Element

6.5.2.1. ***Lateral Load versus Shear Displacement Relations***

Comparisons between experimentally measured and analytically predicted relations of lateral-load-versus-shear-displacement at the top of the wall for Tests 1 to 5 are shown in Figure 6-42 to Figure 6-46, respectively. Overall, the figures indicate that shapes of shear load-deformation responses are highly pinched for all wall specimens, as well as that the magnitudes of *shear* deformations are larger for specimens with lower aspect ratio. Comparison between experimental results for two specimens with aspect ratio of 2.0 (Tests 1 and 2), with almost the same actual axial stress, reveals that the larger shear stress for Test 2 resulted in much larger shear displacements than those in Test 1. Similarly, the comparisons of results for test specimens with aspect ratio of 1.5 indicate that shear displacements in Test 5 were much larger than those in Tests 3 and 4, suggesting that axial stress had a significant impact on the magnitude of the shear

displacement, i.e., shear (sliding) displacements may increase significantly as axial stress decreases.

It can be observed from Figure 6-42 to Figure 6-46 that analytical model captures well the highly pinched shape of load-deformation relationships for all wall specimens, and that the magnitudes of shear deformations are reasonably well predicted by the model. For specimens with aspect ratio of 2.0 (Tests 1 and 2), the model generally underestimates the shear displacements in the last loading cycle, particularly in the second and third cycle of the last drift level of 3.1% and 3.0%. For specimens with aspect ratio of 1.5 (Tests 3, 4 and 5), the magnitudes of shear displacements are slightly overestimated for Test 3, whereas for Tests 4 and 5 model underestimates shear deformations at drift level of 3.0% where shear sliding along the base of the walls was observed during the experiments. In addition, shear stiffness is generally overestimated by the model at drift levels less than 0.75% for all five wall specimens.

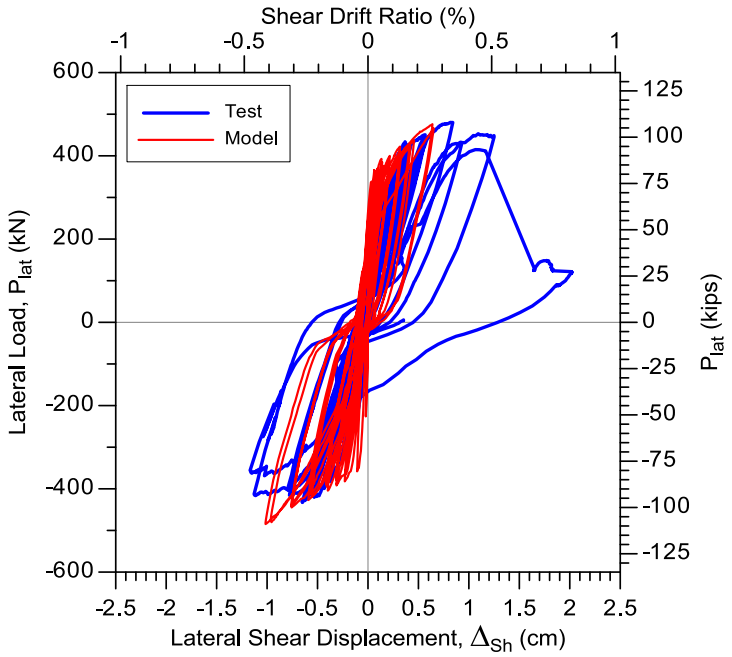

Figure 6-42 Top Shear Displacement for Specimen RW-A20-P10-S38, Test 1

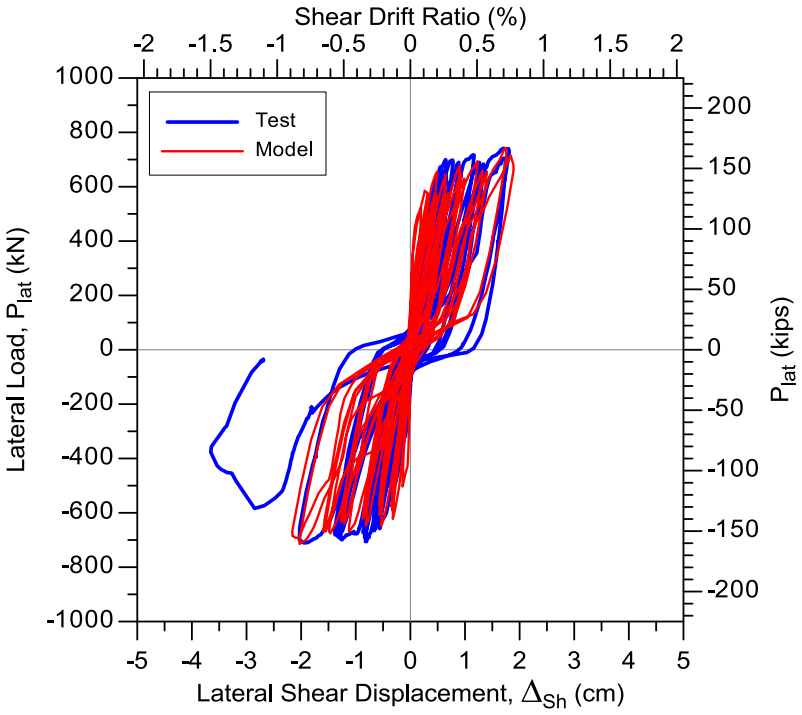

Figure 6-43 Top Shear Displacement for Specimen RW-A20-P10-S63, Test 2

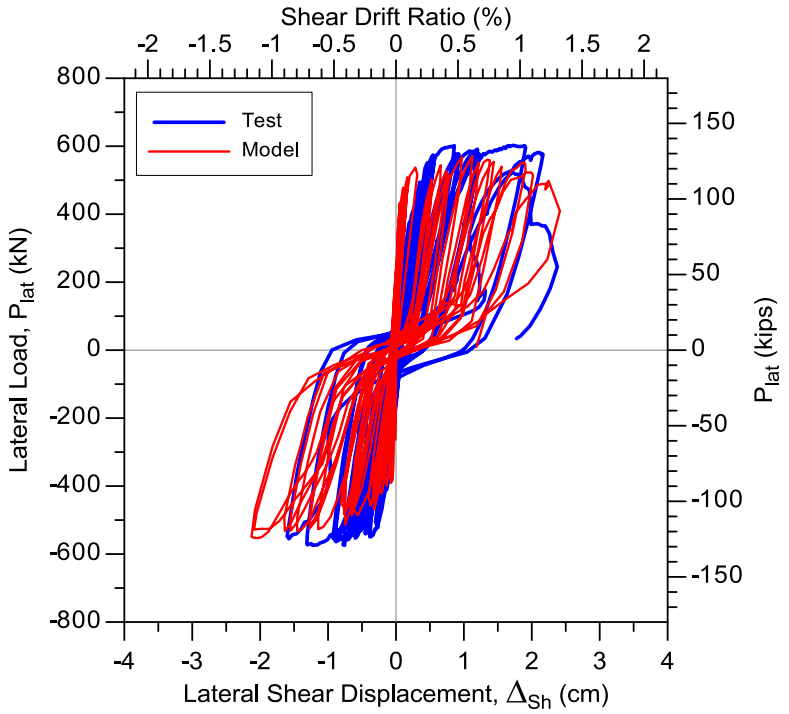

Figure 6-44 Top Shear Displacement for Specimen RW-A15-P10-S51, Test 3

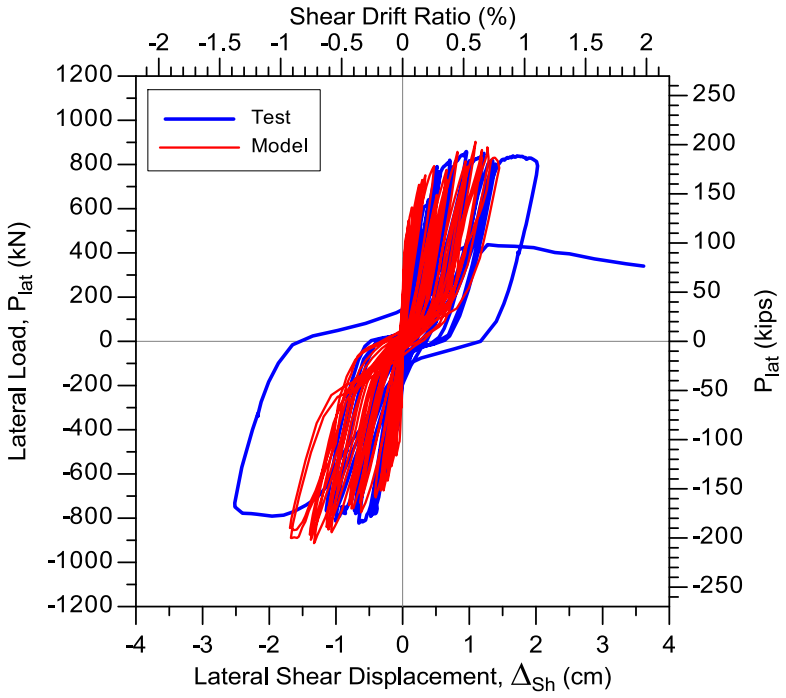

Figure 6-45 Top Shear Displacement for Specimen RW-A15-P10-S78, Test 4

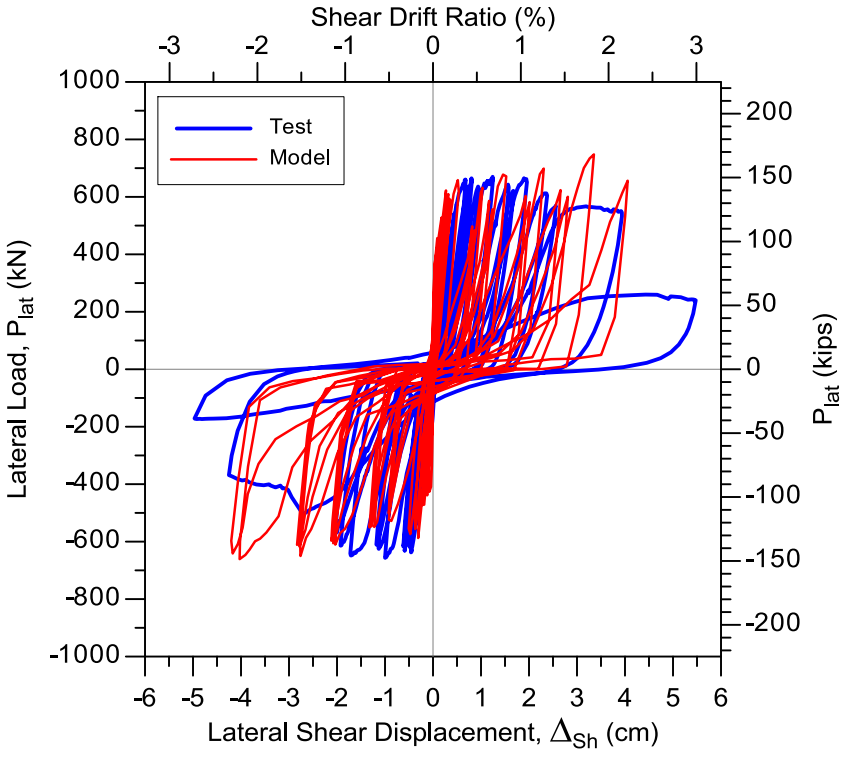

Figure 6-46 Top Shear Displacement for Specimen RW-A15-P2.5-S64, Test 5

6.5.2.2. *Shear Displacement Profiles*

Experimentally measured and analytically predicted profiles of shear displacements over the wall height for Tests 1 to 5 are compared on Figure 6-47 to Figure 6-51, respectively. Similarly to the profiles of total and flexural displacements, the shear displacements were compared at peak total displacements during the first cycle under both positive and negative loadings of the drift levels equal to 0.5%, 0.75%, 1.0%, 1.5%, 2.0%, and 3.0%. Shear displacements were obtained at 24 in. (610 mm), 40 in. (1016 mm), 56 in. (1422 mm), 72 in. (1829 mm), and 96 in. (2438 mm) above the wall-foundation block interface.

As observed from Figure 6-47 to Figure 6-51, the shapes of shear deformation profiles obtained experimentally and analytically agree reasonably well, illustrating that the model captures experimentally observed concentration of shear deformations over the plastic hinge region (up to height of approximately $l_w/2$). The analytical model also predicts that the nonlinear shear deformations occur even for walls that yield in flexure, which has been observed in this and previously conducted experimental studies (Tran and Wallace, 2012; Massone and Wallace, 2004; Oesterle et al., 1976 and 1979). Furthermore, it can be observed from the experimental and analytical results that the magnitudes of shear deformations increase with increasing shear, especially for walls with high shear stress levels, i.e., RW-A20-P10-S63 (Test 2), RW-A15-P10-S78 (Test 4), and RW-A15-P2.5-S64 (Test 5). The model predicts reasonably well the magnitude of shear deformation profiles at low and moderate drift levels, whereas analytical results tend to underestimate the experimentally measured shear displacement profiles at larger drift levels (e.g., 2.0% and 3.0%); discrepancies of the results is more prominent in tests in which shear sliding occurred at the base of the wall at larger drift levels (Tests 4 and 5).

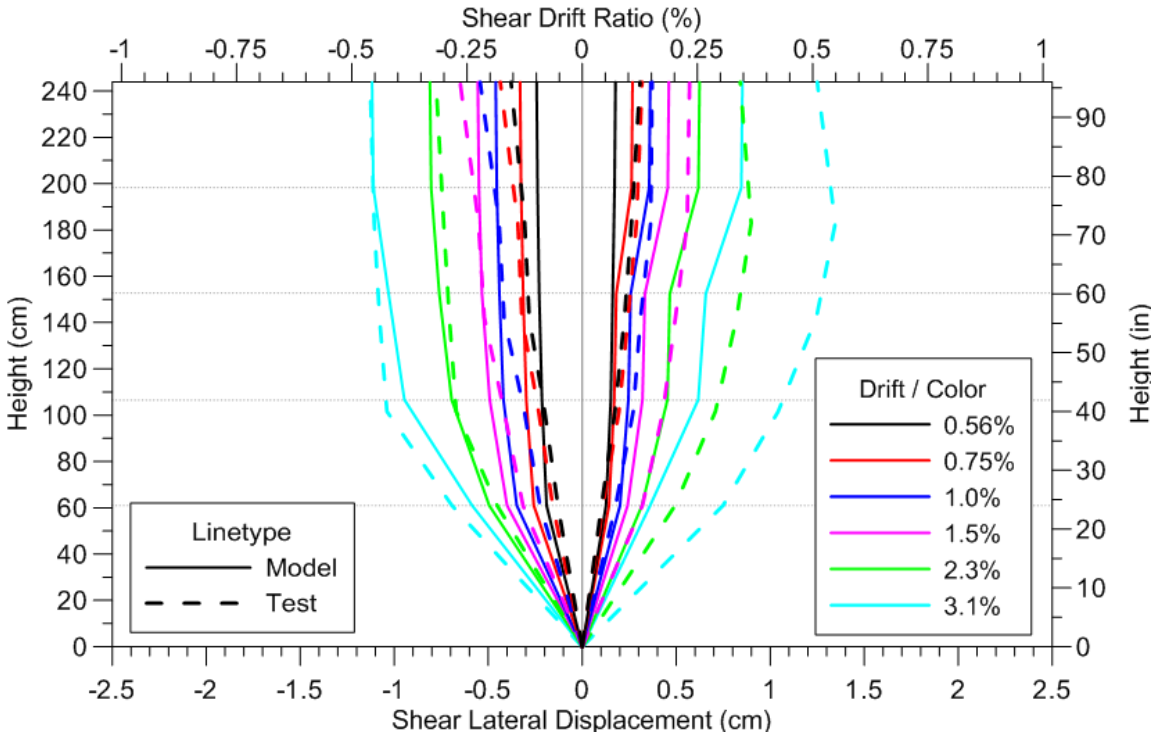

Figure 6-47 Shear Displacement Profile for Specimen RW-A20-P10-S38, Test 1

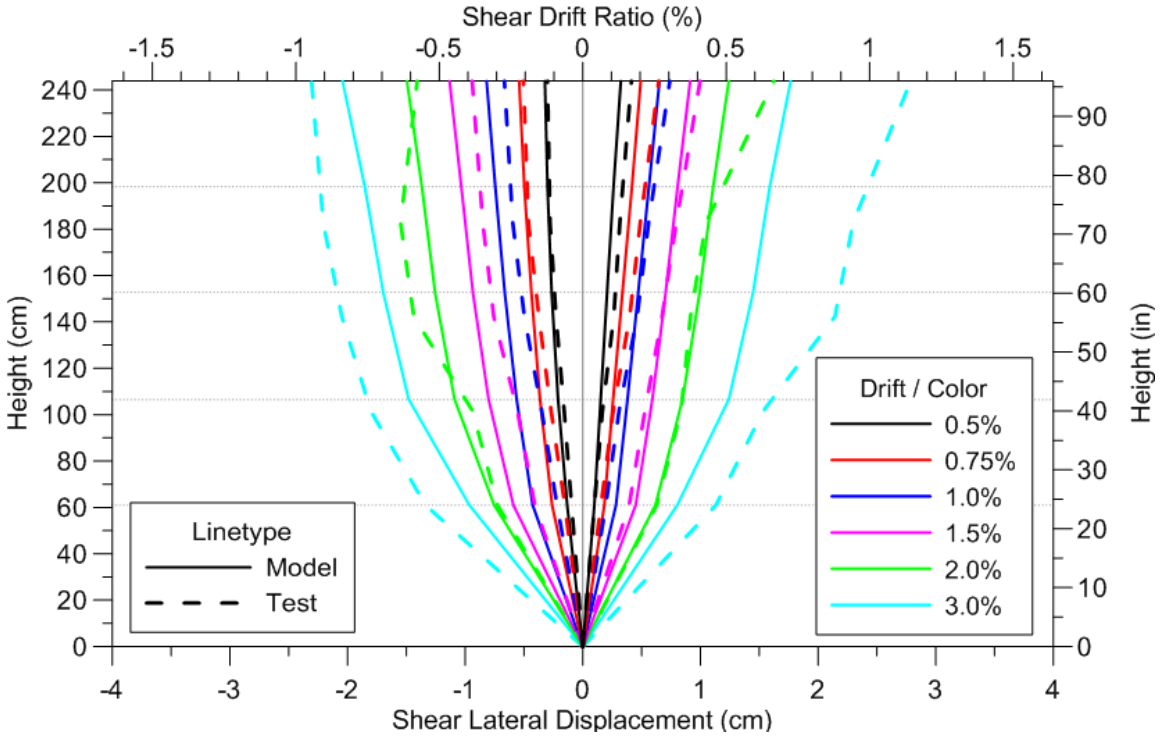

Figure 6-48 Shear displacement profile for Specimen RW-A20-P10-S63, Test 2

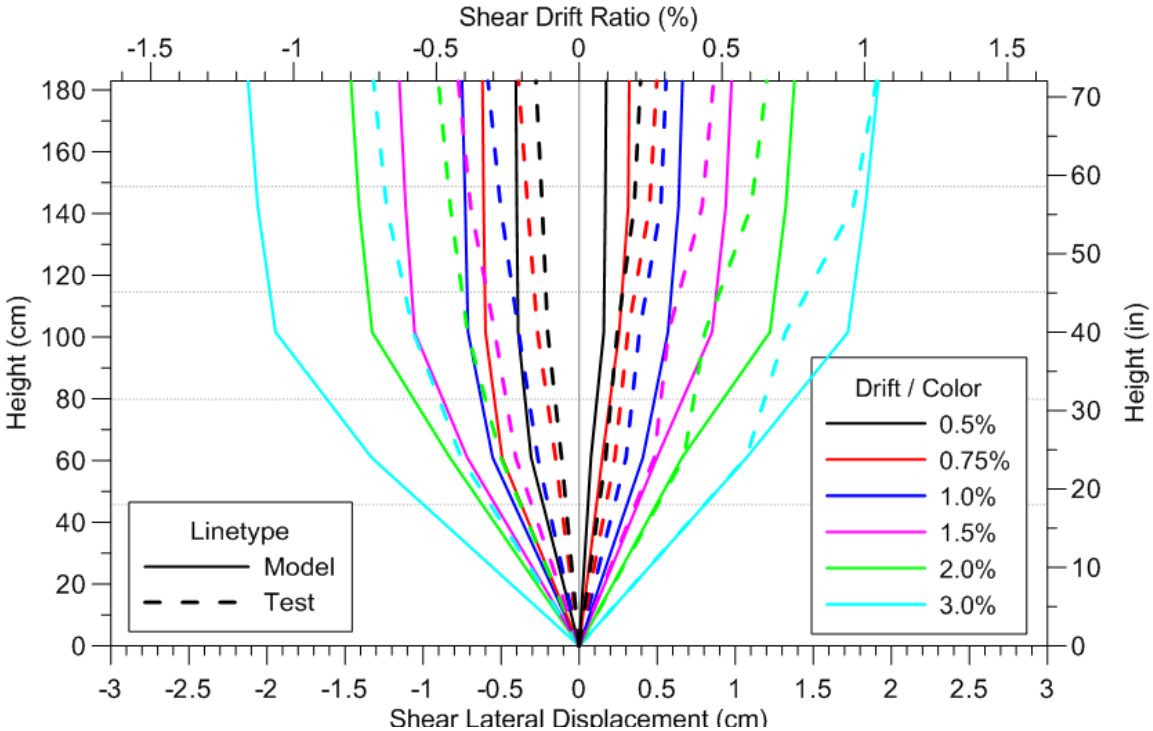

Figure 6-49 Shear displacement profile for Specimen RW-A15-P10-S51, Test 3

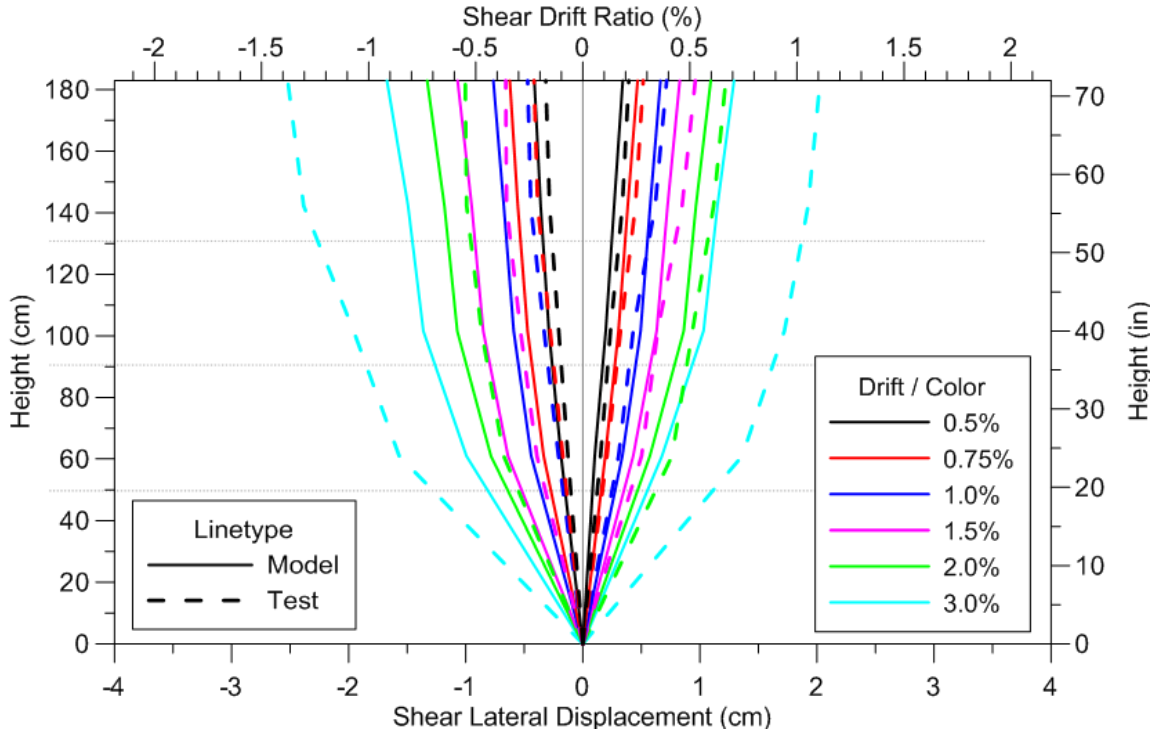

Figure 6-50 Shear displacement profile for Specimen RW-A15-P10-S78, Test 4

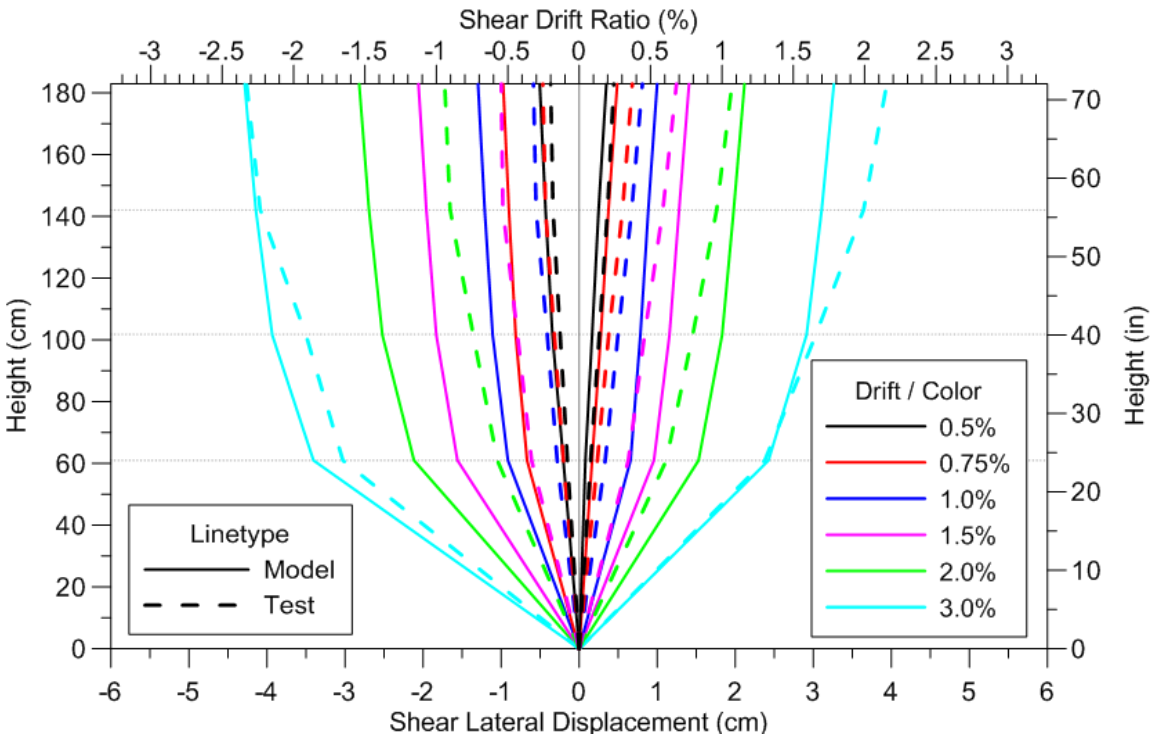

Figure 6-51 Shear displacement profile for Specimen RW-A15-P2.5-S64, Test 5

6.5.3. Contributions of Flexural and Shear Components to Top Lateral Displacement

Contributions of flexural and shear deformations to top lateral displacement derived from experimental and analytical results for Tests 1 to 5 are compared in Figure 6-52 to Figure 6-56, respectively. The contribution of each lateral displacement component was computed at each force or displacement level for the first cycle under both positive and negative loadings. Presented results reveal that the contributions of flexural displacements to total lateral displacements tend to increase slightly from the beginning to the end of the test for walls with moderate shear stress levels (i.e. Tests 1 and 3), whereas the model predicts almost constant contributions throughout the loading history. For the remaining tests (Tests 2, 4 and 5) the experimentally measured contributions of flexural displacements tend to decrease, and the

analytical model predicts reasonably well this trend of flexural deformations. It can be also observed from the figures that the trend of contributions of shear displacements in both experimental and analytical results is opposite to the trend of contributions of flexural deformations.

The analytical models predict very well the contributions of flexural and shear deformations for Tests 2 and 4 (specimens with high shear stress) in both positive and negative directions with results that are within 10% of the experimentally measured values at all drift levels. In contrast, for Tests 1, 3 and 5 the accuracy of analytical predictions throughout the loading history varies, and discrepancies between experimental and analytical results at certain drift levels and loading directions can be significant, e.g. for Test 5 the analytical model predicts 40% higher contribution of shear deformation at drift level of 1.0% in negative loading direction. Figure 6-52 to Figure 6-56 also indicate that the average contributions from all applied drift levels of shear and flexural deformations derived from the experimental results, which are summarized in Table 6-2, are predicted reasonably well by the analytical model since analytical results are generally within 10% of experimentally measured values.

Table 6-2 Average Contributions of Flexural and Shear Deformations

Contributions (%)		Specimen				
		RW-A20-P10-S38	RW-A20-P10-S63	RW-A15-P10-S51	RW-A15-P10-S78	RW-A15-P2.5-S64
Flexure	Test	77	72	63	66	55
	Model	87	77	68	64	50
Shear	Test	21	26	35	32	41
	Model	13	23	32	36	50

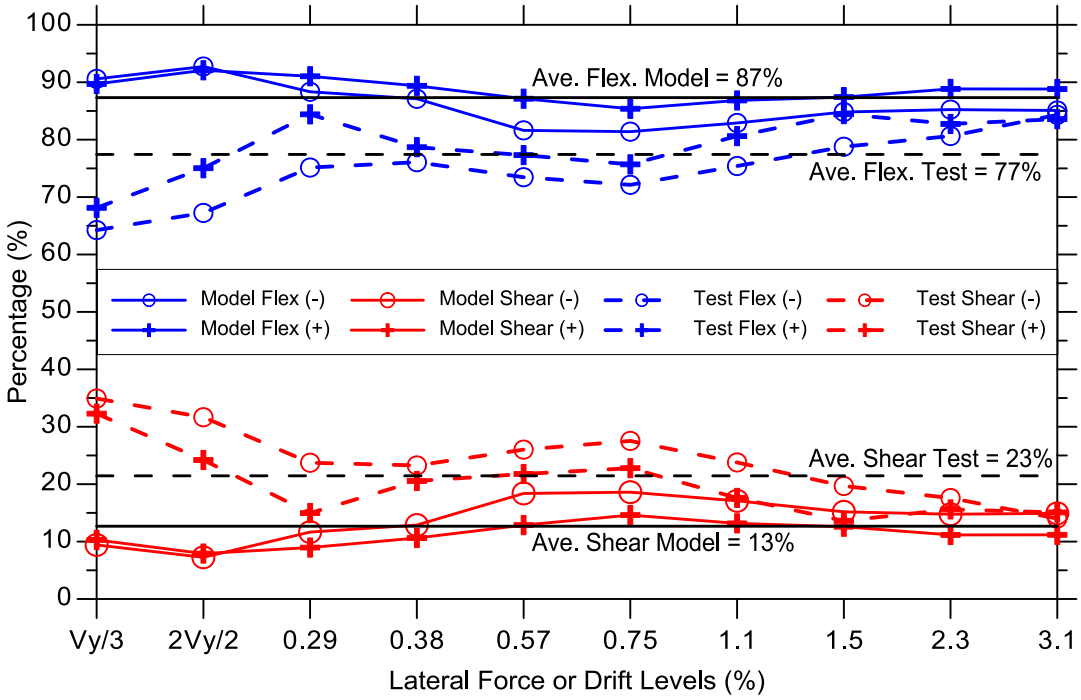

Figure 6-52 Contributions to Top Lateral Displacement for Specimen RW-A20-P10-S38, Test 1

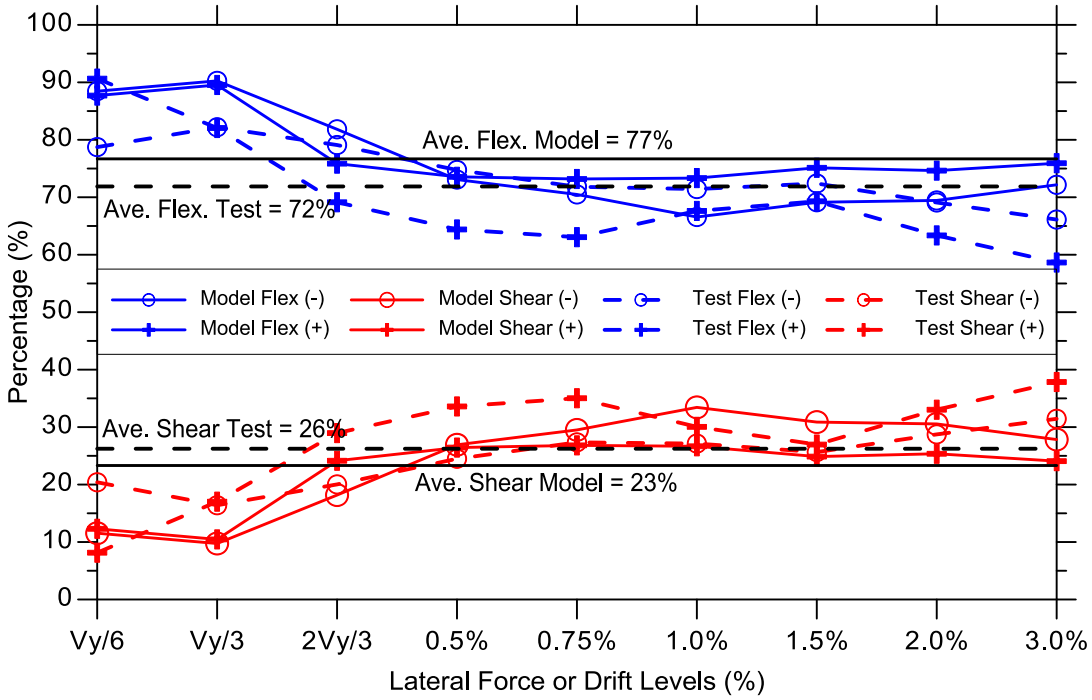

Figure 6-53 Contributions to Top Lateral Displacement for Specimen RW-A20-P10-S63, Test 2

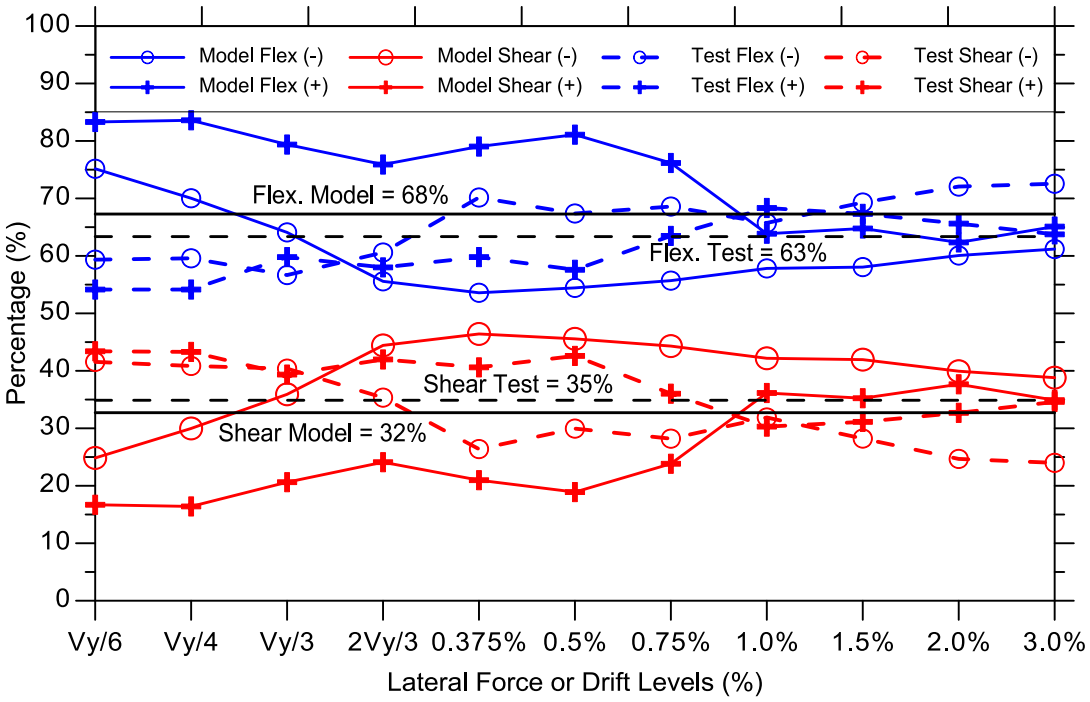

Figure 6-54 Contributions to Top Lateral Displacement for Specimen RW-A15-P10-S51, Test 3

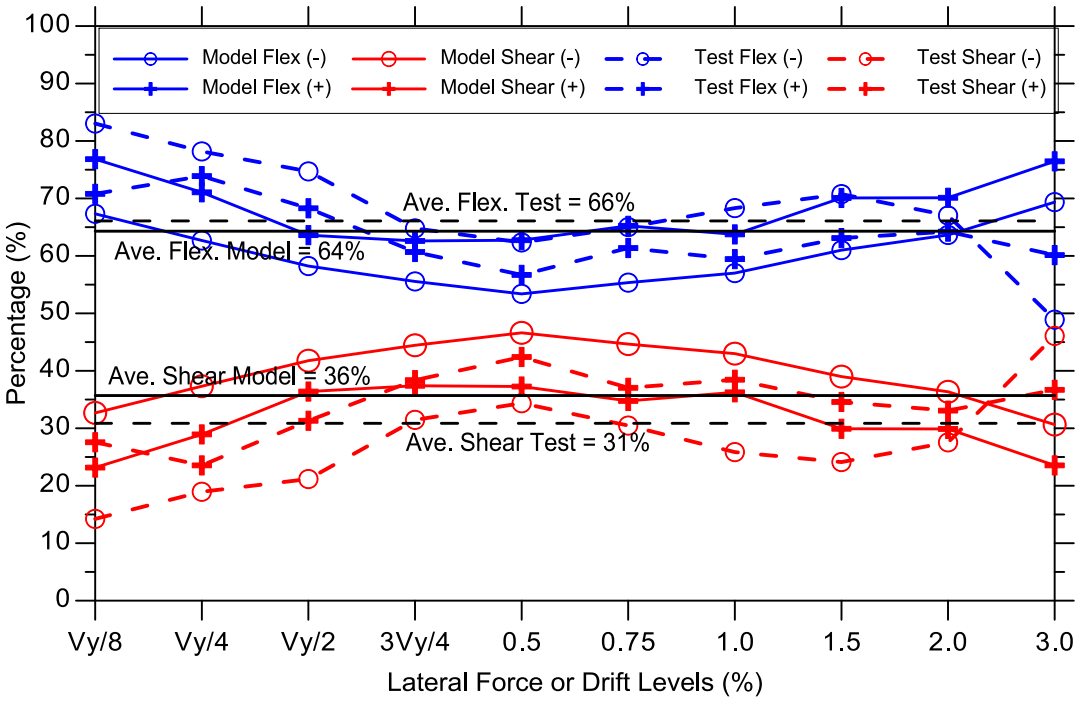

Figure 6-55 Contributions to Top Lateral Displacement for Specimen RW-A15-P10-S78, Test 4

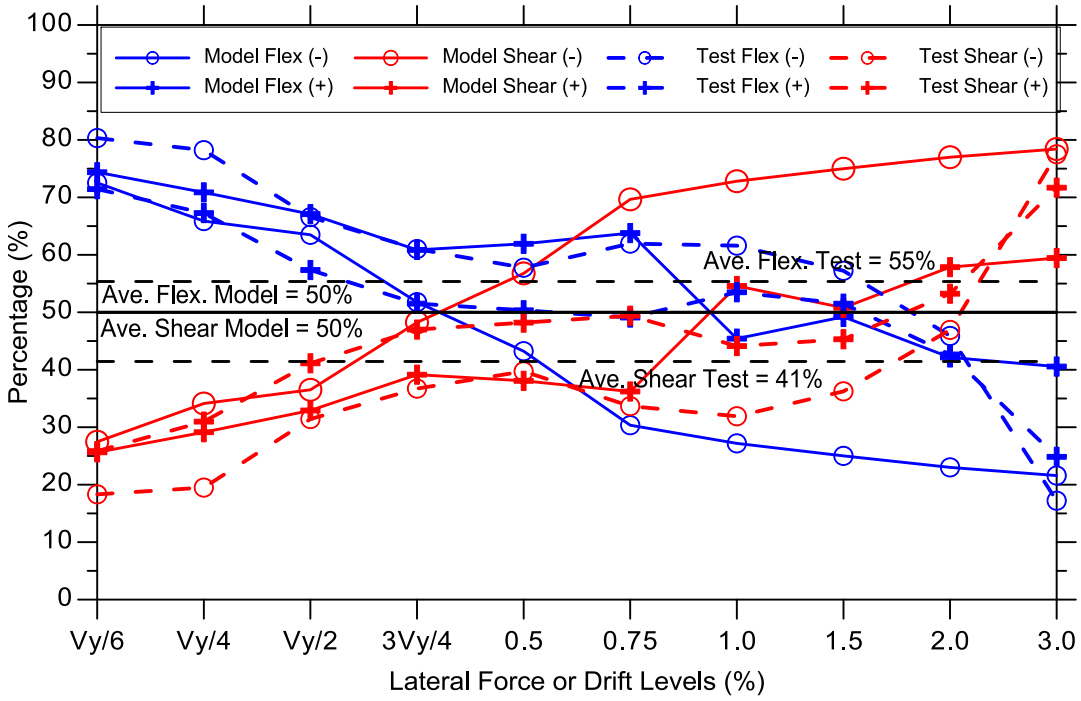

Figure 6-56 Contributions to top lateral displacement for Specimen RW-A15-P2.5-S64, Test 5

6.6. Effective Stiffness

This section includes comparisons for the effective secant flexural and shear stiffness values of wall specimens throughout the applied loading history derived from experimental and analytical results.

6.6.1. Effective Secant Flexural Stiffness

As derived by Tran (2012), the effective secant flexural stiffness of wall specimens is calculated based on the lateral stiffness for cantilever wall from the following expression:

$$F = k_f \cdot \Delta_f \tag{6-8}$$

where $k_f = \frac{3E_c I_{eff}}{h_w^3}$. Therefore, secant flexural stiffness normalized by the concrete gross section flexural stiffness is determined as:

$$\frac{I_{eff}}{I_g} = \frac{E_c I_{eff}}{E_c I_g} = \frac{k_f h_w^3}{3E_c I_g} = \frac{h_w^3}{3E_c I_g}\left(\frac{F}{\Delta_f}\right) \tag{6-9}$$

where F is the lateral load, Δ_f is the flexural displacement at the top of the wall, E_c is Young's modulus of concrete determined using ACI 318 requirements, and h_w is the height of the wall.

Figure 6-57 present relations for effective secant flexural stiffness versus drift ratios obtained from experimental and analytical results using Eq. 6-9 for all five wall specimens tested by Tran and Wallace (2012). It should be mentioned that the presented experimental values were obtained by excluding deformations associated with slip and extension of boundary longitudinal reinforcement for the sake of comparison with analytical results which did not capture these deformations; secant flexural stiffness values including anchorage slip and extension deformations were approximately 30% lower than stiffness values obtained by excluding these deformations, as reported by Tran (2012).

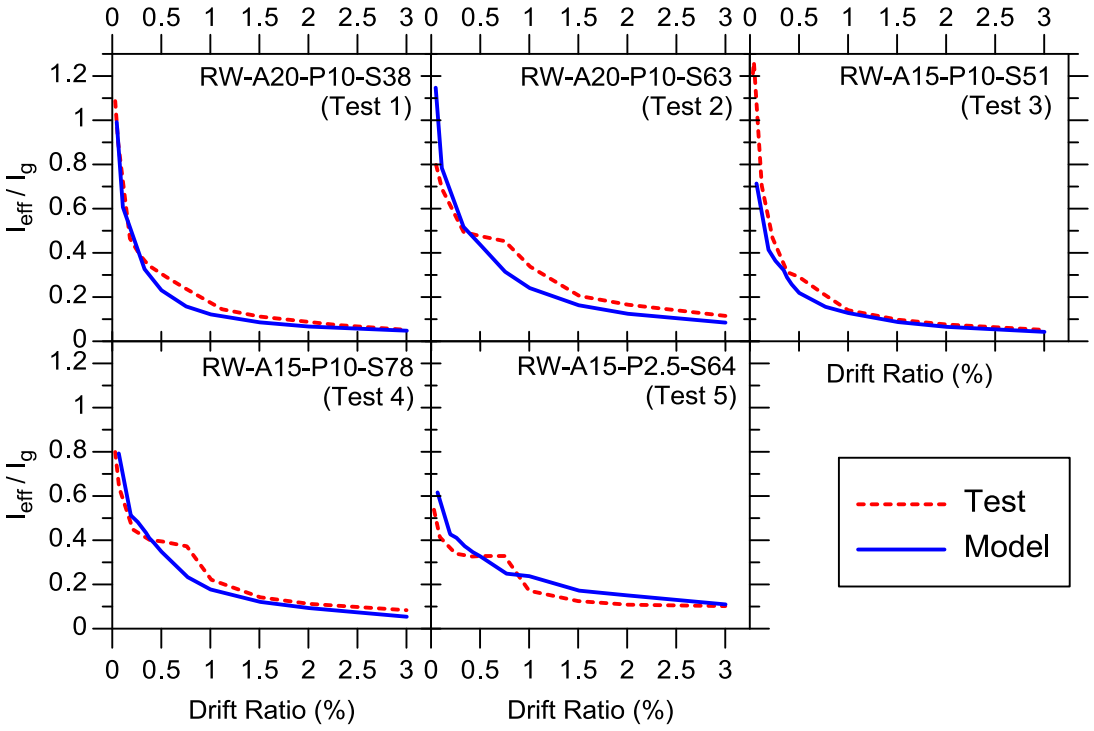

Figure 6-57 Effective Secant Flexural Stiffness: Test Results versus Analytical Model

It can be observed from the figure that analytical model captures reasonably well the secant flexural stiffness for all five wall specimens. For Tests 1, 4 and 5 model closely predicts secant flexural stiffness that is within approximately 10% of experimentally measured stiffness at all drift levels. For Test 2 analytical results are higher by approximately 45% at drift level of 0.05%, and about 10-20% lower than experimental values at drift levels higher than 0.5%. For Test 3 analytical model predicts well secant flexural stiffness at all drift levels, except at 0.05% drift where analytical results are approximately 50% of experimentally determined flexural stiffness.

6.6.2. Effective Shear Stiffness

Effective secant shear stiffness of wall specimens, normalized by $E_c A_w$, is derived from test and analytical results as follows (Tran, 2012):

$$\frac{GA_{eff}}{E_c A_w} = \frac{F/\gamma_s}{E_c A_w} = \frac{h_w}{E_c A_w}\left(\frac{F}{\Delta_s}\right) \tag{6-10}$$

where F is the lateral load, γ_s is the shear strain, Δ_s is the shear displacement at the top of the wall, A_w is the wall cross-section area. Relations of secant shear stiffness versus drift ratios obtained from experimental data and analytical results using Eq. 6-10 for all five specimens are compared on Figure 6-58.

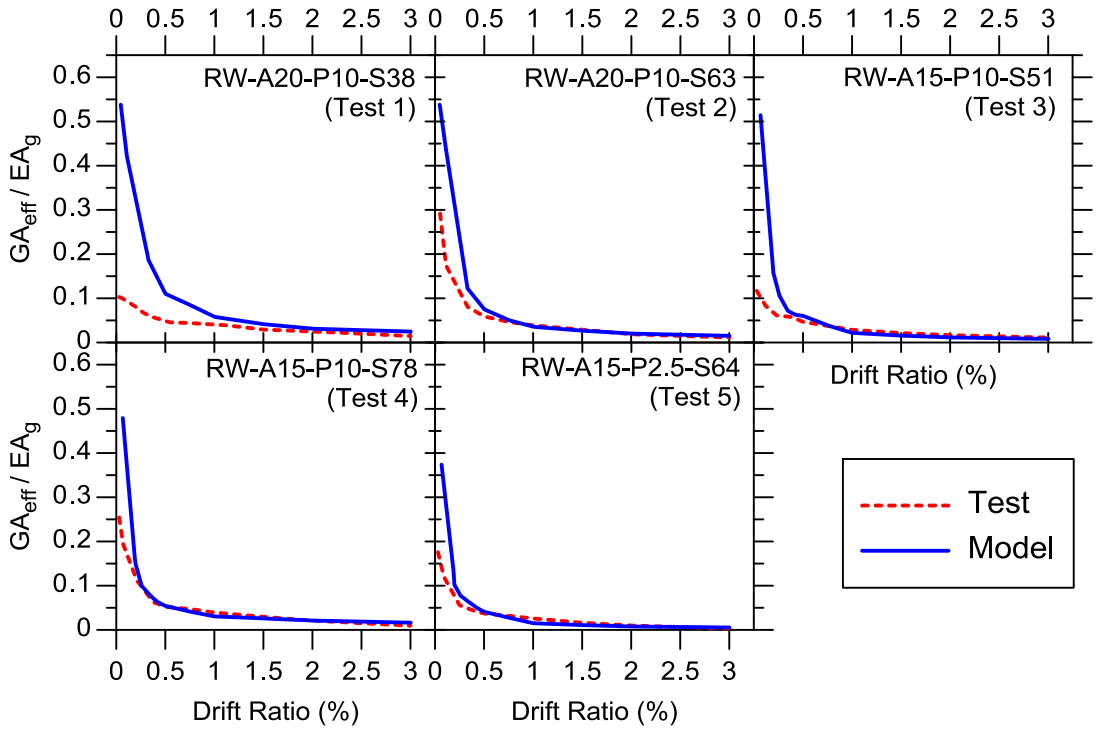

Figure 6-58 Effective Secant Flexural Stiffness: Test Results versus Analytical Model

The comparisons presented reveal that the analytical model significantly overestimates the secant shear stiffness at drift levels lower than 1.0% for Test 1, and drift levels lower than 0.25% for Tests 2, 3, 4, and 5, whereas for the rest of drift levels the secant shear stiffness is closely predicted by the model. For walls with low shear stress (Test1 and Test 3), the predicted initial secant shear stiffness is approximately five times higher than the experimental stiffness, whereas for other specimens (Test 2, 4, and 5), the overestimation at initial drift levels is about two times.

6.7. Local Responses

6.7.1. Vertical Strains

Comparisons between experimentally measured and analytically predicted profiles of vertical strains at the bottom of tested wall specimens, corresponding to lateral drifts of 0.5%, 1.0% and 2.0% for Tests 2 to 5 are presented in Figure 6-59 to Figure 6-62, respectively; the comparison of vertical strain profiles for Test 1 are not presented due to unreliable readings from one of the LVDTs during the experiment. Similar trends were observed in the results for other drift levels and also for peak negative top displacement data points; therefore, only limited results are presented. Experimentally measured concrete strains are derived from four vertical LVDTs located at 10.2 cm (4 in.), 33.0 cm (13 in.), 88.9 cm (35 in.), and 11.8 cm (44 in.) along the length of experimental wall specimens, over the LVDT gage length of 35.6 cm (14 in.) (from 2 in. to 16 in. height from the wall base), whereas analytically predicted strain profiles are obtained from average strains in bottom SFI-MVLEM element of 30.5 cm (12 in.) length.

It can be observed from the figures that the plane-section assumption incorporated in the formulation of the analytical model approximates reasonably well almost linear experimentally

measured vertical strain profiles at drift levels of 0.5% and 1.0% for all four considered wall specimens; both tensile and compressive strains at wall boundaries are predicted within 15%. However, at drift levels of 2.0%, strain relaxation at the wall boundary in tension can be observed in experimentally measured vertical strains for all wall specimens resulting in nonlinear strain profiles. At this drift level, analytical results generally underestimate tensile strains at the wall boundary, whereas compressive strains are reasonably well predicted for Tests 2 and 4 and overestimated for Tests 3 and 5 due to vertical growth of the that wall.

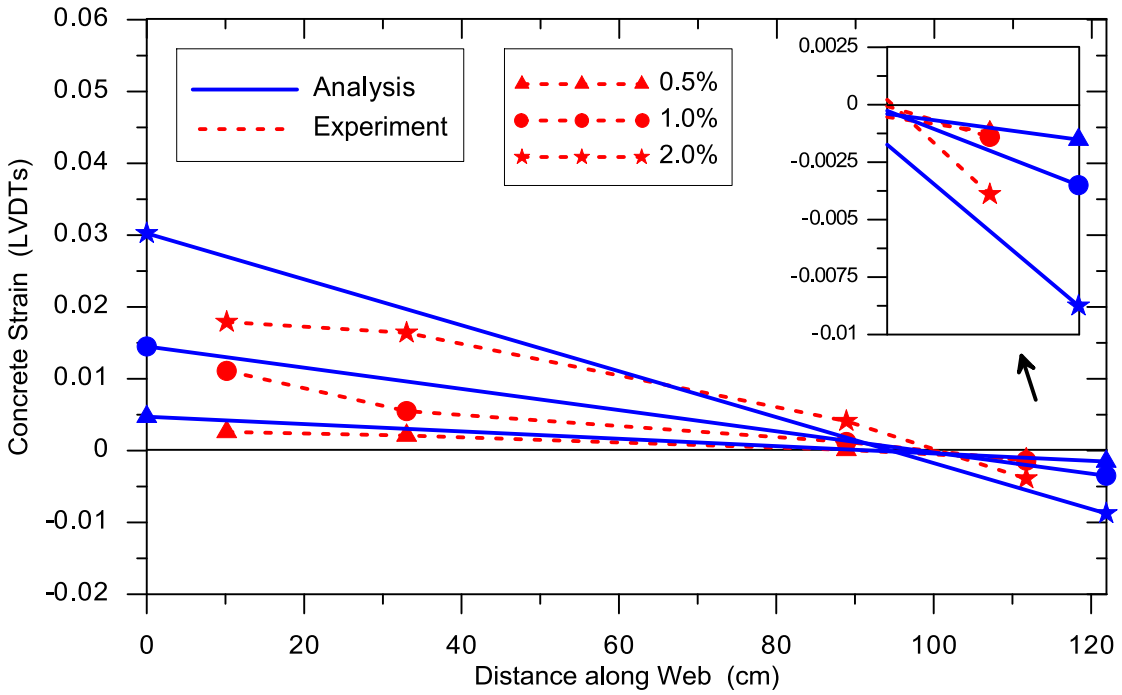

Figure 6-59 Vertical Strain Profiles for Specimen RW-A20-P10-S63, Test 2

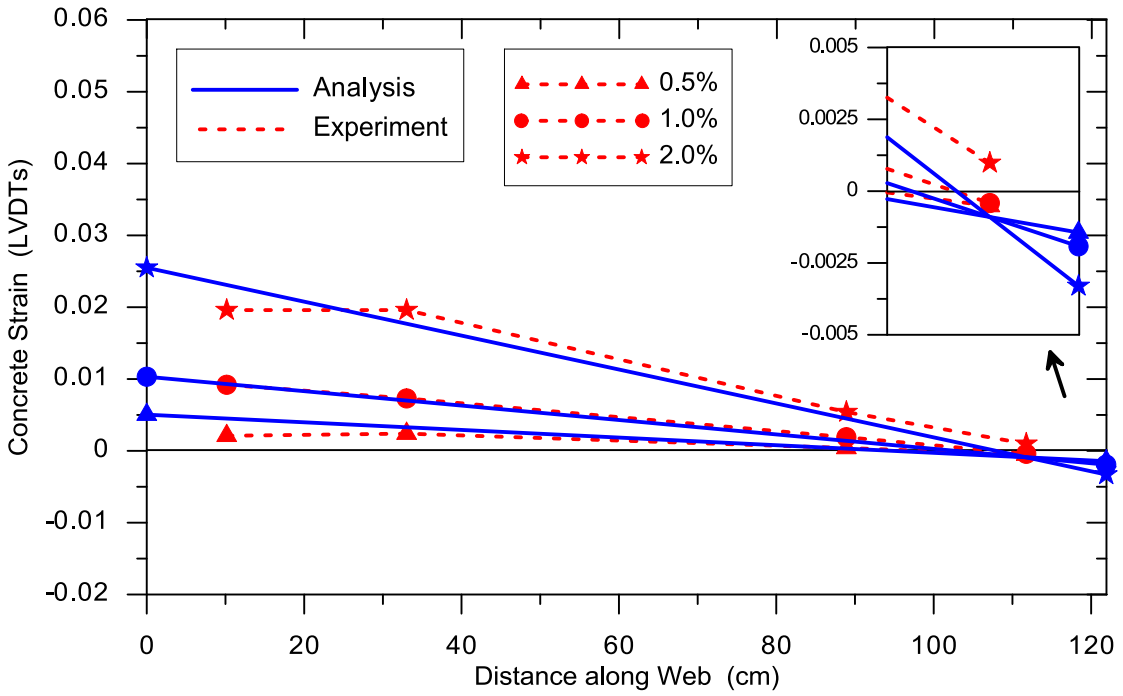

Figure 6- 60 Vertical Strain Profiles for Specimen RW-A15-P10-S51, Test 3

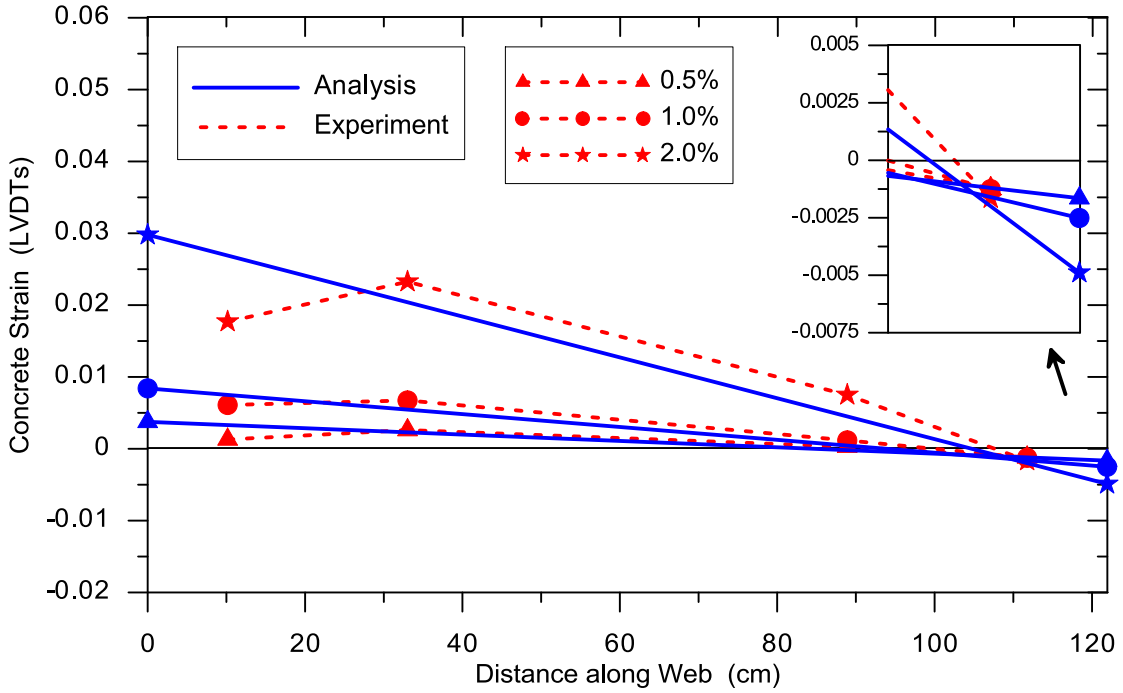

Figure 6-61 Vertical Strain Profiles for Specimen RW-A15-P10-S78, Test 4

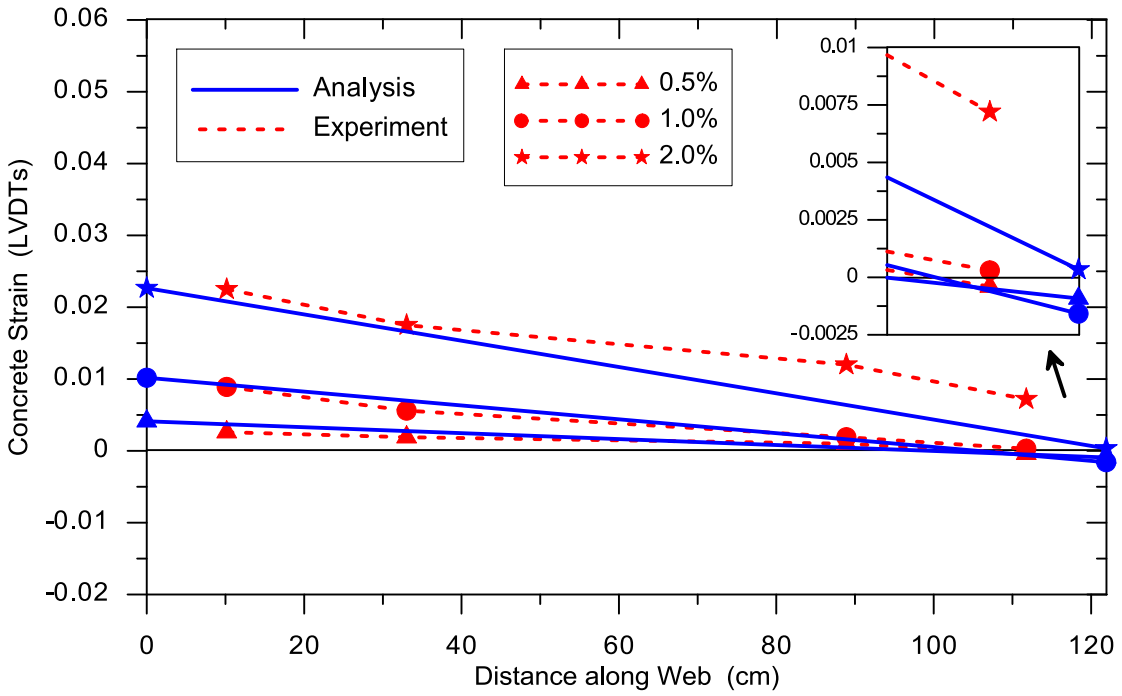

Figure 6-62 Vertical Strain Profiles for Specimen RW-A15-P2.5-S64, Test 5

As discussed by Orakcal and Wallace (2006), the compressive strains obtained using the uncoupled wall model (shear behavior independent from axial/bending behavior) may be underestimated due to inability of the model to capture nonlinear shear deformations even for the relatively slender RC wall specimen (e.g., RW2 tested by Thomsen and Wallace, 1995) in which nonlinear shear deformations are only about 20% of the first story lateral displacement. Therefore, results presented in Figure 6-59 to Figure 6-62 reveal that using the SFI-MVLEM, which accounts for SFI and nonlinear shear deformations, the compressive strains are reasonably well predicted even for wall specimens with much higher contribution of nonlinear shear deformations (e.g., up to 40% of total top lateral displacement for Test 4).

The comparison of experimentally measured and analytically predicted vertical strains at 10 cm (4.0 in.) form the wall boundary corresponding to peak positive and negative drift levels of the first loading cycles for specimen RW-A20-P10-S38 (Test 2) and RW-A15-P10-S78 (Test 4) are presented in Figure 6-63 and Figure 6-64, respectively. Both experimental and analytical results are obtained for the LVDT gauge length of 61 cm (24 in.). Presented results reveal that the analytical model predicts well the vertical strains at the wall boundary throughout the cyclic loading history for both specimens; the tensile strains are generally overestimated by approximately 10 to 15%, whereas compressive strains are underestimated by roughly 35%. As well, analytical model predicts well the growth of vertical strains throughout the loading history observed in Test 4 caused by yielding of the boundary reinforcement that is concentrated within the height of $l_w/2$ from the bottom of the wall.

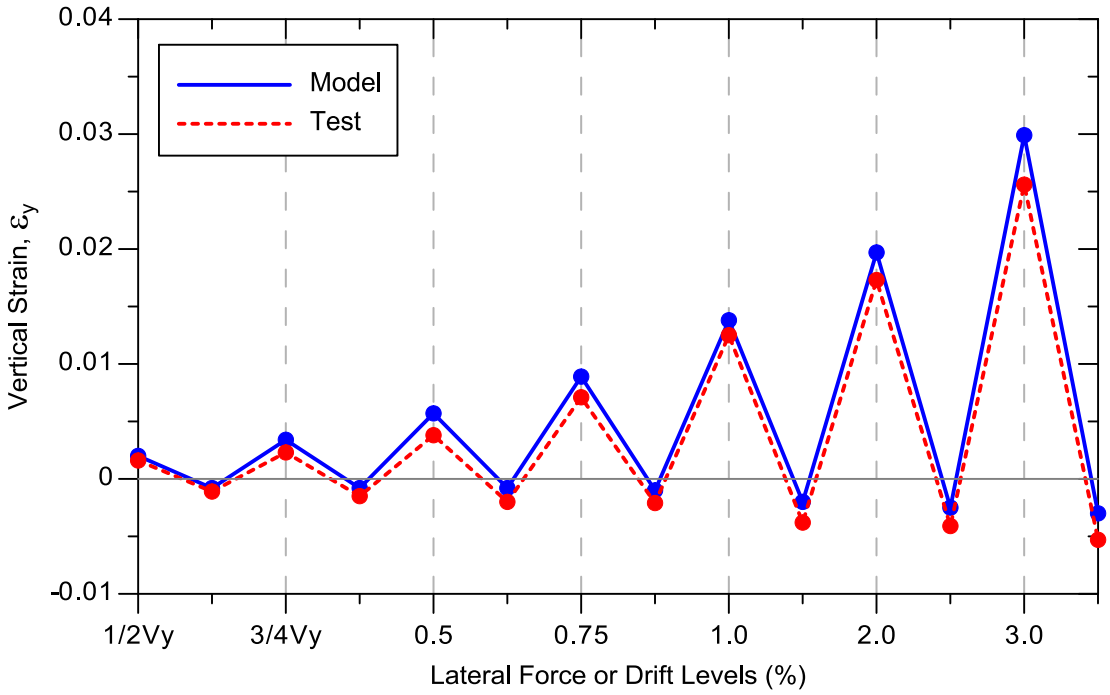

Figure 6-63 Strain Histories (at peak drift levels) for Specimen RW-A20-P10-S63, Test 2

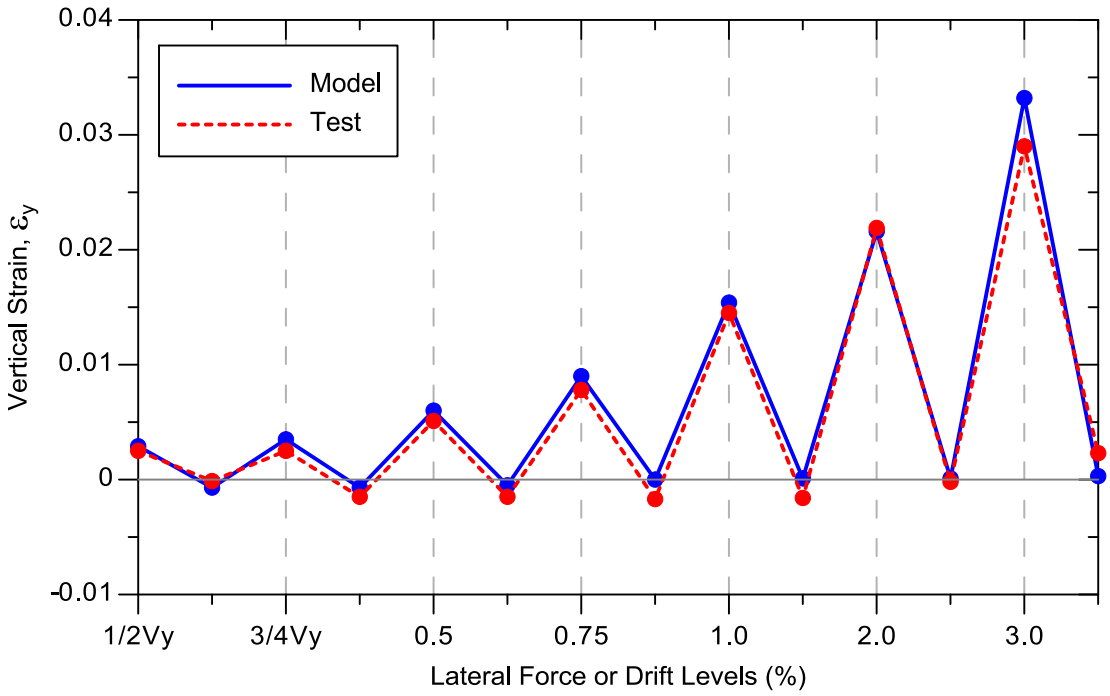

Figure 6-64 Strain Histories (at peak drift levels) for Specimen RW-A15-P10-S78, Test 4

6.7.2. Base Rotations

Experimentally measured and analytically predicted rotations over the bottom 61 cm (24 in.) of the wall specimens (i.e., $l_w/2$, assumed plastic hinge length) corresponding to peak positive and negative drift levels of 0.5%, 0.75%, 1.0%, 1.5%, 2.0% and 3.0% for Tests 2 to 4 are compared in Figure 6-65 to Figure 6-68, respectively. The comparison of rotations for Test 1 is not presented due to unreliable readings from one of the LVDTs during the experiment. Experimental rotations are measured via two vertical wire potentiometers mounted to wall ends by the use of Eq. 6-2, whereas corresponding rotations for the analytical model are derived from the rotational degree of freedom located at the top node of the second SFI-MVLEM at a height of 61 cm (24 in.) from the bottom of the wall model.

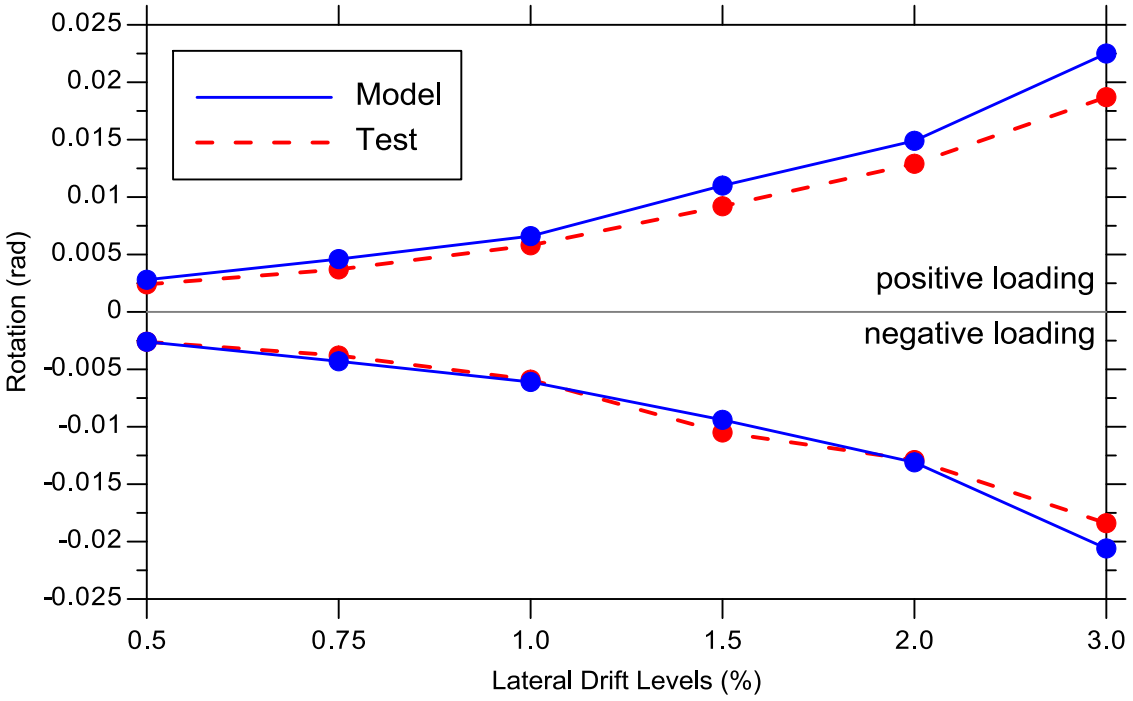

Figure 6-65 Base Rotations for Specimen RW-A20-P10-S63, Test 2

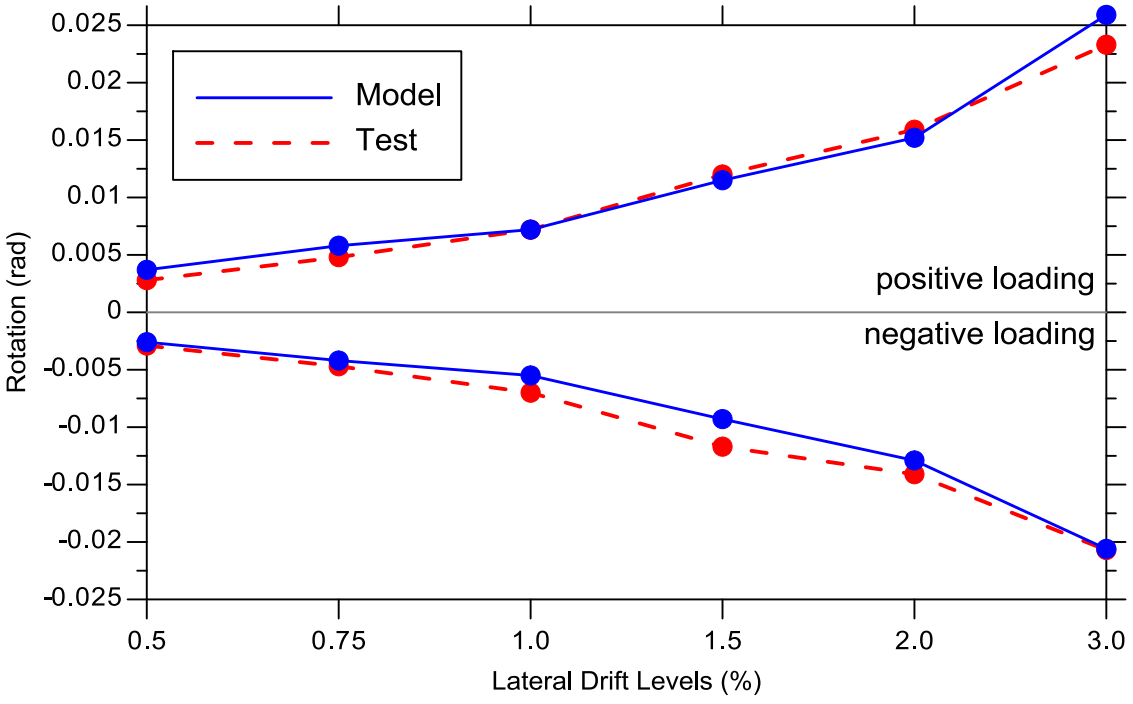

Figure 6-66 Base Rotations for Specimen RW-A15-P10-S51, Test 3

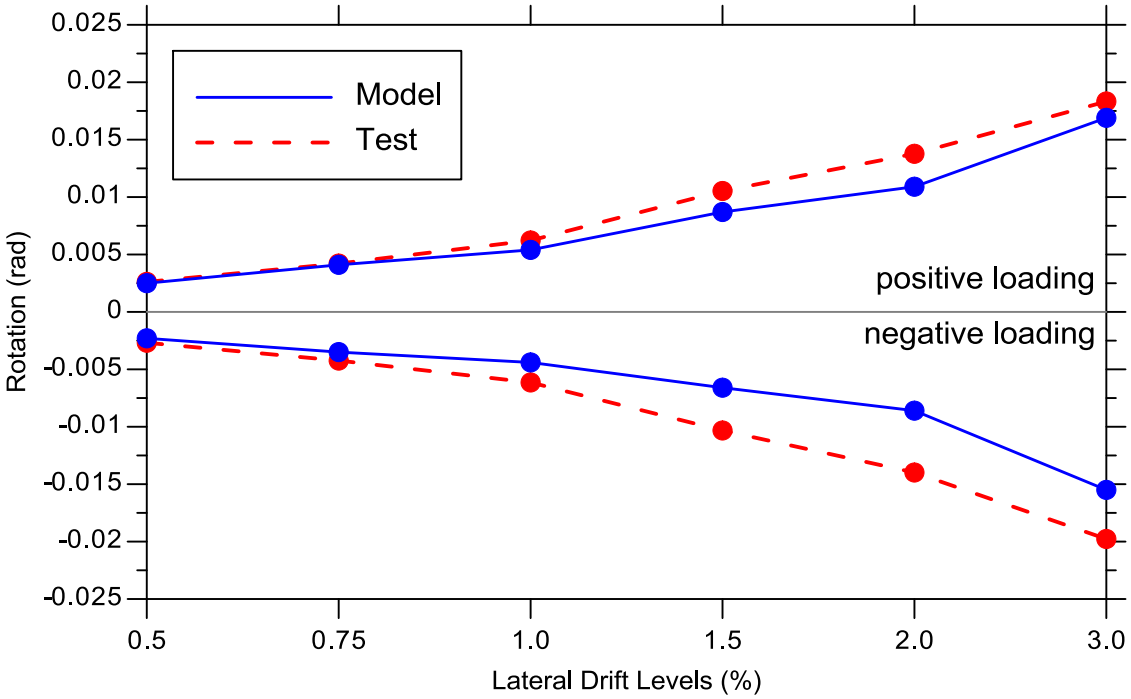

Figure 6-67 Base Rotations for Specimen RW-A15-P10-S78, Test 4

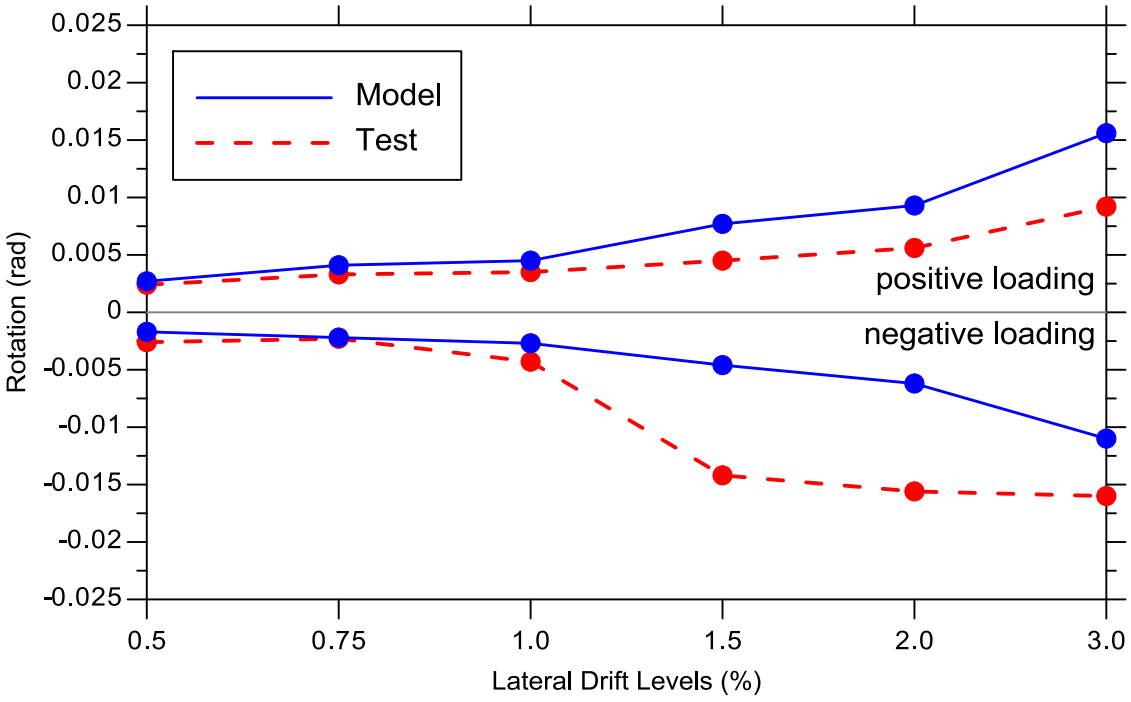

Figure 6-68 Base Rotations for Specimen RW-A15-P2.5-S64, Test 5

It can be observed from the figures that analytically predicted rotations for Tests 2 and 3 are within approximately 20% of experimentally measured rotations at considered peak drift levels. For Tests 4 and 5, analytical results are reasonably accurate (also within 20% of experimental results) up to lateral drift of 1.0%, whereas, for higher drift levels, discrepancies between experimental and analytical results are larger, possibly due to sliding at the base of these wall specimens observed during the tests that could lead to unreliable readings on boundary sensors used for calculation of wall rotations.

6.8. Uncoupled Model versus SFI-MVLEM Results

This section provides comparisons of analytical results obtained using a displacement-based fiber model implemented in computational platform OpenSees (McKenna et al., 2000) and the proposed SFI-MVLEM and experimental results for specimens RW-A20-P10- S38 (Test 2), RW-A15-P10-S78 (Test 4), and RW-A15-P2.5-S64 (Test 5). The results are compared in terms of lateral-load versus total-top-displacement and lateral-load versus top-shear-displacement responses.

6.8.1. Uncoupled Model

Analytical results for RW-A20-P10-S38 (Test 2), RW-A15-P10-S78 (Test 4), and RW-A15-P2.5-S64 (Test 5) are obtained using a displacement-based fiber model implemented in OpenSees (McKenna et al., 2000) in which shear and flexural deformations are uncoupled. Flexural response of a wall is simulated through axial deformation of uniaxial concrete and steel fibers constituting a wall cross-section, whose cyclic constitutive behavior is described using Concrere06 and Steel02, two constitutive material laws incorporated into OpenSees for concrete

and reinforcing steel, respectively. Concrete06 constructs a uniaxial concrete material object with tensile strength and nonlinear tension stiffening. Concrete compressive behavior is modeled with a constitutive material law defined as the Thorenfeldt-based curve, which is similar to the relation by Popovic (1973). The tensile envelope uses the tension stiffening equation by Belarbi and Hsu (1994) with a general exponent. A stiffness of 7.1% of the initial elastic stiffness, i.e. $0.071E_c$, is used for the unloading path in compression as recommended by Palermo and Vecchio (2003). Steel02 simulates a uniaxial Giuffre-Menegotto-Pinto steel material object with isotropic strain hardening. Analytical models for concrete and reinforcing steel are calibrated to reasonably match experimentally measured stress-strain relationships of concrete and steel for considered wall specimens.

Shear behavior is modeled using prescribed shear force-deformation relationship, i.e., independently from flexural modeling parameters. Three relationships are considered in this study: (1) linear-elastic relationship with shear stiffness of $G_c/10 = 0.04E_c$, which corresponds to effective shear stiffness at flexural yielding recommended in PEER-ATC-72-1 (2010) report, (2) bi-linear relationship with initial shear stiffness of $G_c/10$, yielding point defined at shear nominal wall capacity (V_n) and hardening ratio of 3.0% in the post-yielding branch, and (3) bi-linear relationship with initial shear stiffness of $G_c/10$ and yielding point defined at shear force corresponding to wall flexural nominal capacity ($V@M_n$) and hardening ratio of 3.0% in the post-yielding branch; all three shear force-deformation relationships are presented in Figure 6-69 assuming that $V_n > V@M_n$.

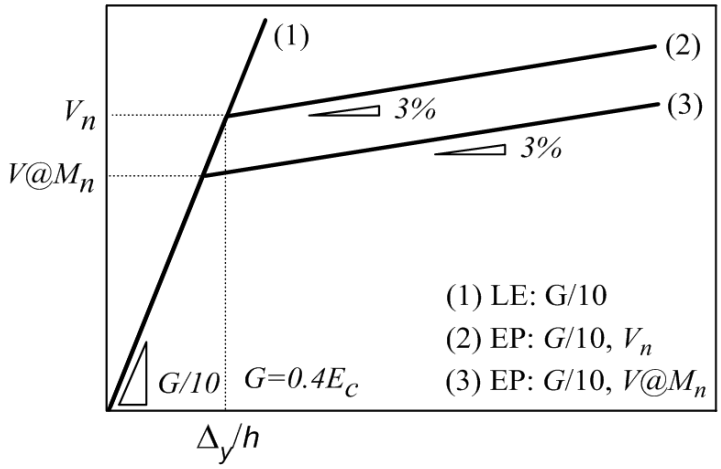

Figure 6-69 Shear Force-Deformation Relaionships

Shear strength V_n for case (2) is calculated using Eq. 21-7 from ACI 318-11 as:

$$V_n = A_{cv}\left(\alpha_c \lambda \sqrt{f'_c} + \rho_t f_y\right) \tag{6-11}$$

where $\alpha_c = 3.0$ for height-to-length ratio, $h_w / l_w \le 1.5$, $\alpha_c = 2.0$ for $h_w / l_w \ge 2.0$, and varies linearly for $1.5 \le h_w / l_w \le 2.0$; λ is 1.0 for normal-weight concrete, A_{cv} represents the cross-section web area of a wall, f'_c is the compressive strength of concrete, ρ_t is the transverse reinforcement ratio, and f_y is the yield strength of transverse reinforcement.

6.8.2. Comparison of Experimental and Analytical Results

Lateral-load-versus-top-displacement relations obtained using SFI-MVLEM and the uncoupled model (i.e., fiber model implemented in OpenSees) are compared against experimental results for RW-A20-P10-S38 (Test 2), A15-P10-S78 (Test 4), and RW-A15-P2.5-S64 (Test 5) in Figure 6-70 to Figure 6-72, respectively. It can be observed from the figures that load-deformation

responses obtained using the uncoupled model with linear-elastic shear stiffness (case (1)) generally overestimate lateral stiffness and lateral load capacity of the walls after yielding of the boundary longitudinal reinforcement. The wall lateral capacity obtained for a more slender wall specimen with aspect ratio of 2.0 (Test 2) is overestimated by approximately 15% at drift levels between 1.0% and 2.0%, whereas at drift level of 3.0% analytical model overestimates lateral load as much as 40% (Figure 6-70(b)). For the case of moderately slender wall specimens of aspect ratio of 1.5 (Test 4 and Test 5) the discrepancies between experimental and analytical results are larger. For a specimen with applied axial load of 10% of its nominal axial load capacity (Test 4), lateral load is overestimated by approximately 15% to 20% at drift levels lower than 1.0%, and up to up to 40% at higher drift levels (Figure 6-71(b)), whereas for a specimen with lower axial load of only 2.5% of its axial load capacity (Test 5), the analytical model overestimates wall lateral capacity up to 70% at drift levels of 2.0% and 3.0% (Figure 6-72(b)). In addition, the uncoupled wall model with linear-elastic shear behavior does not capture pinching characteristics of the hysteretic load-deformation response observed in experimental results, since pinching is generally associated with nonlinear shear deformations, as discussed in Section 4.2.

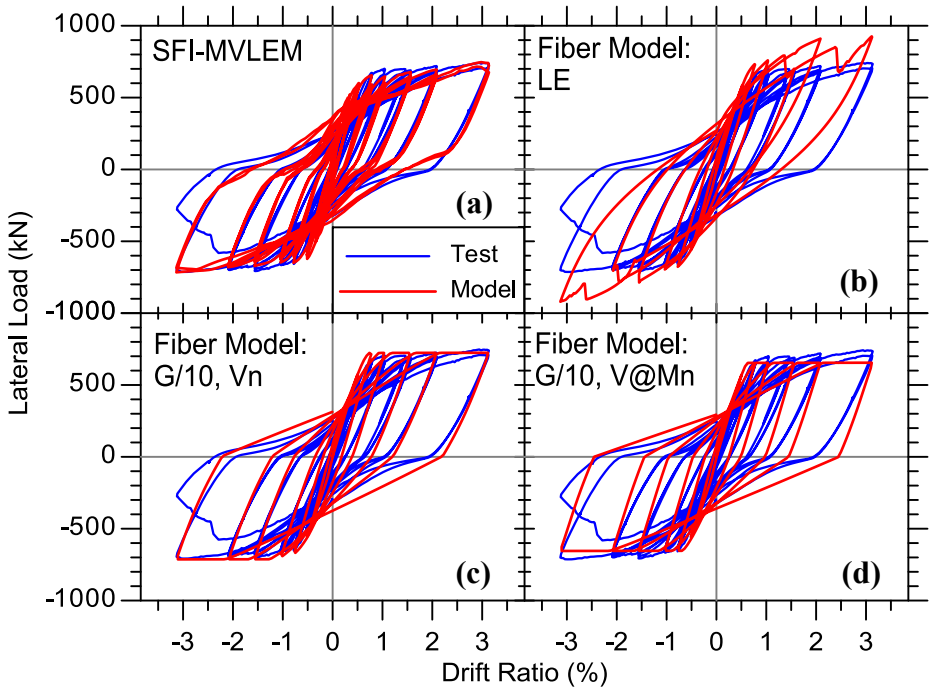

Figure 6-70 Lateral-Load-versus-Top-Total-Deformation Response for RW-A20-P10-S38

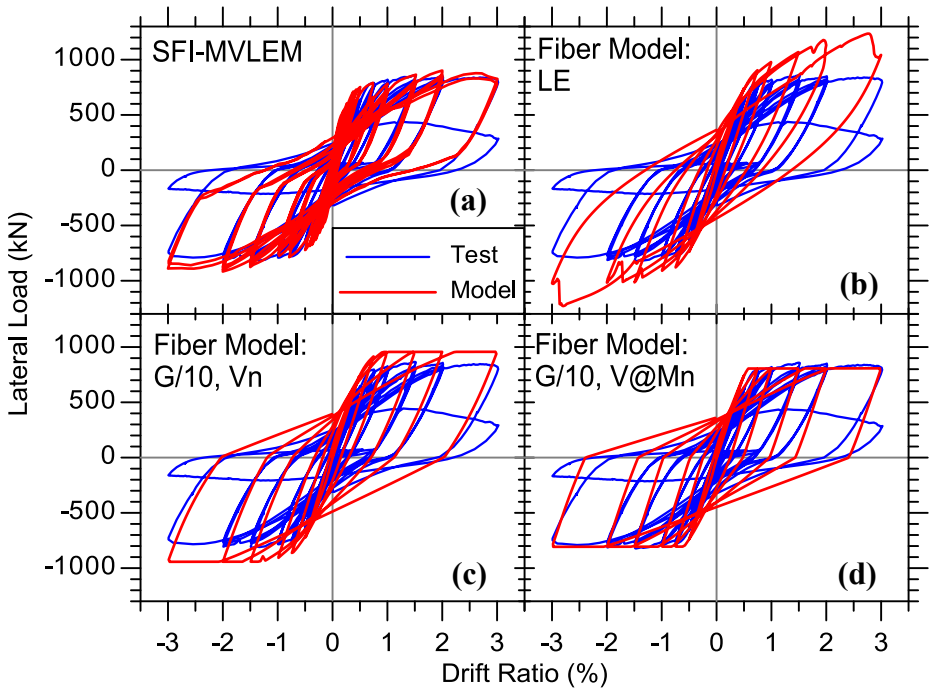

Figure 6-71 Lateral-Load-versus-Top-Total-Deformation Response for RW-A15-P10-S78

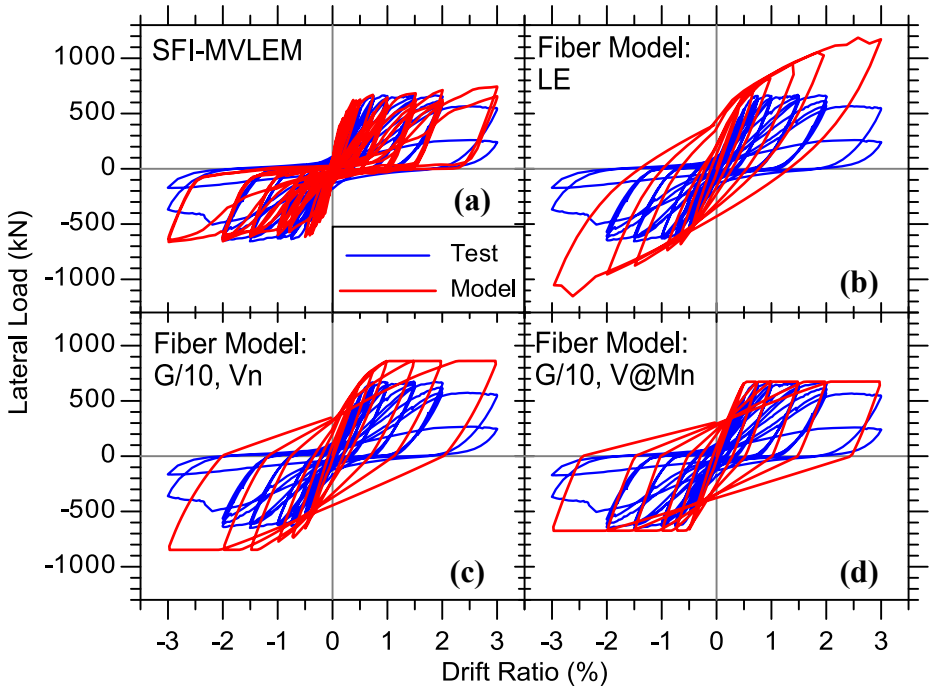

Figure 6-72 Lateral-Load-versus-Top-Total-Deformation Response for RW-A15-P2.5-S64

Figure 6-70 to Figure 6-72 further reveal that the load-deformation responses predicted with the uncoupled model in which shear load-deformation behavior is governed by the bi-linear relationship (cases (2) and (3)) match reasonably well experimentally measured lateral-load-versus-top-wall-displacement responses. The peak lateral load capacity of the walls is generally governed by the yielding force defined in the shear load-deformation relationship, which is either nominal shear strength of the wall (V_n) calculated according to Eq. 6-11 for case (2), or lateral force corresponding to nominal moment capacity of the wall ($V@M_n$) for case (3). The observed agreement between test model results is somehat arbitrary for case (2), since the five walls tested were designed such that $V@M_n$ (case (3)) is 0.80 to 0.90 of $V@V_n$ (case (2)); if $V@M_n$ were considerably less than $V@V_n$, e.g., 0.50 to 0.60, then the agreement would not be as good. For a more slender RC wall specimen (Test 2, aspect ratio of 2.0) experimentally measured maximal

lateral load capacity of the wall agrees very well with the calculated V_n value (Figure 6-70(c)), whereas using $V@M_n$ underestimates wall lateral capacity by approximately 10 % (Figure 6-70(d)). For shorter wall specimens with aspect ratio of 1.5, the analytical model in case (2) (governed by V_n) overestimates lateral wall capacity by approximately 15% and 20% for Test 4 (Figure 6-71(c)) and Test 5 (Figure 6-72(c)), respectively, while the use of $V@M_n$ provides reasonably good match between analytical and experimental results (Figure 6-71(d) and Figure 6-72(d)). Although, the pinching characteristics of the hysteretic load-deformation behavior are improved comparing to the case with linear-elastic shear stiffness (case (1)), the model still underestimates pinching observed in experimental results.

Lateral-load-versus-top-shear-displacement relations obtained using SFI-MVLEM and uncoupled model are compared against experimental results for RW-A20-P10-S38 (Test 2), A15-P10-S78 (Test 4), and RW-A15-P2.5-S64 (Test 5) in Figure 6-73 to Figure 6-75, respectively. It can be observed from Figure 6-73(b), Figure 6-74(b), and Figure 6-75(b) that initial stiffness of G/10 (PEER-ATC-72-1 report), used as the initial shear stiffness in all three considered cases of prescribed shear force-deformation relationship, approximates reasonably well the effective shear stiffness at flexural yielding for the three specimens. The figures further reveal that, after the lateral load reaches either nominal shear capacity of the wall (V_n) for case (2) (Figure 6-73(c), Figure 6-74(c), and Figure 6-75(c)), or shear force corresponding to nominal flexural capacity ($V@M_n$) for case (3) (Figure 6-73(d), Figure 6-74(d), and Figure 6-75(d)), i.e., when the capacity of the implemented shear force-deformation relationship is reached, the majority of lateral deformation of the wall model is associated with shear deformations, implying that shear deformations are significantly overestimated using uncoupled model for cases (2) and (3).

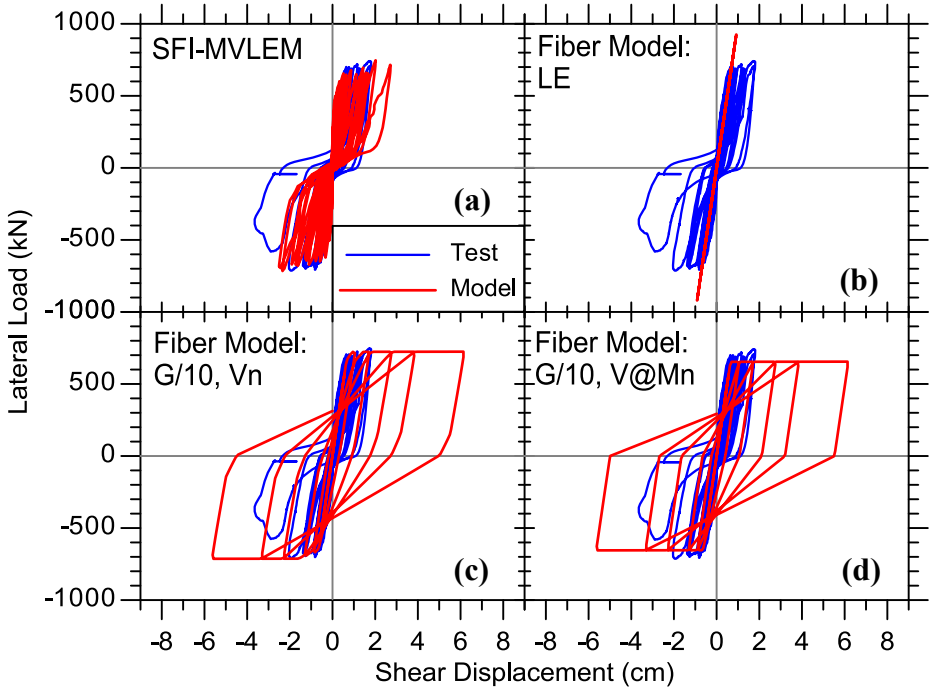

Figure 6-73 Lateral-Load-versus-Top-Shear-Deformation Response for RW-A20-P10-S38

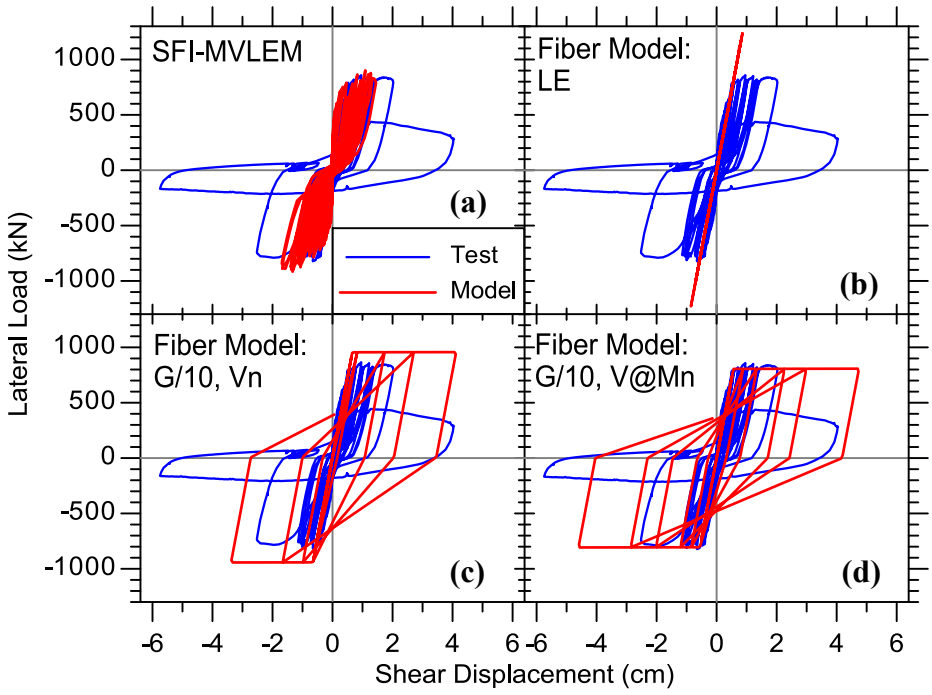

Figure 6-74 Lateral-Load-versus-Top-Shear-Deformation Response for RW-A15-P10-S78

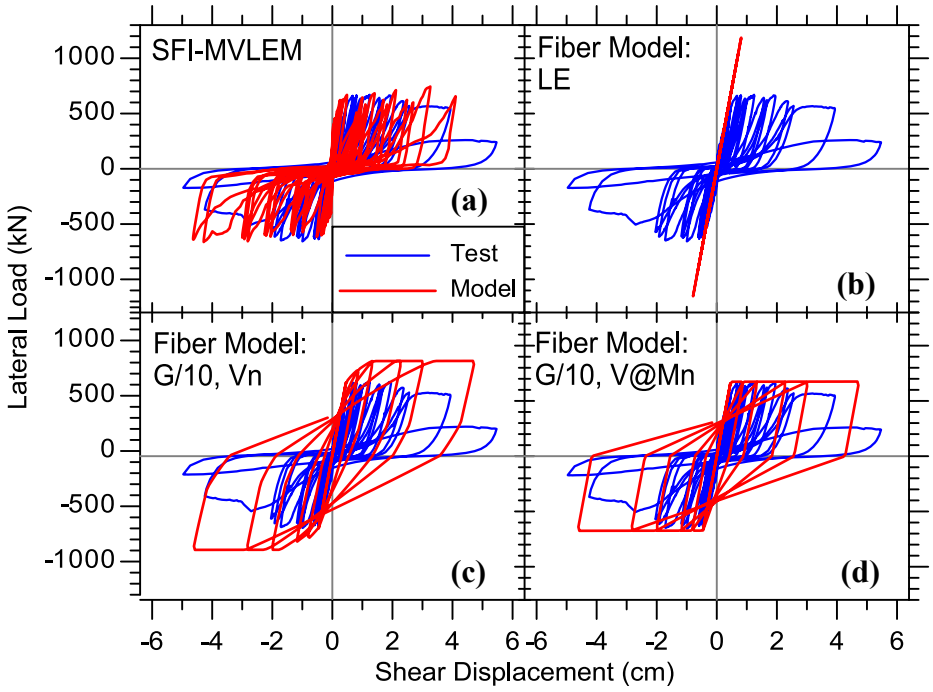

Figure 6-75 Lateral-Load-versus-Top-Shear-Deformation Response for RW-A15-P2.5-S64

Overall, the use of a fiber-based wall model with linear-elastic shear force-deformation behavior can produce reasonably good results for slender walls in which linear-elastic shear deformations are expected, i.e., slender RC walls. As presented here, the use of linear-elastic shear behavior generally overestimates wall lateral load capacity for moderately slender walls after the flexural (and/or shear) yielding occurs. The use of the uncoupled wall model (i.e., fiber model) with implemented bi-linear shear force-deformation relationship (e.g., as described in this section) provides reasonably good predictions of the lateral-load-versus-total-top-displacement responses in terms of the initial stiffness and the wall lateral load capacity. However, the predicted response of the wall does not represent a realistic wall behavior in terms of deformations associated with shear and flexure.

CHAPTER 7

MODELING OF SLENDER RC WALLS

This chapter demonstrates the capability of the proposed analytical approach to predict the behavior of RC walls with flexure dominated behavior by comparing model responses with experimental data for a slender RC wall specimen with aspect ratio equal to 3.0 (specimen RW2 tested by Thomsen and Wallace, 1995, 2004).

7.1. Overview of Experimental Studies

Experimental results were obtained for an approximately quarter-scale rectangular wall specimen (RW2) tested by Thomsen and Wallace (1995, 2004) that was 3.66 m (144 in.) tall, 102 mm (4 in.) thick, and 1.22 m (48 in.) long; therefore, the wall aspect ratio was equal to 3.0. Detailing requirements at the boundaries of the wall specimen were evaluated using the displacement-based design approach presented by Wallace (1994, 1995). Well-detailed boundary elements were provided at the edges of the wall over the bottom 1.22 m (48 in.). A capacity design approach was used to provide sufficient shear capacity using ACI 318-89 Eq. (21-6), to resist the shear that develops for the probable wall moment. The vertical reinforcement was anchored within the pedestal at the base of the walls with sufficient development length as well as 90-degree hooks. Cross-section with reinforcement configuration of a wall specimen RW2 is shown in Figure 7-1.

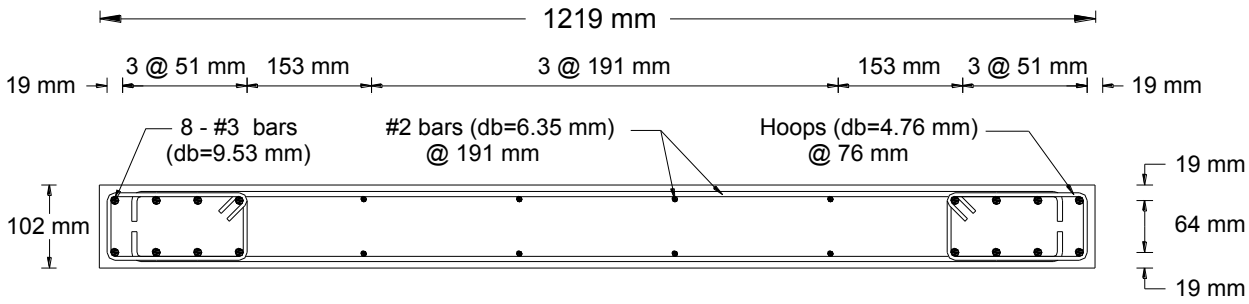

Figure 7-1 Cross-Sectional View of Specimen RW2 (Orakcal, 2004)

The compressive strength of concrete used for design of the wall specimen was 27.6 MPa; however, concrete compressive strengths at the time of testing ranged from 28.7 to 58.4 MPa, with mean compressive strengths at the base of the wall specimen (0 to 0.91 m) of approximately 42.8 MPa and strain that corresponds to the peak compressive stress of approximately 0.002. Concrete stress-strain relationships determined from tests on standard 152.4 x 304.8 mm (6 x 12 in.) concrete cylinders are presented in Figure 7-2.

Three different types of reinforcing steel were used in the test: (1) deformed #3 (d_b = 9.53 mm) bars as longitudinal reinforcement with typical Grade 60 properties (414 MPa), (2) deformed #2 (d_b = 6.35 mm) bars with a yield stress of approximately 448 MPa as uniformly distributed web reinforcement, and (3) 4.76 mm diameter smooth wire as transverse reinforcement in the boundary regions with the yield stress of approximately 448 MPa. Experimentally measured steel stress-strain relationships obtained from tensile tests on rebar samples are presented in Figure 7-3.

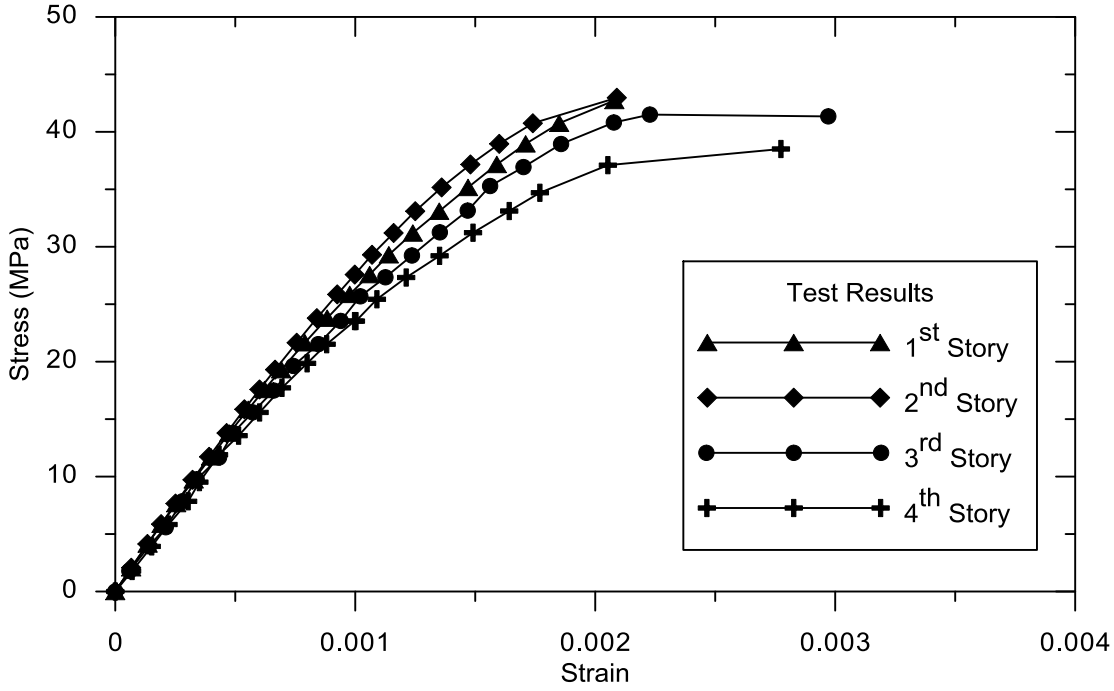

Figure 7-2 Experimentally Measured Concrete Stress-Strain Relations

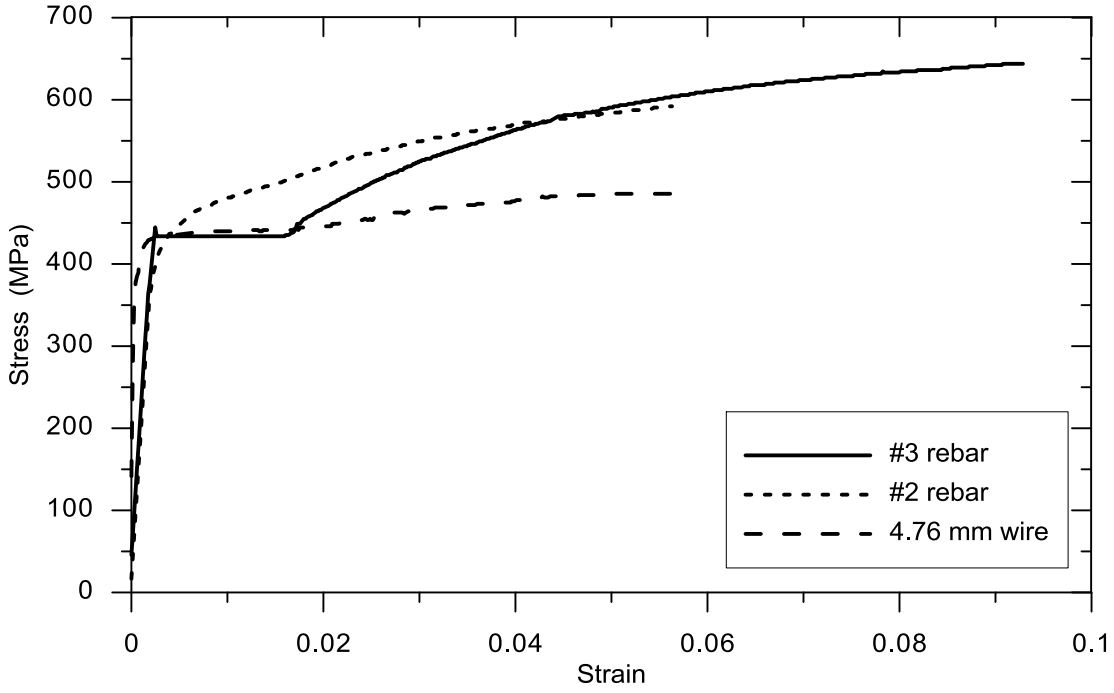

Figure 7-3 Experimentally Measured Steel Stress-Strain Relationships

Instrumentation used to measure displacements, loads, and strains at critical locations of wall specimen is presented in Figure 7-4. Four wire potentiometers (WPs) were mounted to a rigid steel reference frame to measure lateral displacements at 0.91 m (36 in.) intervals over the wall height. A linear potentiometer was also mounted horizontally on the pedestal to measure horizontal slip of the pedestal along the strong floor. Two additional linear potentiometers were mounted vertically at each end of the pedestal to measure rotation caused by uplift of the pedestal from the strong floor. Shear deformations were measured through the use of wire potentiometers mounted on the bottom two stories (in an "X" configuration) of each specimen (Figure 7-4). Sliding shear at the wall-pedestal interface was not observed during the tests.

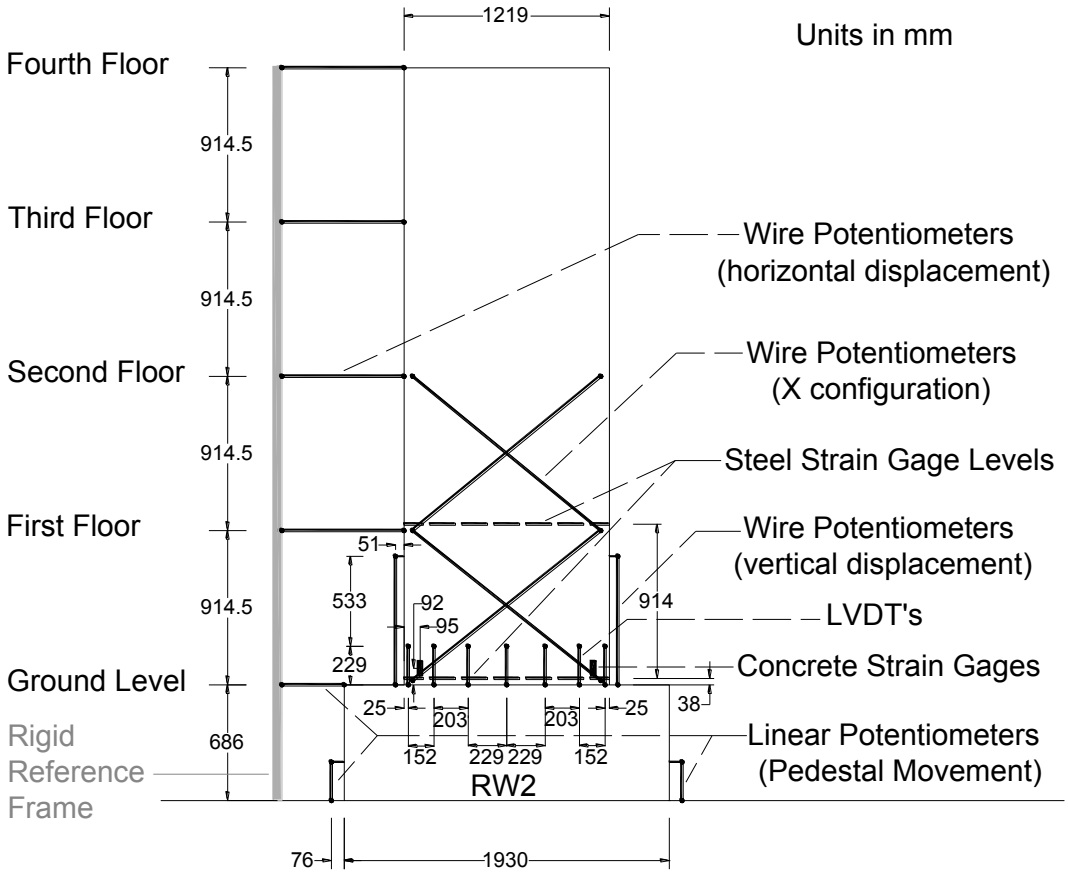

Figure 7-4 Instrumentation on the Wall Specimen (Orakcal, 2004)

Axial (vertical) displacements at the wall boundaries were measured using two WPs mounted directly to the wall. Linear variable differential transducers (LVDTs) were mounted vertically between the wall and the pedestal (Figure 7-4) over a gauge length of 229 mm (9 in.) at various locations along the web of a wall so that axial strains and section curvatures could be calculated. Axial concrete strains within the boundary regions of the specimen were also measured using embedded concrete strain gauges, and strains in the reinforcing steel were measured through the use of strain gauges at wall base and first-story levels (Figure 7-4).

The wall specimen was tested in an upright position. An axial load of approximately $0.07 A_g f'_c$ was applied at the top of the wall by hydraulic jack mounted on top of the load transfer assembly and held constant throughout the duration of each test. Cyclic lateral displacements were applied to the wall using a hydraulic actuator mounted horizontally to a reaction wall. The peak (reversal) lateral top displacement drift levels applied to the specimen were 0.1%, 0.25%, 0.5%, 0.75%, 1.0%, 1.5%, 2.0%, and 2.5%. More detailed information concerning the wall specimen and testing protocol is presented in Thomsen and Wallace (1995, 2003).

7.2. Calibration of the Analytical Model

7.2.1. Geometry

The wall cross section for the analytical model was discretized with six RC panel elements defined along the length of the wall (m = 6) as shown on Figure 7-5(a). The model discretization along the wall height was performed to allow consistent comparisons between model and experimental results at all locations where LVDTs are placed; accordingly, 8 SFI-MVLEM elements (n = 8), all of equal height of 45.7 cm (18 in.), were used along the wall height as

illustrated on Figure 7-5(b). A value of 0.4 was selected for the parameter *c* defining the center of relative rotation for each wall element, based on previous studies (Vulcano et al., 1988; Orakcal and Wallace, 2006).

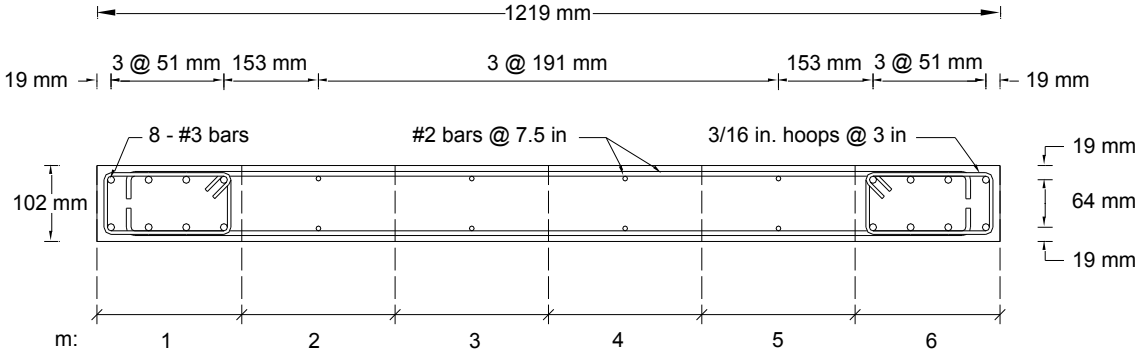

(a) Discretization of a Cross-Section

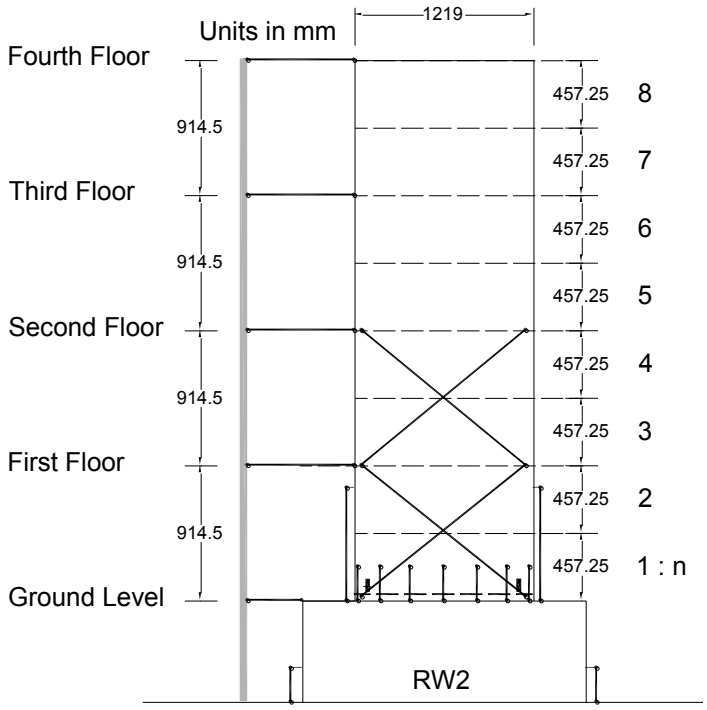

(b) Vertical Discretization

Figure 7-5 Discretization of Specimen RW2

7.2.2. Materials

The analytical stress-strain relationship for concrete was calibrated for selected values of peak stress f'_c, strain at peak stress ε'_c, elastic modulus E_c, and also by the parameter *r* defining the shape of the envelope curve using results of monotonic stress-strain tests conducted at time of testing on standard 152.4 x 304.8 mm (6 x 12 in.) cylinder specimens of the concrete used in the construction of the walls. The experimental and analytical stress-strain relationships for unconfined concrete are presented in Figure 7-6.

The compression envelope used in the analytical model for confined concrete was calibrated using the empirical relations proposed by Mander et al. (1988) for the peak compressive stress and the strain at peak compressive stress. The confined concrete stress-strain behavior was manipulated based on the area, configuration, spacing, and yield stress of the transverse reinforcement (435 MPa for the 4.76 mm wire) in the confined regions within the first story height (0 to 0.91 m) of the test specimens. The confined and unconfined compression envelopes are also illustrated in Figure 7-6.

The postpeak slope of the monotonic stress-strain relations implemented in the wall model for confined and unconfined concrete were calibrated (via the parameter ε_{cr}) to agree with the postpeak slope of the Saatcioglu and Razvi (1992) model for both confined and unconfined concrete. The parameters used for the calibration of the monotonic (envelope) stress-strain relations for confined and unconfined concrete in compression are presented in Table 7-1. The parameters for unconfined concrete also were used for the wall web as well as for cover concrete areas within the boundary regions of the walls.

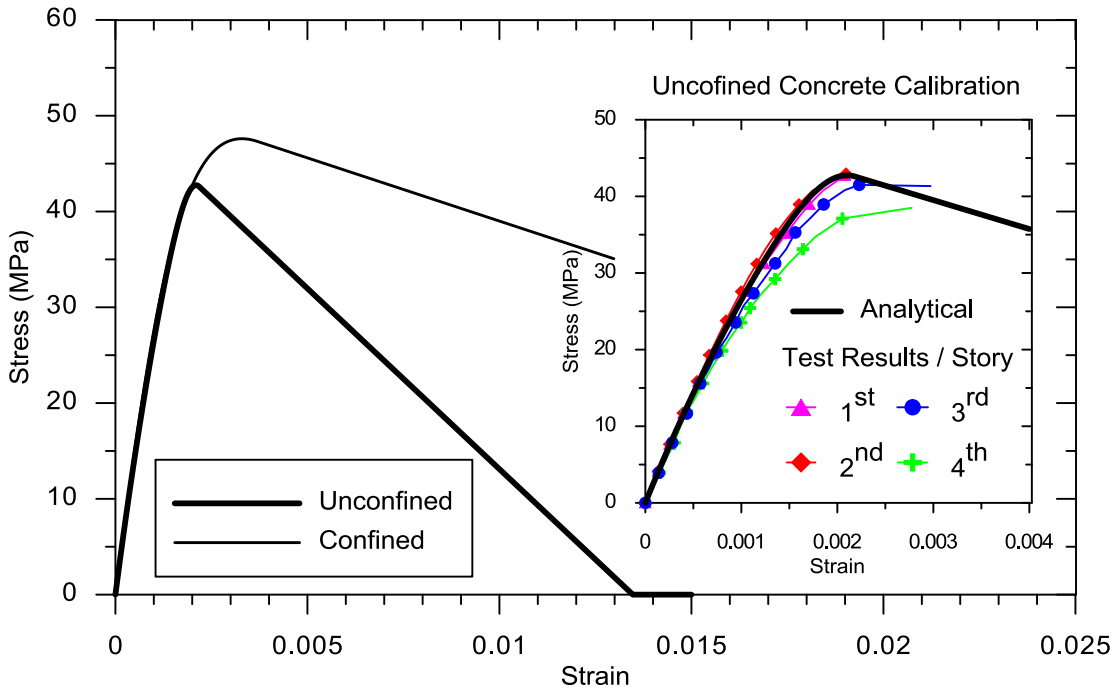

Figure 7-6 Calibration of the Constitutive Model for Confined Concrete

The concrete tensile strength was determined from the relationship $f_t = 0.31\sqrt{f'_c}$ (MPa), and a value of 0.00008 was selected for the strain ε_t at peak monotonic tensile stress, as suggested by Belarbi and Hsu (1994). The shape of the monotonic tension envelope was calibrated via the parameter r to reasonably represent the average postcrack stress-strain relation proposed by Belarbi and Hsu (1994) that considers the effects of tension stiffening on concrete. The parameters used for the calibration of the stress-strain relationship for concrete in tension are presented in Table 7-1. This approach is the same as described in Chapter 5 for specimens tested by Tran and Wallace (2012).

The analytical stress-strain relationship for reinforcing described by the Menegotto and Pinto (1977) model was calibrated to reasonably represent the results of monotonic stress-strain tests

conducted on the #3 (d_b = 9.53 mm = 0.375 in.) and #2 (d_b = 6.35 mm = 0.25 in.) deformed bars used at the wall boundaries and within the web, respectively. Tensile yield strengths of σ_y = 434 MPa (62.9 ksi) and σ_y = 448 MPa (64.98 ksi), an elastic modulus of E_0 = 200 GPa, and a strain-hardening ratio of b = 0.02 were assigned for the bare #3 and #2 bars, respectively. The tensile yield strength and strain-hardening parameters were modified according to the empirical relations proposed by Belarbi and Hsu (1994) to include the effect of tension stiffening on steel bars embedded in concrete. Figure 7-7 shows the calibrated analytical steel stress-strain relations in tension as well as results of stress-strain tests (on bare bars) for the reinforcement used in the construction of the wall specimens. Parameters of steel material stress-strain model used for bars #2 and #3 were presented in Table 7-1.

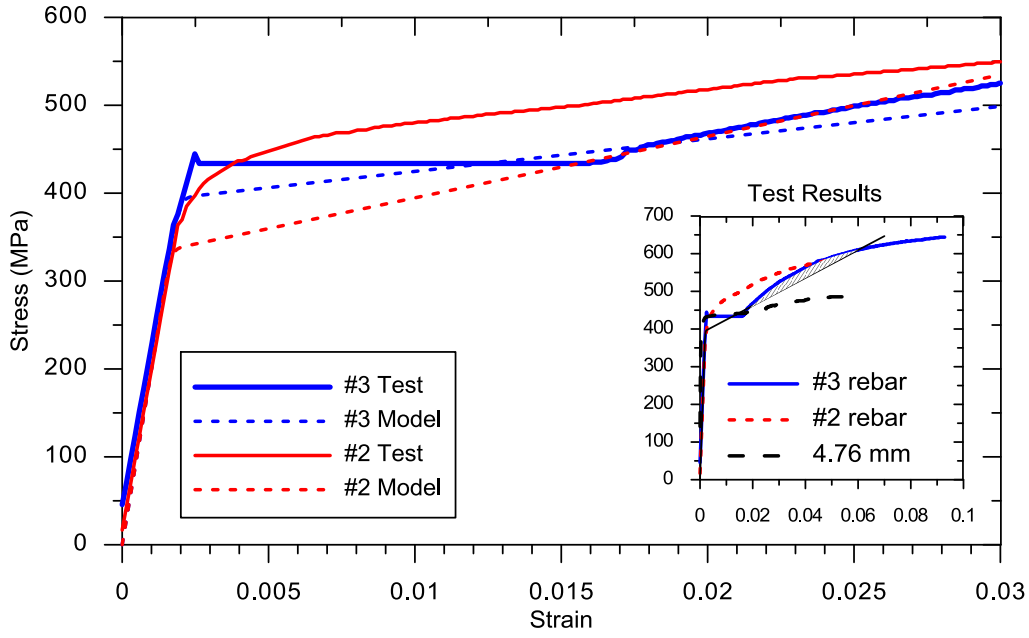

Figure 7-7 Calibration of the Constitutive Model for Reinforcing Steel

The values of parameters R_0, a_1, and a_2, accounting for the cyclic degradation of the curvature coefficient R and the Bauschinger effect, are adopted as proposed by Elmorsi et al. (1998) and were equal to $R_0 = 20$, $a_1 = 18.5$, and $a_2 = 0.0015$.

Table 7-1 Calibrated Parameters of Steel and Concrete Material Constitutive Models

Steel Tension and Compression			Concrete in Tension		Concrete in Compression		
Parameter	#2	#3	Parameter	Unconfined and Confined	Parameter	Confined (boundary)	Unconfined (web)
f_y, MPa (ksi)	336 (48.7)	395 (57.3)	f_t, MPa (ksi)	2.03 (0.29)	f'_c, MPa (ksi)	47.6 (6.90)	42.8 (6.21)
E_0,GPa (ksi $\times 10^3$)	200 (290)	200 (290)	ε_t	0.00008	ε'_c	0.0033	0.0021
b	0.035	0.0185	E_c, MPa (ksi)	31.03 (4500)	E_c, MPa (ksi)	31.03 (4500)	31.03 (4500)
			ε_{cr}	∞	ε_r	0.0037	0.0022
			r	1.2	r	1.9	7

7.2.3. Shear Resisting Mechanism

Calibration of the parameters of shear resisting mechanism, i.e. friction coefficient of shear aggregate interlock model η and stiffness parameter of dowel action α (both described in Section 3.3.2), for wall specimen RW2 (Thomsen and Wallace, 1995) was performed similarly as for wall specimens tested by Tran and Wallace (2012) described in Chapter 5 (Section 5.2.3). Values of $\eta =$ 0.2, 0.5, 1.0, and 1.5, and $\alpha =$ 0.005, 0.01, 0.02, and 0.03 were considered for shear friction coefficient and dowel stiffness parameter, respectively. The combination of parameters

that produced the best match with the experimental results for specimen RW2 in terms of the overall load-deformation response was $\eta = 0.2$ and $\alpha = 0.03$. It can be observed that a lower value of shear friction coefficient is used for specimen RW2 in comparison to wall specimens tested by Tran and Wallace (2012) (i.e. $\eta = 0.2$ versus $\eta = 1.0$), which might be associated with the flexure-dominated behavior of this wall specimen due to its higher aspect ratio (equal to 3.0) compared to wall specimens tested by Tran and Wallace (aspect ratio equal to 2.0 and 1.5). It should be mentioned that the calibration of the shear resisting mechanisms for specimen RW2 presented here is only preliminary given the limited number of parameters η and α considered.

7.3. Comparison of Experimental and Analytical Results

7.3.1. Load versus Total Displacement Relations

Figure 7-8 provides the comparison of experimental and analytical lateral-load-versus-top-wall-displacement response of specimen RW2. It can be observed from the figure that the analytical model captures reasonably well the lateral stiffness and the lateral load capacity of the wall specimen throughout the cyclic loading history; lateral stiffness of the wall specimen is slightly overestimated at drift levels lower than 0.5%, whereas the lateral load is underestimated by approximately 5% in the negative loading direction. In addition, major characteristics of the cyclic wall load-deformation response are reasonably well captured by the analysis including cyclic degradation of stiffness, plastic residual displacement at zero lateral load and pinching.

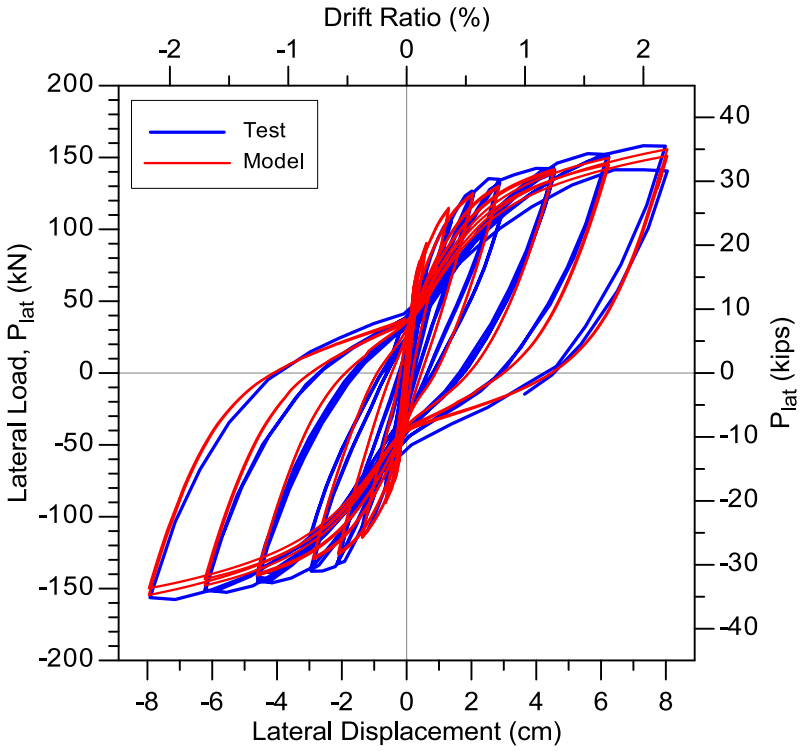

Figure 7-8 Top Lateral Displacements for Specimen RW2

Figure 7-9 compares the experimentally measured and analytically predicted vertical profiles of the total lateral displacements at peak lateral drifts (positive and negative) corresponding to drift levels of 0.5%, 0.75%, 1.0%, 1.5%, 2.0%, and 2.5%. As discussed earlier, the wall discretization is in agreement with the locations of wall instrumentation used to measure lateral displacement profile; therefore, the experimental and analytical displacement profiles were obtained at height levels of 914 mm (36 in.), 1829 mm (72 in.), 2743 mm (108 in.), and 3658 mm (144 in.) above the wall base. Experimentally measured lateral displacement profiles for wall specimen RW2 are nonlinear over the first story level (914 mm or 36 in.), whereas for the remaining stories the profiles are almost linear, which is captured reasonably well in the analytical results, i.e., the analytical results describe well the shape of lateral displacement profiles. Analytical model

predicts closely the lateral displacement profiles at drift levels lower and equal to 1.0%, whereas at higher drift levels, analytical results underestimate lateral deformations along the first story by approximately 10 to15%.

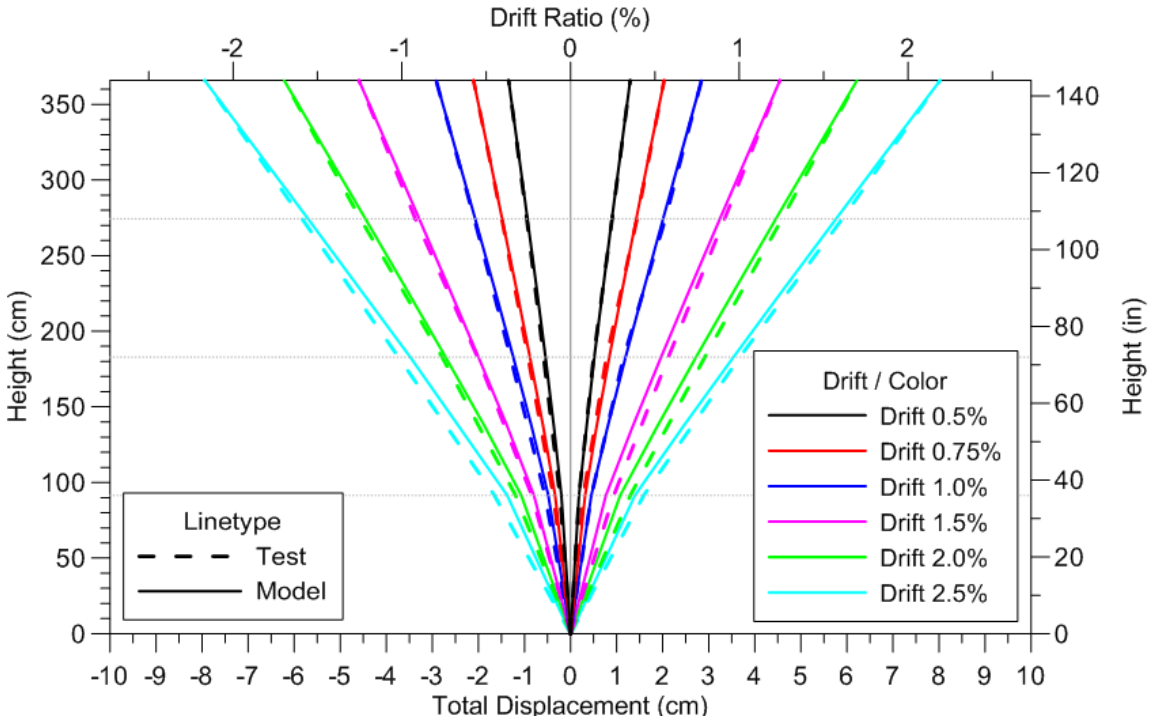

Figure 7-9 Total Displacement Profile for Specimen RW2

7.3.2. Flexural Component of Lateral Deformation

The experimental and analytical relationships between lateral load and flexural component of lateral deformation at the top of the first story level are compared in Figure 7-10. It can be observed from presented results that the analytical model captures reasonably well the flexural stiffness, but overestimates the flexural displacements over the first story by approximately 15% throughout the cyclic loading history. In addition, the analytical model captures reasonably well the moderately pinched shape of the flexural load-deformation response.

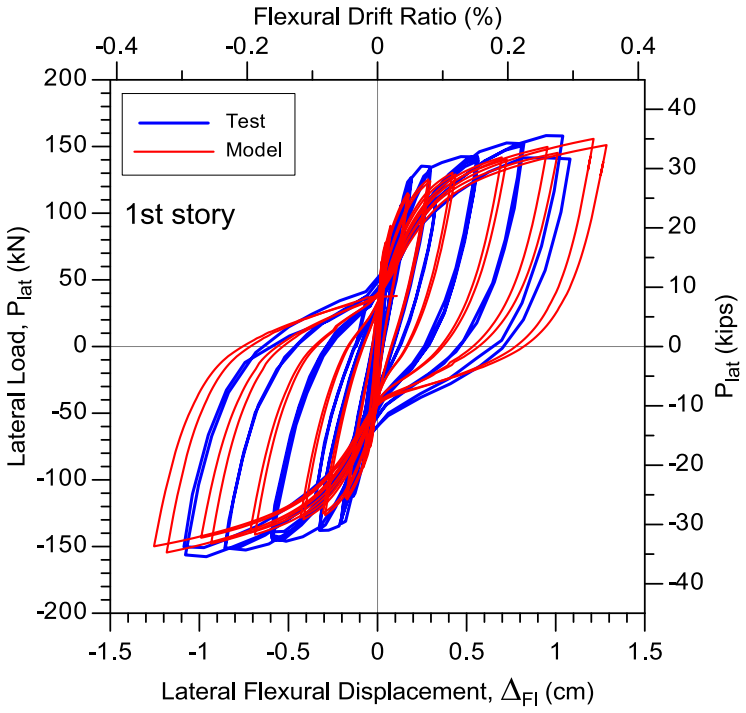

Figure 7-10 1st Story Flexural Displacement for Specimen RW2

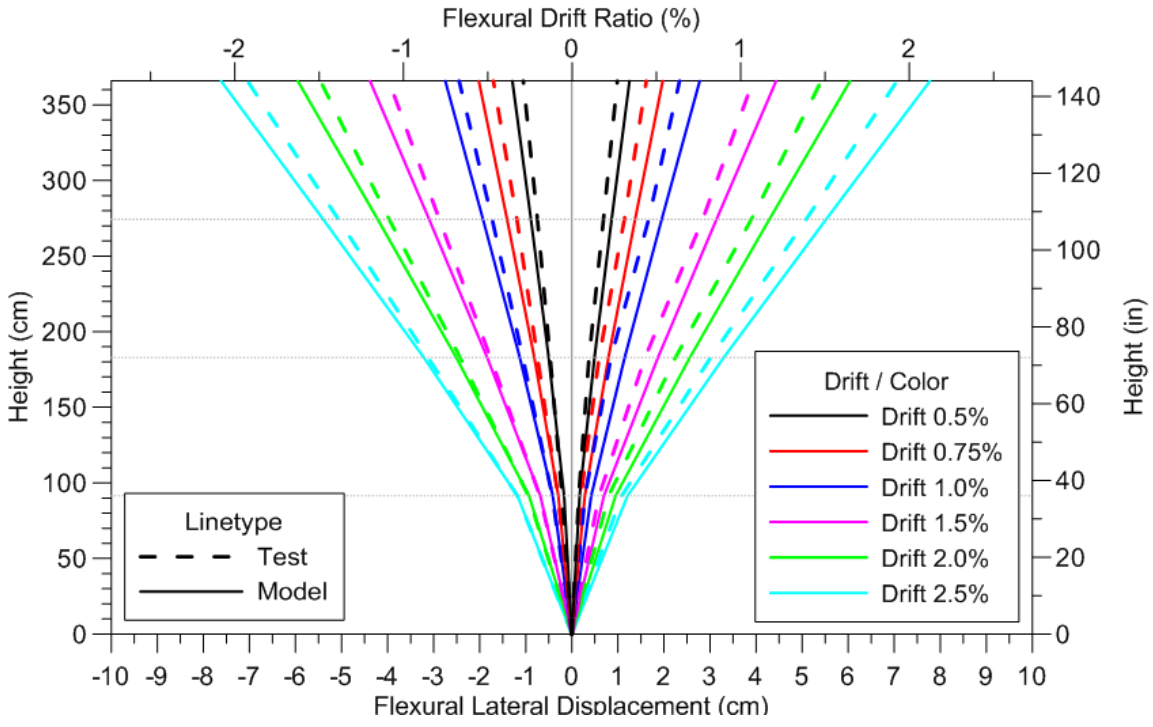

Figure 7-11 Flexural Displacement Profiles for Specimen RW2

Figure 7-11 compares vertical profiles of flexural displacements obtained experimentally and analytically at peak lateral displacements (positive and negative) corresponding to drift levels of 0.5%, 0.75%, 1.0%, 1.5%, 2.0%, and 2.5% derived from flexural deformations at 914 mm (36 in.), 1829 mm (72 in.), 2743 mm (108 in.), and 3658 mm (144 in.) above the wall base. The presented results reveal that analytical model captures well the nonlinear shape of the flexural displacement profiles and the concentration of the nonlinear flexural deformations over the first story height. However, the analytical results overestimate flexural deformations by approximately 10-20% over the wall height at all drift levels.

7.3.3. Shear Component of Lateral Deformation

The experimental shear deformations are derived from the measurements obtained using sensors placed in "X" configuration over the first two story heights as shown in Figure 7-4. The lateral-load-versus-shear-displacement relationships obtained from the experimental and analytical results for the first story are compared in Figure 7-12. It can be observed from the figure that analytical model does not describe properly the shape of the experimentally measured shear force-deformation response and significantly overestimates its pinching characteristics. In addition, the magnitudes of the first story shear deformations predicted by the model are approximately 50% lower than the experimentally measured shear deformations throughout the entire loading history.

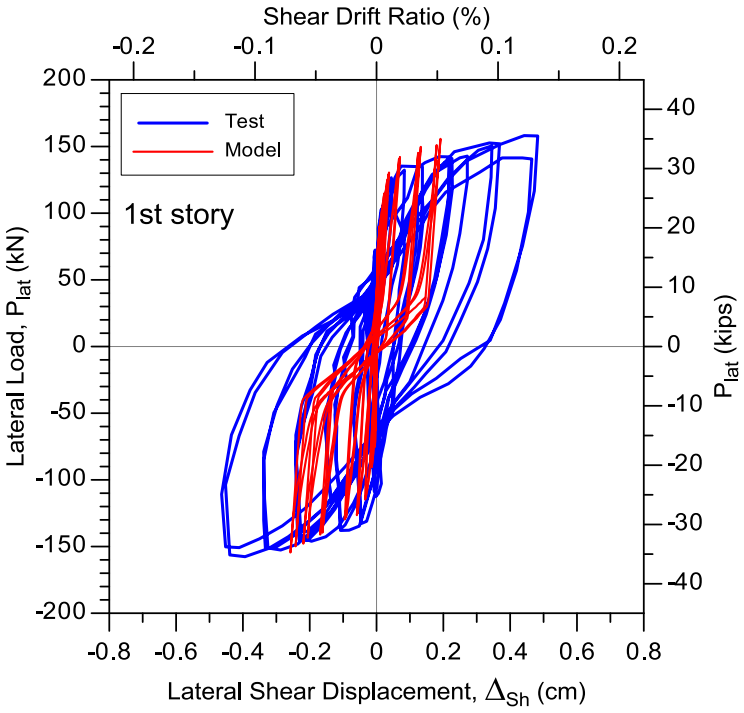

Figure 7-12 1st Story Shear Displacement for Specimen RW2

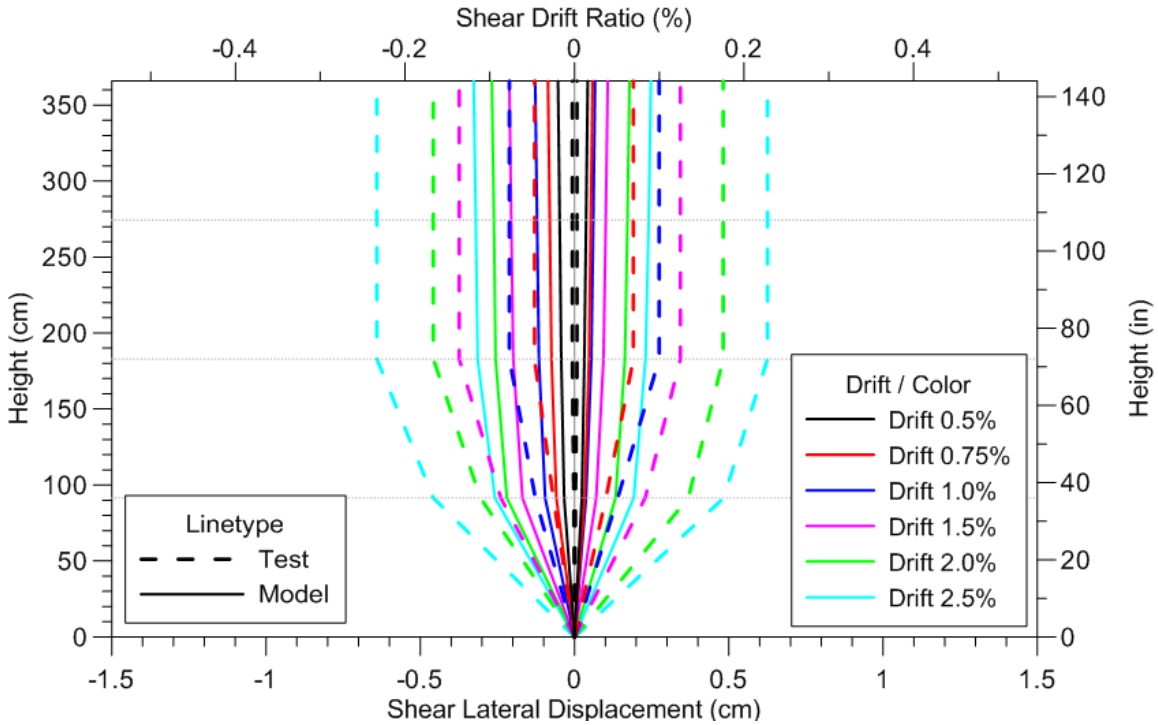

Figure 7-13 Shear Displacement Profiles for Specimen RW2

Analytically derived vertical profiles of shear deformations shown in Figure 7-13 significantly underestimate shear deformations over the height of the wall measured during the experiment. Although the model does not provide good predictions of the magnitude of shear deformations, the analytical results describe reasonably well the concentration of nonlinear shear deformations over the bottom two stories of the wall. Given that there were no sensors placed in "X" configuration over the third and fourth story to measure shear deformations in the experiment, and since the measured shear load-deformation response of the second story was almost linear-elastic, the shear deformations of the third and fourth story were assumed to be the same as the second story shear deformations, i.e. it was assumed that shear behavior of third and fourth stories is also linear-elastic with the same shear stiffness as for the second story.

7.3.4. Contributions of Shear and Flexural Deformations

The experimentally and analytically derived contributions of shear and flexural deformations to the lateral displacement over the first story at peak drift levels of 0.5%, 0.75%, 1.0%, 1.5%, 2.0%, and 2.5% are compared in Figure 7-14. It can be observed from the figure that analytical results capture the experimentally measured constant contribution of flexural and shear deformations throughout the cyclic loading history. However, the analytical results underestimate contributions of shear deformations by approximately 40% (i.e., analytical and experimental shear contributions are 15% and 23%, respectively) and overestimate contributions of flexural deformations by approximately 10% (i.e., analytical and experimental flexural contributions are 85% and 77%, respectively) on the average of all drift levels.

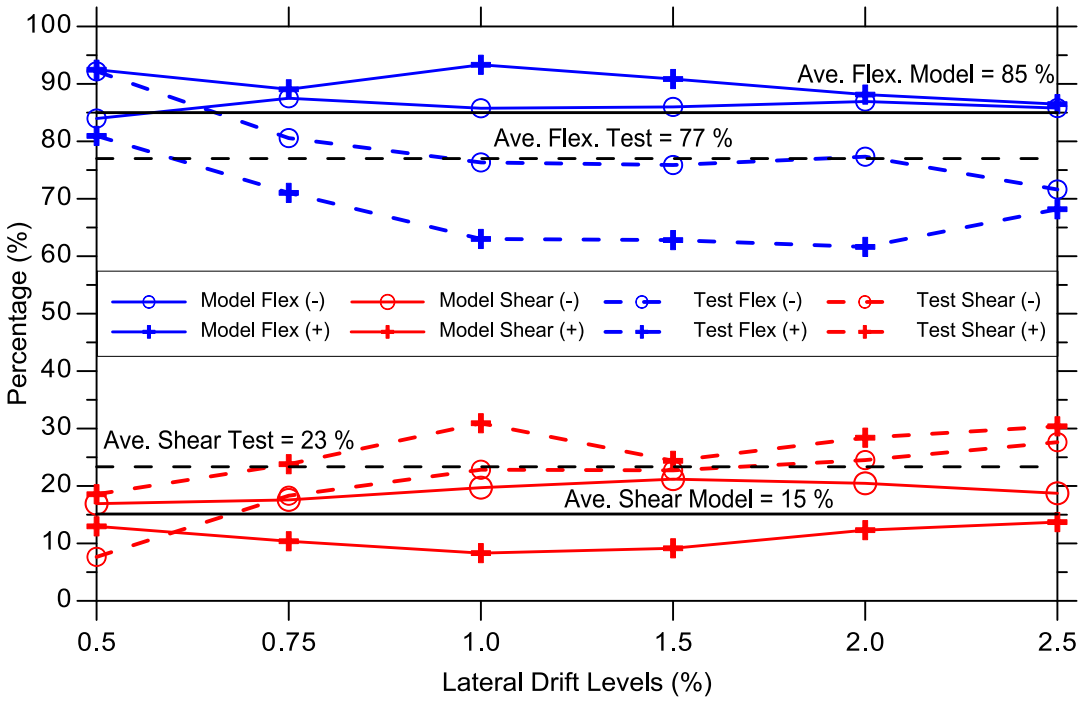

Figure 7-14 Contributions to 1st Story Lateral Displacement for Specimen RW2

7.3.5. Effective Stiffness

Effective secant flexural and shear stiffness are obtained from experimental and analytical results at peak drift levels as described in Chapter 6 (Section 6.7) and compared in Figure 7-15. As it can be observed from Figure 7-15(a), the analytical model predicts reasonably well the effective secant flexural stiffness at all drift levels. The analytical results generally underestimate the experimental effective secant flexural stiffness by approximately 20% in the initial loading cycle and by approximately 5% at lateral drifts lower than 1.5%, whereas at the remaining drift levels analytical results match closely experimentally derived effective secant flexural stiffness of specimen RW2. In contrast, Figure 7-15(b) reveals that the experimentally derived effective secant shear stiffness is significantly overestimated by the analysis (more than two times) at all

drift levels, which is associated with significant underestimation of shear displacements by the analytical model as shown in Section 7.3.3.

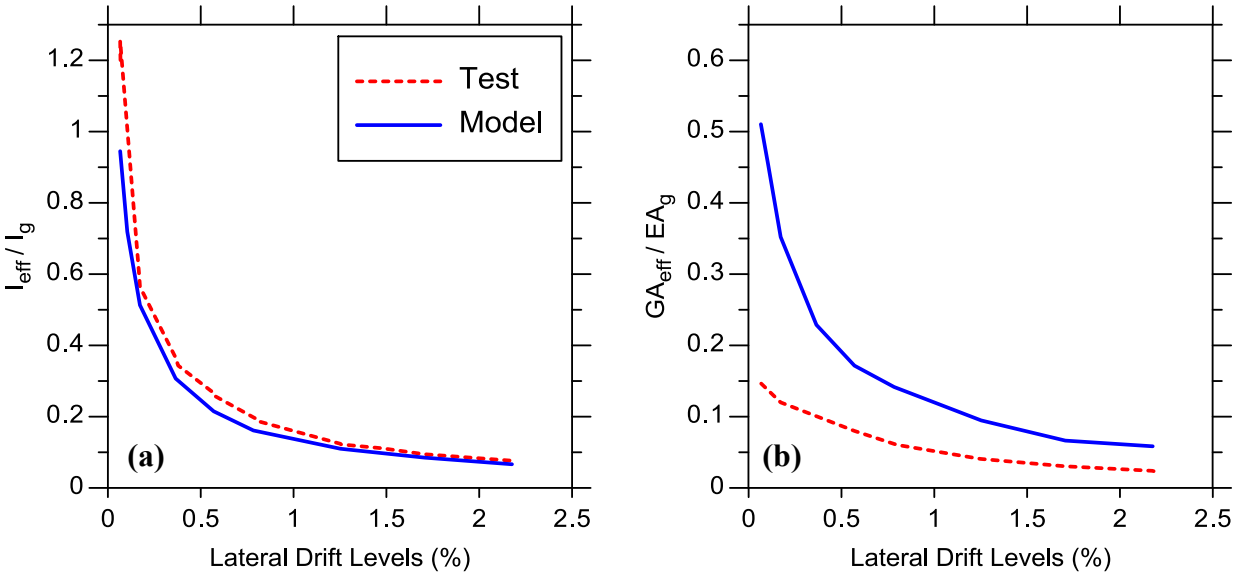

Figure 7-15 Effective Secant Stiffness for Specimen RW2: (a) Flexural, (b) Shear

7.3.6. Local Responses

Measured and predicted responses at specific locations are compared in Figure 7-16, which plots the average concrete strains measured by the seven LVDTs over a 229 mm (9 in.) gauge length at the base of the wall, at applied peak positive top displacement (top displacement reversal) data points, for selected drift levels applied during testing. Similar trends were observed in the results for other drift levels and also for peak negative top displacement data points; therefore, only limited results are presented. Results shown in Figure 7-16 illustrate that the analytical model predicts reasonably well the tensile strain profile, but significantly underestimates the compressive strains. These results are very similar with the one presented by Orakcal and Wallace (2006) who predicted behavior of RW2 using the MVLEM (Orakcal et al., 2004), with

uncoupled shear and flexural behavior, and suggested that the underestimation of compressive strains is likely associated with the inability of the model to capture nonlinear shear deformations. As presented in Section 7.3.3, the SFI-MVLEM significantly underestimates nonlinear shear deformations for specimen RW2, which leads to the underestimation of compressive strains, similarly as in results obtained with the uncoupled wall model. As presented in Section 6.8, for the case of moderately slender RC wall specimens (Tran and Wallace, 2012), nonlinear shear deformations are reasonably well predicted which resulted in improved predictions of compressive strains.

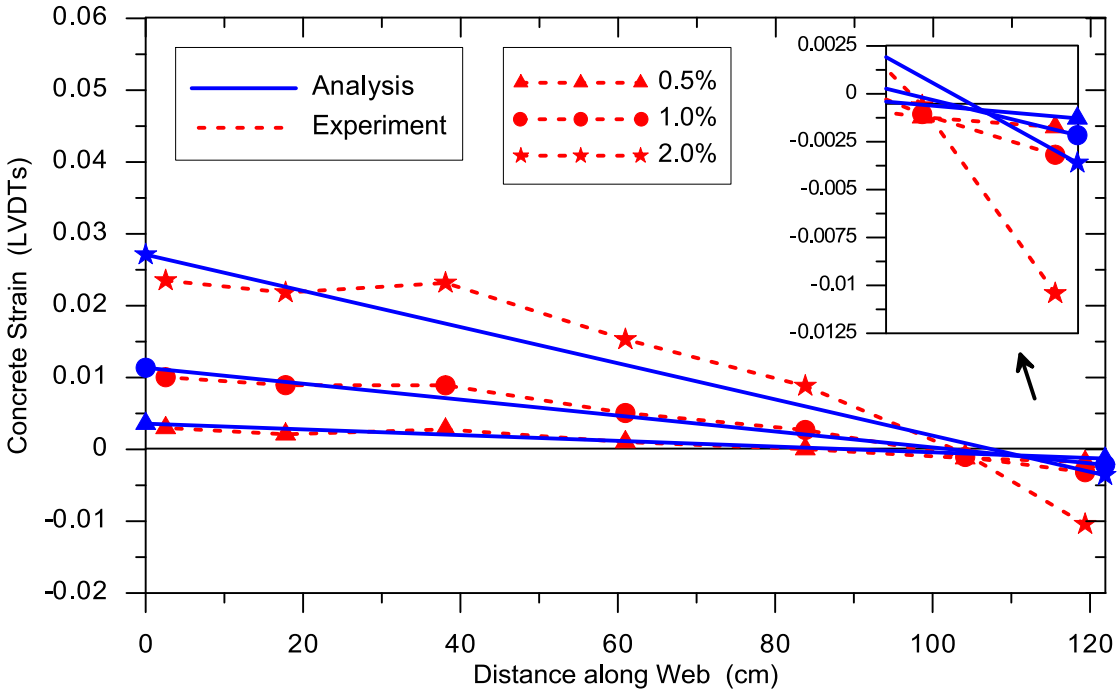

Figure 7-16 Vertical Strain Profiles for Specimen RW2

Figure 7-17 compares experimental and analytical rotations corresponding to peak drift levels in positive and negative directions obtained over the height of the first story (914 mm or 36 in.); in the experimental results the rotations were calculated from vertical deformations over the first

story height obtained from measurements at wall boundaries (Figure 7-4). It can be observed from the figure that analytical model overestimates the first story rotations by approximately 15% throughout the cyclic loading history, which is consistent with results presented in Section 7.3.2 that reveal that the model generally overestimates flexural deformations of the wall by approximately 10 to 20%.

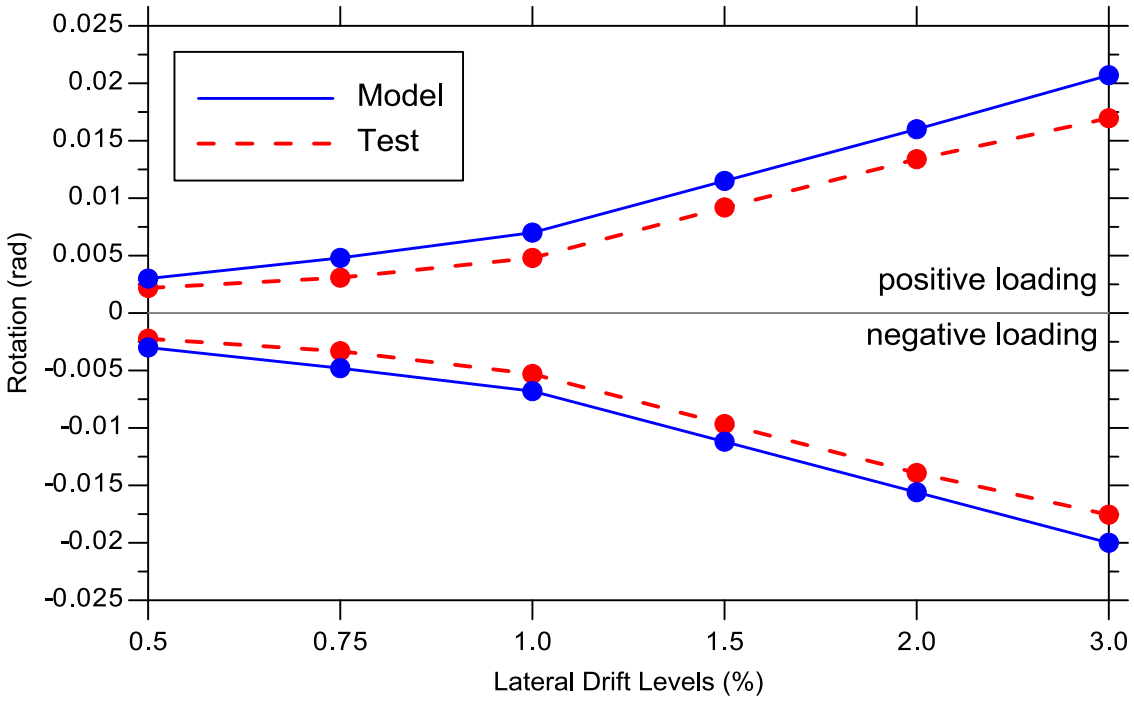

Figure 7-17 Base Rotations for Specimen RW2

Overall, the proposed SFI-MVLEM describes reasonably well the overall load-deformation relationship of the wall specimen RW2 (Thomsen and Wallace, 19995) with flexure-dominated behavior and aspect ratio of 3.0. However, the analytical results are less accurate in terms of contributions of flexural and shear deformations as well as local responses, particularly compressive strains. By comparing the results presented in this and previous chapter (Chapter 6),

it can be observed that the response predictions obtained for wall specimen with flexure-dominated behavior are generally less accurate than the results obtained for moderately slender RC wall specimens in which both nonlinear shear and flexural deformations significantly contribute to the lateral deformation. Therefore, the implemented RC panel model with shear resisting mechanisms (i.e., shear aggregate interlock and dowel action) needs to be improved in order to capture accurately the response of slender RC walls. One possible improvement may include the implementation of more accurate criteria for determination of the crack directions (i.e., direction of the second crack) since in slender walls crack directions can significantly deviate from two perpendicular directions (used in current model formulation). In addition, more detailed calibration of existing shear resisting mechanisms and/or the development of new, more flexible and less sensitive shear resisting mechanism(s) along the cracks of RC panel model would improve analytical predictions for slender RC walls.

CHAPTER 8

SUMMARY AND CONCLUSIONS

The objective of this study was to develop, calibrate and verify using experimental results a modeling approach that integrates flexure and shear interaction under cyclic loading conditions to reliably predict the inelastic response of RC walls. The proposed analytical model incorporates a RC panel behavior described by a fixed-crack angle model into a fiber-based Multiple-Vertical-Line-Element-Model (MVLEM). The interaction of axial and shear behavior is captured at the RC panel (macro-fiber) level, which allows interaction between shear and flexural behavior at the model element level.

Attributes of model responses were investigated to assess the ability of the model to incorporate interaction between nonlinear flexural and shear deformations in RC walls subjected to reversed cyclic loading. In addition, modeling parameters were varied to study the sensitivity of analytically predicted global and local wall responses to changes in these parameters as well as to identify which parameters require the greatest care with respect to model calibration. Finally, detailed studies were conducted to calibrate the model by comparing analytically predicted and experimentally measured or derived responses for five moderate aspect ratio RC wall specimens (aspect ratio 1.5 and 2.0) with significant observed shear-flexure interaction (Tran and Wallace, 2012) and a slender wall specimen (aspect ratio 3.0) with modest observed shear-flexure interaction (specimen RW2; Thomsen and Wallace, 1995). These comparisons were conducted at various locations and response levels to assess the ability of the SFI modeling approach to

capture cyclic responses of RC walls as well as to address model shortcomings and arrive at recommendations for further model improvements.

8.1. Overview of Analytical Model

The baseline model adopted in this study was the fiber-based Multiple-Vertical-Line Element-Model (MVLEM, Orakcal et al., 2004), with uncoupled flexural and shear force-displacement response, which has been shown to provide good predictions of nonlinear flexural behavior of slender RC structural elements. In the proposed coupled wall model (so-called SFI-MVLEM), a RC panel model with a fixed-crack-angle is implemented into a fiber-based model formulation to incorporate the interaction between flexural and shear behavior that has been observed experimentally (Massone and Wallace, 2004). Uniaxial stress-strain relationships are used to represent the behavior of concrete along compression struts, the orientation of which remain unchanged after cracking occurs, whereas the behavior of reinforcing steel is described by uniaxial stress-strain relationships applied along the directions of reinforcing steel bars. Although stress–strain relationships for concrete applied along the directions of fixed concrete struts are fundamentally uniaxial in nature, they incorporate biaxial softening effects including compression softening and biaxial damage. The shear resisting mechanism along cracks of the RC panel model is accomplished using a friction-based shear aggregate interlock model and linear-elastic dowel action model to capture the resistance of reinforcing bars crossing the fixed-angle crack plane. Each shear resisting mechanism is characterized by a parameter that requires calibration, i.e., a friction coefficient for shear aggregate interlock and a stiffness parameter for dowel action. The approach adopted for the interaction model is similar to the formulation used for the MVLEM; however, additional degrees of freedom, axial strains in the horizontal direction

at each RC panel element, are needed to complete the element strain field. Finally, the resultant horizontal stress of concrete and reinforcing steel is set to zero to provide sufficient equations to complete equilibrium of each RC panel macro-fiber.

8.2. General Attributes and Sensitivity of Analytical Model Results

Based on analysis results, it was revealed that the proposed analytical model captures nonlinear shear deformations and their coupling with nonlinear flexural deformations at the model element level under cyclic loading conditions throughout the entire loading history. In addition, it was shown that the model successfully captures the hysteretic characteristics of the overall load-displacement response of walls (for total, flexure, and shear deformations), systematic tendencies in lateral load capacity and contributions of flexural and shear deformations to lateral displacements when varying the walls aspect ratios, and different shear demands at flexural capacity (i.e., varying the behavior modes that is flexure- or shear-dominated).

Apart from material constitutive parameters, the only other parameters associated with the model are the number of uniaxial elements used along the length of the wall cross section, the number of MVLEM elements stacked on top of each other along the height of the wall, and the parameters of shear resisting mechanisms incorporated in the RC panel model formulation. Analytical studies indicated that model results are relatively insensitive to the selection of either the number of MVLEM elements along the height of the wall or the number of uniaxial elements along the wall length, provided that reasonable values are selected in order to adequately represent the overall wall geometry. As well, it was demonstrated that by modifying the post-peak branches of stress-strain relationships of materials according to the element sizes to

maintain the constant fracture strain energy of an element, it is possible to provide analytical results that are insensitive to the choice of the element size after the peak strength is reached.

Investigation of the sensitivity of analytical results to parameters associated with shear resisting mechanisms of RC panel model revealed that the predicted lateral-load-versus-top-lateral-displacement responses and the magnitudes of shear and flexural deformations are relatively insensitive to friction coefficient of shear aggregate interlock; however, these quantities were sensitive to changes in the dowel action stiffness parameter, especially the pinching characteristics of the load-deformation response and magnitude of the contribution associated with shear deformations. In general, an increase in dowel action stiffness increases the lateral load capacity and decreases the relative contribution of shear deformations to the total lateral displacement and the pinching characteristics of the total load-deformation response. For example, doubling the value of parameter α (from 0.005 to 0.01) decreases the contribution of shear deformations by roughly 10% (from approximately 48% to 43%). Given the sensitivity of analytical predictions to the dowel action stiffness parameter, calibration of model results is required for this parameter to achieve accurate predictions of wall responses, which is considered to be the biggest shortcoming of the proposed modeling approach.

8.3. Calibration of the Analytical Model

Since the implemented constitutive RC panel model relates panel response directly to uniaxial constitutive stress-strain behavior of concrete and reinforcing steel, advanced state-of-the-art hysteretic material constitutive relationships were implemented in the model formulation. This allows the user to relate analytical responses directly to physical material behavior and provides

a more robust modeling approach than, e.g., empirical-based models. The constitutive relationships implemented in this study provide a direct and flexible approach to incorporate important material behavioral features (e.g., Bauschinger's effect in reinforcing steel, hysteretic behavior of concrete in continuous compression and tension, progressive gap closure, tension stiffening effect, biaxial damage) into the analysis. For a reliable prediction of wall responses, the constitutive parameters of the stress-strain relationships adopted in the wall model are calibrated based on the mechanical properties of the materials used in the construction of the walls modeled, or based on parameters previously verified by other researchers (e.g., for confinement, tension stiffening, biaxial damage, cyclic stress-strain behavior of steel and concrete).

The calibration of the analytical model with respect to parameters of shear resisting mechanism was performed by adopting a constant value of shear friction coefficient (1.0 for aspect ratio 1.5 and 2.0 walls, and 0.2 for aspect ratio 3.0 walls), since analytical results are insensitive to this parameter, and selecting a value of dowel action stiffness parameter. The value of dowel action stiffness parameter that provided the most accurate predictions of experimentally measured lateral-load-versus-top-wall-displacement responses (in terms of lateral load capacity, lateral stiffness and pinching) was determined for each of the wall specimens and general trends between the values selected for this parameter were observed with respect to wall aspect ratio, axial load level, and shear stress level. A limited set of parameters were used in this study to calibrate the model results with respect to the shear resisting mechanisms; therefore, the calibration study presented here is limited in scope; additional studies should be conducted to verify the observed trends and to possibly develop more robust relationships between wall

characteristics and parameters that describe shear resisting mechanisms (and possibly alternative forms of shear resisting mechanisms).

8.4. Model Correlation with Test Results

Comparisons between experimentally measured and analytically predicted wall responses indicate that the SFI-MVLE model, as implemented in this study, provides accurate predictions of load-versus-total-top-deformation responses for all considered wall specimens in terms of wall stiffness, lateral load capacity, and pinching behavior; analytical results generally overestimate lateral stiffness at drift levels lower than approximately 0.5%, whereas at the remaining drift levels the predicted lateral strength and stiffness closely match experimentally measured results. As well, it was shown that analytical model captures reasonably well the propagation of concrete cracks, as well as distribution and orientation of concrete cracks observed in tests. Various failure mechanisms observed during tests (typically at 3.0% drift) were not appropriately represented in the model due to inability of the model to describe these mechanisms, such as buckling of reinforcing bars and shear sliding at the base of the wall. Model improvements to address these shortcomings are possible within the framework developed.

Comparisons of lateral-load-versus-top-shear and -top-flexural displacement responses indicated that the SFI-MVLEM captures successfully the near-simultaneous occurrence of shear and flexural yielding, indicating that the model describes adequately experimentally observed shear-flexure interaction for all considered wall specimens. Furthermore, lateral deformations associated with flexural and shear deformations at the top of the wall specimens derived from test results were reasonably well predicted throughout the cyclic loading history for the

moderately slender walls (aspect ratio 1.5 and 2.0). Model predictions were generally within 10% of experimentally measured (or derived) values for the relative contributions of flexural and shear deformations to wall lateral displacements over the wall height. However, for the slender wall specimen studied (aspect ratio 3.0), although the model captures well the general trends of flexural and shear deformations during cyclic loading, the shear deformations predicted by the analysis were approximately 50% of the experimentally measured shear deformations. Therefore, additional studies of more slender walls are needed.

Comparisons of vertical profiles of total, shear, and flexural deformations along the height of the wall specimens revealed that analytical results describe well the experimentally derived vertical profiles of total, flexural, and shear deformations and the concentration of nonlinear flexural and shear deformations at the wall base within a height of assumed plastic hinge region of one-half the wall length. In addition, the contributions of flexural and shear deformations along the height of the walls were predicted with reasonably accuracy (approximately within 10% to 20%) for the moderately slender wall specimens with aspect ratios equal to 1.5 and 2.0, whereas for the aspect ratio 3.0 wall specimen, shear deformations were significantly underestimated.

The accuracy of analytical results at local response levels was investigated by comparing experimental and analytical vertical strain profiles, strain histories, and rotations over an assumed plastic hinge length of one-half the wall length for the well-detailed walls. The model predicts with reasonable accuracy the measured tensile and compressive strains and plastic hinge rotations, with analytical predictions that are within 15% of the experimentally measured or derived values. Results revealed that SFI-MVLEM predictions of concrete compressive strains at wall boundaries were significantly better than values obtained from an

uncoupled wall model (e.g., MVLEM), which tends to underestimate concrete compressive strains.

Overall, the macroscopic wall model presented herein provides a flexible platform to assess nonlinear cyclic response for RC walls by incorporating interaction between nonlinear shear and flexural responses under cyclic loading at both the global and local response levels. Implementation of the model into a computational platform (e.g., "OpenSees") will provide design engineers improved analytical capabilities to model the behavior of structural walls and their interaction with other structural elements, which is essential for application of performance-based design.

8.5. Future Studies and Possible Model Improvements

Based on the studies presented, the following topics are suggested as areas to conduct future studies:

1. This study showed that analytical predictions obtained using the proposed SFI-MVLEM are sensitive to parameters of shear resisting mechanisms of RC panel model incorporated in model formulation. Therefore, calibration of these parameters using an extensive experimental wall database that includes specimens with various configurations (i.e., aspect ratio, web and boundary reinforcement, confinement, failure mechanisms) is recommended to derive numerical relationships between these parameters and particular wall characteristics (e.g., aspect ratio, shear stress, axial load). In addition, development and implementation of models that describe the shear resistance along concrete cracks without the use of ad-hoc parameters might improve model reliability and efficiency.

2. The proposed SFI-MVLEM was shown to provide accurate predictions of shear and flexural deformations for moderately slender RC walls (aspect ratio 1.5 and 2.0), whereas for slender RC wall specimen (aspect ratio of 3.0) the deformations associated with shear and flexure were not well predicted. Future studies could focus on development and implementation of a robust RC panel model that will enable accurate modeling of slender RC walls (or walls with low M/Vl_w ratios).

3. Implementation of a constitutive model for reinforcing bars that captures the onset of rebar buckling and post-buckling behavior, as well as the modeling of shear sliding mechanism along the base of the wall, would enable the analytical model to capture significant strength loss that was observed in the experiments but not captured by the current model. Without these features, lateral strength degradation will be under-estimated using the proposed model.

4. Previous studies (e.g., Massone et al., 2009) demonstrated that the assumption of zero resultant horizontal stress at each RC panel macro-fiber is not valid for RC walls with shear span-to-depth ratios lower than approximately 0.35. The implementation of expressions proposed by other researchers (e.g., Massone et al., 2009) to describe the distribution of axial strains in the horizontal direction along the wall length for low shear span-to-depth ratio walls (squat walls) could be incorporated into the formulation of SFI-MVLEM to address this issue.

5. The SFI-MVLEM can also be extended to allow direct modeling of three-dimensional responses by revising the formulation described in Chapter 3 to consider biaxial bending and bi-directional shear behavior.

6. The present model can be extended to incorporate nonlinear dynamic responses via adaptation of an incremental dynamic analysis algorithm.

REFERENCES

1. Bazant Z., Xiang Y. and Prat, P. (1996), “Microplane Model for Concrete—Part I: Stress-Strain Boundaries and Finite Strain,” *Journal of Engineering Mechanics*, Vol. 122, No. 3, p.p. 245-254.
2. Belarbi A. and Hsu T.C. (1994), “Constitutive Laws of Concrete in Tension and Reinforcing Bars Stiffened By Concrete,” *ACI Structural Journal*, Vol. 91, No. 4, p.p. 465-474.
3. Belarbi H. and Hsu T.C. (1994), “Constitutive Laws of Concrete in Tension and Reinforcing Bars Stiffened by Concrete,” *ACI Structural Journal*, Vol. 91, No. 4, p.p. 465-474.
4. Belarbi A. and Hsu T.C. (1995), “Constitutive Laws of Softened Concrete in Biaxial Tension Compression,” *ACI Structural Journal*, Vol. 119, No. 12, p.p. 3590-3610.
5. Beyer K., Dazio A., and Priestley, M. J. N. (2011), "Shear Deformations of Slender Reinforced Concrete Walls under Seismic Loading," *ACI Structural Journal*, Vol. 108, No. 2, p.p. 167-177.
6. Brueggen B. L. and French C.W. (2010), “Simplified Modeling of Non-Rectangular RC Structural Walls,” *Proceedings of 9th U.S. National Conference and 10th Canadian Conference on Earthquake Engineering*, Paper 1713, Ontario, Canada.
7. Chang G.A. and Mander J.B. (1994), “Seismic Energy Based Fatigue Damage Analysis of Bridge Columns: Part I – Evaluation of Seismic Capacity,” *NCEER Technical Report* No. NCEER-94-0006, State University of New York, Buffalo.

8. Chorzepa M., Kim Y. J., Yun G. J., Harmon G. T. and Dyke S. (2011), "Cyclic Shear-Friction Constitutive Model for Finite Element Analysis of Reinforced Concrete Membrane Elements," *ACI Structural Journal*, Vol. 108, No. 3, p.p. 324-331.
9. Clarke M.J. and Hancock G.J. (1990), "A Study of Incremental-Iterative Strategies for Non-Linear Analyses," *International Journal for Numerical Methods in Engineering*, Vol. 29, p.p. 1365-1391.
10. Coleman J. and Spacone E. (2001), "Localization issues in forced-based frame elements," *ASCE Journal of Structural Engineering*, Vol. 127, No. 11, p.p. 1257-1265.
11. Collins M.P. and Mitchell D. (1991), *Prestressed Concrete Structures*, Prentice Hall, New Jersey, USA.
12. Colotti V. (1993), "Shear Behavior of RC Structural Walls," *ASCE Journal of Structural Engineering*, Vol. 119, No. 3, p.p. 728-746.
13. Computer and Structures, Inc. (2006). Perform-3D V4: *Nonlinear Analysis and Performance Assessment for 3D Structures*, Berkeley, CA.
14. Dulacska H. (1972), "Dowel action of reinforcement crossing cracks in concrete," *ACI Structural Journal*, 69:12,754–757.
15. Elmorsi M.; Kianush M.R.; and Tso W.K. (1998), "Nonlinear Analysis of Cyclically Loaded Reinforced Concrete Structures," *ACI Structural Journal*, Vol. 95, No. 6, p.p. 725-739.
16. Elwood K. J. (2002), "Shake Table Tests and Analytical Studies on the Gravity Load Collapse of Reinforced Concrete Frames," *PhD Dissertation*, University of California, Berkeley, p.p. 419.

17. Filippou F. C.; Popov E. G.; and Bertero V. V. (1983), "Effects of Bond Deterioration on Hysteretic Behavior of Reinforced Concrete Joints," *EERC Report No. UCB/EERC–83/19*, Earthquake Engineering Research Center, University of California, Berkeley, California.
18. Fischinger M, Vidic T., Selih J., Fajfar P., Zhang H.Y., and Damjanic F.B. (1990), "Validation of a Macroscopic Model for Cyclic Response Prediction of RC Walls," in N.B. Bicanic and H. Mang (eds.), "Computer Aided Analysis and Design of Concrete Structures," Vol. 2, Pineridge Press, Swansea, p.p.1131-1142.
19. Fischinger M., Rejec K. and Isakovic T. (2012), "Modeling Inelastic Shear Response of RC Walls," *Proceedings of 15th World Conference on Earthquake Engineering*, Lisbon, Portugal.
20. Hofbeck J.A., Ibrahim I.O., and Mattock A. H. (1969), "Shear Transfer in Reinforced Concrete," *ACI Journal Proceedings*, Vol. 66, No. 2, p.p. 119-128.
21. Hsu T.C. (1988), "Softened Truss Model Theory for Shear and Torsion," *ACI Structural Journal,* Vol. 85, No. 6, p.p. 624-635.
22. Hsu T.C. and L. Zhang (1996) "Tension Stiffening in Reinforced Concrete Membrane Elements," *ACI Structural Journal*, Vol. 93, No. 1, p.p. 108-115.
23. Hsu T.C. and R.H. Zhu (2002), "Softened Membrane Model for Reinforced Concrete Elements in Shear," *ACI Structural Journal*, Vol. 99, No. 4, p.p. 460-469.
24. Jiang H. and Kurama Y. (2010), "Analytical Modeling of Medium-Rise Reinforced Concrete Shear Walls," *ACI Structural Journal*, Vol. 107, No 4. p.p. 400-410.

25. Johnson B. (2010) “Anchorage Detailing Effects on Lateral Deformation Components of R/C Shear Walls,” *MS Thesis*, Department of Civil Engineering, University of Minnesota, p.p. 353.
26. Kabeyasawa T., Shiohara H., Otani S., and Aoyama H. (1983), “Analysis of the Full-Scale Seven-Story Reinforced Concrete Test Structure,” *The Second US-Japan Workshop on Performance-Based Earthquake Engineering Methodology for Reinforced Concrete Building Structures*, Sapporo, Hokkaido, September, p.p. 17-29.
27. Lefas, I. D. and Kotsovos, M. D. (1990), “Strength and Deformation Characteristics of Reinforced Concrete Walls under Load Reversals,” *ACI Structural Journal*, Vol. 87, No. 6, pp. 716-726.
28. Mander J.B., Priestley M.J.N. and Park R. (1988), “Theoretical Stress-Strain Model for Confined Concrete,” *ASCE Journal of Structural Engineering*, Vol. 114, No. 8, p.p. 1804-1826.
29. Mansour M.Y. and T.C. Hsu (2005), “Behavior of Reinforced Concrete Elements under Cyclic Shear,” *ASCE Journal of Structural Engineering*, Vol. 131, No. 1, p.p. 44-53.
30. Mansour M.Y., T.C. Hsu and J.Y. Lee (2002), “Pinching Effect in Hysteretic Loops of R/C Shear Elements,” *ACI Special Publications*, Vol. 205, p.p. 293-321.
31. Massone L. M., Orakcal K., and Wallace J. W. (2006), “Modeling Flexural/Shear Interaction in RC Walls, ACI-SP-236, Deformation Capacity and Shear Strength of Reinforced Concrete Members under Cyclic Loadings," *American Concrete Institute*, Farmington Hills, MI, Paper 7, p.p. 127-150.

32. Massone L.M., and J. W. Wallace (2004), “Load – deformation responses of slender reinforced concrete walls,” *ACI Structural Journal* 101(1): 103-113.
33. Massone, L. M., Orakcal K.; and Wallace J. W. (2009), “Modeling of Squat Structural Walls Controlled by Shear," *ACI Structural Journal,* Vol. 106, No. 5, p.p. 646-655.
34. Mattock A.H. (1974), “Shear Transfer in Concrete Having Reinforcement at an Angle to the Shear Plane,” *ACI Special Publication*, Vol. 42, p.p. 17-42.
35. McKenna F., Fenves G. L., Scott M. H., and Jeremic B. (2000), Open System for Earthquake Engineering Simulation (OpenSees), Pacific Earthquake Engineering Research Center, University of California, Berkeley, CA.
36. Menegotto M. and Pinto E. (1973), “Method of Analysis for Cyclically Loaded Reinforced Concrete Plane Frames Including Changes in Geometry and Non-Elastic Behavior of Elements under Combined Normal Force and Bending,” *Proceedings, IABSE Symposium*, Lisbon, Portugal.
37. Mullapudi R.T. and Ayuob A.S. (2009), “Fiber Beam Element Formulation Using the Softened Membrane Model,” *ACI Special Publication*, Vol. 265, p.p. 283-308.
38. Mullapudi R.T., Charkhchi P. and Ayuob A.S. (2009), “Evaluation of Behavior of Reinforced Concrete Shear Walls through Finite Element Analysis,” *ACI Special Publication*, Vol. 265, p.p. 73-100.
39. Oesterle R.G., Fiorato A. E., Johal L.S., Carpenter J.E. and Corley W. G. (1976), “Earthquake Resistant Structural Walls – Tests of Isolated Walls,” Report to the National Science Foundation, Construction Technology Laboratories, Portland Cement Association, Skokie, IL, 315 p.p.

40. Oesterle R., Aristizabal-Ochoa J., Fiorato A., Russel H., and Corley W. (1979), "Earthquake Resistant Structural Walls—Tests of Isolated Walls: Phase II," Portland Cement Association, Skokie, IL, 327 p.p.
41. Orakcal K. (2004), "Nonlinear Modeling and Analysis of Slender Reinforced Concrete Walls," *PhD Dissertation*, Department of Civil and Environmental Engineering, University of California, Los Angeles.
42. Orakcal K., Conte J. P., and Wallace J. W. (2004), "Flexural Modeling of Reinforced Concrete Structural Walls - Model Attributes," *ACI Structural Journal*, V. 101, No. 5, p.p. 688-698.
43. Orakcal K. and Wallace J. W. (2006), "Flexural Modeling of Reinforced Concrete Walls - Experimental Verification," *ACI Structural Journal*, Vol. 103, No. 2, p.p. 196-206.
44. Orakcal K., Ulugtekin D., and Massone L.M. (2012), "Constitutive Modeling of Reinforced Concrete Panel Behavior under Cyclic Loading," *Proceedings of the 15th World Conference on Earthquake Engineering*, Lisbon, Portugal.
45. Ozcebe G., Saatcioglu M. (1989), "Hysteretic shear model for reinforced concrete members," *ASCE Journal of Structural Engineering*, Vol. 115, No. 1, p.p. 132–148.
46. Panagiotou M., Restrepo J. I., Schoettler M. and Kim G. (2012), "Nonlinear Cyclic Truss Model for Reinforced Concrete Walls," *ACI Structural Journal*, Vol. 109, No. 2, p.p. 205-214.
47. Pang D. and T.C. Hsu (1995), "Behavior of Reinforced Concrete Membrane Elements in Shear," *ACI Structural Journal*, Vol. 92, No. 6, p.p. 665-677.

48. Pang D. and T.C. Hsu (1996), "Fixed Angle Softened Truss Model for Reinforced Concrete," *ACI Structural Journal*, Vol. 93, No. 2, p.p. 197-207.

49. Petrangeli M., Pinto P. E., and Ciampi V. (1999), "Fiber element for cyclic bending and shear of RC structures. I: Theory," *ASCE Journal of Engineering Mechanics*, Vol. 125, No. 9, p.p. 994-1001.

50. Powell G. and J. Simons (1981), "Improved Iteration Strategy for Nonlinear Structures," *International Journal for Numerical Methods in Engineering*, Vol.17, p.p. 1455-1467.

51. Ramirez A. J. and Breen E. J. (1991), " Evaluation of a Modified Truss-Model Approach for Beams in Shear," *ACI Structural Journal*, Vol. 88, No. 5, p.p. 562-571.

52. Rejec K. (2011), "Inelastic shear behaviour of RC structural walls under seismic conditions (in Slovenian)," *PhD Dissertation*, University of Ljubljana.

53. Saatcioglu M. and Razvi S.R. (1992), "Strength and Ductility of Confined Concrete," *ASCE Journal of Structural Engineering*, Vol. 118, No. 6, p.p. 1590-1607.

54. Sayre B. (2003), "Performance evaluation of steel reinforced shear walls," *MS Thesis*, University of California, Los Angeles.

55. Stevens N.J. (1987), "Analytical Modeling of Reinforced Concrete Subjected to Monotonic and Reversed Loadings," *PhD Dissertation*, Department of Civil Engineering, University of Toronto.

56. Stevens N.J., M. Uzumeri and M.P. Collins (1991), "Reinforced concrete subjected to reversed cyclic shear-Experiments and constitutive model," *ACI Structural Journal*, Vol. 88, No. 2, p.p. 135-146.

57. Takeda T., Sozen M.A. and Nielsen N.N (1970), “Reinforced concrete response to simulated earthquakes,” *ASCE Journal of Structural Division*, Vol. 96, No. 12, p.p. 2557–2573.

58. Thomsen J.H. and Wallace J.W. (1995), “Displacement-Based Design of Reinforced Concrete Structural Walls: An Experimental Investigation of Walls with Rectangular and T-Shaped Cross-Sections,” *Report* No. CU/CEE-95/06, Department of Civil Engineering, Clarkson University, Postdam, New York.

59. Thomsen J. H., and Wallace J. W. (2004), “Experimental verification of displacement-based design procedures for slender reinforced concrete structural walls,” *ASCE Journal of Structural Engineering*, Vol. 130, No. 4, p.p. 618-630.

60. Tran T. A. (2012), “Experimental and Analytical Studies of Moderate Aspect Ratio Reinforced Concrete Structural Walls,” *PhD Dissertation*, Department of Civil and Environmental Engineering, University of California, Los Angeles.

61. Tran T. A. and Wallace J.W. (2012), "Experimental Study of Nonlinear Flexural and Shear Deformations of Reinforced Concrete Structural Walls," *Proceedings of the 15th World Conference on Earthquake Engineering*, Lisbon, Portugal.

62. Tsai W.T. (1988), “Uniaxial Compressional Stress-Strain Relation of Concrete,” *ASCE Journal of Structural Engineering*, Vol. 114, No. 9, p.p. 2133-2136.

63. Ulugtekin D. (2010), “Analytical Modeling of Reinforced Concrete Panel Elements Under Reversed Cyclic Loadings,” *M.S. Thesis*, Department of Civil Engineering, Bogazici University.

64. Valluvan R., Kreger M.E. and Jirsa J.O. (1999), “Evaluation of ACI-318-95 Shear Friction Provisions,” *ACI Structural Journal*, Vol. 96, No. 4, p.p. 473-482.

65. Vecchio F.J. and M.P. Collins (1986), "The Modified Compression-Field Theory for Reinforced Concrete Elements Subjected to Shear," *ACI Structural Journal*, Vol. 83, No. 2, p.p. 219-231.

66. Vecchio F.J. and M.P. Collins (1988), "Predicting the Response of Reinforced Concrete Beams Subjected to Shear Using Modified Compression Field Theory," *ACI Structural Journal*, Vol. 85, No. 3, p.p. 258-268.

67. Vecchio F.J. and M.P. Collins (1993), "Compression Response of Cracked Reinforced Concrete," *ASCE Journal of Structural Engineering*, Vol. 83, No. 2, p.p. 219-231.

68. Vintzeleou E.N. and Tassios T.P. (1987), "Behavior of dowels under cyclic deformations," *ACI Structural Journal*, Vol. 84, No. 1, p.p. 18-30.

69. Vulcano A., Bertero V. V., and Colotti V. (1988), "Analytical Modeling of RC Structural Walls," *Proceedings of 9th World Conference on Earthquake Engineering*, Vol. 6, Tokyo-Kyoto, Japan, p.p. 41-46.

70. Wood L. S. (1990), "Shear Strength of Low-Rise Reinforced Concrete Walls," *ACI Structural Journal*, Vol. 87, No. 1, p.p. 99-107.

71. Xu SY. and Zhang J. (2010), "Hysteretic Shear-Flexure Interaction Model of Reinforced Concrete Columns for Seismic Response Assessment of Bridges," *Earthquake Engineering and Structural Dynamics*.

72. Yassin, M. H. M. (1994), "Nonlinear Analysis of Presetressed Concrete Structures Under Monotonic and Cyclic Loads," *PhD Dissertation*, Department of Civil Engineering, University of California, Berkeley.

73. Zhang J and Xu SY. (2009), "Seismic Response Simulations of Bridges Considering Shear–Flexural Interaction of Columns," *Structural Engineering and Mechanics*; Vol. 31, No. 5, p.p. 545–566.